

NORTHWESTERN UNIVERSITY

Photoexcited Rylenediimide Radical Anions and Dianions for the Photoreduction of  
Carbon Dioxide Reduction Catalysts

A DISSERTATION

SUBMITTED TO THE GRADUATE SCHOOL  
IN PARTIAL FULLFILLMENT OF THE REQUIREMENTS

for the degree

DOCTOR OF PHILOSOPHY

Field of Chemistry

By

Jose Fabian Martinez

EVANSTON, ILLINOIS

December 2018

© Copyright by Jose Fabian Martinez 2018

All Rights Reserved

## Abstract

### Photoexcited Rylenediimide Radical Anions and Dianions for the Photoreduction of Carbon Dioxide Reduction Catalysts

Jose Fabian Martinez

The development and use of organic anionic chromophores that absorb the entire visible spectrum & into the near-infrared region while providing highly reducing equivalents is pinnacle for artificial photosynthesis. This dissertation investigates the rational design of new donor-acceptor systems for artificial photosynthesis that couple naphthalene diimide (NDI)/perylene diimide (PDI) radical anions to rhenium(I)/manganese(I) tris carbonyl diimine catalysts and the parameters at play that govern photoinduced electron transfer. The synthesis of these new donor-acceptors that incorporate organic radical anions and their characterization via electrochemical and ultrafast spectroscopy grants new insights into the charge-separated species formed upon excitation and their capabilities for reducing thermodynamically difficult substrates. Most notably, photoreduction of carbon dioxide ( $\text{CO}_2$ ) catalysts and the fundamental photoinduced electron transfer events for solar fuel production.

In this work, the first artificial photosynthetic system that incorporates  $\text{NDI}^{\bullet-}$  and  $\text{PDI}^{\bullet-}$  with an organometallic acceptor is explored. Femtosecond and nanosecond transient absorption spectroscopy were utilized to monitor the entire photoreduction process when  $\text{NDI}^{\bullet-}$  or  $\text{PDI}^{\bullet-}$  is attached to the bipyridine on  $\text{Re}(\text{bpy})(\text{CO})_3\text{X}$  or  $\text{Mn}(\text{bpy})(\text{CO})_3\text{X}$ . Femtosecond visible pump mid-infrared probe spectroscopy allowed for direct observation of  $\text{Re}(\text{bpy}^{\bullet-})(\text{CO})_3\text{X}$  or  $\text{Mn}(\text{bpy}^{\bullet-})(\text{CO})_3\text{X}$  upon electron transfer from the photoexcited organic radical chromophore. The extension of the distance between  $\text{NDI}^{\bullet-}$  and  $\text{Re}(\text{bpy})(\text{CO})_3\text{X}$  by incorporating the intermediate

acceptor diphenyl anthracene (DPA) proved fruitful in maintaining a high quantum yield of forward electron transfer while extending the lifetime of the charge separated species generated. In  $\text{Mn}(\text{bpy})(\text{CO})_3\text{X}$ , simply by attaching the  $\text{NDI}^{\bullet-}$  chromophore at the 6-position of bipyridine with no intermediate acceptor lead to nanosecond charge separated species and the formation of  $\text{Mn}(0)(\text{bpy})(\text{CO})_3$ .

## Acknowledgements

Getting a PhD is by no means a single person effort. Just like it takes a village to raise a child, it takes an entire graduate program and university to raise a PhD student. To the department program assistants who work the backend and logistics, to the business office who make sure I get paid and don't end up homeless, to the loading dock staff who make getting packages for research easy, to the facilities management who make the buildings comfortable to work in, to the custodial staff who ease getting rid of waste and cleaning up, to the bus drivers who get me to and from home, to the cafeteria staff who feed me when I'm too "busy" to cook, to the gym staff who make working out easy, to the technical facilities management who make running characterization experiments easy, to the medical staff who make sure I'm still human after all the chemistry I've done, to the IT staff who make accessing the internet at work a no brainer, to the countless other administrations I'm likely forgetting, to the secretaries of the professors who work here, to all my collaborators, to all my lab mates, to my thesis committee, to my advisor, to all my friends, and to my family. Thank you, what I have achieved couldn't have been done without you.

Now, more specifically:

Mike, thank you for allowing to become a member of your research group. Getting the chance to use organic chemistry to create artificial photosynthetic systems has been quite the rewarding experience. In doing so, I've really honed the expertise, strategies, and thought process to further research goals and to gauge progress, which has applications that transcend chemistry. The freedom to pursue different directions and the discussions we had on the projects have been enriching and I hope that the next step in my journey has more like them. If I could do it again, I would choose this group without a moment's hesitation.

Nathan, the best tag team member for doing science. Looks like it's time for me to tag out, I'm sure whoever you wrangle in will be in good hands. Thank you for mentoring me and allowing me to focus on the nitty gritty of doing organic synthesis while you worked on the spectroscopy. I knew every time I handed over a molecule that I poured my heart, sweat, and blood "into" (but not literally), was in good hands. Thank you.

Eunice, thanks for the countless laughs, thanks for the countless conversations, thanks for el pulpo dinners, thanks for the kakao talk phone case, thanks for so much more but most importantly, thanks for always being a great and reliable friend. Your PhD career is unfolding, and I look forward to what you do with your remaining time here and what comes next for you as well.

Joe, sometimes referred to as American Joe for his strength and wisdom, I wouldn't have had any other person join the solar fuels. I learned a lot from you in how to tackle problems and how to discuss chemistry. Hopefully B lab doesn't feel so empty without me and the occasional garbage man approach to organic synthesis.

Tian, the best climbing movie-going archery-going eating-mcdonalds-ice-cream gamenight movie-watching eating-fried-chicken-louisiana ankle-recovery skateboarding trying-new-but-not-actually-tasty-food sugar-high partner one could ever ask for. Let's do them all again.

Joey, my brother from another mother of almost the same color. We've been through thick and thin since high school. Thanks for being there for me throughout grad school despite being on the west side of the country. Looking forward to how your doctor life unfolds, only up and greatness I'm sure. Oh and welcome to the 225 lb club, knew you'd get in here eventually.

Brandon Rugg the man who can deadlift the entire world with one hand, Marek Majewski the greatest canadian to grace me with their presence, Neil Huang the ever hungry american culture beast, Yi-lin Wu the coolest smoothest smartest man, thanks for making the time spent in lab just

as enjoyable as the time outside of lab. To the rest of the Waz group present & past, the mentorship I have received and the chance to teach others science has helped me grow into the scientist I am today, thank you. To Chris Price and Brian Choi, my first year comrades, how I miss you guys but how happy I am to see you guys outside of chemistry. Minh Duc Le, Thu Ra Chopchop, Fia Wulur, my favorite people from Cornell College, thank you. Amy Kuang, Michelle Lee, Steven Gu and the rest of Fam Dinner, my favorite peeps from Northwestern, thank you. Thank you to my undergrad Cornell College and the inspiring teachers I had, Craig Teague, Charlie Liberko, Cynthia Strong, and Jai Shanata. Thank you to RISE at Rutgers, Professor Alan Goldman and Dr. Michael Haibach, and Changjian Guan for training me and teaching me real organic synthesis. Thank you to UIUC, Alexander Scheeline, Andrzej Wieckowski, and Robert Kutz for my first research experience. Thank you to the American Chemical Society for the ACS Scholars Program, Zaida Morales-Martinez, and Robert Hughes for setting me up for success with a chemistry scholarship to attend college.

For the science and the specific chapters: Dr. Nathan La Porte (ultrafast TA & IR spectroscopy – writing – discussions – project direction, Chapters 1-6), Brian Phelan (ultrafast TA spectroscopy, Chapters 1-2), Catie Mauck (ultrafast IR spectroscopy, Chapters 2-3), Ryan Young (ultrafast TA & IR spectroscopy, Chapters 1-2), Svante Hedström (DFT Calculations, Chapter 2), Benjamin Rudshiteyn (DFT Calculations, Chapter 2), Subhajyoti Chaudhuri (DFT Calculations & writing, Chapter 5), Eunice Bae (X-ray Crystallography, Chapter 5), Alessandro Sinopoli (DFT Calculations, Chapters 5 & 6), Muhammad Sohail (Chapters 5 & 6), Victor S. Batista (Chapters 2, 5), Michael R. Wasielewski (Chapters 1-6).

Now, before I had to opportunity to meet all these great people and do any of the great things I accomplished in graduate school or in life, the sacrifices my family have made for me can never be truly repaid, but hopefully I can live up to them.

Dad, apa, fasha – thank you for the sacrifices you made moving to this country and raising five children. Being so young I was naïve of the challenges you and mom faced in making sure we were safe, fed, educated, and with good morals. The constant moving, the constant uncertainty, thanks for taking that head on and doing what you felt was right. I’m happy we’re long passed those days and we can flourish because of the sacrifices you made. My favorite piece of advice you ever gave me, that proved to help countless times during my PhD, “do it nice, or do it twice”.

Ama – gracias por todo, no tengo palabras por todo que me has hecho. Espero que estas orgulloso de todo lo que he hecho. Gracias por cuidarme y apoyarme durante mis estudios y toda mi vida. Recuerdo las días cuando me cocinabas comida antes de la escuela, las días con las gatos, las días cuidandome cuando estuve enfermo, las días trabajando a tu lado en el hotel, nunca olvidaré todo que me has hecho porque sé que has sacrificado todo por yo. Eres la mas fuerte mamá y señora que conosco. Nunca dejaré de ser su hijo, su José, su ya-ya. Gracias Ama.

Carlos – thank you for being the best oldest brother one could ever have. I have been the most fortunate and all my success stems from the sacrifices you made. I know the sacrifices you made were never easy, hopefully I can now help you achieve the dreams you always wanted. My favorite memory of us must be playing Yoshi’s island on the SNES or the countless SEGA football matches until the sun rose. I always wanted to be good at everything to impress you. Thank you.

Daniel – the top 4 Martinez brothers to have ever existed. Your spirit and drive to do what it takes to get what you want are traits that I aspire to have and to improve on. Thank you for always looking out for me. Thank you for instilling the desire to travel and see what else is out

there in this world. My favorite memories have to be watching you get married in Mexico and getting to explore Playa del Carmen.

Francisco – my favorite younger brother. Thank you for moving out to Chicago with me and grounding me with reality. You’ve been there since the very very very beginning. I remember when we used to play Halo 3 or play Manhunt. The moves you demonstrated quite often left me in awe as you excelled above me and I aspire to bring that type of “awe” everywhere I go.

Andrea – my favorite sister. You’ve grown up so much since I left for college, since I’ve been in grad school. I’m sure growing up with 4 older brothers has never been easy, but you’ve championed it all too well. Thank you for keeping mom, dad, and the cats company while I’ve been away, you’re the real MVP. I’m excited to see you grow up even more as you finish college and decide what you want to do next.

To anyone who may be reading this – persist, overcome, and prevail. You can do it too.

## **Dedication**

*For my parents, my brothers, and my sister*

## Table of Contents

<b>Abstract.....</b>	<b>3</b>
<b>Acknowledgements .....</b>	<b>5</b>
<b>Dedication .....</b>	<b>10</b>
<b>Table of Contents .....</b>	<b>11</b>
<b>List of Figures.....</b>	<b>17</b>
<b>List of Tables .....</b>	<b>26</b>
<b>List of Schemes.....</b>	<b>28</b>
<b>Chapter 1 Introduction.....</b>	<b>29</b>
1.1 The Energy Challenge.....	30
1.2 Natural and Artificial Photosynthesis for Solar Fuels .....	31
1.3 CO <sub>2</sub> reduction catalysts .....	32
1.4 Integration of Chromophores with CO <sub>2</sub> Reduction Catalysts.....	33
1.5 Introduction of NDI and PDI .....	35
1.6 Selection for NDI/PDI and Re(bpy)(CO) <sub>3</sub> L/Mn(bpy)(CO) <sub>3</sub> L .....	37
1.7 First Integration of NDI Anion Chromophores with CO <sub>2</sub> reduction Catalysts.....	40
1.8 Thesis Outline .....	44
<b>Chapter 2 Photoinduced Electron Transfer from the Radical Anions and Dianions of Naphthalene and Perylene Diimides to Re(bpy)(CO)<sub>3</sub> Using Red and Near-Infrared Light .....</b>	<b>46</b>
2.1 Introduction.....	47
2.2 Experimental Details.....	50
2.2.1 Synthesis and Methods .....	50
2.2.2 Steady State Spectroscopy .....	51
2.2.3 Electrochemistry .....	51
2.2.4 Femtosecond Transient Absorption Spectroscopy .....	52
2.2.5 Nanosecond Transient Absorption Spectroscopy.....	53
2.2.6 Femtosecond Transient Mid-IR Absorption Spectroscopy .....	53
2.2.7 Computational Methodology for Geometries.....	54
2.2.8 Computational Methodology for TDDFT Calculations .....	54
2.3 Results.....	55

	12
2.3.1 Synthesis.....	55
2.3.2 Electrochemistry.....	56
2.3.3 Steady-State Photophysical Characterization.....	57
2.3.4 Transient Absorption Spectroscopy.....	58
2.4 Discussion.....	60
2.4.1 Electron Transfer Energetics .....	60
2.4.2 Lifetimes and Rates of Forward Electron-Transfer Quenching .....	61
2.4.3 Electron transfer quenching of $^*RDI^{n-}$ .....	64
2.4.4 Back Electron Transfer of $^*RDI^{n-}$ .....	71
2.5 Conclusions.....	73
2.6 Acknowledgements.....	73
2.7 Synthetic Details .....	74
2.8 Supplementary Details .....	90
2.8.1 Transient Absorption SVD/global fitting .....	90
2.8.2 Transient Absorption Data.....	93
2.8.2 Donor-Acceptor Distances .....	101
2.8.3 Electronic Calculations.....	101
2.8.4 Excited State Equilibrium.....	103
<b>Chapter 3 Photodriven Electron from the Highly Reducing Excited State of Naphthalene Diimide Radical Anion to a CO<sub>2</sub> Reduction Catalyst within a Molecular Triad.....</b>	<b>105</b>
3.1 Introduction.....	106
3.2 Experimental Details.....	107
3.2.1 Synthesis and Materials .....	107
3.2.2 Steady State Spectroscopy.....	108
3.2.3 Electrochemistry.....	108
3.2.4 Femtosecond Transient Absorption Spectroscopy .....	108
3.2.5 Nanosecond Transient Absorption Spectroscopy.....	110
3.2.6 Femtosecond Transient Mid-IR Absorption Spectroscopy .....	110
3.2.7 Kinetic Fitting.....	110
3.2.8 Computational Methodology .....	111
3.3 Results.....	111

	13
3.3.1 Synthesis.....	111
3.3.2 Electrochemistry.....	113
3.3.3 Steady-State Spectroscopy.....	114
3.3.4 Transient Absorption Spectroscopy.....	115
3.3.5 Transient mid-IR Spectroscopy.....	117
3.4 Discussion.....	118
3.4.1 Design of the Triad System.....	118
3.4.2 Electron Transfer Energetics.....	119
3.4.3 Electron Transfer within Ligand 5 and Complex 6.....	121
3.5 Conclusions.....	124
3.6 Acknowledgements.....	125
3.7 Synthetic Details.....	125
<b>Chapter 4 Electron Transfer from Photoexcited Naphthalene Diimide Radical Anion to Electrochemically Active <math>\text{Re}(\text{bpy})(\text{CO})_3\text{Cl}</math> in a Molecular Triad.....</b>	<b>130</b>
4.1 Introduction.....	131
4.2 Experimental Details.....	135
4.2.1 Materials.....	135
4.2.2 Electrochemistry.....	136
4.2.3 Femtosecond Transient Vis/NIR Absorption Spectroscopy.....	136
4.2.4 Nanosecond Transient Absorption Spectroscopy.....	137
4.2.5 Femtosecond Time-Resolved mid-IR Spectroscopy.....	138
4.2.6 Computational Methods.....	138
4.2.7 Characterization.....	138
4.3 Results.....	139
4.3.1 Design and Synthesis of the Triad System.....	139
4.3.2 Electrochemistry.....	141
4.3.3 Electrocatalysis.....	143
4.3.4 Electron Transfer Energetics.....	144
4.3.5 Steady-State Photophysical Characterization.....	145
4.3.6 Femto/nanosecond Transient Absorption Spectroscopy.....	146
4.3.7 Time-resolved mid-IR Spectroscopy.....	147

4.4 Discussion.....	148
4.4.1 Electron Transfer Dynamics.....	148
4.4.2 Comparison of Electron Transfer Dynamics to Previous Complexes.....	149
4.5 Conclusions.....	150
4.6 Acknowledgements.....	152
4.7 Synthetic Details.....	152
4.8 Supplementary Details.....	161
4.8.1 Transient Absorption SVD/global fitting.....	161
<b>Chapter 5 Substituent Location Dependence of Photoinduced Electron Transfer Lifetimes to Re(bpy)(CO)<sub>3</sub>X from a Naphthalene Diimide Radical Anion Donor: Effects of Electronic Coupling and Gibbs Free Energy.....</b>	<b>164</b>
5.1 Introduction.....	165
5.2 Experimental Details.....	171
5.2.1 Materials.....	171
5.2.2 Electrochemistry.....	172
5.2.3 Femtosecond Transient Vis/NIR Absorption Spectroscopy.....	172
5.2.4 Nanosecond transient absorption spectroscopy.....	173
5.2.5 Femtosecond time-resolved mid-IR spectroscopy.....	173
5.2.6 Computational methods.....	174
5.3 Results.....	175
5.3.1 Synthesis.....	175
5.3.2 Electrochemistry.....	176
5.3.3 Electron Transfer Energetics.....	179
5.3.4 Steady-State Spectroscopy.....	180
5.3.5 Time-Resolved Visible, Near-infrared, and Mid-infrared Spectroscopy.....	181
5.3.6 NMR Spectroscopy.....	184
5.3.8 X-Ray Crystallography.....	185
5.3.9 Computed Molecular Orbitals.....	187
5.3.10 Thermally Averaged Electronic Coupling.....	190
5.4 Discussion.....	191
5.5 Conclusion.....	198
5.6 Acknowledgements.....	199

5.7 Synthetic Details .....	200
5.8 Supplementary Details .....	213
5.8.1 NMR Characterization.....	213
5.8.2 Fractional Atomic Coordinates and Equivalent Isotropic Displacement Parameters. ....	217
5.8.3 Time-Resolved Visible, Near-infrared, and Mid-infrared Spectroscopy .....	219
<b>Chapter 6 Ten-thousand-fold Enhancement of Photoreduction Lifetime in Mn(bpy)(CO)<sub>3</sub>X Leading to Key Transient Intermediates via Substituent Location Dependence of a Naphthalene Diimide Radical Anion Chromophore .....</b>	<b>231</b>
6.1 Introduction.....	232
6.2 Experimental Details.....	237
6.2.1 Materials .....	237
6.2.2 Steady-State Spectroscopy .....	237
6.2.3 Electrochemistry .....	237
6.2.4 Femtosecond Transient Vis/NIR Absorption Spectroscopy.....	238
6.2.5 Nanosecond transient absorption spectroscopy.....	239
6.2.6 Femtosecond time-resolved mid-IR spectroscopy. ....	239
6.2.7 Synthetic Characterization.....	240
6.3 Results.....	240
6.3.1 Synthesis.....	240
6.3.2 Electrochemistry .....	241
6.3.3 Electrocatalysis.....	243
6.3.4 Electron Transfer Energetics .....	246
6.3.5 Steady-State FTIR .....	247
6.3.6 Steady-State UV-Vis absorption .....	249
6.3.7 Transient Absorption Spectroscopy.....	249
6.3.8 Time-resolved mid-IR Spectroscopy.....	253
6.4 Discussion.....	256
6.5 Conclusion .....	264
6.6 Acknowledgements.....	265
6.7 Synthetic Details .....	266
6.8 Variable Scan Rates & Plots.....	271
6.9 Supplementary Details .....	274

6.9.1 Electronic Absorption.....	274
6.9.2 Electrochemical Studies .....	274
6.9.3 Data Processing / Fitting for Time-Resolved Optical Spectroscopy .....	276
6.9.4 Global Analysis .....	277
<b>References .....</b>	<b>282</b>

## List of Figures

<b>Figure 1.1:</b> Global supply of commercially traded primary energy, from BP 2015.....	31
<b>Figure 1.2:</b> Ground-state absorption spectra of neutral, radical anion, and dianion forms of NDI (top) and PDI (bottom) in DMF + Bu <sub>4</sub> NPF <sub>6</sub> .....	36
<b>Figure 1.3:</b> A) structure of Re(NDI <sub>2</sub> bpy)(CO) <sub>3</sub> Br. B) Energy level diagram of relevant excited and ionic states accessible following a single 100 fs laser pulse.....	40
<b>Figure 1.4:</b> Electrochemistry in DMF with 0.1 M TBAPF <sub>6</sub> using ferrocene/ferrocenium as a reference. A) NDI <sub>2</sub> bpy ligand. B) Re(NDI <sub>2</sub> bpy)(CO) <sub>3</sub> Br complex. ....	41
<b>Figure 1.5:</b> Electrochemistry of Re(NDI <sub>2</sub> bpy)(CO) <sub>3</sub> Br in DMF with 0.1 M TBAPF <sub>6</sub> using ferrocene/ferrocenium as a reference. A) methanol added. B) methanol and CO <sub>2</sub> added. ....	42
<b>Figure 1.6:</b> Photochemistry of Re(NDI <sub>2</sub> bpy)(CO) <sub>3</sub> Br in DMF. A) fsTA spectra as a function of time. B) Electron transfer pathway following absorption of one photon. C) Energy level diagram and time constants for forward and reverse electron transfer. ....	43
<b>Figure 2.1:</b> Top: Spectra of <b>PDI-Phbpy-Re-Py</b> in the neutral (black), PDI <sup>1-</sup> (red) and PDI <sup>2-</sup> (blue) states. Bottom: Spectra of <b>Phbpy-Re-PyPhNDI</b> in the neutral (black) and NDI <sup>1-</sup> (red) states...	57
<b>Figure 2.2:</b> Spectra of chemically reduced samples of C-23 <sub>2</sub> -PDI (black: radical anion, reduced with TDAE, red: dianion, reduced with CoCp <sub>2</sub> ) and 2,6-di <sub>t</sub> Bu-Ph-NDI-Ph (blue: radical anion, reduced with TDAE) in DMF. ....	58
<b>Figure 2.3:</b> (A) Transient absorption spectrum of Phbpy-Re-PyPhPDI <sup>1-</sup> (λ <sub>ex</sub> = 950 nm). (B) Time-resolved mid-IR spectrum of Phbpy-Re-PyPhPDI <sup>1-</sup> (λ <sub>ex</sub> = 704 nm). ....	60
<b>Figure 2.4:</b> Energy level diagram showing general scheme of electron transfer in RDI <sup>n-</sup> -Re(bpy) complexes after excitation. Energy of the charge-transfer state is shown as a range to reflect the different energies of different complexes. ....	61
<b>Figure 2.5:</b> (A) Species-associated fit spectra of the fsTA data for <b>Phbpy-Re-PyPhPDI<sup>1-</sup></b> . Kinetic traces and fits are shown in Figure 2.19. (B) Kinetic traces of the fsIR data shown in Figure 2.3. ....	63
<b>Figure 2.6:</b> Top: (A) Transient absorption spectra and (B) decay-associated spectra for <b>PDI<sup>1-</sup>-Phbpy-Re-Py</b> (λ <sub>ex</sub> = 950 nm). (C) Transient absorption spectra and (D) decay-associated spectra of those spectra for <b>PDI<sup>1-</sup>-Phbpy-Re-Py</b> (λ <sub>ex</sub> = 680 nm). ....	66
<b>Figure 2.7:</b> Frontier molecular orbitals of PDI (left) and [Re(Phbpy)(CO) <sub>3</sub> (py)] <sup>+</sup> molecular fragments calculated using DFT. Frontier MOs of the full PDI-[Re(Phbpy)(CO) <sub>3</sub> (py)] <sup>+</sup> dyad are shown in Figure 2.15.....	67
<b>Figure 2.8:</b> Energy level diagram showing electron transfer in <b>PDI<sup>1-</sup>-Phbpy-Re-Py</b> after excitation at 950 nm (red) or 680 nm (yellow). Energy of the charge-transfer state is shown as a range to reflect the uncertainty of the exact energy of this state. ....	69
<b>Figure 2.9:</b> <i>Left:</i> Calculated vibronic transitions from the ground state to the D1 (black), D2 (red) and D3 (blue) states of PDI <sup>-</sup> . <i>Right:</i> Sum of the three calculated vibronic spectra (black) compared to the experimentally determined spectrum of PDI <sup>-</sup> .....	70

<b>Figure 2.10:</b> (A) Transient absorption and (B) species-associated spectra for complex <b>Phbpy-Re-PyPhNDI<sup>1-</sup></b> ( $\lambda_{\text{ex}} = 605$ nm) showing biphasic back electron transfer kinetics. Kinetic traces and fits are shown in Figure 2.23. (C) fsIR spectra and (D) kinetic traces with fits for complex <b>Phbpy-Re-PyPhNDI<sup>1-</sup></b> ( $\lambda_{\text{ex}} = 605$ nm) showing monophasic back electron transfer kinetics. The instrument response is approximately 2 ps. ....	72
<b>Figure 2.11:</b> From top left to bottom right: Visible and NIR transient absorption spectra of <b>C23<sub>2</sub>-PDI<sup>1-</sup></b> ( $\lambda_{\text{ex}} = 650$ nm), <b>C23<sub>2</sub>-PDI<sup>2-</sup></b> ( $\lambda_{\text{ex}} = 571$ nm) and <b>Cy<sub>2</sub>-NDI<sup>1-</sup></b> ( $\lambda_{\text{ex}} = 605$ nm).....	93
<b>Figure 2.12:</b> Transient absorption spectra, species-associated spectra, global multiple-wavelength kinetic traces and fits, and populations of each species for <b>PDI<sup>1-</sup>-Phbpy-Re-Py</b> ( $\lambda_{\text{ex}} = 950$ nm). ....	93
<b>Figure 2.13:</b> Transient absorption spectra, species-associated spectra, global multiple-wavelength kinetic traces and fits, and populations of each species for <b>PDI<sup>1-</sup>-Phbpy-Re-Py</b> ( $\lambda_{\text{ex}} = 680$ nm). ....	94
<b>Figure 2.14:</b> Time-resolved IR spectra and global multiple-wavelength kinetic traces and fits for <b>PDI<sup>1-</sup>-Phbpy-Re-Py</b> ( $\lambda_{\text{ex}} = 700$ nm). ....	94
<b>Figure 2.15:</b> Transient absorption spectra, species-associated spectra, global multiple-wavelength kinetic traces and fits, and populations of each species for <b>PDI<sup>2-</sup>-Phbpy-Re-Py</b> ( $\lambda_{\text{ex}} = 570$ nm). ....	95
<b>Figure 2.16:</b> Time-resolved IR spectra and global multiple-wavelength kinetic traces and fits for <b>PDI<sup>2-</sup>-Phbpy-Re-Py</b> ( $\lambda_{\text{ex}} = 570$ nm). ....	95
<b>Figure 2.17:</b> Transient absorption spectra, species-associated spectra, and singular value decomposition kinetic traces and fits for <b>NDI<sup>1-</sup>-Phbpy-Re-Py</b> ( $\lambda_{\text{ex}} = 605$ nm). ....	96
<b>Figure 2.18:</b> Time-resolved IR spectra and global multiple-wavelength kinetic traces and fits for <b>NDI<sup>1-</sup>-Phbpy-Re-Py</b> ( $\lambda_{\text{ex}} = 605$ nm).....	96
<b>Figure 2.19:</b> Transient absorption spectra, species-associated spectra, and singular value decomposition kinetic traces and fits for <b>Phbpy-Re-PyPhPDI<sup>1-</sup></b> ( $\lambda_{\text{ex}} = 950$ nm). ....	96
<b>Figure 2.20:</b> Time-resolved IR spectra and global multiple-wavelength kinetic traces and fits for <b>Phbpy-Re-PyPhPDI<sup>1-</sup></b> ( $\lambda_{\text{ex}} = 705$ nm).....	97
<b>Figure 2.21:</b> <i>Left column:</i> Transient absorption spectra for <b>Phbpy-Re-PyPhPDI<sup>2-</sup></b> ( $\lambda_{\text{ex}} = 570$ nm). <i>Middle column:</i> Species-associated spectral fits to the data. <i>Right column:</i> Multiple-wavelength kinetic traces and fits (at short times) and singular value decomposition kinetic traces and fits (at long times) to the kinetic data based on the species-associated fits and lifetimes shown. ....	98
<b>Figure 2.22:</b> Time-resolved IR spectra and global multiple-wavelength kinetic traces and fits for <b>Phbpy-Re-PyPhPDI<sup>2-</sup></b> ( $\lambda_{\text{ex}} = 570$ nm).....	99
<b>Figure 2.23:</b> <i>Left column:</i> Transient absorption spectra for <b>Phbpy-Re-PyPhNDI<sup>1-</sup></b> ( $\lambda_{\text{ex}} = 605$ nm). <i>Middle column:</i> Species-associated spectral fits to the data. <i>Right column:</i> Multiple-wavelength kinetic traces and fits (at short times) and singular value decomposition kinetic traces and fits (at long times) to the kinetic data based on the species-associated fits and lifetimes shown. ....	100
<b>Figure 2.24:</b> Time-resolved IR spectra and multiple-wavelength kinetic traces for <b>Phbpy-Re-PyPhNDI<sup>1-</sup></b> ( $\lambda_{\text{ex}} = 605$ nm).....	100
<b>Figure 2.25:</b> Frontier orbitals for the PDI-[Re(Phbpy)(py)(CO) <sub>3</sub> ] <sup>+</sup> dyad with isodensity=0.03101	

- Figure 2.26:** Calculated SOMO (isovalue=0.03) and spin density (isovalue=0.002, magenta for spin up and teal for spin down) of the  $\text{Re}(\text{Phbpy}^{\bullet-})(\text{CO})_3(\text{PyPh})$  doublet anion, calculated with B3LYP/Def2TZVP//Def2SVP showing that the reducing electron density is largest on the bpy, with some density extending onto the 4-phenyl group. .... 103
- Figure 2.27:** Plot of  $\ln K_{\text{eq}}$  vs.  $1/T$  derived from the  $[\text{PDI}^0]:[\text{PDI}^{1-*}]$  ratio in the SVD spectra of variable-temperature TA experiments on **PDI<sup>1-</sup>-Phbpy-Re-Py**. .... 104
- Figure 3.1:** Cyclic voltammograms of 0.5 mM DMF solutions of (A) **5** and (B) **6**, recorded at  $100 \text{ mV s}^{-1}$  at room temperature with 0.1 M TBAPF<sub>6</sub> as supporting electrolyte. Potentials are reported versus SCE (Fc/Fc<sup>+</sup> occurs at 0.45 V vs SCE). .... 113
- Figure 3.2:** Electronic absorption spectra of ligand **5** and complex **6** in DMF with and without the TDAE reductant added. .... 115
- Figure 3.3:** Transient absorption data for ligand **5** in DMF ( $\lambda_{\text{ex}} = 700 \text{ nm}$ ). (A) Transient absorption spectra; (B) Species-associated spectra; (C) multiple-wavelength kinetic traces and fits. .... 116
- Figure 3.4:** Transient absorption spectra for complex **6** in DMF ( $\lambda_{\text{ex}} = 605 \text{ nm}$ ). (A) Transient absorption spectra. (B) Species-associated spectra. (C) Singular value decomposition kinetic traces and fits to the kinetic data based on the species-associated fits and lifetimes shown. .... 116
- Figure 3.5:** (A) Time-resolved IR spectra and (B) global multiple-wavelength kinetic traces and fits for complex **6** in DMF ( $\lambda_{\text{ex}} = 605 \text{ nm}$ ). .... 118
- Figure 3.6:** Energy-level diagram for complex **6**. Energies are obtained from Table 3.3. .... 124
- Figure 4.1.**  $[\text{Re}(\text{bpy-NDI})(\text{CO})_3]^+ \text{PF}_6^-$  (**1**) and  $[\text{Re}(\text{bpy})(\text{CO})_3(\text{Py-NDI})]^+ \text{PF}_6^-$  (**2**) ..... 133
- Figure 4.2:**  $[\text{Re}(\text{dmb})(\text{CO})_3(\text{Py-DPA-NDI})]^+ \text{PF}_6^-$  (Complex **3**) ..... 135
- Figure 4.3:** Cyclic voltammograms of 0.5 mM DMF solutions of (A) **5** and (B) **4**, recorded at  $100 \text{ mV s}^{-1}$  at room temperature with 0.1 M TBAPF<sub>6</sub> as supporting electrolyte. Potentials are reported versus (Fc/Fc<sup>+</sup> occurs at 0.45 V vs. SCE) ..... 141
- Figure 4.4:** Cyclic voltammograms of a 0.5 mM solution of complex **4** in 0.1 M TBAPF<sub>6</sub> in DMF under argon (red), saturated with CO<sub>2</sub> (black). Scan rate:  $100 \text{ mVs}^{-1}$ , glassy carbon electrode, Ag/AgCl reference electrode, platinum wire counter electrode ..... 143
- Figure 4.5:** Electronic absorption spectra of complex **4** in DMF with and without the TDAE reductant added. .... 145
- Figure 4.6:** Femtosecond (top row) and nanosecond (bottom row) transient absorption data for complex **4<sup>-</sup>** in DMF ( $\lambda = 605 \text{ nm}$ ) (A) Transient absorption spectra; (B) species-associated spectra; (C) multiple-wavelength kinetic traces and fits. .... 147
- Figure 4.7:** (A,B) Time-resolved IR spectra and (C) global multiple-wavelength kinetic traces and fits for complex **4<sup>-</sup>** in DMF ( $\lambda = 605 \text{ nm}$ ). .... 147
- Figure 4.8:** Energy-level diagram for  $\text{Re}(\text{bpy-DPA-NDI}^{\bullet-})(\text{CO})_3\text{Cl}$  (**4<sup>-</sup>**) ..... 150
- Figure 5.1:** Photoinduced Electron transfer from  $\text{NDI}^{\bullet-}$  to  $\text{Re}(\text{bpy})(\text{CO})_3$  via various attachment motifs and distances. .... 169

<b>Figure 5.2:</b> Cyclic voltammograms of 0.5 mM DMF solutions of complexes <b>1-3</b> (A), <b>4-6</b> (B), and <b>7-9</b> (C), recorded at 100 mVs <sup>-1</sup> at room temperature with 0.1 M TBAPF <sub>6</sub> as supporting electrolyte. Potentials are reported versus (Fc/Fc <sup>+</sup> occurs at 0.45 V vs SCE in DMF). .....	176
<b>Figure 5.3:</b> UV/Visible/NIR (left) and mid-IR (right) steady-state spectra of <b>3</b> in DMF without (black) and with excess TDAE (red). The mid-IR spectrum is identical in the presence or absence of TDAE.....	180
<b>Figure 5.4:</b> <i>Left:</i> fsTA spectrum of Re(6-bpy-NDI <sup>-</sup> )(CO) <sub>3</sub> Cl in DMF with excess TDAE ( $\lambda_{\text{ex}} = 605$ nm). <i>Center:</i> Species-associated spectra obtained from global analysis of TA data using Singular Value Decomposition (SVD) kinetic traces. Best-fit lifetimes of each spectral component are given in the legend. <i>Right:</i> Kinetic traces (solid) and fits (dashed) obtained by SVD of fsTA data. Best-fit lifetimes are given in the legend for the species-associated spectra. ....	183
<b>Figure 5.5:</b> <i>Left:</i> fsIR spectrum of Re(6-bpy-NDI <sup>-</sup> )(CO) <sub>3</sub> Py in DMF with excess TDAE ( $\lambda_{\text{ex}} = 605$ nm). <i>Right:</i> Kinetic traces and fits to the lifetime shown of the fsIR at the given frequencies. ....	184
<b>Figure 5.6:</b> <sup>1</sup> H-NMR of complexes <b>6</b> (top) and <b>3</b> (bottom), respectively. Broadening of two protons on their respective phenyl substituent are circled. ....	184
<b>Figure 5.7:</b> <sup>1</sup> H-NMR (left) and <sup>13</sup> C-NMR (right) of complex <b>9</b> . Broadening of two protons and carbons on the phenyl substituent are illustrated. ....	185
<b>Figure 5.8:</b> X-ray crystallographically derived molecular structure of complex <b>9</b> .....	186
<b>Figure 5.9:</b> Optimized geometries and plots of HOMO-1, HOMO, LUMO and LUMO+1 orbitals for complexes <b>1, 4</b> and <b>7</b> . ....	188
<b>Figure 5.10:</b> Calculated molecular orbital energy level diagram for complexes <b>1-9</b> . Model complexes <b>7-9</b> are displayed next to <b>1-3</b> to better appreciate the effect of the NDI fragment. ..	189
<b>Figure 5.11:</b> (A) (Bottom) Energies for different structures of complexes <b>1, 2</b> and <b>3</b> obtained by scanning the dihedral between Re(bpy)(CO) <sub>3</sub> Cl <sup>-</sup> and NDI and (Top) Electronic couplings for the back-electron transfer for structures with energies < 1 kcal/mol. (B) (Bottom) Energies for different structures of complexes <b>1, 2</b> and <b>3</b> obtained by scanning the dihedral between Re(bpy)(CO) <sub>3</sub> Py <sup>-</sup> and NDI and (Top) Electronic couplings for the back-ET for structures with energies < 1 kcal/mol. Boltzmann averaged electronic couplings $ H_{ifB} $ for back-ET complexes (C) <b>1, 2</b> & <b>3</b> and (D) <b>4, 5</b> & <b>6</b> . ....	191
<b>Figure 5.12:</b> <sup>13</sup> C Dept-135 experiment of complex <b>9</b> . ....	213
<b>Figure 5.13:</b> COSY NMR of complex <b>9</b> . ....	214
<b>Figure 5.14:</b> HSQC NMR of complex <b>9</b> . ....	214
<b>Figure 5.15:</b> <sup>1</sup> H NMRs of complexes <b>7-9</b> . No broadening of protons is found in complexes <b>7</b> or <b>8</b> . All taken in CDCl <sub>3</sub> .....	215
<b>Figure 5.16:</b> <sup>1</sup> H NMRs of complexes <b>4-6</b> . No broadening of protons is found in complexes <b>4</b> or <b>5</b> . All taken in CDCl <sub>3</sub> (7.26ppm) .....	216
<b>Figure 5.17:</b> <sup>1</sup> H NMRs of complexes <b>1-3</b> . No broadening of protons is found in complexes <b>1</b> or <b>2</b> . All <sup>1</sup> H NMRs taken in CDCl <sub>3</sub> (7.26ppm) .....	217

- Figure 5.18:** *Top left:* Electronic absorption spectrum of NDI-4Phbpy-ReCl in DMF without (black) and with (red) excess TDAE. *Bottom left:* fsTA spectrum of NDI-4Phbpy-ReCl in DMF with excess TDAE ( $\lambda_{\text{ex}} = 605$  nm). *Top right:* Species-associated spectra obtained from global analysis of TA data using Singular Value Decomposition (SVD) kinetic traces. Best-fit lifetimes of each spectral component are given in the legend. *Bottom right:* Kinetic traces (solid) and fits (dashed) obtained by SVD of fsTA data. Best-fit lifetimes are given in the legend for the species-associated spectra..... 219
- Figure 5.19:** *Top left:* FTIR spectrum of NDI-4Phbpy-ReCl in DMF. *Bottom left:* fsIR spectrum of NDI-4Phbpy-ReCl in DMF with excess TDAE ( $\lambda_{\text{ex}} = 605$  nm). *Top right:* Kinetic traces of the fsIR at the given frequencies..... 220
- Figure 5.20:** *Top left:* Electronic absorption spectrum of NDI-4Phbpy-RePy in DMF without (black) and with (red) excess TDAE. *Bottom left:* fsTA spectrum of NDI-4Phbpy-RePy in DMF with excess TDAE ( $\lambda_{\text{ex}} = 605$  nm). *Top right:* Species-associated spectra obtained from global analysis of TA data using Singular Value Decomposition (SVD) kinetic traces. Best-fit lifetimes of each spectral component are given in the legend. *Bottom right:* Kinetic traces (solid) and fits (dashed) obtained by SVD of fsTA data. Best-fit lifetimes are given in the legend for the species-associated spectra..... 221
- Figure 5.21:** *Top left:* FTIR spectrum of NDI-4Phbpy-RePy in DMF. *Bottom left:* fsIR spectrum of NDI-4Phbpy-RePy in DMF with excess TDAE ( $\lambda_{\text{ex}} = 605$  nm). *Top right:* Kinetic traces and fits to the specified lifetime of the fsIR at the given frequencies. .... 222
- Figure 5.22:** *Top left:* Electronic absorption spectrum of NDI-5Phbpy-ReCl in DMF without (black) and with (red) excess TDAE. *Bottom left:* fsTA spectrum of NDI-5Phbpy-ReCl in DMF with excess TDAE ( $\lambda_{\text{ex}} = 605$  nm). *Top right:* Species-associated spectra obtained from global analysis of TA data using Singular Value Decomposition (SVD) kinetic traces. Best-fit lifetimes of each spectral component are given in the legend. *Bottom right:* Kinetic traces (solid) and fits (dashed) obtained by SVD of fsTA data. Best-fit lifetimes are given in the legend for the species-associated spectra..... 223
- Figure 5.23:** *Top left:* FTIR spectrum of NDI-5Phbpy-ReCl in DMF. *Bottom left:* fsIR spectrum of NDI-5Phbpy-ReCl in DMF with excess TDAE ( $\lambda_{\text{ex}} = 605$  nm). *Top right:* Kinetic traces of the fsIR at the given frequencies..... 224
- Figure 5.24:** *Top left:* Electronic absorption spectrum of NDI-5Phbpy-RePy in DMF without (black) and with (red) excess TDAE. *Bottom left:* fsTA spectrum of NDI-5Phbpy-RePy in DMF with excess TDAE ( $\lambda_{\text{ex}} = 605$  nm). *Top right:* Species-associated spectra obtained from analysis of TA data using kinetic traces at multiple wavelengths. Best-fit lifetimes of each spectral component are given in the legend. *Middle right:* Calculated populations of each spectral component over time using lifetimes given. *Bottom right:* Kinetic traces and fits at given wavelengths..... 225
- Figure 5.25:** *Top left:* FTIR spectrum of NDI-5Phbpy-RePy in DMF. *Bottom left:* fsIR spectrum of NDI-5Phbpy-RePy in DMF with excess TDAE ( $\lambda_{\text{ex}} = 605$  nm). *Top right:* Kinetic traces and fits to the specified lifetime of the fsIR at the given frequencies. .... 226

- Figure 5.26:** *Top left:* Electronic absorption spectrum of NDI-6Phbpy-ReCl in DMF without (black) and with (red) excess TDAE. *Bottom left:* fsTA spectrum of NDI-6Phbpy-ReCl in DMF with excess TDAE ( $\lambda_{\text{ex}} = 605$  nm). *Top right:* Species-associated spectra obtained from global analysis of TA data using Singular Value Decomposition (SVD) kinetic traces. Best-fit lifetimes of each spectral component are given in the legend. *Bottom right:* Kinetic traces (solid) and fits (dashed) obtained by SVD of fsTA data. Best-fit lifetimes are given in the legend for the species-associated spectra..... 227
- Figure 5.27:** *Top left:* FTIR spectrum of NDI-6Phbpy-ReCl in DMF. *Bottom left:* fsIR spectrum of NDI-6Phbpy-ReCl in DMF with excess TDAE ( $\lambda_{\text{ex}} = 605$  nm). *Top right:* Kinetic traces of the fsIR at the given frequencies..... 228
- Figure 5.28:** *Top left:* Electronic absorption spectrum of NDI-6Phbpy-RePy in DMF without (black) and with (red) excess TDAE. *Bottom left:* fsTA spectrum of NDI-6Phbpy-RePy in DMF with excess TDAE ( $\lambda_{\text{ex}} = 605$  nm). *Top right:* Species-associated spectra obtained from global analysis of TA data using Singular Value Decomposition (SVD) kinetic traces. Best-fit lifetimes of each spectral component are given in the legend. *Bottom right:* Kinetic traces (solid) and fits (dashed) obtained by SVD of fsTA data. Best-fit lifetimes are given in the legend for the species-associated spectra..... 229
- Figure 5.29:** *Top left:* FTIR spectrum of NDI-6Phbpy-RePy in DMF. *Bottom left:* fsIR spectrum of NDI-6Phbpy-RePy in DMF with excess TDAE ( $\lambda_{\text{ex}} = 605$  nm). *Top right:* Kinetic traces and fits to the specified lifetime of the fsIR at the given frequencies. .... 230
- Figure 6.1:** Photoexcitation of  $\text{NDI}^{\cdot-}$  within a molecular triad covalently attached to  $[\text{Re}(\text{bpy})(\text{CO})_3(\text{Py})][\text{PF}_6]$  through a diphenyl anthracene intermediate acceptor to form the transiently observed species  $[\text{Re}(\text{bpy}^{\cdot-})(\text{CO})_3(\text{X})][\text{PF}_6]$ ..... 235
- Figure 6.2:** Photoexcitation of  $\text{RDI}^{\cdot-}$  ( $\text{NDI}^{\cdot-}$  or  $\text{PDI}^{\cdot-}$ ) covalently attached to  $[\text{Re}(\text{bpy})(\text{CO})_3(\text{Py})][\text{PF}_6]$  forms the transiently observed species  $[\text{Re}(\text{RDI}^0\text{-bpy}^{\cdot-})(\text{CO})_3(\text{Py})][\text{PF}_6]$ . .... 235
- Figure 6.3:** Cyclic voltammograms of 1.0 mM solutions of (A) **1** in DMF (B) **2** in MeCN (C) **3** in DMF, recorded at  $100 \text{ mV s}^{-1}$  at room temperature with 0.1 M TBAPF<sub>6</sub> as supporting electrolyte. .... 241
- Figure 6.4:** Cyclic voltammograms of 1.0 mM solutions in DMF of (A) **4** (B) **5** (C) **1**, recorded at  $100 \text{ mV s}^{-1}$  at room temperature with 0.1 M TBAPF<sub>6</sub> as supporting electrolyte..... 242
- Figure 6.5:** Cyclic voltammograms of a 1.0 mM solution of (A) complex **1** with 0.1 M TBAPF<sub>6</sub> in DMF, (B) complex **2** with 0.1 M TBAPF<sub>6</sub> in MeCN, (C) and complex **3** with 0.1 M TBAPF<sub>6</sub> in DMF under argon (black), saturated with CO<sub>2</sub> (dashed red line) with MeOH (3M). Scan rate:  $100 \text{ mV s}^{-1}$ , glassy carbon electrode, platinum counter electrode, and silver reference wire..... 244
- Figure 6.6:** Resting state solution phase FTIR of complexes (A) **1** (DMF), (B) **2** (MeCN), and (C) **3** (DMF). .... 248
- Figure 6.7:** Resting state solution phase FTIR of complexes (A) **4** (DMF), (B) **5** (DMF)..... 248
- Figure 6.8:** Electronic absorption spectra of complex **1** (DMF), **2** (MeCN), and **3** (DMF) with and without the TDAE reductant added. .... 249

- Figure 6.9:** (top row) (A) fsTA spectra of complex  $4^{\bullet-}$  (B) fsTA spectra of complex  $5^{\bullet-}$  (C), fsTA spectra of complex  $1^{\bullet-}$ , (bottom row) (D) species-associate spectra for complex  $4^{\bullet-}$  (E) species-associate spectra for complex  $5^{\bullet-}$  (F) species-associate spectra for complex  $1^{\bullet-}$ .  $\lambda_{\text{ex}} = 605$  nm, solvent = DMF. .... 251
- Figure 6.10:** (top row) (A) fsTA spectra of complex  $2^{\bullet-}$  (B) species-associated spectra (C), transient kinetics at selected wavelengths, (bottom row) (D) nsTA spectra of complex  $2^{\bullet-}$  (E) species-associated spectra for complex  $2^{\bullet-}$  (F) nanosecond transient kinetics at selected wavelengths.  $\lambda_{\text{ex}} = 605$  nm, solvent = MeCN. .... 252
- Figure 6.11:** (top row) (A) fsTA spectra of complex  $3^{\bullet-}$  (B) species-associated spectra (C), transient kinetics at selected wavelengths, (bottom row) (D) nsTA spectra of complex  $3^{\bullet-}$  (E) species-associated spectra for complex  $3^{\bullet-}$  (F) nanosecond transient kinetics at selected wavelengths.  $\lambda_{\text{ex}} = 605$  nm, solvent = DMF. .... 253
- Figure 6.12:** (top row) (A) TRIR spectra of complex  $4^{\bullet-}$  (B) TRIR spectra of complex  $5^{\bullet-}$  (C), TRIR spectra of complex  $1^{\bullet-}$ , (bottom row) (D) transient kinetics at selected  $\nu(\text{CO})$  of  $4^{\bullet-}$  (E) transient kinetics at selected  $\nu(\text{CO})$  of  $5^{\bullet-}$  (F) transient kinetics at selected  $\nu(\text{CO})$  of  $1^{\bullet-}$ .  $\lambda_{\text{ex}} = 605$  nm, solvent = DMF. .... 254
- Figure 6.13:** (top row) (A) TRIR spectra of complex  $2^{\bullet-}$  (B) species-associated spectra (bottom row) (C) transient kinetics at selected  $\nu(\text{CO})$  (D) Singular value decomposition kinetic traces and fits based on the species-associated fits and lifetimes shown.  $\lambda_{\text{ex}} = 605$  nm, solvent = MeCN. 255
- Figure 6.14:** (top row) (A) TRIR spectra of complex  $3^{\bullet-}$  (B) species-associated spectra (bottom row) (C) transient kinetics at selected  $\nu(\text{CO})$  (D) Singular value decomposition kinetic traces and fits based on the species-associated fits and lifetimes.  $\lambda_{\text{ex}} = 605$  nm, solvent = DMF. .... 256
- Figure 6.15:** Jablonski diagram of  $1^{\bullet-}$  -  $5^{\bullet-}$  upon excitation ( $\lambda = 605$  nm). .... 264
- Figure 6.16:** **A)** Cyclic voltammograms of 1.0 mM Complex **4** in N,N-DMF with 0.1 M TBAPF<sub>6</sub> solution under Argon saturation, showing response to variable scan rate. **B)** Variable scan rate plots of Complex **4**. Working electrode is glassy carbon (3 mm diameter), counter electrode is Pt, and pseudoreference is Ag wire. .... 271
- Figure 6.17:** **A)** Cyclic voltammograms of 1.0 mM Complex **5** in N,N-DMF with 0.1 M TBAPF<sub>6</sub> solution under Argon saturation, showing response to variable scan rate. **B)** Variable scan rate plots of Complex **5**. Working electrode is glassy carbon (3 mm diameter), counter electrode is Pt, and pseudoreference is Ag wire. .... 272
- Figure 6.18:** **A)** Cyclic voltammograms of 1.0 mM Complex **1** in N,N-DMF with 0.1 M TBAPF<sub>6</sub> solution under Argon saturation, showing response to variable scan rate. **B)** Variable scan rate plots of Complex **1**. Working electrode is glassy carbon (3 mm diameter), counter electrode is Pt, and pseudoreference is Ag wire. .... 272
- Figure 6.19:** **A)** Cyclic voltammograms of 1.0 mM Complex **2** in MeCN with 0.1 M TBAPF<sub>6</sub> solution under Argon saturation, showing response to variable scan rate. **B)** Variable scan rate plots of Complex **2**. Working electrode is glassy carbon (3 mm diameter), counter electrode is Pt, and pseudoreference is Ag wire. .... 273
- Figure 6.20:** **A)** Cyclic voltammograms of 1.0 mM Complex **3** in N,N-DMF with 0.1 M TBAPF<sub>6</sub> solution under Argon saturation, showing response to variable scan rate. **B)** Variable scan rate

plots of Complex <b>3</b> . Working electrode is glassy carbon (3 mm diameter), counter electrode is Pt, and pseudoreference is Ag wire.....	273
<b>Figure 6.21:</b> <b>A)</b> Electronic absorption spectra of complex <b>4</b> (DMF) with and without the TDAE reductant added. <b>B)</b> Electronic absorption spectra of complex <b>5</b> (DMF) with and without the TDAE reductant added. ....	274
<b>Figure 6.22:</b> Cyclic voltammograms of a 1.0 mM solution of complex <b>4</b> with 0.1 M TBAPF <sub>6</sub> in DMF, under argon (black), saturated with CO <sub>2</sub> (dashed red line) with MeOH (3 M, 6 M, 12 M, respectively). Scan rate: 100 mVs <sup>-1</sup> , glassy carbon electrode, platinum counter electrode, and silver reference wire.....	274
<b>Figure 6.23:</b> Cyclic voltammograms of a 1.0 mM solution of complex <b>5</b> with 0.1 M TBAPF <sub>6</sub> in DMF, under argon (black), saturated with CO <sub>2</sub> (dashed red line) with MeOH (3 M, 6 M, 12 M, respectively). Scan rate: 100 mVs <sup>-1</sup> , glassy carbon electrode, platinum counter electrode, and silver reference wire.....	275
<b>Figure 6.24:</b> Cyclic voltammograms of a 1.0 mM solution of complexes <b>1</b> , <b>4</b> , and <b>5</b> with 0.1 M TBAPF <sub>6</sub> in DMF, under argon (black), saturated with CO <sub>2</sub> (dashed red line) with MeOH (12 M). Scan rate: 100 mVs <sup>-1</sup> , glassy carbon electrode, platinum counter electrode, and silver reference wire. ....	275
<b>Figure 6.25:</b> Cyclic voltammograms of a 1.0 mM solution of complex <b>3</b> with 0.1 M TBAPF <sub>6</sub> in DMF, <b>A)</b> under argon (black), saturated with CO <sub>2</sub> (dashed red line) with MeOH (3 M). <b>B)</b> under argon (black), under argon with MeOH (4M) (purple), saturated with CO <sub>2</sub> (dashed blue line) with MeOH (4 M). Scan rate: 100 mVs <sup>-1</sup> , glassy carbon electrode, platinum counter electrode, and silver reference wire.....	276
<b>Figure 6.26:</b> Cyclic voltammograms of a 1.0 mM solution of complex <b>1</b> with 0.1 M TBAPF <sub>6</sub> in DMF, <b>A)</b> under argon with MeOH (1M) (pink), under argon with MeOH (4M) (blue) <b>B)</b> under argon with MeOH (1M) (pink), under argon with MeOH (4M) (black). Scan rate: 100 mVs <sup>-1</sup> , glassy carbon electrode, platinum counter electrode, and silver reference wire. ....	276
<b>Figure 6.27:</b> Complex <b>4</b> <sup>-</sup> . λ = 605 nm, 1.0 μJ/pulse, DMF. (A) Species-associated spectra obtained by global fitting. (B) Transient kinetics at selected wavelengths. (C) Populations of the transient species. ....	279
<b>Figure 6.28:</b> Complex <b>5</b> <sup>-</sup> . λ = 605 nm, 1.0 μJ/pulse, DMF. (A) Species-associated spectra obtained by global fitting. (B) Transient kinetics at selected wavelengths. (C) Populations of the transient species. ....	279
<b>Figure 6.29:</b> Complex <b>1</b> <sup>-</sup> . λ = 605 nm, 1.0 μJ/pulse, DMF. (A) Species-associated spectra obtained by global fitting. (B) Transient kinetics at selected wavelengths. (C) Populations of the transient species. ....	280
<b>Figure 6.30:</b> Complex <b>2</b> <sup>-</sup> . λ = 605 nm, 1.0 μJ/pulse, DMF. (A) Species-associated spectra obtained by global fitting. (B) Transient kinetics at selected wavelengths. (C) Populations of the transient species. ....	280

**Figure 6.31:** Complex  $3^{\bullet-}$ .  $\lambda = 605$  nm,  $1.0 \mu\text{J/pulse}$ , DMF. (A) Species-associated spectra obtained by global fitting. (B) Transient kinetics at selected wavelengths. (C) Populations of the transient species. .... 281

## List of Tables

<b>Table 1.1.</b> Photophysical properties of N,N'-bis(2,5-di- <i>tert</i> -butylphenyl) PDI and NDI in the neutral (N), radical anion (R <sup>-</sup> ), and dianion (R <sup>2-</sup> ) forms. All data taken from <sup>45</sup> unless noted. ...	35
<b>Table 2.1:</b> Electrochemical redox potentials for the complexes under study, as well as model compounds. ....	56
<b>Table 2.2:</b> Rates and Gibbs free energy of electron transfer reactions discussed in this study. ..	62
<b>Table 2.3:</b> The TD-DFT vibronic absorption maximum peak wavelengths $\lambda$ of the first two electronic transitions, and the vertical wavelengths $\lambda$ , oscillator strengths $f$ , and dominant orbital characters for the lowest-energy calculated electronic transitions of the reduced PDI <sup>-</sup> radical. The full set of the lowest ten transitions is given in Table 2.7. ....	68
<b>Table 2.4.</b> Donor-acceptor distances in the complexes under study, calculated from the DFT-optimized geometries. ....	101
<b>Table 2.5:</b> Relevant orbital energies in eV for all species as non-reduced singlets. ....	102
<b>Table 2.6:</b> The wavelengths $\lambda$ , oscillator strengths $f$ , and dominant orbital characters for the 10 lowest-energy calculated vertical electronic transitions of [Re(Phbpy)(py)(CO) <sub>3</sub> ] <sup>+</sup> . ....	102
<b>Table 2.7:</b> The calculated vibronic absorption maximum peak wavelengths $\lambda$ of the first three electronic transitions, and the vertical wavelengths $\lambda$ , oscillator strengths $f$ , and dominant orbital characters for the 10 lowest-energy calculated electronic transitions of the reduced PDI <sup>-</sup> radical. ....	102
<b>Table 3.1:</b> Redox potentials (vs. SCE using a Fc/Fc <sup>+</sup> reference at 0.45 V vs SCE). ....	113
<b>Table 3.2:</b> Donor-acceptor distances in complex <b>2</b> calculated from the DFT-optimized geometries. ....	120
<b>Table 3.3:</b> Driving force for electron transfer reactions in ligand <b>5</b> and complex <b>6</b> . ....	121
<b>Table 4.1:</b> Redox potentials (vs. SCE using a Fc/Fc <sup>+</sup> reference at 0.45 V vs SCE). ....	142
<b>Table 4.2:</b> Free energy changes for electron transfer reactions in complex <b>4</b> <sup>-</sup> . ....	145
<b>Table 5.1:</b> Redox potentials of complexes <b>1-3</b> vs SCE (Fc/Fc <sup>+</sup> reference at 0.45 V vs SCE in DMF) ....	177
<b>Table 5.2:</b> Redox potentials of complexes <b>4-6</b> vs SCE (Fc/Fc <sup>+</sup> reference at 0.45 V vs SCE in DMF) ....	178
<b>Table 5.3.</b> Redox potentials of complexes <b>7-10</b> vs SCE (Fc/Fc <sup>+</sup> reference at 0.45 V vs SCE in DMF).....	178
<b>Table 5.4:</b> Free energy changes for electron transfer reactions in complex <b>1</b> <sup>-</sup> - <b>6</b> <sup>-</sup> . ....	180
<b>Table 5.5:</b> Forward- and back-electron transfer lifetimes for complexes <b>1</b> <sup>-</sup> - <b>6</b> <sup>-</sup> in DMF with excess TDAE ( $\lambda_{\text{ex}} = 605$ nm), calculated from analysis of fsTA spectra. ....	183
<b>Table 5.6:</b> Crystal data and structure refinement for complex <b>9</b> . ....	186
<b>Table 5.7:</b> Computed geometry parameters for the investigated complexes. ....	187
<b>Table 5.8:</b> Calculated HOMO and LUMO energies for complexes <b>1-9</b> . ....	190
<b>Table 5.9:</b> Fractional Atomic Coordinates ( $\times 10^4$ ) and Equivalent Isotropic Displacement Parameters ( $\text{\AA}^2 \times 10^3$ ) for complex <b>9</b> . $U_{\text{eq}}$ is defined as 1/3 of the trace of the orthogonalised $U_{\text{IJ}}$ tensor. ....	217

<b>Table 6.1:</b> Redox potentials of complexes 1-5 vs SCE (Fc/Fc <sup>+</sup> reference at 0.45 V vs SCE in DMF and 0.40 V vs SCE in MeCN).....	242
<b>Table 6.2:</b> Comparison of $i_{cat}/i_p$ and TOF Values for complexes <b>1 – 5</b> with MeOH. ....	245
<b>Table 6.3:</b> Free energy changes for electron transfer reactions in complex <b>1<sup>-</sup> - 5<sup>-</sup></b> . ....	247
<b>Table 6.4:</b> FTIR CO stretches of <b>1-5</b> complexes. Complexes <b>1, 3-5</b> were dissolved in DMF and complex <b>2</b> in MeCN.....	248
<b>Table 6.5:</b> Observed time constants and rates of electron transfer for complexes <b>1<sup>-</sup> - 5<sup>-</sup></b> .....	250

## List of Schemes

<b>Scheme 1.1:</b> Thermodynamic potentials for the reduction of CO <sub>2</sub> under standard conditions in aqueous solution: pH 7, 25 °C, 1 atmosphere of gases, and 1 M solutes.....	33
<b>Scheme 1.2:</b> Structures of naphthalenediimide (NDI), perylenediimide (PDI), Re(bpy)(CO) <sub>3</sub> L, and Mn(bpy)(CO) <sub>3</sub> L.....	38
<b>Scheme 2.1:</b> Synthesis of RDI-Phbpy-Re-Py and Phbpy-Re-PyPhRDI. ....	56
<b>Scheme 3.1:</b> Synthetic scheme for Py-DPA-NDI ( <b>5</b> ) and [Re(dmb)(CO) <sub>3</sub> (Py-DPA-NDI)] <sup>+</sup> PF <sub>6</sub> <sup>-</sup> ( <b>6</b> ).....	112
<b>Scheme 4.1:</b> Synthetic scheme for bpy-DPA-NDI ( <b>5</b> ) and Re(bpy-DPA-NDI)(CO) <sub>3</sub> Cl ( <b>4</b> )...	140
<b>Scheme 5.1:</b> Synthetic scheme for Re(4-, 5-, 6-(bpy-NDI)(CO) <sub>3</sub> Cl ( <b>1, 2, 3</b> ) and [Re(4-, 5-, 6-bpy-NDI)(CO) <sub>3</sub> Py][PF <sub>6</sub> ] ( <b>4, 5, 6</b> ).....	175
<b>Scheme 5.2:</b> Synthetic scheme for Re(4-, 5-, 6-Ph-bpy)(CO) <sub>3</sub> Cl ( <b>7, 8, 9</b> ).....	176
<b>Scheme 6.1:</b> Synthetic scheme for complexes <b>1-5</b> .....	241

## **Chapter 1 Introduction**

## 1.1 The Energy Challenge

The rapid and ever growing global energy demand poses one of the greatest global and scientific challenges humanity has ever faced. As the world's population is expected to grow to 8.5 billion by the year 2030, the amount of energy required to sustain the population growth and gross domestic product (GDP) is expected to exceed 27W.<sup>1</sup> This amount of energy is approximately double the global demand for energy in the year 2001.<sup>2</sup> With ~87% of the world's energy usage coming from the combustion of fossil fuels, the repercussions of seeping carbon dioxide (CO<sub>2</sub>) and greenhouse gasses into the atmosphere is beginning to have major repercussions on the global scale and will continue to do so without human intervention. If humanity continues along the current path, by the year 2100, climate change will force the mass migration of over one billion people. In the meantime, storms and their destructive forces will become stronger and more apparent, as The United States of America and Puerto Rico have faced in recent times.

As we grapple with climate change, the only clean and renewable source of energy available to meet the global energy demand is the sun. The sun is a nuclear reactor in the center of our solar system that is expected to continue to provide solar photons for the next five billion years, ~7 million future generations of human life. As we stand, only 10% of the global energy supply comes from renewable energy while most of the rest comes from fossil fuels, Figure 1.1.<sup>2</sup> The amount of solar photons that reach the earth's surface is not limiting solar technologies from producing electricity on the multi-TW. Current strategies towards harvesting the sun's photons aim to generate electricity through solar photovoltaic devices including crystalline silicon cells,<sup>3-4</sup> organic photovoltaics,<sup>5-7</sup> or dye-sensitized solar cells<sup>8-9</sup>. In comparison to fossil fuels, the energy storage densities for electricity is still low compared to the energy stored in the chemical bonds of

liquid fuels (though much needed research is currently being pursued to improve battery technologies).<sup>10-12</sup>

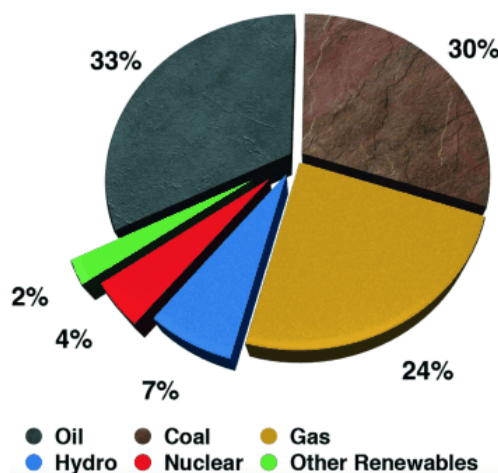


**Figure 1.1:** Global supply of commercially traded primary energy, from BP 2015.

## 1.2 Natural and Artificial Photosynthesis for Solar Fuels

The storage of solar energy into chemical bonds, “solar fuels”, is one that can be found in nature. For the past billions of years, plants have been using solar photons to convert water ( $\text{H}_2\text{O}$ ) into highly reducing equivalents for the conversion of  $\text{CO}_2$  to glucose.<sup>13-14</sup> For example, within green plants, are two photosynthetic reaction centers named photosystem I (PSI) and photosystem II (PSII) that linearly transport electrons from  $\text{H}_2\text{O}$  splitting in oxygenic photosynthesis via a Z-scheme model.<sup>15</sup> The transfer of electrons and protons within PSI and PSII to  $\text{CO}_2$  is aided by a third protein cytochrome  $b_6f$  (Cyt  $b_6f$ ). The three supramolecular structures, Cyt  $b_6f$ , PSI, and PSII are in the photosynthetic membrane so that the flow of electrons to  $\text{NADP}^+$  is vectorial, generating a proton gradient across the membrane. This proton gradient is used chemiosmotically by  $\text{CF}_0 - \text{CF}_1$ , to drive the ATP synthase to convert ADP to ATP in order to provide chemical energy for the  $\text{CO}_2$ -reduction process.<sup>13</sup> These naturally occurring processes in green plants demonstrate how

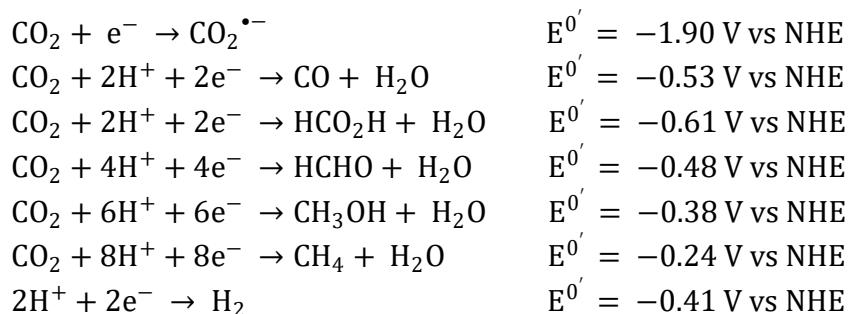
nature effectively balances light absorption, charge separation, charge accumulation, and catalysis, giving chemists a blueprint for developing artificial supramolecular systems, whether it be for H<sub>2</sub>O splitting or CO<sub>2</sub> reduction.

Over the past several decades, scientists have coined the term “artificial photosynthesis” to describe the development of systems that mimic or utilize processes “illustrated” in nature’s blueprint. While much progress has been made in understanding and mimicking photosynthesis in artificial systems, researchers have not yet developed components that can effectively convert and store solar energy in chemical bonds on a large scale. Additionally, the targets for solar fuels (e.g. hydrogen (H<sub>2</sub>), methanol, or methane) add additionally complexity. While hydrogen is a clean burning fuel, many challenges arise in incorporating the molecule into today’s room temperature liquid driven fuel infrastructure.<sup>16</sup> Instead, the reduction of carbon dioxide (CO<sub>2</sub>) to carbon monoxide (CO) is an attractive feedstock option as the industrially utilized Fischer–Tropsch process regularly converts CO and H<sub>2</sub> into fuel that would fit into today’s trillion dollar fuel industry.<sup>17</sup> To date, the focus has been to design and synthesize electrocatalysts that can be incorporated into assemblies that generate charge separation via light.<sup>18</sup>

### **1.3 CO<sub>2</sub> reduction catalysts**

The thermodynamic potential for the direct reduction of CO<sub>2</sub> to CO<sub>2</sub><sup>•-</sup> is quite negative and requires nearly two eV of free energy.<sup>19-20</sup> To lower this thermodynamic potential, a proton/multiple electron-assisted approach to CO<sub>2</sub> reduction significantly lowers the thermodynamic potential, scheme 1.1. Transition metal complexes have the capability to bind and facilitate multi electron and proton assisted pathways and grant chemists a diverse toolkit and platform to conduct catalysis. The capability to fine tune properties via ligand structures and metal

oxidation states allows chemists to drastically alter their electro- or photocatalytic capabilities. Of the transition metal complexes that can electrochemically reduce CO<sub>2</sub> to CO, fac-Re(b



**Scheme 1.1:** Thermodynamic potentials for the reduction of CO<sub>2</sub> under standard conditions in aqueous solution: pH 7, 25 °C, 1 atmosphere of gases, and 1 M solutes

py)(CO)<sub>3</sub>Cl (bpy = 2,2'-bipyridine) and its derivatives demonstrate high rates, selectivity, and lifetimes in comparison to other transition metal complexes.<sup>21-24</sup> While the transition metals found on the second- and third-row of the periodic table have shown superior activities and stabilities for CO<sub>2</sub> reduction when compared to their first-row counterparts, their low abundance on Earth makes them expensive and not ideal for use on an industrial scale. Rhenium (Re) is approximately 1.3 million times less abundant than manganese (Mn) in the Earth's crust and complexes that utilize manganese more practical for large scale-up. Bourrez et al. discovered that the rhenium in Re(bpy)(CO)<sub>3</sub>Cl could be replaced with manganese to form Mn(bpy)(CO)<sub>3</sub>Br, with the help of an external Brønsted acid, upon double reduction could also reduce CO<sub>2</sub>.<sup>25</sup> Smieja et al then demonstrated that by selecting the proper conditions, Mn(tbu<sub>2</sub>-bpy)(CO)<sub>3</sub>Br could outperform the rhenium analogue.<sup>26</sup>

#### 1.4 Integration of Chromophores with CO<sub>2</sub> Reduction Catalysts

One of the major challenges in artificial photosynthesis is to reduce CO<sub>2</sub> using solar photons that span the solar spectrum.<sup>27</sup> Typical electrocatalysts (like Re(bpy)(CO)<sub>3</sub>Cl or

Mn(bpy)(CO)<sub>3</sub>Br) employed to reduce CO<sub>2</sub> function at potentials between 1.0–1.9 V vs SCE,<sup>28-31</sup> a potential accessible using organometallic chromophores that absorb at wavelengths shorter than 550 nm.<sup>32-36</sup> In addition, many of these highly reducing chromophores incorporate non-earth-abundant metals such as Ir,<sup>37-38</sup> Pt,<sup>39</sup> or Re.<sup>40</sup> There are reports of covalent assemblies of organometallic chromophores with CO<sub>2</sub> reduction catalysts, the most widely researched of which are the Ru<sup>II</sup>(bpy)<sub>3</sub>–Re(I)(bpy)(CO)<sub>3</sub> assemblies reported by Ishitani and co-workers,<sup>31, 41</sup> which achieve photocatalysis at wavelengths <500 nm. There has also been a report of a complex of an Ir<sup>III</sup>(1-phenylisoquinoline)<sub>2</sub>(bpy) complex attached to a Re(bpy)(CO)<sub>3</sub> catalyst, in which catalysis is achieved upon illumination at 480 nm.<sup>42</sup> Other assemblies that function at slightly longer wavelengths (<600 nm) incorporate zinc or magnesium porphyrins<sup>43</sup> or Os<sup>III</sup>(bpy)<sub>3</sub>.<sup>44</sup> Though there currently is no report of covalently attached photosensitizers to Mn(bpy)(CO)<sub>3</sub>.

In contrast to organometallic chromophores, purely organic chromophores that absorb in the visible region do not typically possess the excited-state reduction power required to photosensitize CO<sub>2</sub> reduction catalysts. However, it has been shown that certain organic chromophores, when reduced by one or two electrons, become powerful excited-state super-reductants that absorb long-wavelength visible and even near-infrared light while still exhibiting long enough lifetimes for use in donor–acceptor systems.<sup>45</sup> The use of a pre-reduced chromophore to transfer electrons to a CO<sub>2</sub> reduction catalyst has been previously demonstrated by Neumann and co-workers in a system in which a colorless polyoxometalate is reduced at mild potential in the presence of protons to generate an intensely absorbing chromophore.<sup>46</sup> The polyoxometalate is coordinated to a bimetallic CO<sub>2</sub> reduction catalyst, and photoexcitation of the reduced chromophore results in the reduction of CO<sub>2</sub> to CO.

## 1.5 Introduction of NDI and PDI

The photophysical properties of the anions and dianions of NDI and PDI were first investigated by the Wasielewski group. Shown in Figure 1.2 are the spectra of NDI and PDI in their neutral and reduced forms.<sup>47</sup> Gosztola and co-workers using electrochemical reduction of neutral NDI or PDI in DMF solutions in an optically transparent thin layer electrochemical (OTTLE) cell observed the reduced counterparts. Gosztola et al. also collected transient absorption data on the radical anions of NDI and PDI produced by electrochemical reduction in order to determine their excited-state lifetimes (Table 1.1). Outside of the Wasielewski group, Rybtchinski and co-workers reduced a water-soluble PDI in aqueous solution with sodium dithionite and determined the lifetime of the PDI dianion by fluorescence lifetime measurement.<sup>48</sup> The results of these various experiments are presented in table 1.1. These data allow us to use time-resolved UV-Vis-NIR spectroscopy (fsTA and nsTA, for femtosecond-scale and nanosecond-scale spectroscopy, respectively) to determine the excited-state and oxidation state dynamics of complexes containing RDI moieties.

**Table 1.1.** Photophysical properties of N,N'-bis(2,5-di-*tert*-butylphenyl) PDI and NDI in the neutral (N), radical anion (R<sup>•-</sup>), and dianion (R<sup>2-</sup>) forms. All data taken from<sup>45</sup> unless noted.

Compound	N: $\lambda$ (nm) ( $\epsilon$ (M <sup>-1</sup> cm <sup>-1</sup> ))	R <sup>•-</sup> : $\lambda$ (nm) ( $\epsilon$ (M <sup>-1</sup> cm <sup>-1</sup> ))	R <sup>2-</sup> : $\lambda$ (nm) ( $\epsilon$ (M <sup>-1</sup> cm <sup>-1</sup> ))	<sup>1</sup> N: $\tau$ (ps)	<sup>2</sup> R <sup>•-</sup> : $\tau$ (ps)	<sup>1</sup> R <sup>2-</sup> : $\tau$ (ps)
<b>NDI</b>	361 (15100)	474 (26000)	400 (19500)		141 ± 7	
	381 (16400)	605 (7200)	423 (26700)			
		698 (2400)	520 (2600)			
		777 (4100)	563 (6300)			
			612 (10600)			
<b>PDI</b>	458 (19300)	680 (50600)	532 (42400)	3800 ± 100	145 ± 15	6500 <sup>48</sup>
	490 (51000)	700 (79800)	570 (80000)			
	526 (80000)	712 (74200)	597 (36700)			
		766 (21600)	646 (18100)			
		795 (49600)	720 (3400)			
		955 (28200)				

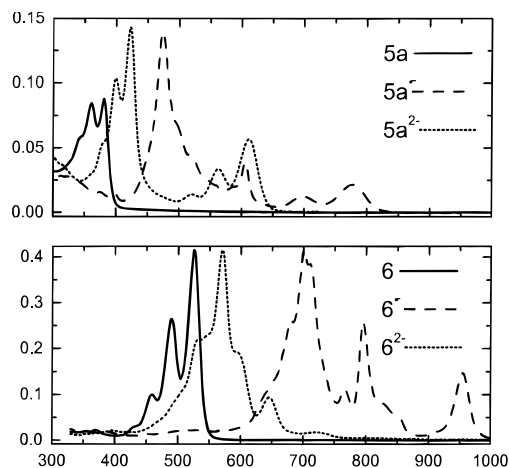


**Figure 1.2:** Ground-state absorption spectra of neutral, radical anion, and dianion forms of NDI (top) and PDI (bottom) in DMF + Bu<sub>4</sub>NPF<sub>6</sub>.

The Wasielewski group first investigated the photoexcitation of NDI<sup>-</sup> in the context of molecular photoswitches.<sup>49-50</sup> In those reports, NDI<sup>-</sup> was generated transiently via excited-state electron transfer from an attached chromophore and was then excited by a second pump pulse. This scheme is usually called, pump-pump-probe spectroscopy. The excited NDI<sup>-</sup> was able to undergo oxidative quenching to transfer an electron to an acceptor that could not have been reduced by the excited state of the first chromophore. While described at the time as a type of molecular photoswitch, the system also resembles a simplified version of the photosynthetic Z scheme, in which a difficult-to-reduce substrate is reduced using visible light photons absorbed by a series of chromophores.

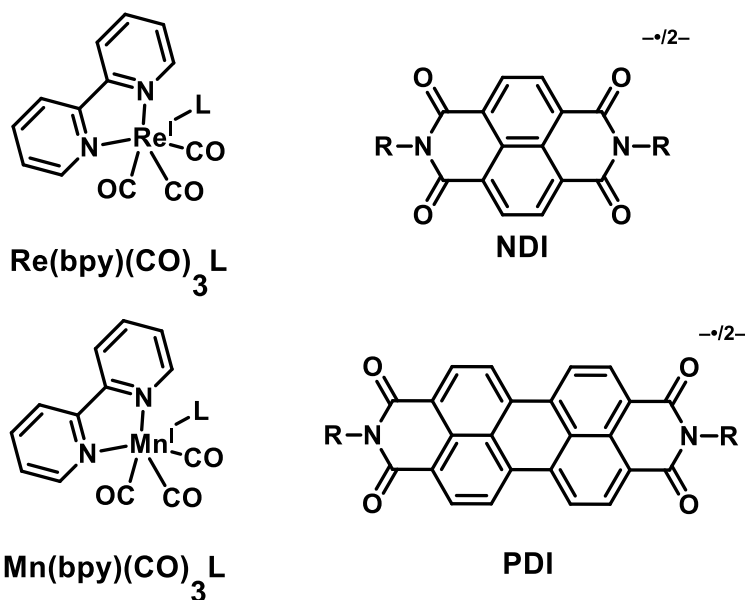
The first report of an application of a PDI anion chromophore was published by König and co-workers in 2014.<sup>51</sup> In that paper, the authors report the dehalogenation of thermodynamically difficult to reduce substrates by the photoexcitation of PDI<sup>-</sup>. Neutral PDI was found to convert quantitatively to the PDI radical anion upon irradiation with 455 nm light and triethylamine as the sacrificial electron donor. Photocatalytic experiments using 455 nm light were subsequently

performed in the presence of a halogenated aromatic electron acceptor, and it was found that aromatic dehalogenation occurred with substrates whose reduction potentials fell below that of the excited state oxidation potential of the  $\text{PDI}^{\bullet-}$ . The authors postulate a Z-scheme-like mechanism in which neutral PDI is excited and reductively quenched by  $\text{NEt}_3$  to produce the PDI radical anion. Subsequent excitation of the  $\text{PDI}^{\bullet-}$  results in reduction of the aryl halide to its radical anion, followed by halide loss and reaction of the aryl radical with  $\text{NEt}_3^{\bullet+}$  and a solvent molecule to produce the dehalogenated aryl product. Curiously, the reaction mechanism proposed and substantiated through various control experiments implies the photoexcitation of the PDI radical anion by 455 nm light, a wavelength at which the  $\text{PDI}^{\bullet-}$  does not absorb. No explanation is given for this discrepancy. Though recent work has postulated that a degradation product initiates the dehalogenation product as opposed to  $\text{PDI}^{\bullet-}$ .<sup>52</sup>

### **1.6 Selection for NDI/PDI and $\text{Re}(\text{bpy})(\text{CO})_3\text{L}/\text{Mn}(\text{bpy})(\text{CO})_3\text{L}$**

NDI/PDI derivatives have been previously incorporated into all-organic donor-acceptor systems, but have not yet been shown to reduce organometallic centers. RDI anion chromophores were chosen on the basis of their relatively long excited-state lifetimes and the ease with which they can be incorporated synthetically into donor-acceptor assemblies, including metal centers capable of reducing  $\text{CO}_2$ . Chosen for our initial studies was the prototypical  $\text{CO}_2$  reduction catalyst  $\text{Re}(\text{bpy})(\text{CO})_3\text{L}$  and  $\text{Mn}(\text{bpy})(\text{CO})_3\text{L}$ . These metal centers were chosen for several reasons: first, their spectroscopic properties are well-understood, allowing for facile interpretation of our TA data; second, its ligand arrangement allows the chromophore to be attached to the metal center using a variety of geometries, allowing us to explore the effect of geometry on the rate and yield of charge separation; third, there is precedent for photodriving the rhenium complex as a catalyst using a covalently attached chromophore.<sup>31, 44, 53-57</sup> Finally, the complex is known to reduce  $\text{CO}_2$

through a different set of pathways depending on whether the complex is reduced by one or two electrons before catalysis is initiated.<sup>58-60</sup> This property leaves open the possibility, which we have not yet explored extensively, of attaching multiple chromophores to the metal center and photodriving catalysis via the two-electron pathway.



**Scheme 1.2:** Structures of naphthalenediimide (NDI), perylenediimide (PDI),  $\text{Re}(\text{bpy})(\text{CO})_3\text{L}$ , and  $\text{Mn}(\text{bpy})(\text{CO})_3\text{L}$

An alluring property of NDI and PDI with respect to the use of their anions as chromophores is the ease with which they can be reversibly reduced.<sup>45</sup> The reduction potential remains fairly invariant despite changes to the substituent on the imide, reflecting the lack of electronic coupling between the RDI core and the imide. Gosztola et al studied NDI with both 2,5-di-*tert*-butylphenyl and *n*-octyl substituents and found that in both cases, the first reduction occurred at  $-0.48$  V vs SCE, while the second occurred at  $-0.99$  V. The first reduction of PDI was found to occur only slightly more positive of the first reduction of NDI, at  $-0.43$  V vs SCE, while the second reduction was significantly less negative than that of NDI, at  $-0.70$  V. The positive

shift in reduction potential as the RDI core is expanded is attributed to the delocalization of the extra electron across a larger aromatic region.<sup>61</sup> In the molecules studied in this study, the distal imide position on the NDI was substituted with 2,5-di-*tert*-butylphenyl, and the distal imide on the PDI was substituted with a tricosan-12-yl group to ensure the solubility of the respective diimides, and allows for desired chemistry to partake.

The electrochemistry of the  $\text{Re}(\text{bpy})(\text{CO})_3\text{L}$  and  $\text{Mn}(\text{bpy})(\text{CO})_3\text{L}$  systems has been extensively studied.<sup>25, 60, 62-69</sup> Briefly, the Re complex can be reduced twice under inert atmosphere, with the first reduction, occurring around  $-1.1$  V vs SCE, corresponding to the reduction of the bipyridine ligand from 0 to  $-1$ , and the second, occurring around  $-1.5$  V vs SCE, to the reduction of the Re center from  $+1$  to 0 and the simultaneous loss of the 6<sup>th</sup> coordinating ligand. The three most notable differences between the Mn and Re analogues are their  $\text{CO}_2$  reduction overpotential and reduction pathways. For example, the  $\text{Mn}(\text{bpy})(\text{CO})_3\text{Br}$  complexes reduce  $\text{CO}_2$  to CO at  $\sim 0.3$  V less, the first reduction is metal based while the second reduction is bipyridine localized, and the Mn complexes upon single-electron reduction rapidly lose Br and dimerize to form  $\text{Mn}^0\text{-Mn}^0$  complexes.<sup>68</sup> Overall, varying the substituents on the bpy ligand from electron donating to electron withdrawing can tune its reduction potential over a range of more than 700 mV while having a smaller effect on the reduction of the Re or Mn center. Varying the charge on the L ligand from neutral to anionic varies the reduction of the bpy ligand over a smaller range ( $\sim 100\text{--}200$  mV) while having a similar effect on the reduction of the Re or Mn center. It has also been observed that in general, better activity as a photo- or electrocatalyst correlates with a more negative potential for the reductions of both the bpy ligand and the Re/Mn center, although there are other properties that affect catalytic ability.<sup>28, 40, 62, 70</sup>

### 1.7 First Integration of NDI Anion Chromophores with CO<sub>2</sub> reduction Catalysts

Our work at the beginning of this project has focused on a set of dyads in which two NDI radical anion chromophores are attached to Re(bpy)(CO)<sub>3</sub> through the bipyridine ligand. Our ultimate goal is to employ the corresponding earth abundant Mn(bpy)(CO)<sub>3</sub> complex for CO<sub>2</sub> reduction catalysis. However, the Re complex is more stable and can serve to test the design strategy of the new photosensitizers we are employing. The NDI chromophores are reduced with a mild reducing agent (tetrakisdiethylamino, TDAE), after which excitation of NDI<sup>-</sup> with long-wavelength red or near-infrared light leads to reduction of the Re complex. The kinetics of electron transfer from the photoexcited anions to the Re complex are monitored using femtosecond

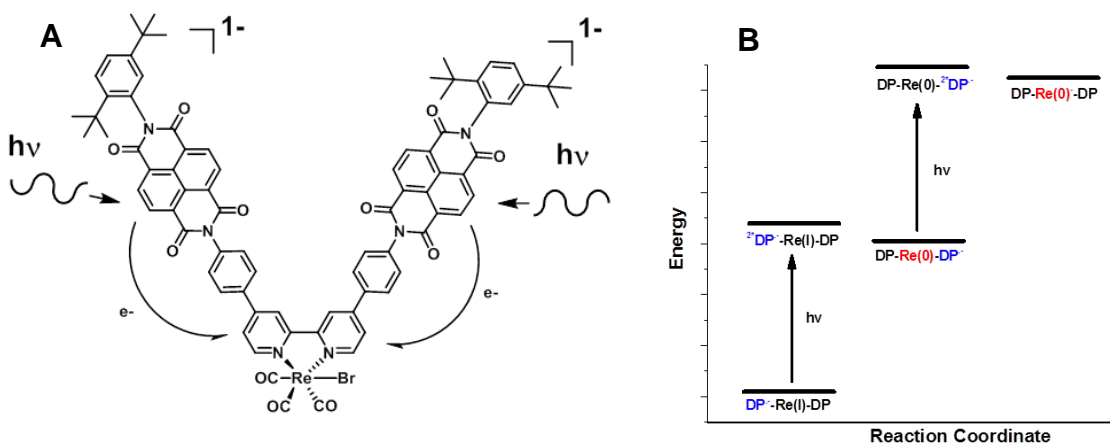


**Figure 1.3:** A) structure of Re(NDI<sub>2</sub>bpy)(CO)<sub>3</sub>Br. B) Energy level diagram of relevant excited and ionic states accessible following a single 100 fs laser pulse.

transient visible/near-IR (fsTA) and mid-IR (fsIR) spectroscopy. The photo-driven charge shift from the NDI<sup>-</sup> to the complex occurs in picoseconds, but back electron transfer is found to be slower.

We prepared the  $\text{Re}(\text{bpy})(\text{CO})_3$  complex shown in Figure 1.3A having two NDI chromophore attached to the bpy of the complex. Thus far in this project we have excited one of the two reduced NDI chromophores to test whether the single phenyl linker group between the NDI molecules and the bpy ligand decreases the electronic coupling between them sufficiently to give the reduced bpy a long enough lifetime to allow the second reduction to occur. The relevant electrochemistry for the  $\text{NDI}_2\text{bpy}$  ligand is shown in Figure 1.4A, while that of the  $\text{Re}(\text{NDI}_2\text{bpy})(\text{CO})_3\text{Br}$  complex is shown in Figure 1.4B. In both cases there are two distinct reversible reduction waves for NDI as it is reduced to the anion and dianion. This is followed by reduction of bpy at nearly -2.0 V in the ligand and -1.3 V in the complex. The final reduction of

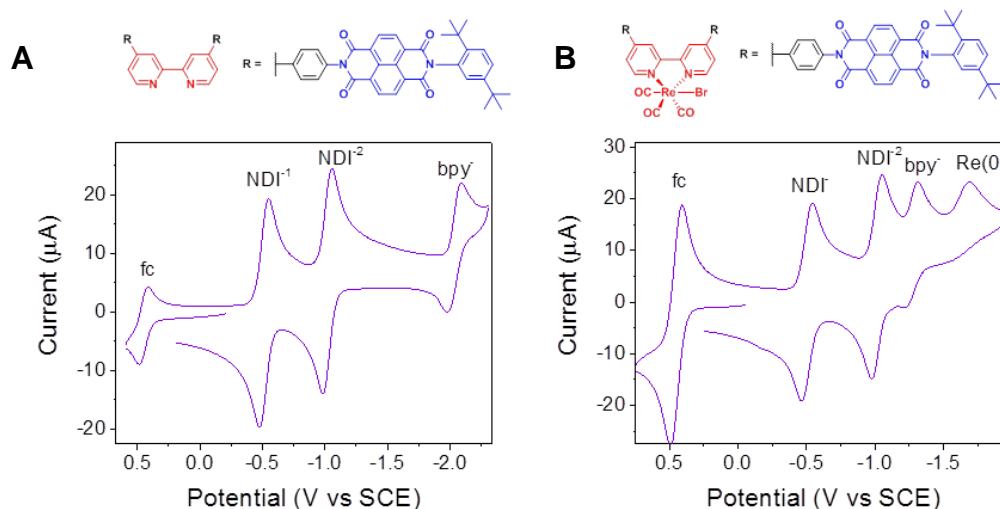


**Figure 1.4:** Electrochemistry in DMF with 0.1 M  $\text{TBAPF}_6$  using ferrocene/ferrocenium as a reference. A)  $\text{NDI}_2\text{bpy}$  ligand. B)  $\text{Re}(\text{NDI}_2\text{bpy})(\text{CO})_3\text{Br}$  complex.

the complex occurs at the Re center at -1.6 V which coincides with the loss of the bromide. Both the bpy ligand and the Re center in the complex can be reduced by the excited state of the  $\text{NDI}^-$  because it can deliver -2.1 V of reducing potential to a substrate.

An important question that occurs whenever a photosensitizer is covalently attached to a catalyst is whether the catalyst remains active to the same degree as when it functions as an

electrocatalyst. We tested the  $\text{Re}(\text{NDI}_2\text{bpy})(\text{CO})_3\text{Br}$  complex by performing electrocatalytic reduction of  $\text{CO}_2$  to  $\text{CO}$ . Catalysis must be performed in the presence of a weak acid. The cyclic voltammograms in Figure 1.5A show the changes in redox behavior that occur when increasing concentrations of methanol, which acts as a weak acid are added to a *N,N*-dimethylformamide (DMF) solution of the complex. While some of the potentials shift, all remain essentially reversible. Figure 1.5B shows the clear appearance of a strong catalytic wave in the voltammetry when  $\text{CO}_2$  is added to the solution along with methanol. The catalytic wave indicates that the Re complex is fully functional as a  $\text{CO}_2$  reduction catalyst even though two NDI photosensitizers have been appended to the bpy.

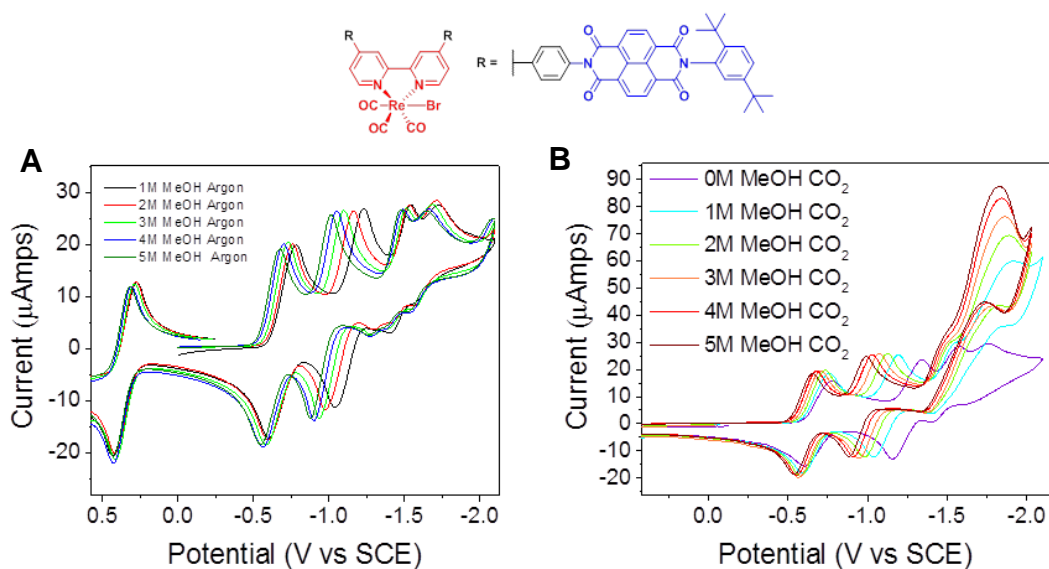


**Figure 1.5:** Electrochemistry of  $\text{Re}(\text{NDI}_2\text{bpy})(\text{CO})_3\text{Br}$  in DMF with 0.1 M  $\text{TBAPF}_6$  using ferrocene/ferrocenium as a reference. A) methanol added. B) methanol and  $\text{CO}_2$

Figure 1.6A shows the fsTA spectra of  $\text{Re}(\text{NDI}_2\text{bpy})(\text{CO})_3\text{Br}$  in DMF as a function of time following a 100 fs laser pulse. The spectrum of  $\text{NDI}^-$  bleaches immediately and electron transfer occurs from  $\text{NDI}^-$  to bpy in  $\tau = 2$  ps. The corresponding back electron transfer process occurs in

$\tau = 30$  ps. The energy levels and electron transfer pathways are shown in Figure 1.6C. The lifetime of the reduced bpy ligand needs to be increased to be a functional in CO<sub>2</sub> reduction catalysis. This can be done by inserting additional phenyl spacers between the NDI photosensitizer and the bpy. Based on our earlier work on organic donor-spacer-acceptor systems, each phenyl should result in about a factor of 10 increase in lifetime. Alternatively, we can employ an intermediary electron acceptor in a two-step electron transfer process, which could increase the lifetime by a factor of 10<sup>6</sup>. Our future work will explore both design options, so that we can develop a system in which the sequential application of two laser pulses can give us the doubly-reduced complex. This complex will bind CO<sub>2</sub> and begin the catalytic cycle for CO production. Using our fsIR spectroscopy apparatus, we should be able to monitor key intermediates in the process as the vibrational frequencies of the carbonyl ligands respond to electronic changes within the complex.

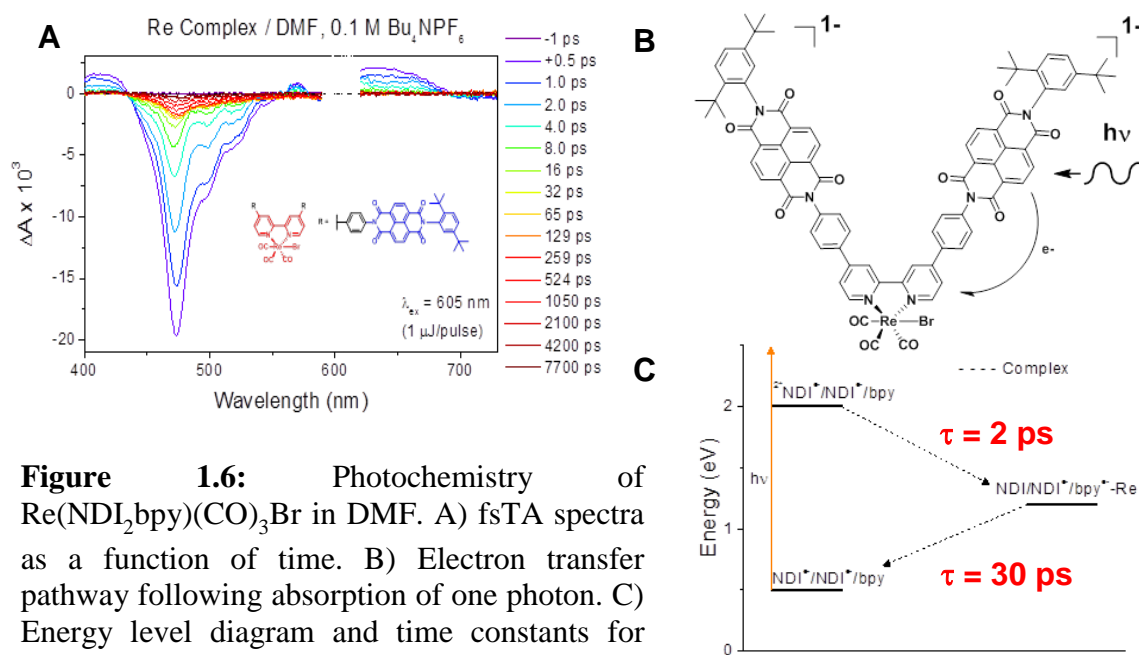


**Figure 1.6:** Photochemistry of Re(NDI<sub>2</sub>bpy)(CO)<sub>3</sub>Br in DMF. A) fsTA spectra as a function of time. B) Electron transfer pathway following absorption of one photon. C) Energy level diagram and time constants for forward and reverse electron transfer.

## 1.8 Thesis Outline

The primary intention of this work is to investigate the electron transfer events from the naphthalene diimide and perylene diimide radical anions to rhenium and manganese tris carbonyl diimine catalysts by time-resolved techniques. Our initial study involved covalently attaching two NDI chromophores to  $\text{Re}(\text{bpy})(\text{CO})_3\text{Br}$  as our end goal was to observe two sequential electron transfer processes upon selective excitation of the  $\text{NDI}^-$  chromophores, this is detailed at the end of the introduction in **Chapter 1**. The issue though was the lifetime of the reduced complex,  $\text{Re}(\text{bpy}^-)(\text{CO})_3\text{L}$ , was inherently too short for pump-pump-probe transient absorption spectroscopy, as a result we aimed to systematically study the attachment of NDI to  $\text{Re}(\text{bpy})(\text{CO})_3\text{L}$  in order to understand the electron transfer processes further. Proceeding this study, in **Chapter 2**, different motifs were synthesized with NDI or PDI which involved direct attachment of the RDI chromophore to the  $\text{Re}(\text{bpy})(\text{CO})_3$  complex by either through the bipyridine ligand or through the pyridine ligand. In **Chapters 3 and 4**, a second generation of molecules comprised the same attachment geometries but with the addition of an intermediate electron acceptor. This intermediate acceptor was inserted in order to facilitate a longer lifetime of the final charge-separated state without compromising the rate of formation of that state. The complexes described in **Chapter 3** had a critical element that was improved in **Chapter 4**, in that the intermediate acceptor was linked through the bipyridine instead of directly to the rhenium center. Proceeding these developments, in **Chapter 5 & 6** we investigated the substituent position of NDI chromophore around the 4, 5, and 6 positions of bipyridine and the Gibbs free energy for back electron transfer for Mn & Re complexes. With respect to Re, these complexes illustrated that the electronic coupling in the final charge separated state dictated the longer charge separated lifetimes in 6 than in the 5 or 4 bound complexes. Surprisingly, the Mn complex that had the  $\text{NDI}^-$

chromophore at the 6 positions of bipyridine produced long lived intermediates and new transition flow that had not been observed before.

## **Chapter 2 Photoinduced Electron Transfer from the Radical Anions and Dianions of Naphthalene and Perylene Diimides to $\text{Re}(\text{bpy})(\text{CO})_3$ Using Red and Near-Infrared Light**

N. T. La Porte, J. F. Martinez, S. Hedström, B. Rudshiteyn, B. T. Phelan, C. M. Mauck, R. M. Young, V. S. Batista and M. R. Wasielewski, *Chem. Sci.*, 2017, **8**, 3821. DOI: 10.1039/C6SC05103K - Published by The Royal Society of Chemistry.

## 2.1 Introduction

One desirable component in the development of artificial photosynthetic systems is a chromophore having an excited state capable of reducing thermodynamically demanding organometallic catalysts using the majority of the solar spectrum available at Earth's surface, including low energy photons in the near-infrared region. In the field of organometallic photochemistry, highly reducing chromophores have been developed, but these chromophores often incorporate non-earth-abundant metals such as Ir<sup>37-38</sup>, Pt,<sup>39</sup> or Re<sup>40</sup> and none absorb light at wavelengths longer than 550 nm.<sup>32-34, 36, 71</sup> There are very few reports of such highly reducing chromophores being incorporated into donor-acceptor assemblies, with only one report to date of an Ir-based photosensitizer and a CO<sub>2</sub> reduction catalyst, in which an Ir<sup>III</sup>(1-phenylisoquinoline)<sub>2</sub>(bpy) complex is attached to a Re(bpy)(CO)<sub>3</sub> catalyst, and catalysis is achieved upon illumination at 480 nm.<sup>42</sup> There have also been a handful of reports of donor-acceptor assemblies run at wavelengths as long as 600 nm that incorporate less highly reducing chromophores such as zinc or magnesium porphyrins<sup>43</sup> and Os<sup>III</sup>(bpy)<sub>3</sub>.<sup>72</sup>

In the field of fully organic photochemistry, most highly reducing chromophores absorb in the blue or UV regions, while those that absorb in the longer-wavelength visible region are typically not powerful enough reductants to reduce carbon dioxide reduction catalysts. However, the radical anions and dianions of the rylene diimide (RDI) dyes perylene-3,4:9,10-bis(dicarboximide) (PDI) and naphthalene-1,4:5,8-bis(dicarboximide) (NDI) are much stronger reductants than their neutral counterparts, while their absorption spectra extend significantly into the red or even near-infrared.<sup>45</sup> When stored under inert atmosphere, these chromophores are stable in organic or even aqueous solution.<sup>48</sup> A similar strategy, in which a reduced chromophore is used to sensitize a Re(bpy)(CO)<sub>3</sub> center, has been reported very recently by Neumann and co-workers

in a system incorporating a reduced polyoxometalate as a long-wavelength-absorbing chromophore.<sup>73</sup> This method, in which a highly reducing chromophore is easily generated using chemical or electrochemical means and subsequently used to drive a highly endothermic electron transfer reaction, is applicable not only to the study of carbon dioxide reduction, but could also be employed to facilitate other transformations such as photoelectrocatalytic N<sub>2</sub> reduction or photoredox reactions involving electron-rich organic substrates that are not easily reduced using typical photoredox chromophores.

When used as electron acceptors, rylenediimides have been incorporated into numerous donor-acceptor assemblies using well-developed synthetic procedures. In a limited number of reports, assemblies have been developed to use the excited states of the PDI and NDI radical anions as electron donors to other organic molecules,<sup>49-50, 74-75</sup> but to date there have been no similar reports of electron transfer from the excited closed-shell dianions of either molecule, nor have there been any reports of electron transfer from any excited PDI or NDI anionic species to organometallic acceptors. In the present report, we describe donor-acceptor complexes comprised of the radical anions or dianions of RDI chromophores bound to Re(bpy)(CO)<sub>3</sub> metal centers. These complexes photoreduce a Re(bpy)(CO)<sub>3</sub> metal center using long-wave visible (>600 nm) or near-infrared (950 nm) light.

Previous to this report, photo-driven reduction of the Re(bpy)(CO)<sub>3</sub> complex using long-wavelength (>600 nm) visible light has only been confirmed in a handful of cases, in one case with the use of zinc tetraphenylchlorin<sup>55</sup> and another case using Os(bpy)<sub>3</sub>-derived chromophores.<sup>72</sup> In these complexes, reduction of the Re(bpy)(CO)<sub>3</sub> center proceeds via quenching of the excited state of the chromophore by a sacrificial donor, followed by thermal electron transfer from the reduced chromophore to Re(bpy)(CO)<sub>3</sub>. One complex has been reported in which reduction does proceed

via excited state electron transfer, but the bpy ligand on the Re center has been modified to dramatically lower its reduction potential below the threshold at which CO<sub>2</sub> reduction could theoretically occur.<sup>76</sup> Our lab recently reported on a set of compounds in which a reduced naphthalenediimide chromophore photoreduces a Re(bpy)(CO)<sub>3</sub> center through an intermediate diphenylanthracene acceptor.<sup>77</sup> That work explored the effect of changing the attachment geometry of the diphenylanthracene to the Re center, however the NDI radical anion chromophore was always covalently bound to the diphenylanthracene acceptor in the same fashion and so there was no change in the excited-state electron transfer kinetics. Furthermore, in that study we only examined the NDI radical anion chromophore, while the present report also describes electron transfer to the Re(bpy)(CO)<sub>3</sub> center from the excited states of the PDI radical anion and dianion.

In the complexes presented in this report, the RDI anion chromophore is bound to the Re(bpy)(CO)<sub>3</sub> center either through the bpy ligand or directly to the Re center through a pyridine ligand. The forward- and back-electron transfer kinetics of the complexes are investigated using a combination of femto- and nanosecond transient absorption spectroscopies in the visible/NIR (fsTA, nsTA) and mid-IR (fsIR) to observe the transient photoproducts of both the chromophore and the metal center. The difference between the two architectures is notable: while both types of complexes exhibit ultrafast charge shift kinetics, the complexes in which the RDI anion is attached to the bpy ligand have back-electron transfer lifetimes in the tens of picoseconds, while the complexes in which the RDI anion is attached directly to the Re center have back-electron transfer lifetimes in the nanosecond regime. In both cases, fsIR confirms that the bpy ligand is reduced in the Re(bpy)(CO)<sub>3</sub> complex, the reaction known to be the first step in the photocatalytic mechanism of CO<sub>2</sub> reduction by such complexes.

We recognize that to expand this work to a fully catalytic system is not a trivial task, since catalysis is typically initiated upon the generation of the doubly-reduced  $\text{Re}^0(\text{bpy}^{\cdot-})(\text{CO})_3$  species. To do so requires either multiple chromophores attached to a single reaction center, or rapid regeneration of the ground-state chromophore using a sacrificial electron donor. Work on both of those avenues is ongoing in our lab. We also recognize that in this regard, the pyridine-ligated chromophore will be of less utility than the bpy-ligated chromophore, since in order to initiate  $\text{CO}_2$  binding, the pyridine ligand must dissociate from the Re center, and this dissociation would prevent catalytic turnover. Nevertheless, we feel that our observation of the difference in electron transfer rate between complexes in which the chromophore is bound to the bipyridine ligand and complexes in which the chromophore is bound directly to the Re center is applicable to the design of future catalytic systems for the following reasons: first, Ishitani and co-workers have developed  $\text{Re}(\text{diimine})$  complexes that are catalytic for  $\text{CO}_2$  reduction and which contain redox-innocent ligands such as phosphines that do not dissociate during catalysis, to which a chromophore could be attached.<sup>53</sup> Second, Kubiak and co-workers recently reported a Mn-based  $\text{CO}_2$  reduction catalyst that contains only redox-innocent isocyanide ligands that do not dissociate during catalysis.<sup>78</sup> These two reports suggest that there is the potential to attach a reduced RDI chromophore to either the redox-active bpy ligand or directly the Re center, and consequently it is valuable to understand the effect that these different attachment motifs have on the electron transfer behavior of the complex.

## **2.2 Experimental Details**

### **2.2.1 Synthesis and Methods**

DCM and MeOH used for synthesis were obtained from Fisher Scientific and used as received. Acetonitrile, toluene, DMF and THF used for synthesis and spectroscopic experiments were dried on a commercial system (GlassContour, Laguna Beach, CA). For spectroscopy, DMF was further transferred under argon into a N<sub>2</sub>-filled glovebox (MBraun Unilab) for use and storage. Commercially available reagents were purchased from Sigma-Aldrich and used as received. Compounds were reduced in the glovebox using tetrakisdiaminoethylene (TDAE) from Tokyo Chemical Industries or CoCp<sub>2</sub> from Sigma-Aldrich. <sup>1</sup>H NMR spectra were recorded on a Bruker Avance 500 TCI Cryoprobe Spectrometer. Chemical shifts are recorded in ppm (δ) in CDCl<sub>3</sub> (internal reference set to δ 7.26 ppm). <sup>13</sup>C NMR (126 MHz) spectra were recorded using a Bruker Avance III QNP Cryoprobe with simultaneous decoupling of <sup>1</sup>H nuclei and externally referenced to TMS set to 0 ppm. All spectra were recorded at 298 K. High resolution mass spectrometry (ESI-MS) were performed by Northwestern University's Integrated Molecular Structure Education and Research Center.

### **2.2.2 Steady State Spectroscopy**

UV-vis spectra were acquired on a Shimadzu UV-1800 spectrophotometer at room temperature. The samples were normalized to the greatest peak. FT-IR spectra were measured on a Shimadzu IRAffinity<sup>-1</sup> spectrophotometer in absorbance mode at 2 cm<sup>-1</sup> resolution. Samples were prepared in under an argon atmosphere, contained in a liquid demountable cell (Harrick Scientific) with 2.0 mm thick CaF<sub>2</sub> windows and 500 μm Teflon spacers.

### **2.2.3 Electrochemistry**

Electrochemical measurements were performed using a CH Instruments Model 660A electrochemical workstation. A single-compartment cell was used for all cyclic voltammetry experiments with a 1.0 mm diameter glassy carbon disk working electrode, a platinum counter electrode, a silver wire pseudoreference electrode, and 0.1 M tetra-*n*-butylammonium hexafluorophosphate (TBAPF<sub>6</sub>) as the supporting electrolyte in DMF. The ferrocene/ferrocenium redox couple (0.45 V vs SCE in DMF)<sup>79</sup> was used as an internal standard. TBAPF<sub>6</sub> was recrystallized twice from ethanol prior to use. Electrochemical cells were shielded from light during experiments and done in the dark. All solutions were continuously purged with argon before and during the cyclic voltammetry experiments.

#### **2.2.4 Femtosecond Transient Absorption Spectroscopy**

Femtosecond transient absorption experiments were performed employing a regeneratively amplified Ti:sapphire laser system operating at 828 nm and a 1 kHz repetition rate as previously described.<sup>80-81</sup> The output of the amplifier was frequency-doubled to 414 nm using a BBO crystal and that light was used to pump a laboratory-built collinear optical parametric (OPA) amplifier<sup>82</sup> for visible-light excitation or a commercial non-collinear optical parametric amplifier (TOPAS-White, Light-Conversion, LLC.) for NIR excitation. Approximately 1-3 mW of the fundamental was focused onto a sapphire disk to generate the visible white-light probe spanning 430-850 nm, or into a 5 mm quartz cuvette containing a 1:1 mixture of H<sub>2</sub>O:D<sub>2</sub>O to generate a UV/visible white light probe spanning 385-750 nm, or onto a proprietary medium (Ultrafast Systems, LLC) to generate the NIR white-light probe spanning 850-1620 nm. The total instrument response function was 300 fs.

Experiments were performed at a randomized pump polarization to suppress contributions from orientational dynamics. Spectral and kinetic data were collected with a CMOS or InGaAs array detector for visible and NIR detection, respectively, and a 8 ns pump-probe delay track (customized Helios, Ultrafast Systems, LLC). Transient spectra were averaged for at least 3 seconds. All spectra were acquired in DMF solution. Samples had an absorbance of 0.2-0.7 at the excitation wavelength and were irradiated in 2 mm quartz cuvettes with 0.4-0.8  $\mu\text{J}/\text{pulse}$  focused to  $\sim 0.2$  mm diameter spot. Samples were stirred to avoid effects of local heating or sample degradation. The samples were prepared in the glovebox and degassed by multiple freeze-pump-thaw cycles prior to analysis.

### **2.2.5 Nanosecond Transient Absorption Spectroscopy**

Nanosecond transient absorption experiments were performed using the femtosecond excitation beam described above and a commercial spectrometer (Eos, Ultrafast Systems, LLC) utilizing a photonic crystal fiber ultra-broadband probe source. The pump polarization was randomized to suppress rotational dynamics. Samples were stirred to avoid effects of local heating or sample degradation.

### **2.2.6 Femtosecond Transient Mid-IR Absorption Spectroscopy**

Femtosecond transient mid-IR absorption spectroscopy was performed using a commercial Ti:sapphire oscillator/amplifier (Solstice 3.5W, Spectra-Physics) to pump two optical parametric amplifiers (TOPAS-C, Light Conversion), one which provided a 100 fs, 2  $\mu\text{J}$  excitation pulse at 705 or 605 nm and the other which provided 100 fs probe pulses from 2150–1800  $\text{cm}^{-1}$ . The overall instrument response was 0.3 ps. The spectra were acquired with a liquid  $\text{N}_2$ -cooled dual channel (2 x 64) MCT array detector that is coupled to a Horiba iHR320 monochromator as part

of a Helios-IR spectrometer (Ultrafast Systems, LLC) with a 300 l/mm grating ( $3\text{ cm}^{-1}$  resolution). Samples were prepared in DMF contained in a liquid demountable cell (Harrick Scientific) with  $\text{CaF}_2$  windows and a 500  $\mu\text{m}$  or 630  $\mu\text{m}$  Teflon spacer. The sample cell was mounted on a motorized stage and rastered during acquisition to reduce sample degradation.

### 2.2.7 Computational Methodology for Geometries

Geometries were optimized using density functional theory (DFT) with Q-Chem Version 4.3<sup>83</sup> using the B3P86 functional and LANL2DZ ECP basis set for Re-containing molecules,<sup>84</sup> and the B3LYP functional and 6-31G\* basis set for purely organic molecules. Alkyl and aryl groups on the PDI and NDI moieties, respectively, were replaced with Me groups to reduce computational time.

### 2.2.8 Computational Methodology for TDDFT Calculations

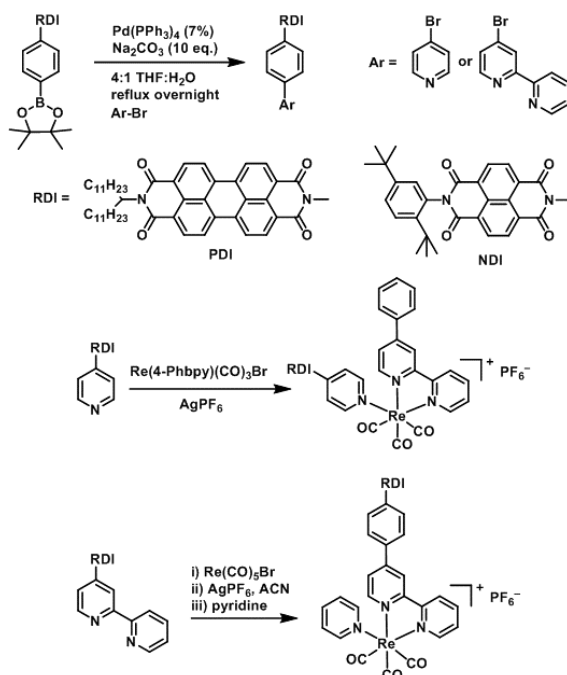
All density functional theory (DFT) calculations utilized the B3LYP functional,<sup>85</sup> as implemented in Gaussian 09, Revision D.01<sup>86</sup> software. The Def2SVP basis set (with corresponding pseudopotential on Re)<sup>87</sup> was used for geometry optimizations, and time-dependent DFT (TDDFT) calculations. The Def2TZVP basis set (pseudopotential on Re) was used for more accurate single-point energies as well as orbital analysis.<sup>87</sup> The Gaussian09 “ultrafine” numerical integration grid was used throughout, as well as the “tight” optimization criteria. All calculations were performed in the presence of a dielectric continuum of N,N-dimethylformamide (DMF) ( $\epsilon = 37.219$ )<sup>86</sup> as described by the SMD model.<sup>88-91</sup> Vertical TDDFT calculations on the first 40 singlet excited states were performed.<sup>92-98</sup> The first three transitions in the PDI anion (D1, D2, D3) were subject to TDDFT excited-state optimizations and numerical frequency calculations, to create absorption spectra incorporating vibronic effects.<sup>99</sup> The D1 and D2 vibronic spectral lines were

broadened with Gaussian functions with full-width half-maximum (FWHM) values of  $270\text{ cm}^{-1}$ . For the D3 state, a single remaining imaginary frequency was projected out of the Hessian, and the D3 spectral lines used a broadening with  $\text{FWHM}=800\text{ cm}^{-1}$ . Alkyl and aryl groups on the PDI and NDI moieties, , were replaced with Me groups for computational expediency. The D3 state consistently crossed over to the D2 or D1 state during optimization, so a slightly truncated structure with the methyl group replaced by hydrogen was used to optimize the D3 state. The states of PDI vary from neutral singlet to anionic doublet to doubly anionic singlet upon two sequential reductions. The states of  $[\text{Re}(\text{Phbpy})(\text{py})(\text{CO})_3]^+$  (as well as the dyad) vary from cationic singlet to neutral doublet to anionic singlet upon two sequential reductions. Spin contamination in the cases of the doublets was found to be negligible using unrestricted DFT.

## 2.3 Results

### 2.3.1 Synthesis

PDI and NDI chromophores were linked to  $\text{Re}(\text{bpy})(\text{CO})_3$  fragments both through the bipyridine ligand and through the pyridine ligand. Synthesis of the RDI-containing Re complexes was accomplished through Suzuki coupling of the appropriate RDI-Ph-Bpin to 4-bromopyridine or 4-bromobipyridine, followed by reaction with the appropriate Re precursor (Scheme 2.1) and purification on silica to produce the desired complex. Detailed synthetic procedures and characterization of compounds are provided down below.



**Scheme 2.1:** Synthesis of RDI-Phbpy-Re-Py and Phbpy-Re-PyPhRDI.

### 2.3.2 Electrochemistry

The electrochemical redox potentials of the complexes and model complex  $\text{Re}(\text{Phbpy})(\text{CO})_3(\text{py})$  are shown in Table 2.1. Attachment of the RDI chromophore has a very minor

**Table 2.1:** Electrochemical redox potentials for the complexes under study, as well as model compounds.

	$E(\text{RDI}^{0/-})^b$ (V)	$E(\text{RDI}^{-/2-})^b$ (V)	$E(\text{bpy}^{0/-})$ (V)	$E(\text{Re}^{I/0})$ (V)
<b>PDI<sup>c</sup></b>	-0.43	-0.70	-	-
<b>NDI<sup>c</sup></b>	-0.48	-0.99	-	-
<b>Phbpy-Re-Py</b>	-	-	-1.08	-1.53 <sup>d</sup>
<b>PDI-Phbpy-Re-Py</b>	-0.51	-0.78	-1.11	-1.45 <sup>d</sup>
<b>NDI-Phbpy-Re-Py</b>	-0.50	-1.01	-1.11	-1.47 <sup>d</sup>
<b>Phbpy-Re-PyPhPDI</b>	-0.47	-0.74	-1.06	-1.47 <sup>d</sup>
<b>Phbpy-Re-PyPhNDI</b>	-0.50	-1.05	-1.10	-1.47 <sup>d</sup>

<sup>a</sup> All electrochemical experiments were performed in DMF with 0.1 M TBAPF<sub>6</sub>, using a platinum disk working electrode, a platinum wire counter electrode, and a silver wire pseudoreference electrode. Potentials were referenced to a ferrocene internal standard ( $E(\text{Fc}^{+/0}) = 0.45$  V vs SCE) and are given versus the saturated calomel electrode (SCE). <sup>b</sup> RDI<sup>-</sup> is equivalent to the RDI<sup>•-</sup> radical anion <sup>c</sup> From ref. 45 <sup>d</sup> Irreversible,  $E_{\text{peak}}$  from CV given.

effect on the bpy-centered and Re-centered reductions of the complexes, indicating that there is little electronic communication between the RDI and Re(bpy) moieties.

### 2.3.3 Steady-State Photophysical Characterization

Titration with the appropriate reductant under an inert atmosphere reduced the RDI moiety to  $\text{RDI}^{n-}$ . TDAE ( $E = -0.60$  V vs SCE)<sup>100</sup> allowed access to the  $\text{RDI}^{\bullet-}$  states without the risk of formation of  $\text{RDI}^{2-}$ , while the use of  $\text{CoCp}_2$  ( $E = -0.87$  V vs SCE in  $\text{CH}_2\text{Cl}_2$ )<sup>79</sup> allowed access to the  $\text{PDI}^{2-}$  states without the risk of reduction of the bpy ligand. It was not possible to obtain

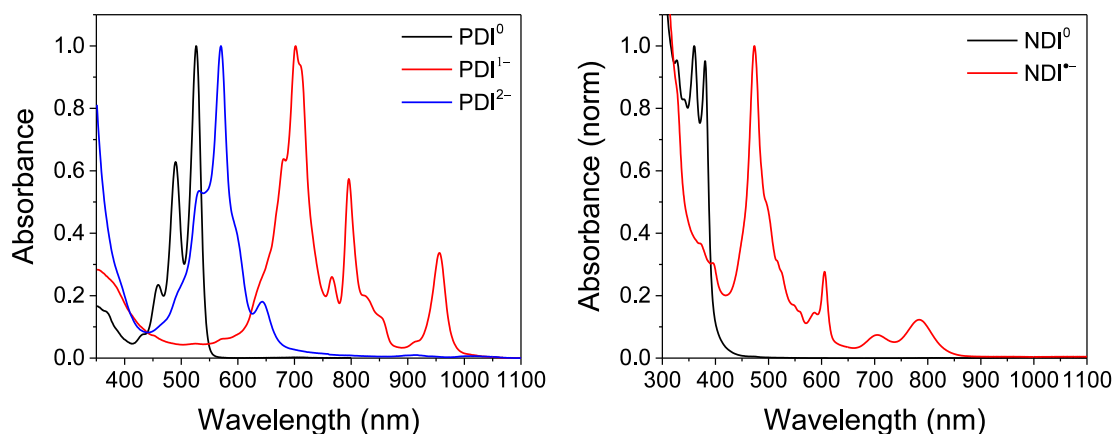


**Figure 2.1:** Top: Spectra of **PDI-Phbpy-Re-Py** in the neutral (black),  $\text{PDI}^{1-}$  (red) and  $\text{PDI}^{2-}$  (blue) states. Bottom: Spectra of **Phbpy-Re-PyPhNDI** in the neutral (black) and  $\text{NDI}^{1-}$  (red) states.

quantitatively reduced  $\text{NDI}^{2-}$  states of the complexes that incorporated that chromophore because the redox potentials of  $\text{NDI}^{\bullet/2-}$  and  $\text{bpy}^{0/\bullet-}$  are too similar. Spectra of the  $\text{RDI}$ ,  $\text{RDI}^{\bullet-}$  and  $\text{RDI}^{2-}$  states of the complexes are shown in Figure 2.1, and their similarity to the reported spectra of neutral and reduced  $\text{RDI}^{45}$  similarly indicates weak electronic coupling between the two moieties.

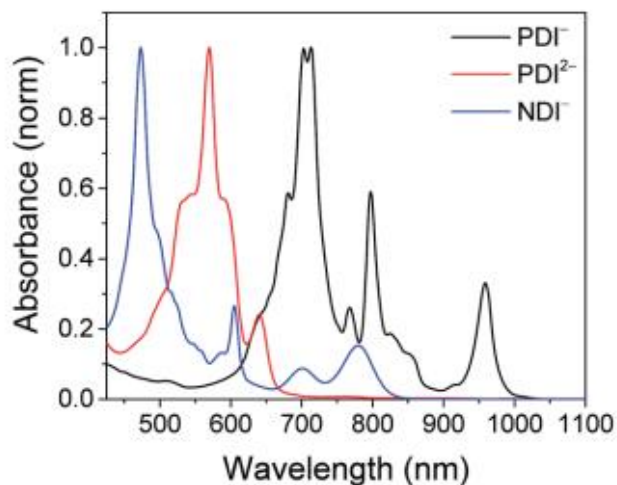


**Figure 2.2:** Spectra of chemically reduced samples of C-23<sub>2</sub>-PDI (black: radical anion, reduced with TDAE, red: dianion, reduced with CoCp<sub>2</sub>) and 2,6-di<sub>t</sub>Bu-Ph-NDI-Ph (blue: radical anion, reduced with TDAE) in DMF.

### 2.3.4 Transient Absorption Spectroscopy

For femtosecond transient absorption (fsTA) experiments, the complexes could also be reduced in a spectroelectrochemical cell, resulting in identical steady-state spectra, albeit with a large scattering background due to the presence of the Pt mesh working electrode. The fsTA spectra obtained from electrochemically reduced samples of **PDI-Phbpy-Re-Py** were found to be identical to those obtained from chemically reduced samples.

Shown in Figure 2.11 are the visible and NIR transient absorption spectra of the uncomplexed RDI<sup>n-</sup> chromophores. They display negative  $\Delta A$  features corresponding to the loss of ground state absorptions and appearance of excited state stimulated emission, and positive  $\Delta A$  features corresponding to excited state induced absorptions. For the doublet radical anions PDI<sup>•-</sup> and NDI<sup>•-</sup>, these features all decay concurrently with lifetimes consistent with the reported lifetimes of  $145 \pm 15$  ps and  $141 \pm 7$  ps, respectively.<sup>45</sup> For the singlet dianion PDI<sup>2-</sup>, the decay of

the singlet excited state features is accompanied by the rise of new features which live for tens of nanoseconds and are presumed on the basis of their lifetime to correspond to the dianion triplet excited states. The lifetime of the  $\text{PDI}^{2-}$  singlet excited state has been reported as 6.5 ns.<sup>48</sup>

Excitation of the  $\text{RDI}^{n-}$  moiety of each complex leads to instantaneous bleaching of the  $\text{RDI}^{n-}$  ground state absorption bands and formation the  $\text{RDI}^{n-}$  excited state bands. The lifetime of the excited state was diminished relative to the native  $\text{RDI}^{n-}$  chromophores, and at later times, bands characteristic of the  $\text{RDI}^{(n-1)-}$  states are observed. For example, Figure 2.3A shows the time evolution of the transient absorption spectra for **Phbpy-Re-PyPhPDI<sup>1-</sup>**, showing induced absorptions of  $\text{PDI}^{*-}$  at 459 nm and 550-630 nm, ground state bleaching of  $\text{PDI}^*$  centered at 700 nm and 797 nm, overlapped ground state bleach and stimulated emission bands at 959 nm and stimulated emission bands of  $\text{PDI}^*$  at 1100 nm and 1300 nm which decay to new induced absorptions of  $\text{PDI}^0$  at 490 nm and 525 nm. Similar spectra for the other molecules in the study are shown in Figures 2.11 – 2.24. The lifetimes of the excited states of the various complexes are given in Table 2.2.

In the femtosecond time-resolved mid-IR transient absorption (fsIR) experiments, the CO stretching region of the  $\text{Re}(\text{bpy})(\text{CO})_3$  moiety ( $1850\text{-}2100\text{ cm}^{-1}$ ) was monitored. All complexes exhibited the same spectral features, with only the kinetics differing from complex to complex. FsIR spectra for **Phbpy-Re-PyPhPDI<sup>1-</sup>** are shown in Figure 2.3B, and similar spectra for the other molecules in the study are shown in Figures 2.11-2.24. After excitation, bleaching of the ground-state absorptions at  $2046\text{ cm}^{-1}$  and  $1928\text{ cm}^{-1}$  was observed, and induced absorptions were observed at  $2020\text{ cm}^{-1}$  and  $1885\text{ cm}^{-1}$ .

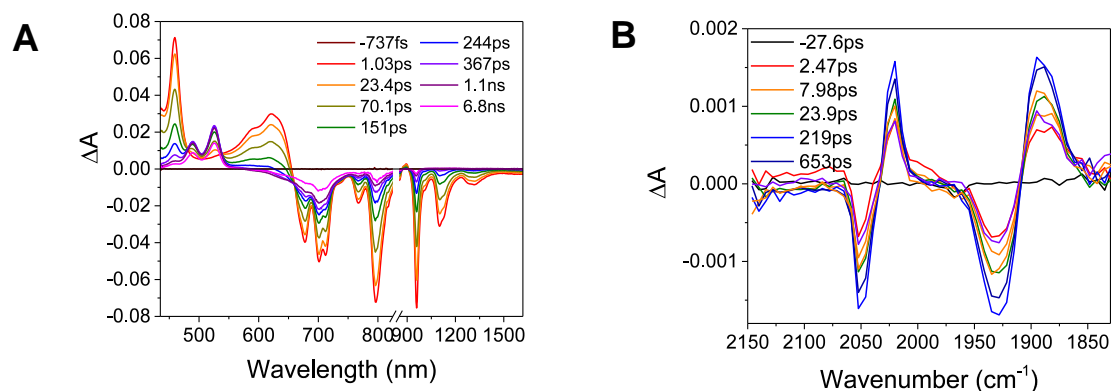


**Figure 2.3:** (A) Transient absorption spectrum of Phbpy-Re-PyPhPDI<sup>1-</sup> ( $\lambda_{\text{ex}} = 950 \text{ nm}$ ). (B) Time-resolved mid-IR spectrum of Phbpy-Re-PyPhPDI<sup>1-</sup> ( $\lambda_{\text{ex}} = 704 \text{ nm}$ ).

## 2.4 Discussion

### 2.4.1 Electron Transfer Energetics

Based on the redox potentials shown above, the Gibbs free energy for the excited state electron transfer reactions of each complex can be estimated using the following equation:

$$\Delta G_{\text{ET}} = (E_{\text{ox}} - E_{\text{red}}) - E_{00} \quad (1)$$

where  $E_{\text{ox}}$  and  $E_{\text{red}}$  are the oxidation and reduction potentials of the donor and acceptor respectively, and  $E_{00}$  is the energy of the <sup>\*</sup>NDI<sup>-</sup>, <sup>\*</sup>PDI<sup>-</sup>, or <sup>\*</sup>PDI<sup>2-</sup> excited state. There is no electrostatic work term for this reaction because the reaction is a charge shift, not a charge separation. In addition, there is no solvation correction term because the experiments are performed in the same solvent as the electrochemical data is obtained. The Gibbs free energy for the thermal forward and back electron transfer reactions can be estimated using the following equation.

$$\Delta G_{\text{ET}} = (E_{\text{ox}} - E_{\text{red}}) \quad (2)$$

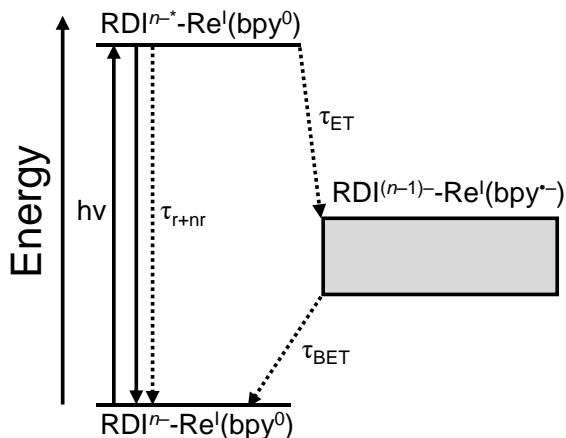


**Figure 2.4:** Energy level diagram showing general scheme of electron transfer in  $\text{RDI}^{n-}\text{-Re}(\text{bpy})$  complexes after excitation. Energy of the charge-transfer state is shown as a range to reflect the different energies of different complexes.

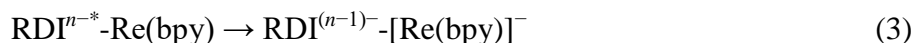
From the equations above, the Gibbs free energies for each electron transfer step are shown in Table 2.2 below.

#### 2.4.2 Lifetimes and Rates of Forward Electron-Transfer Quenching

For every complex except **PDI<sup>1-</sup>-Phbpy-Re-Py**, which will be discussed further below, the fsTA and fsIR data fit to a model in which the excited state decays to a charge-shifted state with the lifetime shown in Table 2.2, which then undergoes back-electron transfer to regenerate the ground state. The back-electron transfer lifetime is <100 ps for the bipyridine-ligated complexes, and >10 ns for the pyridine-ligated complexes. Plots showing the kinetic analysis of the visible/NIR and mid-IR spectra and kinetic fits for each complex are shown in Figures 2.11-2.24. A Jablonski diagram showing the general electron-transfer behavior of the complexes is shown in Figure 2.4.

Observation of the induced absorptions of  $\text{RDI}^{(n-1)-}$  and concomitant growth of induced absorptions in the mid-IR characteristic of the bpy-localized reduction of the  $\text{Re}(\text{bpy})(\text{CO})_3$  moiety

(see below) indicates that the excited states decay via electron transfer to the Re(bpy)(CO)<sub>3</sub> moiety, as shown in Eq. 3:



The lifetimes and rates of forward electron transfer quenching  $\tau_{ET}$  and  $k_{ET}$  are shown in Table 2.2 and can be calculated based on the observed excited state lifetime  $\tau_{obs}$  and the intrinsic lifetime of the chromophore  $\tau_0 = \tau_{r+nr}$ :

$$\tau_{ET} = \frac{1}{k_{ET}} = \frac{1}{\frac{1}{\tau_{obs}} - \frac{1}{\tau_0}} \quad (4)$$

The time constants and rates of back-electron transfer  $\tau_{BET}$  and  $k_{BET}$  can be calculated by observing the decay of the  $\text{RDI}^{(n-1)-}$  induced absorption bands, from the recovery of the  $\text{RDI}^{n-}$  ground state bleach, or from the decay of the induced absorptions and recovery of the ground state bleaches in

**Table 2.2:** Rates and Gibbs free energy of electron transfer reactions discussed in this study.

	$\text{RDI}^{n-}$	$\tau_{obs}$ (ps)	$\tau_{ET}$ (ps)	$k_{ET}$ ( $10^{10}$ s <sup>-1</sup> )	$\Delta G$ (eV)	$\tau_{BET}$	$k_{BET}$ (s <sup>-1</sup> )	$\Delta G_{BET}$ (eV)
<b>PDI-bpy-Re-py</b>	1-	53.5 ± 1.4	23.4 <sup>a</sup>	5.3	-0.81	53.5 ± 1.4 ps	1.87 × 10 <sup>10</sup>	-0.49
	2-	<0.3	<0.3	>333	-1.47	107 ± 1 ps	9.35 × 10 <sup>9</sup>	-0.25
<b>NDI-bpy-Re-py</b>	1-	0.4 ± 0.1	0.4	249	-1.10	31.8 ± 0.8 ps	3.14 × 10 <sup>10</sup>	-0.50
<b>Phbpy-Re-PyPhPDI</b>	1-	105 ± 0.9	381	0.26	-0.82	17.1 ± 0.2 ns	5.85 × 10 <sup>7</sup>	-0.48
	2-	0.9 ± 0.2	0.9	111	-1.49	268 ± 1 ns	3.73 × 10 <sup>6</sup>	-0.23
<b>Phbpy-Re-PyPhNDI</b>	1-	1.5 ± 0.1	1.5	66	-1.11	29.7 ± 0.2 ns	3.37 × 10 <sup>7</sup>	-0.49

$\tau_{ex}$ : Observed excited state lifetime;  $\tau_{ET}$ : Calculated excited state electron transfer rate;  $k_{ET}$ : Calculated excited state electron transfer rate;  $\Delta G_q$ : Driving force for  $\text{RDI}^{n-*} \rightarrow \text{bpy}$  electron transfer;  $\tau_{BET}$ : Back electron transfer lifetime;  $k_{BET}$ : Back electron transfer rate;  $\Delta G_{BET}$ : Gibbs free energy for  $\text{bpy}^* \rightarrow \text{RDI}^{(n-1)-}$  back electron transfer

<sup>a</sup> Calculated based on the growth of the charge-shifted state as determined by the kinetics at 525 nm (see Figure 6).  
<sup>b</sup>  $\tau_0$  values obtained from the literature. PDI<sup>1-</sup>: 145 ps<sup>13</sup>; PDI<sup>2-</sup>: 6.5 ns<sup>14</sup>; NDI<sup>1-</sup>: 141 ps<sup>13</sup>

the fsIR spectra. The data were fit as described (singular value decomposition global fitting or multiple-wavelength global fitting) and the back-electron transfer lifetime  $\tau_{BET}$  extracted from the

global fits. For every complex except **Phbpy-Re-PyPhPDI**<sup>2-</sup> and **Phbpy-Re-PyPhNDI**<sup>1-</sup>, the complexes exhibited monoexponential decay of the charge-shifted state features. The charge-shifted-state features in the complexes **Phbpy-Re-PyPhPDI**<sup>2-</sup> and **Phbpy-Re-PyPhNDI**<sup>1-</sup> exhibited biexponential decay kinetics, which will be discussed further below.

The time window of the fsIR data only extends to 7.5 ns, so it was not possible to obtain accurate fits for the fsIR data where lifetimes extended into the nanosecond regime. For the bpy-ligated complexes **RDI**<sup>n-</sup>-**Phbpy-Re-Py**, where lifetimes could be fit accurately, back-electron transfer lifetimes from fsIR matched those obtained from fsTA to within fitting error. For **Phbpy-Re-PyPhPDI**<sup>1-</sup>, the decay was also monoexponential but could not be fit accurately due to its long lifetime. For the complexes **Phbpy-Re-PyPhPDI**<sup>2-</sup> and **Phbpy-Re-PyPhNDI**<sup>1-</sup>, where the fsTA data exhibited biexponential decay kinetics, the fsIR data only exhibited a monoexponential decay

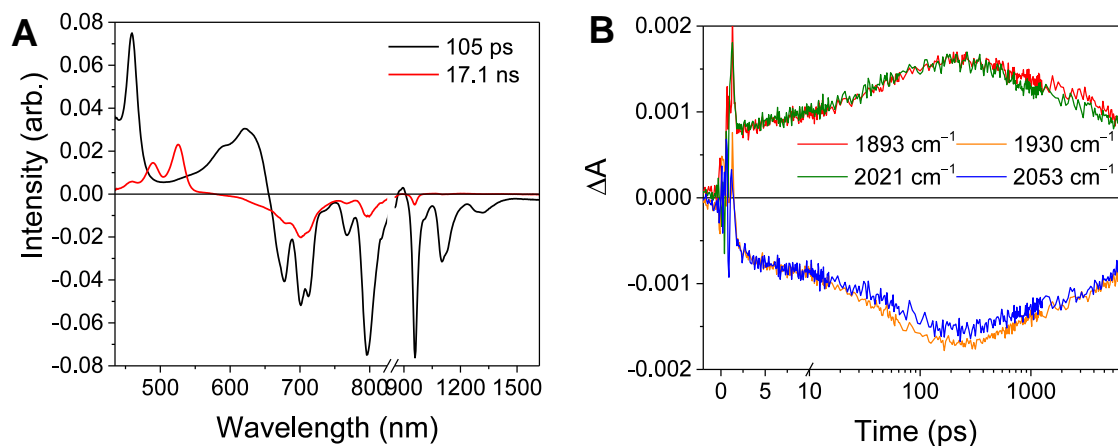


**Figure 2.5:** (A) Species-associated fit spectra of the fsTA data for **Phbpy-Re-PyPhPDI**<sup>1-</sup>. Kinetic traces and fits are shown in Figure 2.19. (B) Kinetic traces of the fsIR data shown in Figure 2.3.

which roughly corresponded to the longer component of the biexponential decay in the visible/NIR, but was too long to fit accurately. Successive fsIR scans of the same sample sometimes exhibited biexponential decay with a short component. We assign this component

corresponds to the product of photoreaction with trace oxygen under laser illumination, and that this product is also responsible for the short decay observed in the fsTA. Consequently, the lifetimes we report for back-electron transfer in the complexes **Phbpy-Re-PyPhPDI**<sup>2-</sup> and **Phbpy-Re-PyPhNDI**<sup>1-</sup> are the lifetimes of the long components of the visible/NIR TA. The back-electron-transfer lifetimes and rates are also shown in Table 2.2. A sample of the visible/NIR species-associated spectra and fsIR kinetics for **Phbpy-Re-PyPhPDI**<sup>1-</sup> in are shown in Figures 2.5A and 2.5B, respectively, and the full set of spectra and fits is included as Figures 2.11-2.24.

### 2.4.3 Electron transfer quenching of \*RDI<sup>n-</sup>

Using fsIR, we can determine the nature of the charge-shifted state. Steady-state FTIR spectroscopy has been shown to allow facile differentiation among the various oxidation and ligand-field states of Re(bpy)(CO)<sub>3</sub> complexes,<sup>70, 101-104</sup> and time-resolved mid-IR spectroscopy has been shown to be sensitive not only to the oxidation state of the Re center but also to transient electron density changes associated with excited states of a chromophoric ligand.<sup>43, 105-107</sup> A shift of ~25-45 cm<sup>-1</sup> of the CO stretches to lower energy corresponds exclusively to complexes in which the Re center remains Re<sup>I</sup> while the bpy ligand is reduced to bpy<sup>-•</sup>. We therefore assign the charge-shifted state as **RDI<sup>(n-1)-Re<sup>I</sup>(bpy<sup>-•</sup>)(CO)<sub>3</sub></sup>**.

Given that in the charge-shifted state of all the complexes, the electron is localized on the bipyridine ligand, the dramatic increase in back-electron-transfer lifetime upon switching from bipyridine to pyridine ligation can be rationalized. In the bipyridine-ligated complexes, the reduced bipyridine is separated from the oxidized chromophore by a single phenyl group. Indeed, DFT calculations of the **Phbpy-Re-Py** model compound show that upon reduction, the electron density extends onto the 4-phenyl group of 4-phenylbipyridine (see Figure 2.7). However, in the pyridine-

ligated complexes, the through-space distance between the reduced bipyridine and the oxidized chromophore is quite significant (centroid-to-centroid distance of 16.9 Å in **Phbpy-Re-PyPhPDI** and 14.5 Å in **Phbpy-Re-PyPhNDI**), and the electron must either travel through intercalated solvent molecules in that space or through the difficult-to-reduce  $\text{Re}^{\text{I}}$  center in order to return. Similar lifetimes have been observed for systems in which back-electron transfer occurs over a similar distance from a  $\text{Re}(\text{bpy}^{\cdot-})(\text{CO})_3$  to an oxidized tryptophan linked through an pyridine-amido linker.<sup>108</sup>

In the complex **PDI<sup>I</sup>-Phbpy-Re-Py**, the electron transfer kinetics are more complicated. When the complex is excited at 950 nm, the excited state features (Fig. 2.6B, black trace, consisting of absorbances at 459 nm and 550–650 nm and stimulated emission features at 1100 nm and 1300 nm) persist, but decrease in intensity while bands corresponding to the charge shifted state grow in with a time constant of  $23.6 \pm 0.6$  ps. These features (Fig. 2.6B, red trace) subsequently decay together with a lifetime of  $52.4 \pm 0.6$  ps. When the complex is excited at 680 nm instead of 950 nm, bands characteristic of the charge shifted state appear within the instrument response alongside excited-state features (Fig. 2.6D, black trace). This set of bands sharpens with a lifetime of 1.8 ps,

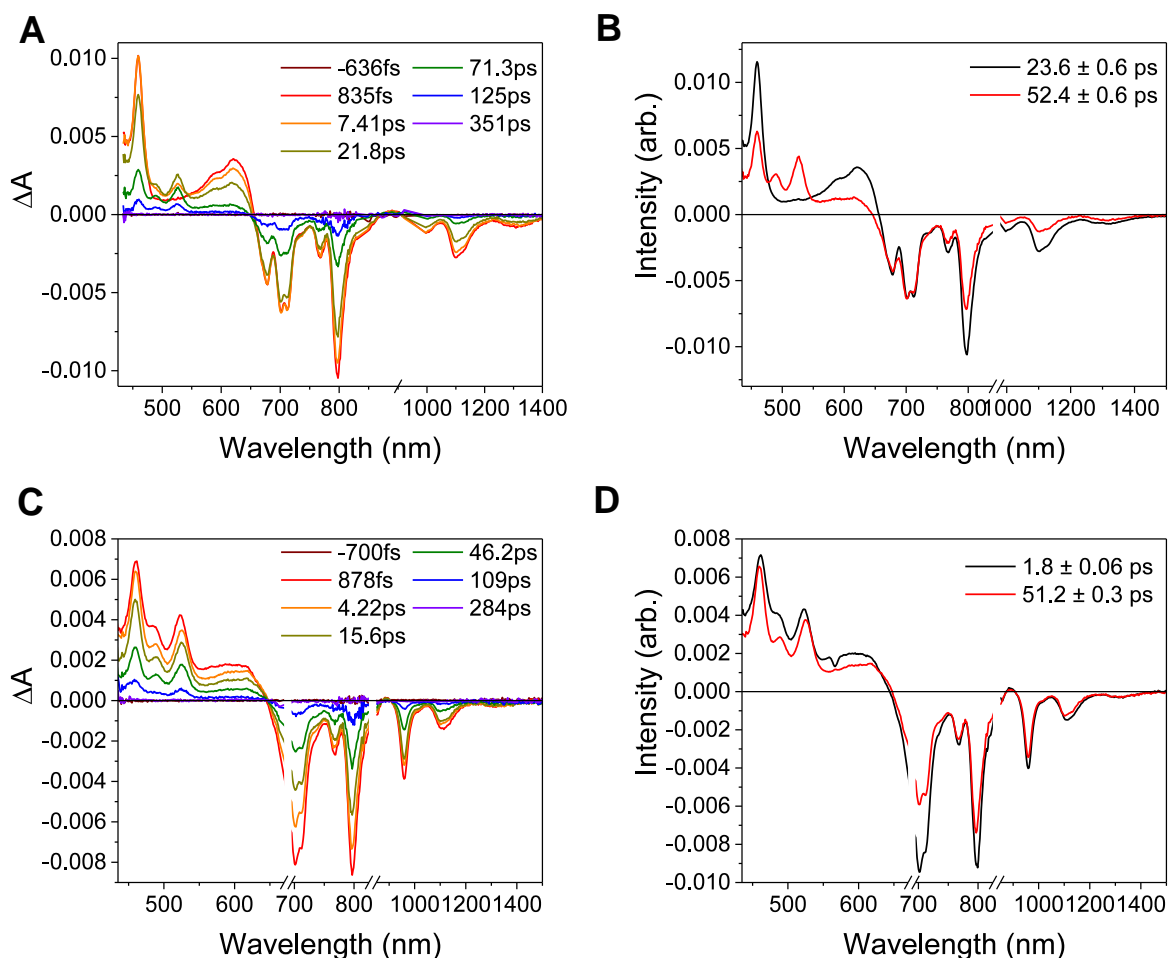


**Figure 2.6:** Top: (A) Transient absorption spectra and (B) decay-associated spectra for **PDI<sup>1-</sup>-Phbpy-Re-Py** ( $\lambda_{\text{ex}} = 950$  nm). (C) Transient absorption spectra and (D) decay-associated spectra of those spectra for **PDI<sup>1-</sup>-Phbpy-Re-Py** ( $\lambda_{\text{ex}} = 680$  nm).

producing a spectrum that is very similar to the final spectrum produced by 950 nm excitation (Fig. 2.6D, red trace), which then decays with a lifetime of  $51.2 \pm 0.3$  ps.

To understand these results we must assign the absorption bands of **PDI<sup>1-</sup>**. Using TD-DFT calculations, these absorptions are shown to arise from three different electronic transitions of **PDI<sup>1-</sup>**, where the two different pump wavelengths promote distinct transitions. The relevant orbitals of the PDI chromophore fragment, calculated using DFT, are shown in Fig. 2.7. The orbitals of the full **PDI-Phbpy-Re-Py** dyad are shown in Fig. 2.15. As reflected by the mostly

unperturbed orbital energies given in Table 2.5, these orbitals are essentially a combination of the MOs of the PDI and Phbpy-Re-Py fragments, with the exception of LUMO+4 orbital in which some mixing of the orbitals of each fragment occurs, see Fig. 2.15.

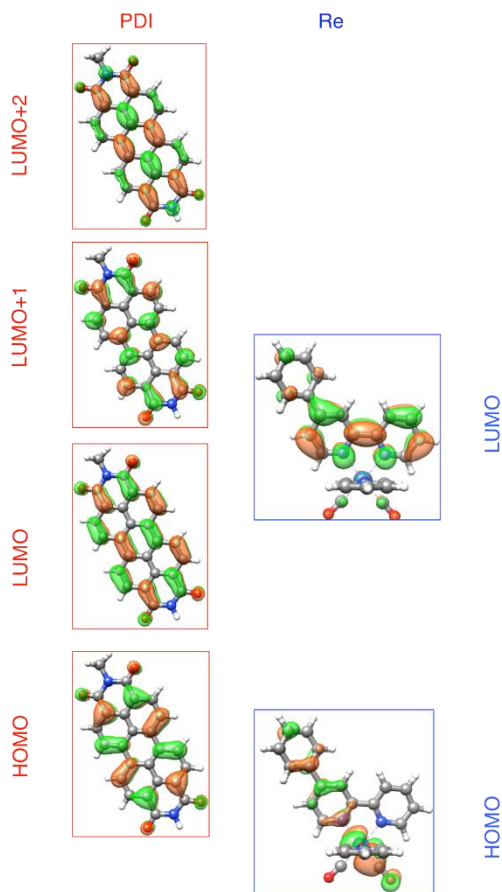


**Figure 2.7:** Frontier molecular orbitals of PDI (left) and  $[\text{Re}(\text{Phbpy})(\text{CO})_3(\text{py})]^+$  molecular fragments calculated using DFT. Frontier MOs of the full PDI- $[\text{Re}(\text{Phbpy})(\text{CO})_3(\text{py})]^+$  dyad are shown in Figure 2.15.

The ten lowest-energy electronic transitions calculated by TDDFT, are listed in Tables 2.6 and 2.7 for the  $\text{Re}(\text{Phbpy})(\text{py})(\text{CO})_3$  and  $\text{PDI}^-$  fragments, respectively. The three lowest-energy transitions of  $\text{PDI}^-$  are labeled D1, D2, and D3 in order of increasing energy of their vertical, non-vibronic transitions, see Table 2.3. These excited states were structurally optimized, followed by excited-state numerical frequency calculations, permitting the calculation of vibronically resolved

absorption spectra. The calculated vibronic spectra for each transition are shown in Fig. 2.8A, and the sum of the three transitions is compared to the experimentally determined spectrum of PDI<sup>-</sup> in Fig. 2.8B, exhibiting excellent agreement of the 700 nm and 950 nm peaks.

From this data, it is determined that absorption around 680 nm is due to both the D2 and D3 transitions, while the transition to the D1 state completely dominates at 950 nm. From the transition wavelengths and oscillator strengths shown in Table 2.3 and Fig. 2.8, it is apparent that excitation at 950 nm produces a vertically excited state of mostly HOMO / LUMO character which structurally relaxes to the optimized D1 excited state, while excitation at 680 nm produces a state with mostly LUMO / LUMO+1 character, but also some HOMO / LUMO and LUMO / LUMO+2 character. This vertical state predominantly relaxes to the optimized D3 excited state, but some optimized D1 and D2 is also expected. These states are shown in the energy-level diagram for the complex given in Fig. 2.9.

TD-DFT calculations reveal that the complex also has a CT excited state which we label as \*[PDI<sup>0</sup>-Re(bpy<sup>-•</sup>)], and which corresponds to direct charge-transfer excitation of the unpaired electron on the PDI<sup>-</sup> to the empty LUMO on the bpy ligand. Due to extremely poor orbital overlap, this transition has negligible oscillator strength and is not predicted to contribute detectably to the

**Table 2.3:** The TD-DFT vibronic absorption maximum peak wavelengths  $\lambda$  of the first two electronic transitions, and the vertical wavelengths  $\lambda_v$ , oscillator strengths  $f$ , and dominant orbital characters for the lowest-energy calculated electronic transitions of the reduced PDI<sup>-</sup> radical. The full set of the lowest ten transitions is given in Table 2.7

State	$\lambda_{\text{vibronic}}$ [nm]	$\lambda$ [nm]	$f$	Primary Transition Character	%	Secondary Transition Character	%
D1	974.4	844.3	0.032	$\beta$ HOMO $\rightarrow$ LUMO	74	$\alpha$ LUMO $\rightarrow$ LUMO+1	26
D2	688.4	668.6	0.052	$\alpha$ LUMO $\rightarrow$ LUMO+2	97	N/A	0
D3	710.8	621.4	0.885	$\alpha$ LUMO $\rightarrow$ LUMO+1	72	$\beta$ HOMO $\rightarrow$ LUMO	24

ground-state absorption spectrum of PDI<sup>-</sup>-Phbpy-Re-Py. This CT state, shown as a gray box to

reflect the uncertainty in its energy, is calculated to be approximately isoenergetic with the  ${}^{\text{D1}}\text{PDI}^{-*}\text{-Re}^{\text{I}}(\text{bpy})^{\text{0}}$  state, with which it is in equilibrium (see below).

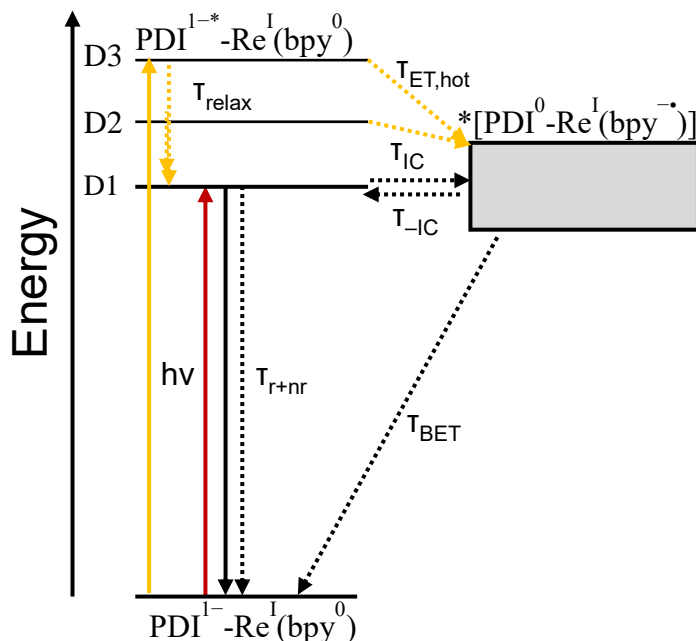


**Figure 2.8:** Energy level diagram showing electron transfer in  $\text{PDI}^{\text{1-}}\text{-Phbpy-Re-Py}$  after excitation at 950 nm (red) or 680 nm (yellow). Energy of the charge-transfer state is shown as a range to reflect the uncertainty of the exact energy of this state.

As shown in Fig. 2.9, the D2 and D3 states relax via a set of processes that can be described as a combination of internal conversion to the D1 state, internal conversion to the  ${}^*[\text{PDI}^{\text{0}}\text{-Re}(\text{bpy}^{-*})]$  state (collectively denoted  $\tau_{\text{IC1}}$ ), and electron transfer to the  ${}^*[\text{PDI}^{\text{0}}\text{-Re}(\text{bpy}^{-*})]$  state ( $\tau_{\text{ET, hot}}$ ). It is likely that relaxation and electron transfer from the D3 state occurs within the instrument response, accounting for the immediate appearance of  $\text{PDI}^{\text{0}}$  bands in the  $\lambda = 680$  nm TA spectrum shown in Fig. 2.6C, while relaxation and electron transfer from the D2 state occurs with a lifetime of 1.8 ps, accounting for the evolution of the spectrum in the first several picoseconds (Fig. 2.6D, black trace).

As mentioned above, once the molecule reaches the D1 state, an equilibrium forms between

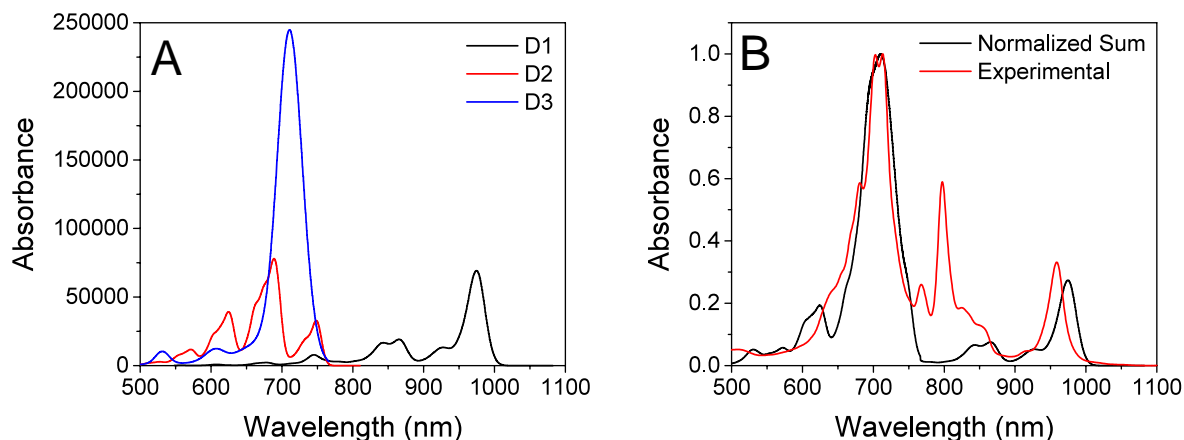


**Figure 2.9:** *Left:* Calculated vibronic transitions from the ground state to the D1 (black), D2 (red) and D3 (blue) states of PDI<sup>-</sup>. *Right:* Sum of the three calculated vibronic spectra (black) compared to the experimentally determined spectrum of PDI<sup>-</sup>.

the PDI-localized D1 state (which we can denote  ${}^{\text{D1}}\text{PDI}^{-*}\text{-Re}(\text{bpy})$ ) and the  ${}^*[\text{PDI}^0\text{-Re}(\text{bpy}^{-*})]$  CT state via a fast internal conversion mechanism (shown as  $\tau_{\text{IC2}}$  and  $\tau_{\text{IC2}}$ ). This equilibrium accounts for the persistence of the PDI<sup>-\*</sup> bands in the TA spectra as the PDI<sup>0</sup> bands grow in, and the parallel decay of the excited-state and charge-shifted-state features. Because of the low oscillator strength of the transition to the  ${}^*[\text{PDI}^0\text{-Re}(\text{bpy}^{-*})]$  state, this state does not decay radiatively on the picosecond timescale; instead this equilibrium decays via a combination of excited-state decay from the  ${}^{\text{D1}}\text{PDI}^{-*}\text{-Re}(\text{bpy})$  state ( $\tau_{\text{r}} + n\tau$ ) and back-electron transfer from the  ${}^*[\text{PDI}^0\text{-Re}(\text{bpy}^{-*})]$  state ( $\tau_{\text{BET}}$ ), resulting in the observed lifetime of 52 ps.

Variable-temperature transient absorption experiments in the range 0–90 °C support the existence of the  ${}^{\text{D1}}\text{PDI}^{-*}\text{-Re}(\text{bpy}) \leftrightarrow {}^*[\text{PDI}^0\text{-Re}(\text{bpy})]$  equilibrium and suggest that the charge shift to the  ${}^*[\text{PDI}^0\text{-Re}(\text{bpy}^{-*})]$  state is slightly uphill. Analysis of the SVD spectra for each set of TA data shows a dependence of the  $[\text{PDI}^0] : [\text{PDI}^{1-*}]$  ratio on temperature (see section 2.8.4 for

details on the calculation of  $[PDI^0] : [PDI^{1-*}]$ ). A plot of  $\ln K_{eq}$  vs.  $1/T$ , shown in Fig. 27, gives a  $\Delta G$  for the equilibrium of  $0.21 \pm 0.02$  eV, supporting the existence of a  ${}^D1PDI^- - Re \leftrightarrow *[PDI^0 - Re(bpy^{-*})]$  equilibrium that favors the  $*[PDI^0 - Re(bpy^{-*})]$  state at higher temperature.

#### 2.4.4 Back Electron Transfer of $*RDI^{n-}$

In the  **$RDI^{n-}$ -bpy-Re-py** complexes, and in **Phbpy-Re-PyPhPDI $^{1-}$** , the final charge-shifted state exhibits straightforward single-exponential decay kinetics with the lifetimes shown in Table 2.2. For the complexes **Phbpy-Re-PyPhNDI $^-$**  and **Phbpy-Re-PyPhPDI $^{2-}$**  the charge-shifted state exhibits biexponential decay in the visible/NIR TA, but monoexponential decay in the fsIR, as shown in Figure 2.10-2.12.

Several trends in electron-transfer rate are apparent from the data. In all cases, attachment of the chromophore to the bipyridine ligand results in faster quenching than attachment of the same chromophore to a pyridine ligand on the Re center. It is also apparent that an increase in the driving force for electron transfer quenching for a given attachment motif generally results in an increase in electron transfer rate, although the rate for quenching of  $NDI^{n-*}$  ligated through bipyridine is slightly faster than quenching of  $PDI^{2-*}$  with the same attachment motif. Similarly, the rate of back-electron transfer appears to correlate with the free energy change for that process, and back-electron transfer is orders of magnitude faster in the  $RDI$ -bipyridine-ligated complexes than in the  $RDI$ -pyridine-ligated complexes. This result is consistent with the fact that in the  $RDI$ -bipyridine-ligated complexes, the reduced bpy is separated from the oxidized chromophore by one phenyl spacer, whereas in the  $RDI$ -pyridine-ligated complexes the reduced bpy ligand is much further away from the oxidized chromophore.

While freshly prepared samples of **Phbpy-Re-PyPhNDI<sup>-</sup>** and **Phbpy-Re-PyPhPDI<sup>2-</sup>** exhibit monoexponential decay in the fsIR experiment, as mentioned above, repeated fsIR scans of the same samples begin to exhibit a short decay component in addition to the long decay

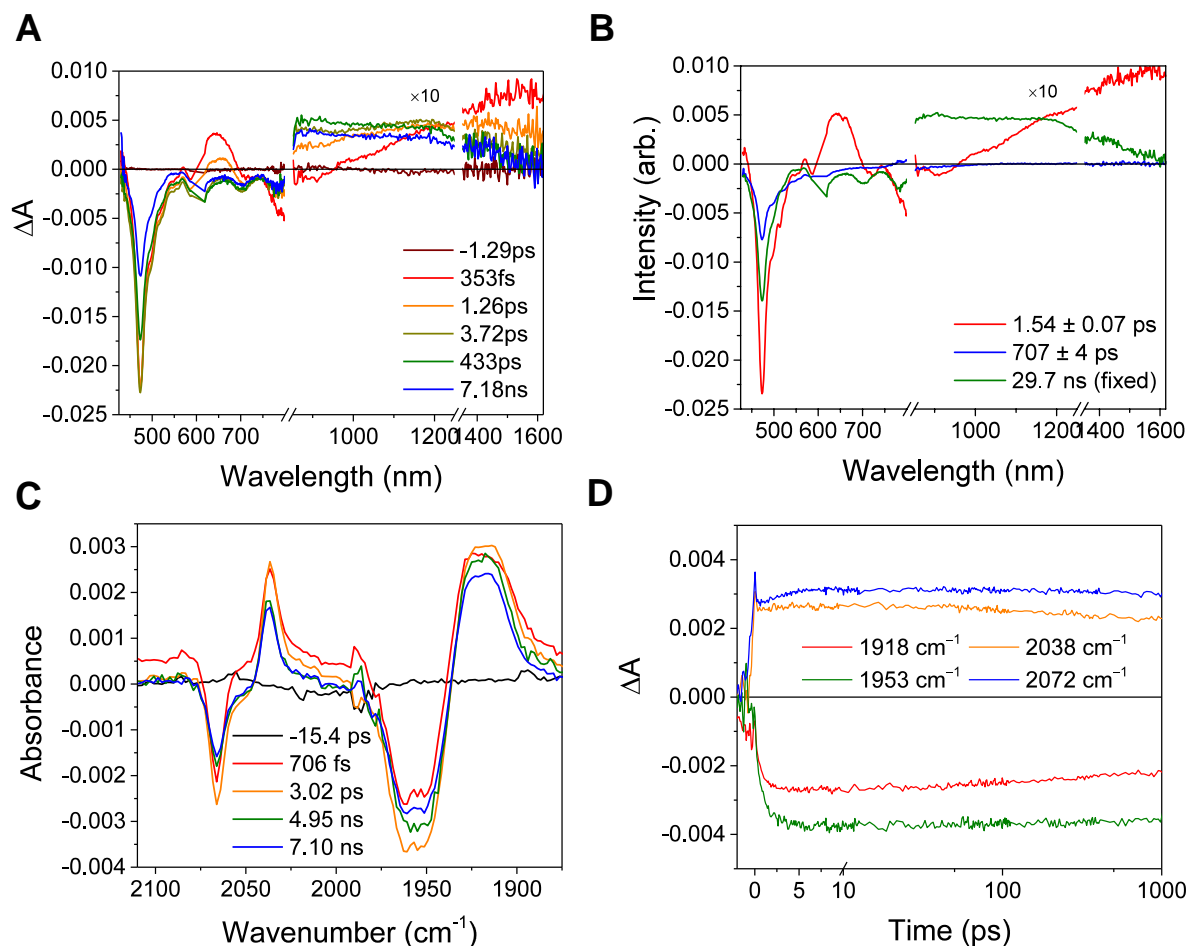


**Figure 2.10:** (A) Transient absorption and (B) species-associated spectra for complex **Phbpy-Re-PyPhNDI<sup>-</sup>** ( $\lambda_{\text{ex}} = 605$  nm) showing biphasic back electron transfer kinetics. Kinetic traces and fits are shown in Figure 2.23. (C) fsIR spectra and (D) kinetic traces with fits for complex **Phbpy-Re-PyPhNDI<sup>-</sup>** ( $\lambda_{\text{ex}} = 605$  nm) showing monophasic back electron transfer kinetics. The instrument response is approximately 2 ps.

component. At the same time, the samples are observed to bleach irreversibly in the regions of the sample cell where the laser beam was rastered, indicating photodegradation, likely in the presence of trace oxygen either trapped in or leaking into the sample cell. The short component of the decay in the visible/NIR TA data is therefore postulated to arise from a photodegraded product with a

shorter charge-shift time constant, while the long component is assigned as the actual charge-shifted lifetime of the complex. The charge-shift lifetimes and rates are shown in Table 2.2.

## 2.5 Conclusions

Several trends in electron-transfer rate are apparent from the data. In all cases, attachment of the chromophore to the bipyridine ligand results in faster quenching than attachment of the same chromophore to a pyridine ligand on the Re center. It is also apparent that an increase in the driving force for electron transfer quenching for a given attachment motif generally results in an increase in electron transfer rate, although the rate for quenching of  $\text{NDI}^{-*}$  ligated through bipyridine is slightly faster than quenching of  $\text{PDI}^{2-*}$  with the same attachment motif. Similarly, the rate of back-electron transfer appears to correlate with the free energy change for that process, and back-electron transfer is orders of magnitude faster in the bipyridine-ligated complexes than in the pyridine-ligated complexes. This result is consistent with the fact that in the bipyridine-ligated complexes, the reduced bpy is separated from the oxidized chromophore by one phenyl spacer, whereas in the pyridine-ligated complexes the reduced bpy ligand is much further away from the oxidized chromophore.

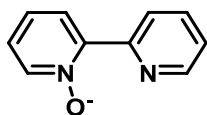
## 2.6 Acknowledgements

We thank Dr Matthew D. Krzyaniak for assistance with fitting the kinetic data and Drs Saman Shafaie and S. Habibi Goudarzi for collecting high-resolution mass spectrometric data. Yilei Wu synthesized Cy2-NDI. This work was supported by the ArgonneNorthwestern Solar Energy Research (ANSER) Center, an Energy Frontier Research Center funded by the U.S. Department of Energy (DOE), Office of Science, Office of Basic Energy Sciences, under award number DE-SC0001059. B. R. acknowledges support from the National Science Foundation

Graduate Research Fellowship (NSF GRFP) under Grant No. DGE1122492. C. M. M. acknowledges support from the NSF GRFP Grant No. DGE-1324585. V. S. B. acknowledges supercomputer time from NERSC and the Yale University Faculty of Arts and Sciences High Performance Computing Center partially funded by the NSF Grant CNS 08-21132. This work used the Extreme Science and Engineering Discovery Environment (XSEDE), which is supported by National Science Foundation grant number ACI-1053575.

## 2.7 Synthetic Details

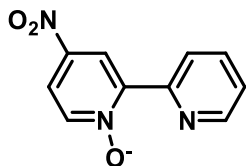
**C23-PDI-PhBr** and **C23-PDI-PhI** were synthesized using a modification of a literature procedure.<sup>109</sup> 12-aminotricosane was synthesized according to a literature procedure.<sup>110</sup> 4-bromobipyridine was synthesized by a modification of literature procedures.<sup>111-112</sup>



### 2,2'-bipyridine-N-oxide

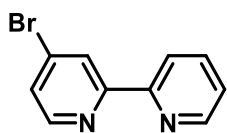
2,2-Bipyridine (6.00 g, 38.44 mmol) was dissolved in 100 mL of trifluoroacetic acid under air. 30 mass % hydrogen peroxide solution (12 mL) was added and the mixture obtained was stirred at ambient temperature for 5 h. Then 5M NaOH (100 mL) was slowly added to the solution and allowed to stir for 1hr. The solution was mixed with dichloromethane (300 mL) and washed with 5M NaOH (3 x 150 mL). Water phase was reextracted twice with dichloromethane (2 x 100 mL) and the combined organic phases dried with MgSO<sub>4</sub>, filtered, and dried under reduced pressure. The product was obtained as a pale yellow oil which crystalized after overnight into an off-white solid (6.16 g, 93%). <sup>1</sup>H NMR (500 MHz, Chloroform-*d*) δ 8.89 (dt, *J* = 4.6, 1.3 Hz, 1H), 8.71 (dd,

$J = 8.1, 1.1 \text{ Hz, 1H}$ ),  $8.29 \text{ (dd, } J = 6.6, 1.2 \text{ Hz, 1H)}$ ,  $8.16 \text{ (dd, } J = 8.1, 2.2 \text{ Hz, 1H)}$ ,  $7.81 \text{ (td, } J = 7.8, 1.9 \text{ Hz, 1H)}$ ,  $7.36 - 7.30 \text{ (m, 2H)}$ ,  $7.27 - 7.23 \text{ (m, 1H)}$ .



#### 4-nitro-2,2'-bipyridine-N-oxide

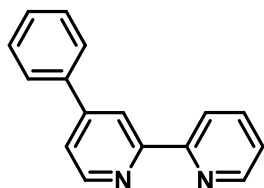
2,2'-bipyridine-N-oxide (6.10 g, 35.46 mmol) and potassium nitrate (19.60 g, 193.90 mmol) in concentrated sulfuric acid (50 mL) was stirred at  $80 \text{ }^\circ\text{C}$  for 30 hours. Then, the mixture was poured onto ice (100 g) and neutralized with 25 mass % NaOH to pH 9.0. The precipitate was filtered off, washed with cold water and dried under a high vacuum at  $100 \text{ }^\circ\text{C}$ . An off-white solid was obtained (2.31 g, 30%).  $^1\text{H NMR}$  (500 MHz, Chloroform-*d*)  $\delta$  9.17 (d,  $J = 3.3 \text{ Hz, 1H}$ ), 8.89 (dt,  $J = 8.1, 1.1 \text{ Hz, 1H}$ ), 8.79 (ddd,  $J = 4.7, 1.9, 1.0 \text{ Hz, 1H}$ ), 8.36 (d,  $J = 7.2 \text{ Hz, 1H}$ ), 8.06 (dd,  $J = 7.2, 3.3 \text{ Hz, 1H}$ ), 7.88 (td,  $J = 7.9, 1.8 \text{ Hz, 1H}$ ), 7.43 (ddd,  $J = 7.6, 4.7, 1.2 \text{ Hz, 1H}$ ).



#### 4-bromo-2,2'-bipyridine

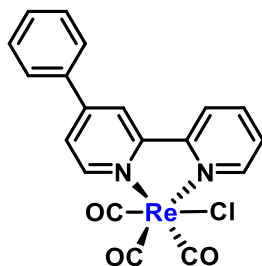
4-nitro-2,2'-bipyridine-N-oxide (1.0 g, 4.6 mmol) was dissolved in glacial acetic acid (20 mL). While stirring, acetyl bromide was added. After a short while, a yellow precipitate was formed. At this time, phosphorous tribromide (5 mL) was added to the resulting suspension and heated to  $40 \text{ }^\circ\text{C}$  for 15 minutes. The solution was then heated to reflux under air for 1 hr, whereby a new incredibly viscous precipitate formed. After cooling to room temperature, the solution was

decanted and the remaining sticky residue was dissolved in water. The acid solution was neutralized to pH 9 with concentrated NaOH and filtered to obtain a yellow solid. The crude product was purified further by sublimation to yield an off-white solid (72%, 0.8 g). **<sup>1</sup>H NMR** (500 MHz, Chloroform-*d*)  $\delta$  8.69 (ddd,  $J = 4.8, 1.8, 0.9$  Hz, 1H), 8.63 (d,  $J = 1.9$  Hz, 1H), 8.49 (d,  $J = 5.2$ , 1H), 8.39 (dt,  $J = 8.0, 1.1$  Hz, 1H), 7.83 (td,  $J = 7.7, 1.8$  Hz, 1H), 7.48 (dd,  $J = 5.2, 2.0$  Hz, 1H), 7.34 (ddd,  $J = 7.5, 4.8, 1.2$  Hz, 1H).



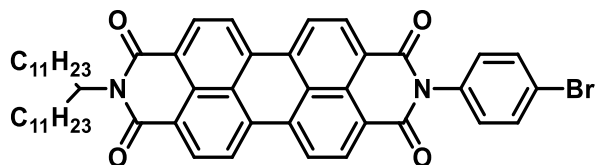
#### **4-phenyl-2,2'-bipyridine**

In an oven dried round bottom flask with a magnetic stirrer and reflux condenser, Phenylboronic acid (0.187, 1.534mole), 4-Bromo-2,2'-bipyridine (0.30 g, 1.28 mmol), and Na<sub>2</sub>CO<sub>3</sub> (1.02 g, 9.60 mmol) were dissolved in THF (50 mL) and H<sub>2</sub>O (15 mL) and put under N<sub>2</sub>. After 15 minutes of purging, fresh Pd[PPh<sub>3</sub>]<sub>4</sub> (0.07 g, 5% eq) was added via the second port and purged for 5 minutes. The solution was set to reflux overnight. The solution was cooled to room temperature and the solvent was removed under reduced pressure. The crude material was dissolved in dichloromethane and ran through a celite plug. The solvent was removed under reduced pressure. The compound was not purified further and a conversion of 100% was assumed for further purposes.



### Phby-Re-Cl

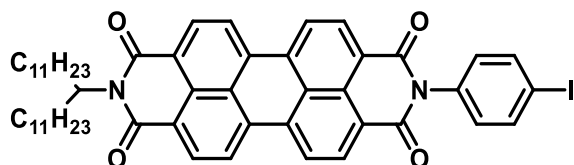
In a nitrogen filled glove box, an oven dried pressure flask with a magnetic stirrer was filled with 4-phenyl-2,2'-bipyridine (0.30 g, 1.29 mmol),  $\text{Re}(\text{CO})_5\text{Cl}$  (0.55 g, 1.55 mmol), and toluene (30 mL). The pressure flask was capped and brought out of the glovebox and heated to 80 °C overnight. The solution was cooled to room temperature and the solvent was removed by reduced pressure. The solid was then column chromatographed on silica using a gradient between dichloromethane and Acetone (100 → 98:2). The compound was then dissolved in minimal dichloromethane and layered with diethyl ether. Upon filtering, a bright yellow compound was obtained (0.46 g, 66%).  $^1\text{H NMR}$  (500 MHz, Chloroform-*d*)  $\delta$  9.10 (ddd,  $J = 5.5, 1.6, 0.8$  Hz, 1H), 9.07 (d,  $J = 5.8$  Hz, 1H), 8.32 (d,  $J = 1.8$  Hz, 1H), 8.30 (dt,  $J = 8.1, 1.0$  Hz, 1H), 8.09 (td,  $J = 7.9, 1.6$  Hz, 1H), 7.72 – 7.68 (m, 3H), 7.62 – 7.54 (m, 4H).



### C23PDI-PhBr

1.40 g (3.57 mmol) perylene-3,4,9,10-dianhydride (PDA) and 736 mg (4.28 mmol) 4-bromoaniline were combined with 19 g imidazole in a 50 mL roundbottom flask. The flask was purged for 45

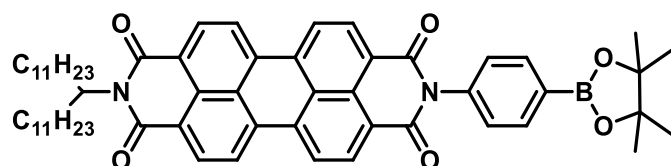
minutes with N<sub>2</sub> and 1.9 mL (1.47 g, 4.35 mmol) 12-aminotricosane that had been melted over a steam bath was added via syringe. The flask was placed in a preheated 130° oil bath and stirred for 2 hours. The flask was then cooled to room temperature and the contents suspended in 125 mL dichloromethane with the aid of sonication and washed with 100 mL 2 M HCl. The emulsion was broken with 50 mL isopropanol and the aqueous layer was washed twice with 100 mL dichloromethane. The organic layers were combined, dried over MgSO<sub>4</sub>, gravity filtered and stripped. **C23PDI-PhBr** was separated from the symmetric **C23<sub>2</sub>-PDI** on a silica column with 80-100% DCM:hexanes (desired product eluted second). Yield: 1.42 g (38%) <sup>1</sup>H NMR (500 MHz, Chloroform-*d*) δ 8.53 (s, 2H), 8.48 (d, *J* = 7.9 Hz, 4H), 8.28 (dd, *J* = 8.1, 5.8 Hz, 4H), 7.63 (d, *J* = 8.3 Hz, 2H), 7.23 (d, *J* = 8.5 Hz, 2H), 5.44 – 4.77 (m, 1H), 2.18 (dtd, *J* = 14.1, 9.5, 4.7 Hz, 2H), 1.86 (ddt, *J* = 14.7, 11.1, 5.4 Hz, 2H), 1.29 (tt, *J* = 13.2, 5.9 Hz, 8H), 1.15 (d, *J* = 10.3 Hz, 36H), 0.78 (t, *J* = 6.9 Hz, 8H).



### **C23PDI-PhI**

1.40 g (3.57 mmol) perylene-3,4,9,10-dianhydride (PDA) and 937 mg (4.28 mmol) 4-iodoaniline were combined with 19 g imidazole in a 50 mL roundbottom flask. The flask was purged for 45 minutes with N<sub>2</sub> and 1.9 mL (1.47 g, 4.35 mmol) 12-aminotricosane that had been melted over a steam bath was added via syringe. The flask was placed in a preheated 130° oil bath and stirred for 2 hours. The flask was then cooled to room temperature and the contents suspended in 125 mL dichloromethane with the aid of sonication and washed with 100 mL 2 M HCl. The aqueous layer

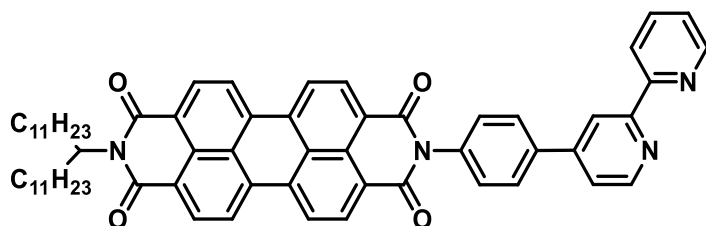
was washed twice with 125 mL dichloromethane. The organic layers were combined, dried over  $\text{Na}_2\text{CO}_3$ , gravity filtered and dried under vacuum. C23PDI-PhI was separated from the symmetric C23<sub>2</sub>-PDI on a silica column with 80-100% DCM:hexanes followed by 0-8% ethyl acetate:DCM (desired product eluted second). Yield: 674 mg (17%). <sup>1</sup>H NMR (500 MHz, Chloroform-*d*)  $\delta$  8.70 (d,  $J = 8.0$  Hz, 1H), 8.67 – 8.58 (d,  $J = 8.1$  Hz, 2H), 7.88 (d,  $J = 8.4$  Hz, 2H), 7.10 (d,  $J = 8.4$  Hz, 2H), 5.16 (m,  $J =$ , 1H), 2.23 (dtd,  $J = 14.2, 9.6, 4.8$  Hz, 2H), 1.85 (ddt,  $J = 14.7, 10.7, 4.8$  Hz, 2H), 1.42-1.12 (m, 36H), 0.82 (t,  $J = 6.9$  Hz, 6H).



### C23PDI-PhBpin

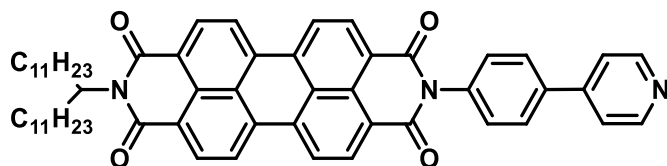
520 mg (0.6 mmol) **C23PDI-PhBr** and 315 mg (1.2 mmol) bispinacolatoboron ( $\text{B}_2\text{pin}_2$ ) or 500 mg (0.54 mmol) **C23PDI-PhI** and 285 mg (1.1 mmol)  $\text{B}_2\text{pin}_2$  were combined with 180 mg potassium acetate and 45 mg (0.06 mmol)  $\text{Pd}(\text{dppf})\text{Cl}_2$  in a 100 mL two-neck roundbottom flask fitted with a condenser. The flask was evacuated and backfilled three times with  $\text{N}_2$ . 50 mL dry, degassed DMF was injected and the flask was stirred at  $100^\circ$  overnight (C23PDI-PhBr) or for one hour (C23PDI-PhI). The flask was cooled to room temperature, the contents diluted with 50 mL DCM, and washed with 3x100 mL DI  $\text{H}_2\text{O}$ . The organic layer was concentrated to 3 mL and 50 mL MeOH was added to precipitate the product, which was collected by centrifugation, washed with an additional 50 mL MeOH and dried. Yield: 529 mg (from **C23PDI-PhBr**, 96%), 430 mg (from **C23PDI-PhI**, 87%). <sup>1</sup>H NMR (500 MHz, Chloroform-*d*)  $\delta$  8.68 (m, 8H), 8.01 (d,  $J = 8.0$

Hz, 2H), 7.35 (d,  $J = 8.0$  Hz, 2H), 5.25-5.06 (m, 1H), 2.23 (m, 2H), 1.84 (m, 2H), 1.36 (s, 12H), 1.42-1.10 (m, 36H), 0.82 (t,  $J = 6.9$  Hz, 6H).



### C23PDI-Phbpy

425 mg (0.33 mmol) **C23PDI-PhBpin**, 81 mg (0.33 mmol) 4-bromobipyridine, and 361 mg (3.33 mmol) were combined in 40 mL THF and 10 mL DI H<sub>2</sub>O in a two-neck 100 mL roundbottom flask and sparged 30 minutes with N<sub>2</sub>. 52 mg (0.033 mmol) Pd(PPh<sub>3</sub>)<sub>4</sub> (Strem) was added under flow of N<sub>2</sub> and the solution sparged for an additional ten minutes, then refluxed overnight. The flask was cooled to room temperature, the contents diluted with 300 mL DCM, washed with 3x200 mL DI H<sub>2</sub>O, gravity filtered and dried under vacuum. The precipitate was dissolved in minimal DCM and 50 mL MeOH added to precipitate product. The product was collected by centrifugation, washed with an additional 50 mL MeOH and dried. Yield: 287 mg (91%). <sup>1</sup>H NMR (500 MHz, Chloroform-*d*) δ 8.76-8.61 (m, 8 H), 8.75 (d,  $J = 8.1$  Hz, 1H), 8.71 (d,  $J = 4.6$  Hz, 1H), 8.66 (s, 1H), 8.45 (d,  $J = 8.0$ , 1H), 7.96 (d,  $J = 8.4$  Hz, 2H), 7.84 (td,  $J = 7.7, 1.8$  Hz, 1H), 7.60 (dd,  $J = 5.0, 1.6$  Hz, 1H), 7.50 (d,  $J = 8.3$  Hz, 2H), 7.33 (dd,  $J = 7.7, 4.6$  Hz, 1H), 5.17 (tt,  $J = 9.5, 5.7$  Hz 1H), 2.23 (m, 2H), 1.84 (m, 2H), 1.42-1.10 (m, 36H), 0.82 (t,  $J = 6.9$  Hz, 6H).

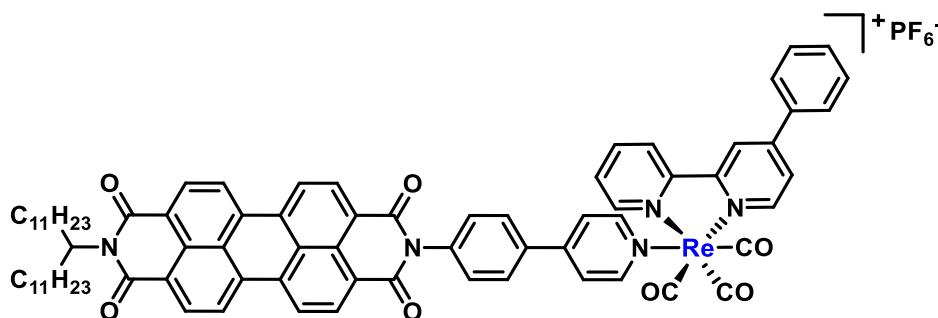


### C23PDI-PhPy

128 mg (0.10 mmol) **C23PDI-PhBpin**, 21.4 mg (0.11 mmol) 4-bromopyridine HCl, and 108 mg (1.0 mmol)  $\text{Na}_2\text{CO}_3$  were combined in 20 mL THF and 5 mL DI  $\text{H}_2\text{O}$  in a 50 mL two-necked roundbottom flask and sparged 30 minutes with  $\text{N}_2$ . 16 mg (0.01 mmol)  $\text{Pd}(\text{PPh}_3)_4$  was added under flow of  $\text{N}_3$  and the solution sparged for an additional ten minutes, then refluxed overnight. A great deal of insoluble red product forms on the inside of the flask, likely trapping product within it. The flask was cooled to room temperature, diluted with 50 mL DCM, washed with 50 mL saturated KOH and 3x100 mL DI  $\text{H}_2\text{O}$  and dried under vacuum. The precipitate was dissolved in minimal DCM and 50 mL MeOH was added to precipitate product. The suspension was filtered through Celite and the precipitate washed with MeOH, then washed off the Celite with DCM. The solution was collected and dried under vacuum. Yield: 15 mg (17%).

**C23PDI-PhPy** was also prepared from **C23PDI-PhBr** by the following method: In an oven dried round bottom flask with a magnetic stirrer and reflux condenser, **C23PDI-PhBr** (0.10 g, 0.12 mmol), 4-Pyridinylboronic acid (0.03 g, 0.23 mmol), and  $\text{Na}_2\text{CO}_3$  (0.70 g, 6.60 mmol) were dissolved in THF (150 mL) and  $\text{H}_2\text{O}$  (30 mL) and put under  $\text{N}_2$ . After 15 minutes of purging, fresh  $\text{Pd}(\text{PPh}_3)_4$  (0.007 g, 5% eq) was added via the second port and purged for 5 minutes. The solution was set to reflux overnight. The solution was cooled to room temperature and the solvent was removed under reduced pressure. The remaining solid was suspended in MeOH and filtered through a celite plug. Dichloromethane was then used to elute the product. After the solvent was

removed under reduced pressure a dark red solid was obtained (40%, 0.04g).  $^1\text{H NMR}$  (500 MHz, Chloroform-*d*)  $\delta$  8.73 (d,  $J = 10.0$  Hz, 2H), 8.71 – 8.66 (m, 8H), 7.83 – 7.81 (m, 2H), 7.60 – 7.57 (m, 2H), 7.52 – 7.48 (s, 2H), 5.14 – 5.08 (m, 1H), 2.25-2.15 (m, 2H), 1.87-1.83 (m, 2H), 1.23-1.17 (m, 36H), 0.82 (t,  $J = 7.5$  Hz, 6H)

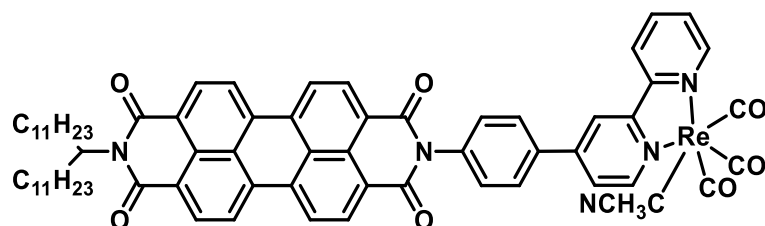


### Phbpy-Re-PyPhPDI

In a nitrogen filled glove box, an oven dried pressure flask with a magnetic stirrer was filled with **C23PDI-PhPy** (0.04 g, 0.046 mmol), **Phby-Re-Cl** (0.03 g, 0.055 mmol),  $\text{AgPF}_6$  (0.015 mg, 0.059 mmol), and dichloromethane (40 mL). The pressure flask was capped and brought out of the glovebox and heated to 80 °C overnight. The solution was cooled to room temperature and filtered through Celite. The solvent was removed under reduced pressure and then column chromatographed on silica using a gradient between dichloromethane and Acetone (100 → 96:4 → 90:10 → 80:20). A dark red compound was obtained (0.03 g, 14%).  $^1\text{H NMR}$  (500 MHz, Chloroform-*d*)  $\delta$  9.10 – 9.02 (m, 2H), 8.74 (d,  $J = 8.3$  Hz, 1H), 8.70 (d,  $J = 1.9$  Hz, 1H), 8.69 – 8.55 (m, 8H), 8.36 (td,  $J = 8.0, 1.8$  Hz, 1H), 8.24 – 8.19 (m, 2H), 7.90 – 7.85 (m, 3H), 7.76 – 7.70 (m, 3H), 7.64 – 7.60 (m, 2H), 7.60 – 7.52 (m, 3H), 7.44 – 7.40 (m, 2H), 5.17-5.12 (m, 1H), 2.25-2.15 (m, 2H), 1.87-1.83 (m, 2H), 1.20-1.17 (m, 36H), 0.82 (t, 6H)  $^{13}\text{C NMR}$  (126 MHz,  $\text{CDCl}_3$ )  $\delta$  163.4, 157.5, 156.3, 155.9, 153.8, 152.8, 152.7, 152.0, 151.1, 141.8, 137.4, 135.9, 135.4, 135.0,

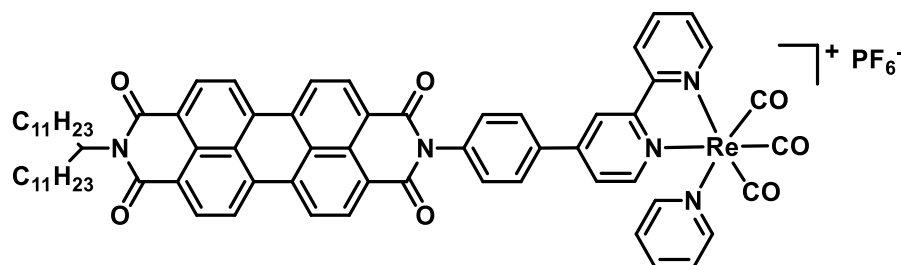
134.2, 132.0, 131.5, 130.0, 129.9, 129.6, 128.9, 128.4, 127.8, 126.8, 126.5, 126.3, 126.1, 124.9, 123.5, 123.3, 123.2, 123.0, 105.3, 55.0, 32.5, 32.0, 29.8, 29.7, 29.7, 29.6, 29.4, 27.1, 22.8, 14.2

**HRMS-ESI** ( $m/z$ ): calculated  $C_{77}H_{75}N_5O_7Re$  [ $M - PF_6$ ] $^+$ : 1368.5224, found 1368.5217



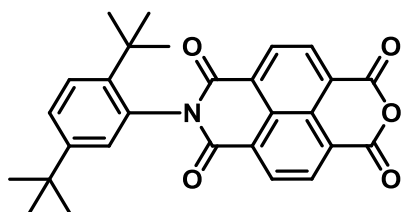
### PDI-Phbpy-Re-ACN

68 mg  $Re(CO)_5Br$  and 188 mg **C23PDI-Phbpy** were combined in 50 mL toluene in a 100 mL pressure tube in the glovebox and heated to  $110^\circ$  for 90 minutes. Toluene was removed under vacuum and the precipitate was dissolved in 20 mL DCM. 4 mL acetonitrile and 56 mg  $AgPF_6$  were added and the solution was heated in the pressure tube at  $55^\circ$  overnight. The solvent was removed under vacuum and the precipitate dissolved in 100 mL acetonitrile, filtered through Celite, and dried under vacuum. Yield: 198 mg (50%).  $^1H$  NMR (500 MHz, Chloroform- $d$ )  $\delta$  8.95 (t,  $J = 6.5$  Hz, 2H), 8.75-8.58 (m, 10H), 8.27 (td,  $J = 8.0, 1.1$  Hz, 1H), 8.06 (d,  $J = 8.2$  Hz, 2H), 7.83 (dd,  $J = 5.7, 1.1$  Hz, 1H), 7.65 (t,  $J = 6.0$  Hz, 1H), 7.62 (d,  $J = 8.1$  Hz, 2H), 5.16 (m, 1H), 2.23 (m, 2H), 2.20 (s, 3H), 1.84 (m, 2H), 1.36 (s, 12H), 1.42-1.10 (m, 36H), 0.82 (t,  $J = 6.9$  Hz, 6H)



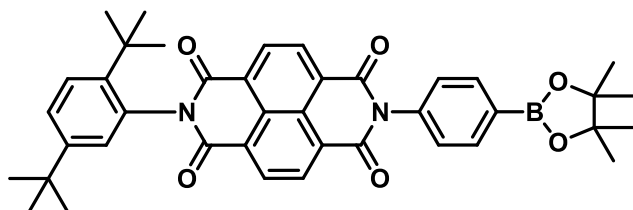
### PDI-Phbpy-Re-Py

45 mg **PDI-Phbpy-Re-ACN** and 50  $\mu$ L pyridine were dissolved in 25 mL chloroform and refluxed overnight. Solvent was removed under vacuum. Product was chromatographed on silica with 0-5% MeOH:DCM. The main band was collected and solvent evaporated under vacuum. Precipitate was dissolved in DCM and poured over a silica plug. The red material that remained at the top of the plug was exhaustively washed with DCM until eluent was colorless. The layer of silica containing red material was scraped off the top of the plug and extracted with 10% MeOH:DCM. The solvent was evaporated under vacuum to produce pure product.  **$^1\text{H}$  NMR** (500 MHz, Chloroform-*d*)  $\delta$  9.06 (t,  $J = 5.0$  Hz, 2H), 8.81-8.60 (m, 10H), 8.34 (m, 1H), 8.17 (d,  $J = 5.1$  Hz, 2H), 8.08 (d,  $J = 7.9$  Hz, 2H), 7.91 (d,  $J = 5.7$  Hz, 1H), 7.83 (t,  $J = 7.3$  Hz, 1H), 7.73 (t,  $J = 6.5$  Hz, 1H), 7.60 (d,  $J = 7.3$  Hz, 2H), 7.40 (m, 2H), 5.16 (m, 1H), 2.23 (m, 2H), 1.84 (m, 2H), 1.36 (s, 12H), 1.42-1.10 (m, 36H), 0.82 (t,  $J = 6.9$  Hz, 6H)  **$^{13}\text{C}$  NMR** (126 MHz, Chloroform-*d*)  $\delta$  195.69, 190.93, 163.24, 156.23, 155.76, 152.93, 152.58, 151.63, 141.63, 139.94, 137.92, 135.41, 135.15, 133.91, 131.78, 130.28, 129.62, 129.32, 128.86, 128.75, 127.24, 126.41, 126.21, 125.97, 123.35, 123.02, 122.79, 54.88, 32.36, 31.91, 29.64, 29.62, 29.58, 29.34, 27.06, 22.67, 14.11. **HRMS-ESI** ( $m/z$ ): calculated  $\text{C}_{71}\text{H}_{71}\text{N}_5\text{O}_7\text{Re} [\text{M} - \text{PF}_6]^+$ : 1292.4911, found 1292.4900



### DtB-NIA

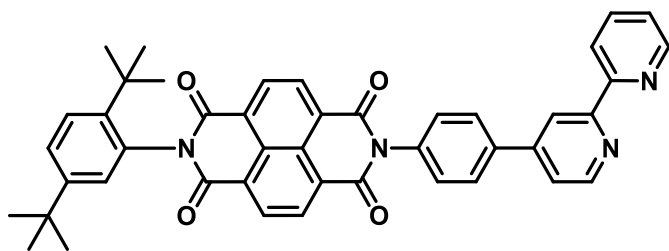
In an oven dried round bottom flask with a magnetic stirrer, reflux condenser, and addition funnel. Naphthalene-1,4,5,8-tetracarboxylic dianhydride (13.08 g, 48.78 mmol) was added to the flask with pyridine (200 mL) and DMF (200 mL) and heated to reflux 120 °C under N<sub>2</sub>. 2,5-Di-tert-butylaniline (5.0 g, 24.39) was dissolved in pyridine (50 mL) and added via the addition funnel and slowly added over a 30-minute period. The reaction was allowed to go overnight. The solution was cooled to room temperature and the solvent was removed under reduced pressure. The product was then extracted with dichloromethane (200 mL) and washed with water (3 x 100 mL). The organic layer was separated and the solvent was removed under reduced pressure. The remaining solid was purified by column chromatography using dichloromethane and dichloromethane:Acetone (99:1) to obtain an off-white solid (2.50 g, 23%). <sup>1</sup>H NMR (500 MHz, Chloroform-*d*) δ 8.91 – 8.83 (m, 4H), 7.61 (d, *J* = 8.6 Hz, 1H), 7.50 (dd, *J* = 8.6, 2.2 Hz, 1H), 6.98 (d, *J* = 2.1 Hz, 1H), 1.34 (s, 9H), 1.26 (d, 9H).



### DtB-NDI-PhBpin

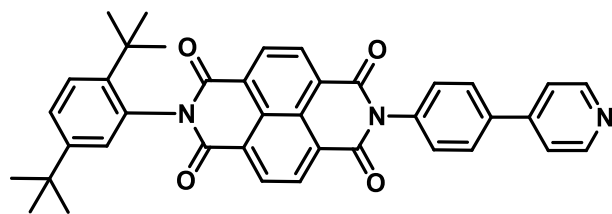
In an oven dried round bottom flask with a magnetic stirrer and reflux condenser, **DtB-NIA** (1.50 g, 3.29 mmol) and 4-(tetramethyl-1,3,2-dioxaborolan-2-yl)aniline (1.02 g, 4.65 mmol) were dissolved in pyridine (50 mL) and heated to 120 °C under N<sub>2</sub> overnight. The solution was cooled to room temperature and pyridine was removed in vacuo. The gooey material was then dissolved in 30 mL of dichloromethane and washed with 30 mL of 1M HCl. The organic layer was separated

and the solvent was removed under reduced pressure. The remaining solid was washed with 20 mL MeOH, affording an off-white colored powder (1.50 g, 70%).  $^1\text{H NMR}$  (500 MHz, Chloroform-*d*)  $\delta$  8.85 (s, 4H), 8.04 (d,  $J = 8.1$  Hz, 2H), 7.61 (d,  $J = 8.6$  Hz, 1H), 7.49 (dd,  $J = 8.6$ , 2.2 Hz, 1H), 7.37 – 7.32 (m, 2H), 7.01 (d,  $J = 2.2$  Hz, 1H), 1.38 (s, 12H), 1.33 (s, 9H), 1.28 (s, 9H).



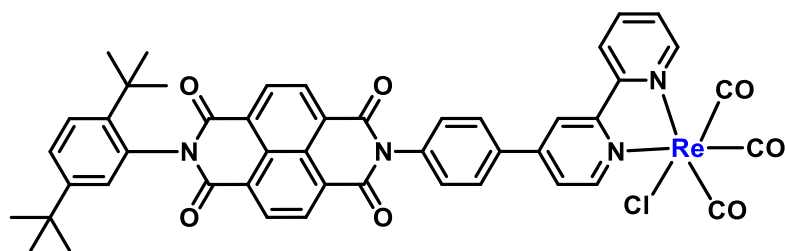
### DtB-NDI-Phbpy

In an oven dried round bottom flask with a magnetic stirrer and reflux condenser, compound **N2** (0.10 g, 0.15 mmol), **B3** (0.04 g, 0.18 mmol), and  $\text{Na}_2\text{CO}_3$  (0.127 g, 1.2 mmol) were dissolved in THF (33mL) and  $\text{H}_2\text{O}$  (7mL) and put under  $\text{N}_2$ . After 15 minutes of purging, fresh  $\text{Pd}[\text{PPh}_3]_4$  (8.7mg, 5% eq) was added via the second port and purged for 5 minutes. The solution was set to reflux overnight. The solution was cooled to room temperature and the solvent was removed under reduced pressure. The crude material was then dissolved in dichloromethane and ran through a celite plug. The solvent was removed under reduced pressure. The remaining solid was sonicated in minimal MeOH and allowed to sit overnight in a freezer. The solution was filtered and the light brown solid was collected (20%, 0.043g).  $^1\text{H NMR}$  (500 MHz, Chloroform-*d*)  $\delta$  8.89 (s, 4H), 8.80 – 8.71 (m, 3H), 8.48 (dt,  $J = 8.0$ , 1.2 Hz, 1H), 7.99 (d,  $J = 8.3$  Hz, 2H), 7.86 (td,  $J = 7.8$ , 1.8 Hz, 1H), 7.64 – 7.59 (m, 2H), 7.52 – 7.48 (m, 3H), 7.38 – 7.34 (m, 1H), 7.03 (d,  $J = 2.2$  Hz, 1H), 1.34 (s, 9H), 1.29 (s, 9H).



### DtB-NDI-PhPy

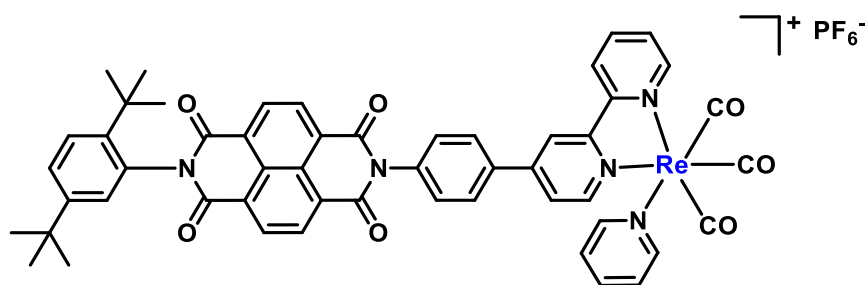
In an oven dried round bottom flask with a magnetic stirrer and reflux condenser, **DtB-NDI-PhBpin** (0.50 g, 0.15 mmol), 4-Bromopyridine hydrochloride (0.22 g, 1.13 mmol), and  $\text{Na}_2\text{CO}_3$  (0.70 g, 6.60 mmol) were dissolved in THF (150 mL) and  $\text{H}_2\text{O}$  (30 mL) and put under  $\text{N}_2$ . After 15 minutes of purging, fresh  $\text{Pd}[\text{PPh}_3]_4$  (0.06 g, 5% eq) was added via the second port and purged for 5 minutes. The solution was set to reflux overnight. The solution was cooled to room temperature and the solvent was removed under reduced pressure. The remaining solid was put through a silica plug. Using dichloromethane, and ultimately dichloromethane:MeOH (90:10) to elute the product. The solid was then sonicated in minimal MeOH and filtered to obtain an off-white solid (49%, 0.043g).  $^1\text{H NMR}$  (500 MHz, Chloroform-*d*)  $\delta$  8.86 (d, 4H), 8.71 (d, 2H), 7.85-7.80 (d, 2H), 7.62-7.53 (m, 3H), 7.50-7.43 (m, 3H), 7.02 (s, 1H), 1.32 (s, 9H), 1.27 (s, 9H).



### NDI-Phbpy-Re-Cl

In a nitrogen filled glove box, an oven dried pressure flask with a magnetic stirrer was filled with compound **N3** (0.1 g, 0.15 mmol), pentacarbonylchlororhenium(I) (0.065 g, 0.18 mmol), and

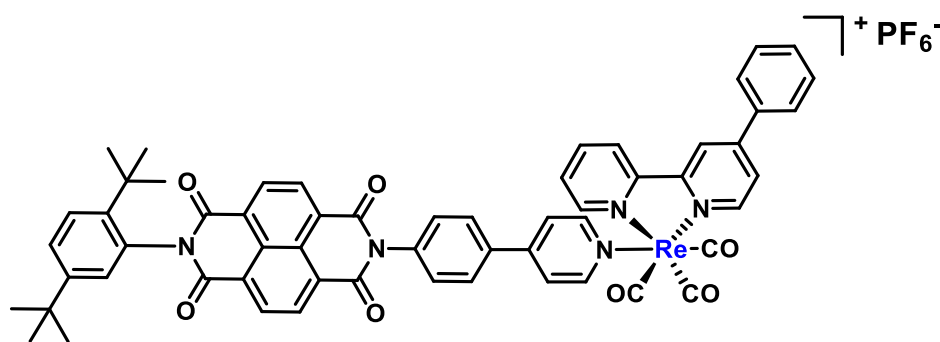
dichloromethane (30 mL). The pressure flask was capped and brought out of the glovebox and heated to 80 °C overnight. The solution was cooled to room temperature and the solvent was removed by reduced pressure. The solid was then column chromatographed on silica using a gradient between dichloromethane and Ethyl Acetate (100 → 98:2 → 85:15). The compound was then dissolved in minimal dichloromethane and layered with diethyl ether. Upon filtering, a bright yellow compound was obtained with sufficient purity to carry through to the next step. Yield: (0.03 g, 20%). <sup>1</sup>H NMR (500 MHz, Chloroform-*d*) δ 9.12 (td, *J* = 5.6, 1.1 Hz, 2H), 8.90 (s, 4H), 8.38 (d, *J* = 1.8 Hz, 1H), 8.35 – 8.30 (m, 1H), 8.10 (td, *J* = 7.6, 3.7 Hz, 1H), 7.93 – 7.87 (m, 2H), 7.75 (dt, *J* = 5.9, 1.9 Hz, 1H), 7.65 – 7.58 (m, 2H), 7.58 – 7.54 (m, 2H), 7.51 (dd, *J* = 8.6, 2.2 Hz, 1H), 7.03 (d, *J* = 2.2 Hz, 1H), 1.34 (s, 9H), 1.29 (s, 9H).



### NDI-Phbpy-Re-Py

In a nitrogen filled glove box, an oven dried pressure flask with a magnetic stirrer was filled with **NDI-Phbpy-Re-Cl** (30 mg, 0.030 mmol), AgPF<sub>6</sub> (8 mg, 0.033 mmol), pyridine (10 μL, 0.036), and dichloromethane (40 mL). The pressure flask was capped and brought out of the glovebox and heated to 80 °C overnight. The solution was cooled to room temperature and filtered through celite. The solvent was removed under reduced pressure and then column chromatographed on silica using a gradient between dichloromethane and Acetone (100 → 90:10). The compound was then

dissolved in minimal dichloromethane and layered with diethyl ether. Upon filtering, a bright yellow compound was obtained (3 mg, 8%).  $^1\text{H NMR}$  (500 MHz, Chloroform-*d*)  $\delta$  9.10 – 9.03 (m, 2H), 8.86 (s, 4H), 8.77 – 8.69 (m, 2H), 8.32 (td,  $J = 7.9, 1.5$  Hz, 1H), 8.16 (dt,  $J = 5.2, 1.5$  Hz, 2H), 8.10 (d,  $J = 8.5$  Hz, 2H), 7.91 (dd,  $J = 5.9, 1.9$  Hz, 1H), 7.82 (tt,  $J = 7.7, 1.5$  Hz, 1H), 7.72 (ddd,  $J = 7.4, 5.6, 1.1$  Hz, 1H), 7.63 – 7.54 (m, 3H), 7.48 (dd,  $J = 8.6, 2.2$  Hz, 1H), 7.42 – 7.35 (m, 2H), 7.01 (d,  $J = 2.2$  Hz, 1H), 1.32 (s, 9H), 1.27 (s, 9H)  $^{13}\text{C NMR}$  (126 MHz,  $\text{CDCl}_3$ )  $\delta$  163.9, 162.9, 156.5, 155.9, 152.8, 152.8, 152.6, 151.7, 150.5, 143.8, 141.8, 140.1, 137.5, 136.0, 132.1, 131.7, 131.6, 130.3, 129.1, 129.1, 128.9, 127.6, 127.5, 127.5, 127.4, 126.9, 126.4, 126.2, 123.8, 35.7, 34.4, 31.9, 31.3 **HRMS-ESI** ( $m/z$ ): calculated  $\text{C}_{52}\text{H}_{41}\text{N}_5\text{O}_7\text{Re}$  [ $\text{M} - \text{PF}_6$ ] $^+$ : 1034.2563, found 1034.2561



### Phbpy-Re-PyPhNDI

In a nitrogen filled glove box, an oven dried pressure flask with a magnetic stirrer was filled with **Phby-Re-Cl** (0.05 g, 0.01 mmol), **DtB-NDI-PhPy** (0.06 g, 0.10 mmol),  $\text{AgPF}_6$  (0.03 mg, 0.13 mmol), and dichloromethane (40 mL). The pressure flask was capped and brought out of the glovebox and heated to 80 °C overnight. The solution was cooled to room temperature and filtered through celite. The solvent was removed under reduced pressure and then column

chromatographed on silica using a gradient between dichloromethane and Acetone (100 → 90:10). The compound was then dissolved in minimal dichloromethane and layered with diethyl ether. Upon filtering, a bright yellow compound was obtained (0.03 g, 40%). **<sup>1</sup>H NMR** (500 MHz, Chloroform-*d*) δ 9.10 (d, *J* = 6.5 Hz, 1H), 9.06 (d, *J* = 5.8 Hz, 1H), 8.87 – 8.82 (m, 4H), 8.76 – 8.73 (d, *J* = 9.0 Hz, 1H), 8.71 (d, *J* = 1.8 Hz, 1H), 8.36 (td, *J* = 8.0, 1.6 Hz, 1H), 8.26 – 8.21 (m, 2H), 7.93 – 7.87 (m, 3H), 7.81 – 7.77 (m, 2H), 7.76 – 7.72 (m, 1H), 7.69 – 7.65 (m, 2H), 7.63 – 7.55 (m, 4H), 7.50 – 7.47 (m, 1H), 7.45 – 7.41 (m, 2H), 7.01 (d, *J* = 2.2 Hz, 1H), 1.33 (s, 9H), 1.27 (s, 9H) **<sup>13</sup>C NMR** (126 MHz, CDCl<sub>3</sub>) δ 163.8, 162.9, 156.3, 156.0, 153.9, 152.7, 152.0, 151.0, 150.5, 143.8, 141.8, 136.9, 136.3, 135.1, 132.0, 131.7, 131.6, 131.5, 129.9, 129.9, 129.1, 128.9, 128.5, 127.7, 127.6, 127.5, 127.4, 126.8, 126.3, 126.1, 125.0, 123.5, 35.7, 34.4, 31.8, 31.3. **HRMS-ESI** (*m/z*): calculated C<sub>71</sub>H<sub>71</sub>N<sub>5</sub>O<sub>7</sub>Re [M – PF<sub>6</sub>]<sup>+</sup>: 1292.4911, found 1292.4900

## 2.8 Supplementary Details

### 2.8.1 Transient Absorption SVD/global fitting

#### Treatment of Transient Absorption Data

Prior to kinetic analysis, the fsTA data were background/scatter-subtracted and chirp-corrected, and the visible and NIR data sets were spectrally merged (Surface Explorer 4, Ultrafast Systems, LLC).

#### Kinetic Fitting of Transient Absorption Data

The kinetic analysis was performed using home written programs in MATLAB<sup>113</sup> and was based on a global fit to either selected single-wavelength kinetics or kinetic vectors following singular value decomposition (method is specified for each compound in Figures 2.11-2.24). The time-resolution is given as  $w = 300$  fs (full width at half maximum, FWHM); the

assumption of a uniform instrument response across the frequency domain and a fixed time-zero ( $t_0$ ) are implicit in global analysis.

### ***Singular Value Decomposition***

Factoring of the two-dimensional (signal vs time & frequency) data set by Singular Value Decomposition (SVD) is performed as implemented in the MATLAB software package.<sup>113</sup> This factoring produces an orthonormal set of basis spectra that describe the wavelength dependence of the species and a corresponding set of orthogonal vectors that describe the time-dependent amplitudes of the basis spectra.<sup>114</sup> These kinetic vectors are then fit using the global analysis method described below.

### ***Multiple-Wavelength Global Fitting***

The kinetic data from multiple different wavelengths are fit using the global analysis described below. Each wavelength is given an initial amplitude that is representative of the spectral intensity at time  $t_0$ , and varied independently to fit the data. The time/rate constants and  $t_0$  are shared between the various kinetic data and are varied globally across the kinetic data in order to fit the species-associated model described below.

### ***Species-Associated Fitting***

We globally fit the dataset to a specified kinetic model and use the resultant populations to deconvolute the dataset and reconstruct species-associated spectra.

We use a first-order kinetic model with rate matrix  $K$  whose dimensions depend on the number of components in the model. For an  $A \rightarrow B \rightarrow (G)$  round model, used to fit all the data except the short-time data for **Phbpy-Re-PyPhNDI<sup>1-</sup>** and **Phbpy-Re-PyPhPDI<sup>2-</sup>**, the matrix is:

$$K = \begin{pmatrix} -k_{A \rightarrow B} & 0 \\ k_{A \rightarrow B} & -k_{B \rightarrow G} \end{pmatrix}$$

For the  $A \rightarrow B+C \rightarrow (G)$  round model used to fit the short-time data for **Phbpy-Re-PyPhNDI**<sup>1-</sup> and **Phbpy-Re-PyPhPDI**<sup>2-</sup>, the matrix is:

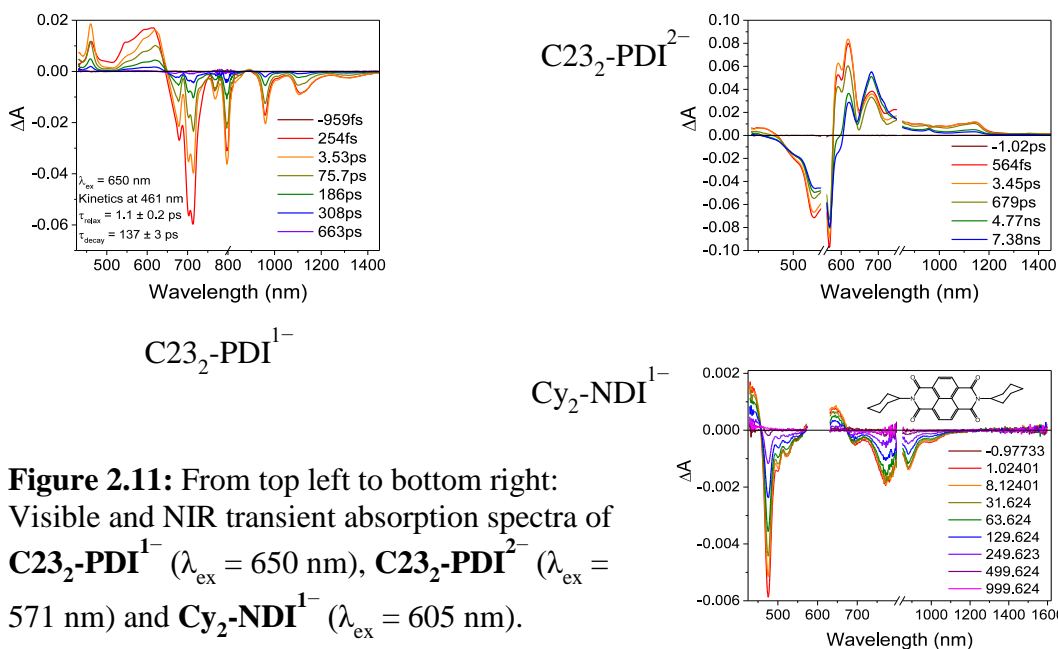
$$K = \begin{pmatrix} -k_{A \rightarrow B+C} & 0 & 0 \\ k_{A \rightarrow B+C} & -k_{B \rightarrow G} & 0 \\ k_{A \rightarrow B+C} & 0 & -k_{C \rightarrow G} \end{pmatrix}$$

The MATLAB program numerically solves the differential equations through matrix methods,<sup>115</sup> then convolutes the solutions with a Gaussian instrument response function with width  $w$  (FWHM), before employing a least-squares fitting using a Levenberg-Marquardt or Simplex method to find the parameters which result in matches to the kinetic data.

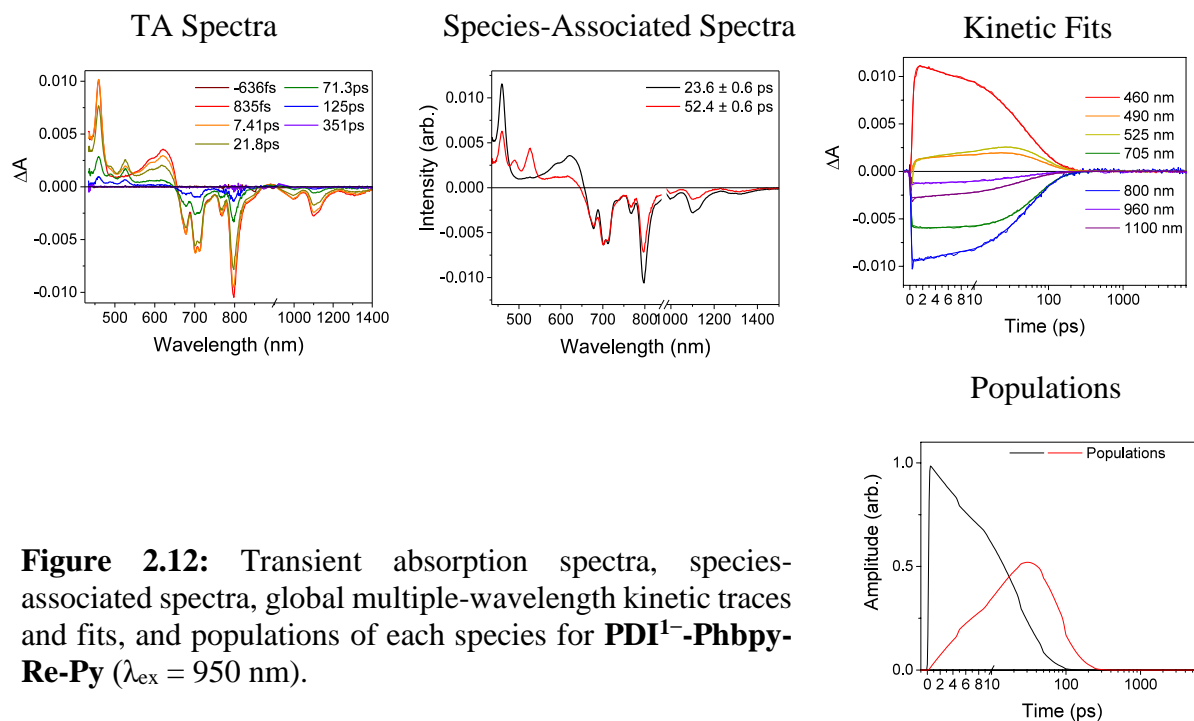
### *Spectral Reconstruction*

Once the fit parameters are established, they are fed directly into the differential equations, which were solved for the populations of the states in model—i.e.,  $A(t)$ ,  $B(t)$  and  $C(t)$ . Finally, the raw data matrix (with all the raw data) is deconvoluted with the populations as functions of time to produce the spectra associated with each species.

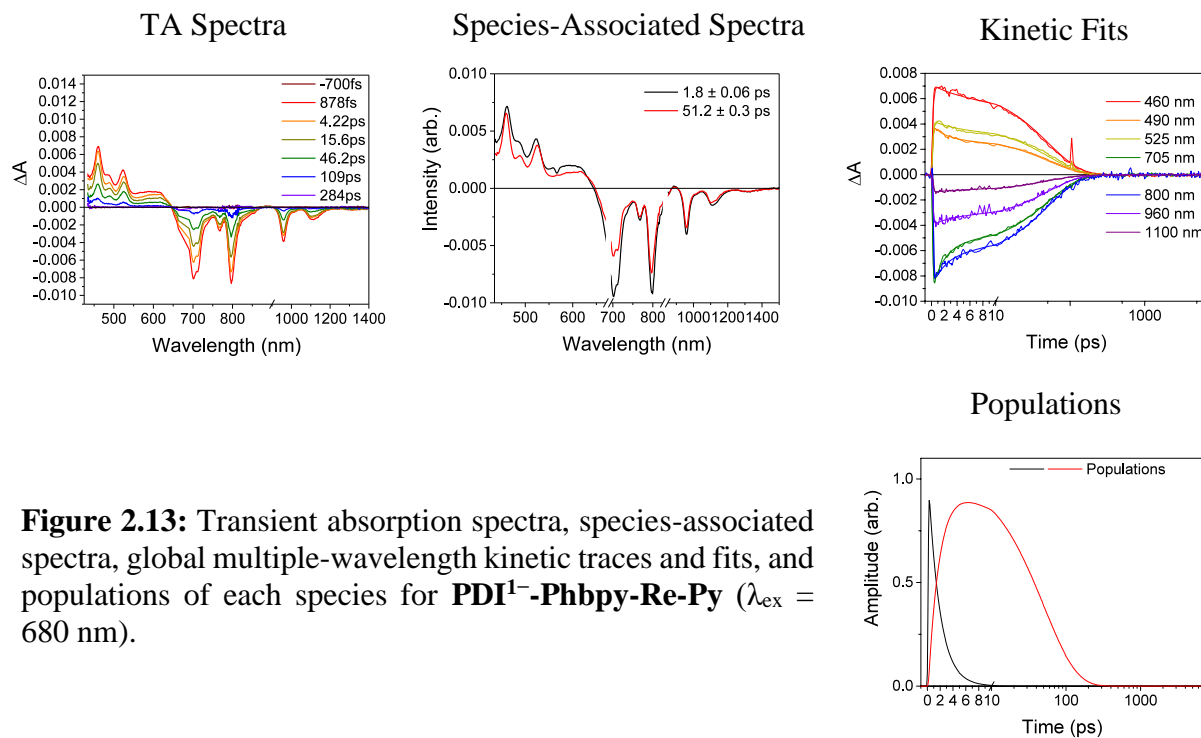
## 2.8.2 Transient Absorption Data



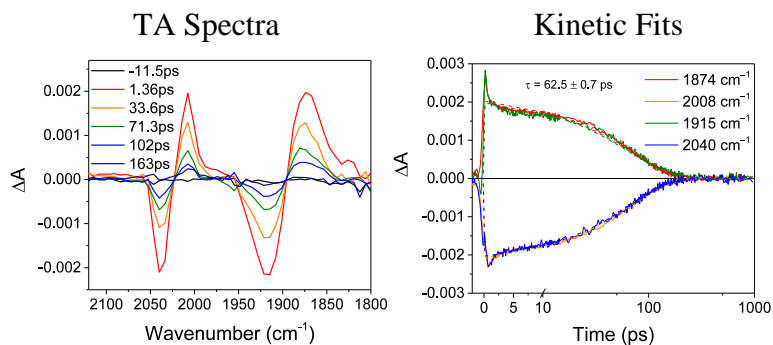
**Figure 2.11:** From top left to bottom right: Visible and NIR transient absorption spectra of  $\text{C23}_2\text{-PDI}^{1-}$  ( $\lambda_{\text{ex}} = 650 \text{ nm}$ ),  $\text{C23}_2\text{-PDI}^{2-}$  ( $\lambda_{\text{ex}} = 571 \text{ nm}$ ) and  $\text{Cy}_2\text{-NDI}^{1-}$  ( $\lambda_{\text{ex}} = 605 \text{ nm}$ ).



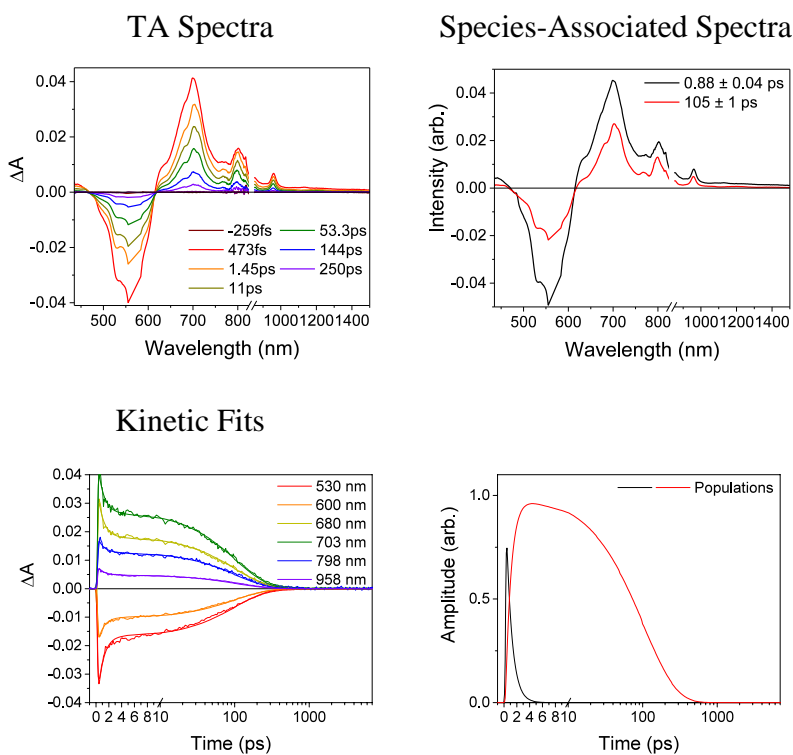
**Figure 2.12:** Transient absorption spectra, species-associated spectra, global multiple-wavelength kinetic traces and fits, and populations of each species for  $\text{PDI}^{1-}\text{-Phbpy-Re-Py}$  ( $\lambda_{\text{ex}} = 950 \text{ nm}$ ).



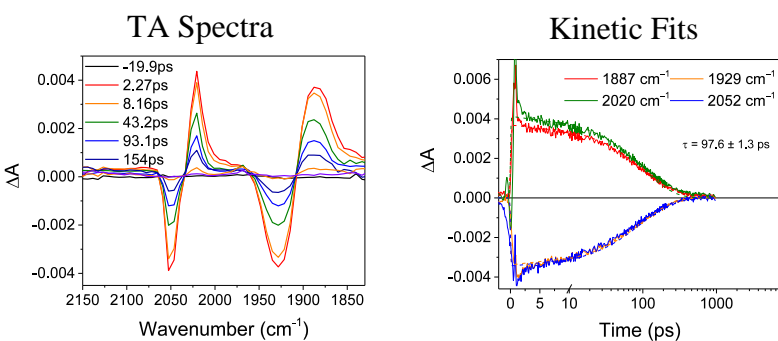
**Figure 2.13:** Transient absorption spectra, species-associated spectra, global multiple-wavelength kinetic traces and fits, and populations of each species for **PDI<sup>1-</sup>-Phbpy-Re-Py** ( $\lambda_{\text{ex}} = 680$  nm).



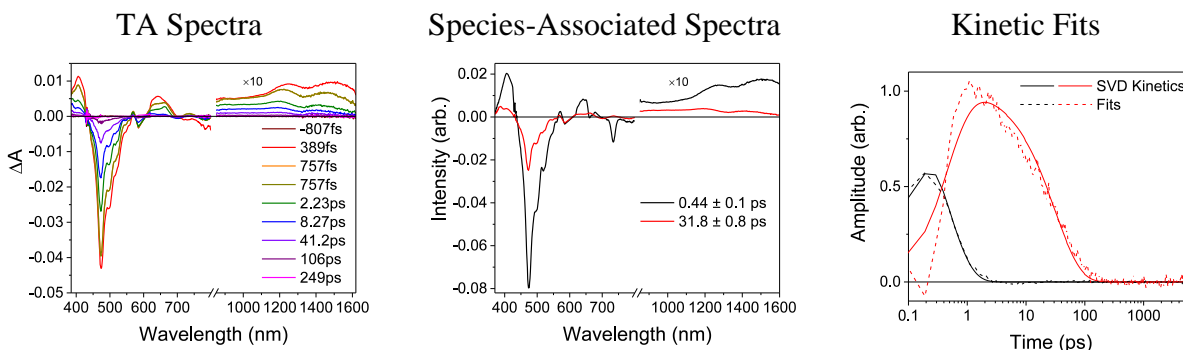
**Figure 2.14:** Time-resolved IR spectra and global multiple-wavelength kinetic traces and fits for **PDI<sup>1-</sup>-Phbpy-Re-Py** ( $\lambda_{\text{ex}} = 700$  nm).



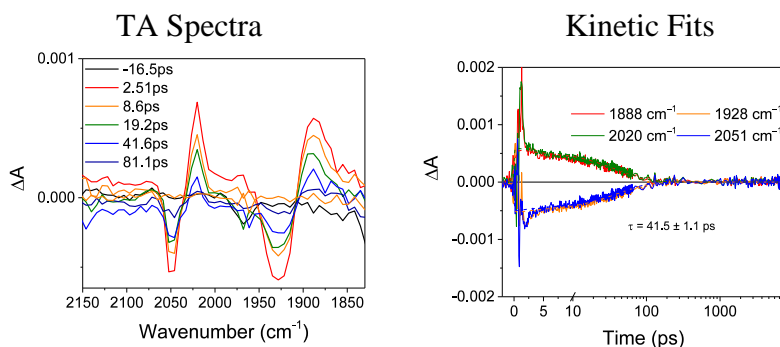
**Figure 2.15:** Transient absorption spectra, species-associated spectra, global multiple-wavelength kinetic traces and fits, and populations of each species for  $\text{PDI}^{2-}\text{-Phbpy-Re-Py}$  ( $\lambda_{\text{ex}} = 570$  nm).



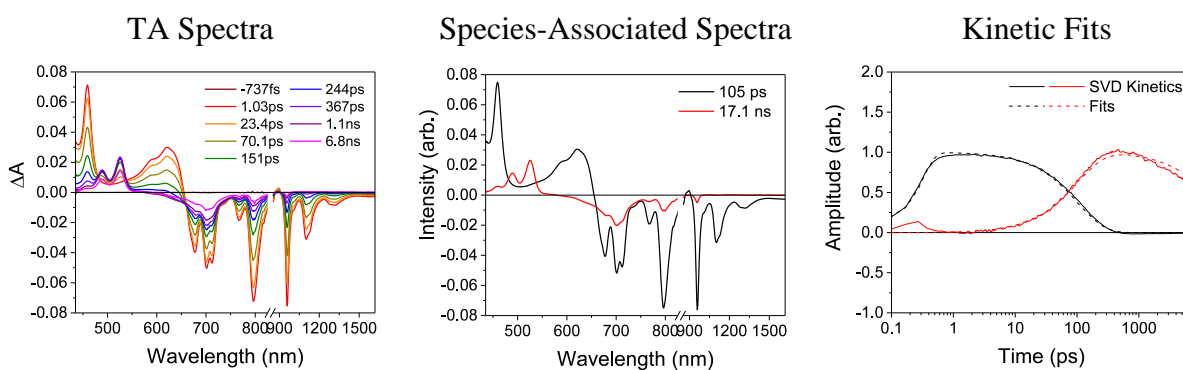
**Figure 2.16:** Time-resolved IR spectra and global multiple-wavelength kinetic traces and fits for  $\text{PDI}^{2-}\text{-Phbpy-Re-Py}$  ( $\lambda_{\text{ex}} = 570$  nm).



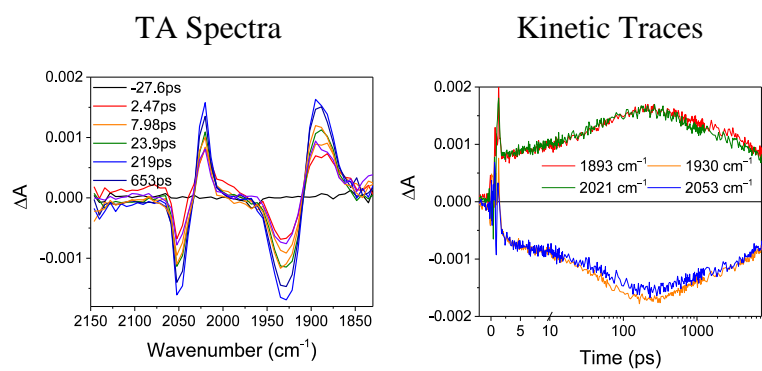
**Figure 2.17:** Transient absorption spectra, species-associated spectra, and singular value decomposition kinetic traces and fits for  $\text{NDI}^{1-}\text{-Phbpy-Re-Py}$  ( $\lambda_{\text{ex}} = 605$  nm).



**Figure 2.18:** Time-resolved IR spectra and global multiple-wavelength kinetic traces and fits for  $\text{NDI}^{1-}\text{-Phbpy-Re-Py}$  ( $\lambda_{\text{ex}} = 605$  nm).

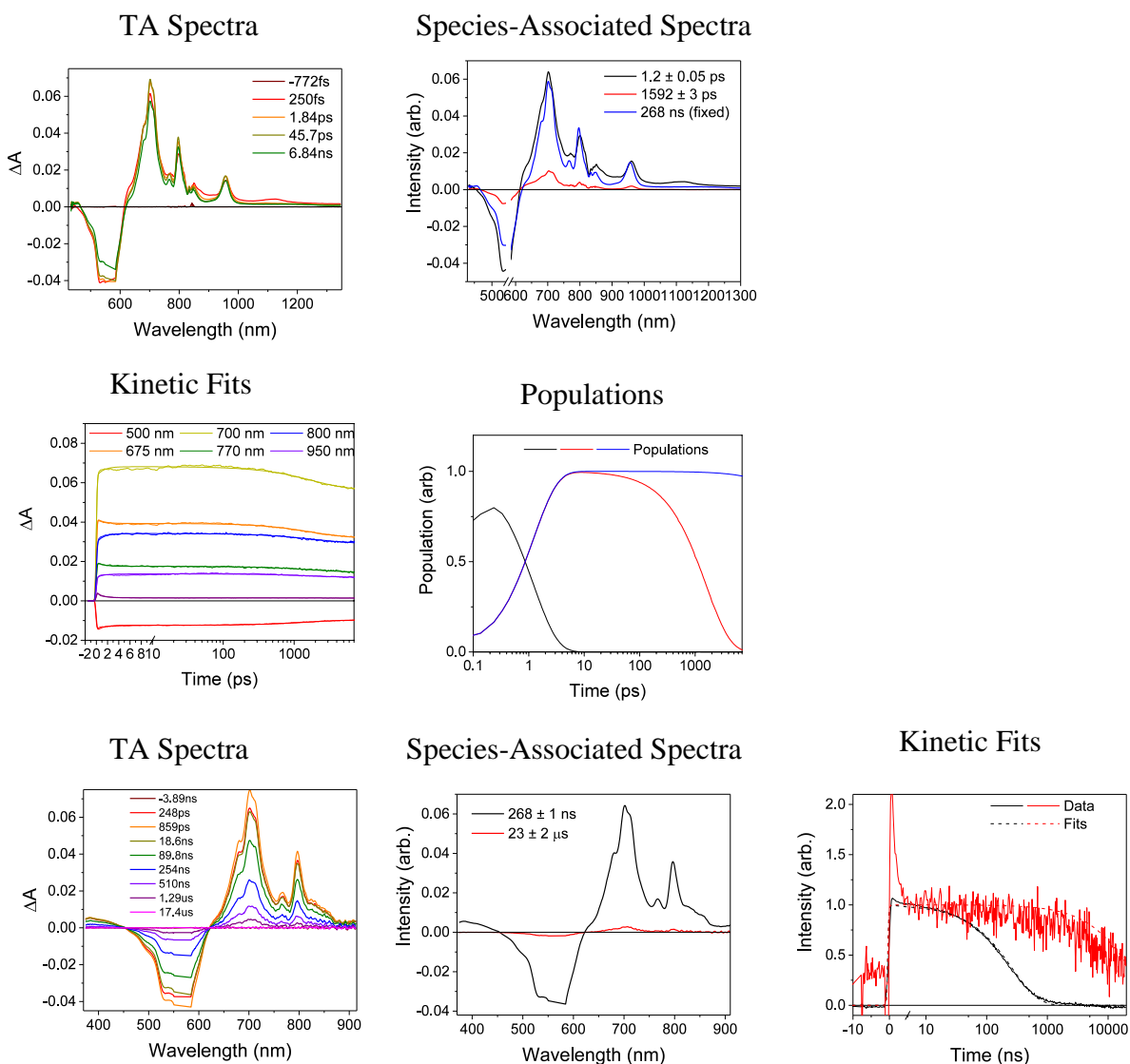


**Figure 2.19:** Transient absorption spectra, species-associated spectra, and singular value decomposition kinetic traces and fits for  $\text{Phbpy-Re-PyPhPDI}^{1-}$  ( $\lambda_{\text{ex}} = 950$  nm).

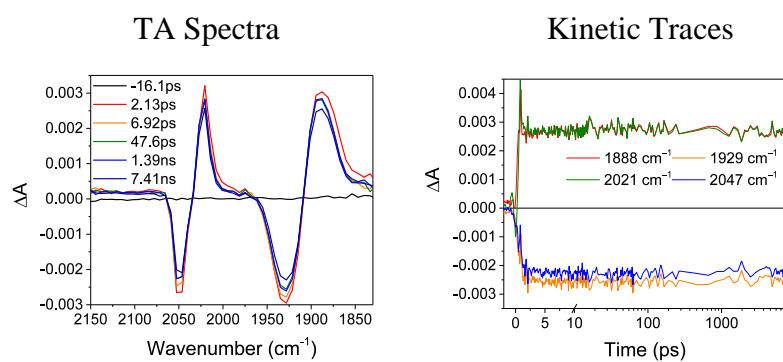


**Figure 2.20:** Time-resolved IR spectra and global multiple-wavelength kinetic traces and fits for **Phbpy-Re-PyPhPDI<sup>1-</sup>** ( $\lambda_{\text{ex}} = 705 \text{ nm}$ ).

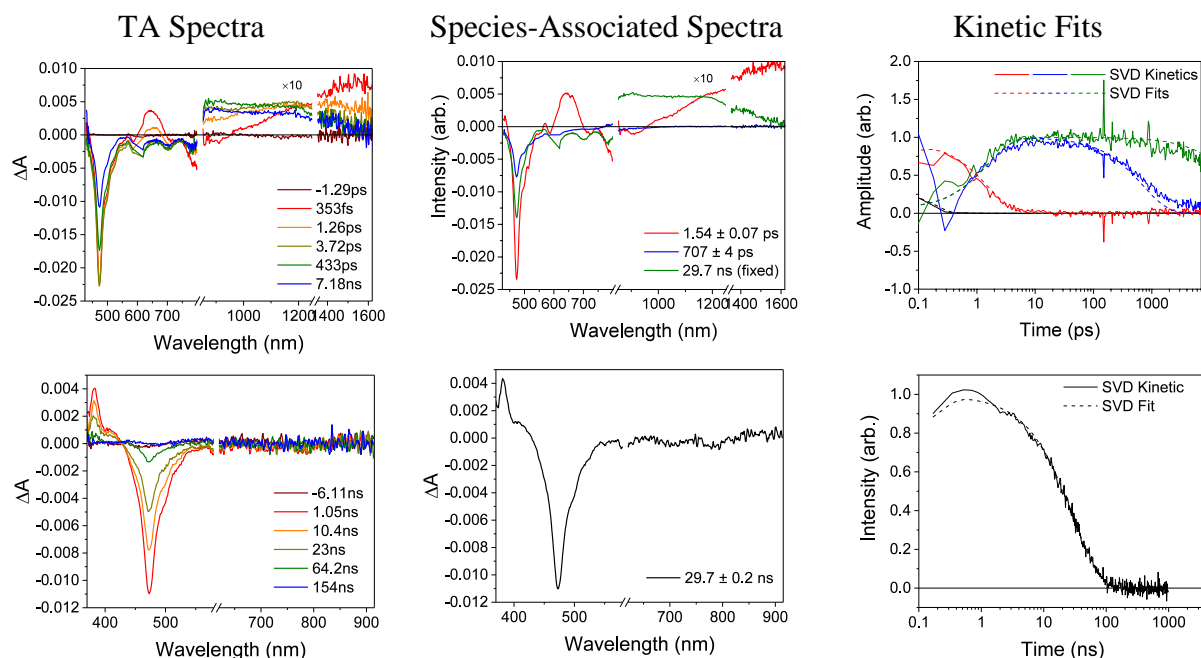
### Phbpy-Re-PyPhPDI<sup>2-</sup>



**Figure 2.21:** *Left column:* Transient absorption spectra for **Phbpy-Re-PyPhPDI<sup>2-</sup>** ( $\lambda_{\text{ex}} = 570$  nm). *Middle column:* Species-associated spectral fits to the data. *Right column:* Multiple-wavelength kinetic traces and fits (at short times) and singular value decomposition kinetic traces and fits (at long times) to the kinetic data based on the species-associated fits and lifetimes shown.



**Figure 2.22:** Time-resolved IR spectra and global multiple-wavelength kinetic traces and fits for **Phbp-Re-PyPhPDI**<sup>2-</sup> ( $\lambda_{\text{ex}} = 570 \text{ nm}$ )

**Phbpy-Re-PyPhNDI<sup>1-</sup>**

**Figure 2.23:** Left column: Transient absorption spectra for **Phbpy-Re-PyPhNDI<sup>1-</sup>** ( $\lambda_{\text{ex}} = 605$  nm). Middle column: Species-associated spectral fits to the data. Right column: Multiple-wavelength kinetic traces and fits (at short times) and singular value decomposition kinetic traces and fits (at long times) to the kinetic data based on the species-associated fits and lifetimes shown.

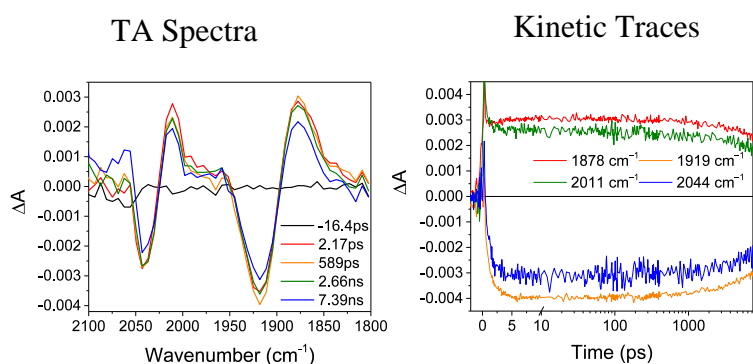


**Figure 2.24:** Time-resolved IR spectra and multiple-wavelength kinetic traces for **Phbpy-Re-PyPhNDI<sup>1-</sup>** ( $\lambda_{\text{ex}} = 605$  nm)

## 2.8.2 Donor-Acceptor Distances

**Table 2.4.** Donor-acceptor distances in the complexes under study, calculated from the DFT-optimized geometries.

	$r_{\text{RDI,bpy}} (\text{\AA})$	$r_{\text{RDI,Re}} (\text{\AA})$	$r_{\text{Re,bpy}} (\text{\AA})$
PDI-Phbpy-Re-Py	14.2	16.4	2.95
NDI-Phbpy-Re-Py	12.1	14.2	2.95
Phbpy-Re-PyPhPDI	16.9	16.4	2.83
Phbpy-Re-PyPhNDI	14.5	14.3	2.95

## 2.8.3 Electronic Calculations

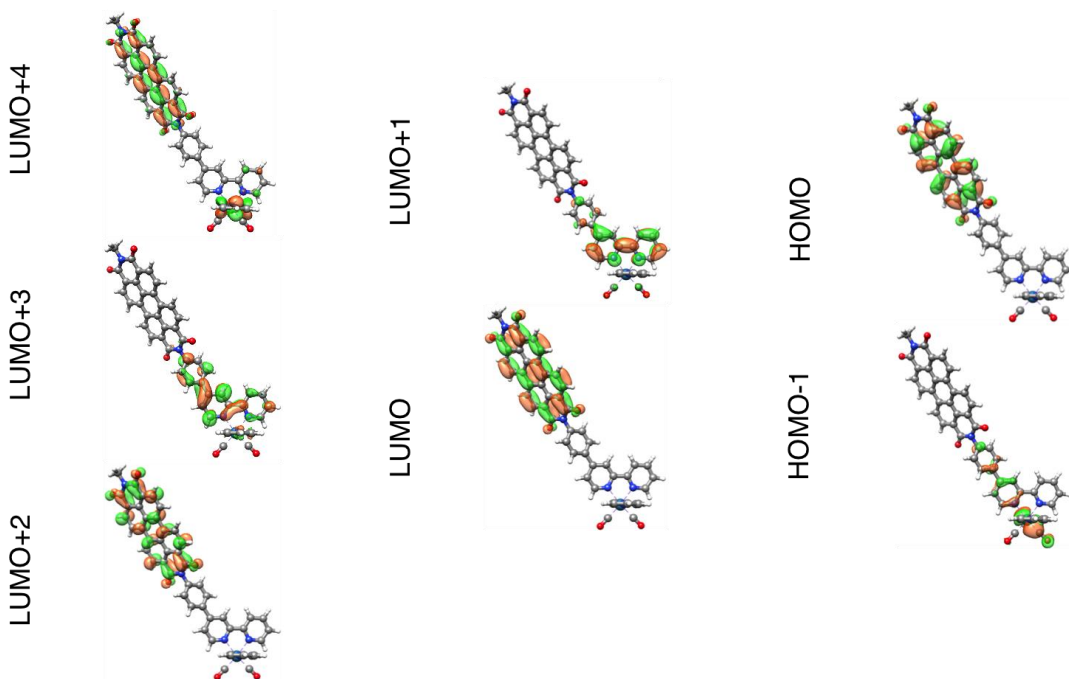


**Figure 2.25:** Frontier orbitals for the PDI-[Re(Phbpy)(py)(CO)<sub>3</sub>]<sup>+</sup> dyad with isodensity=0.03

**Table 2.5:** Relevant orbital energies in eV for all species as non-reduced singlets.

	[Re(Phbpy)(py)(CO) <sub>3</sub> ] <sup>+</sup>	Dyad	PDI
LUMO+3		-1.88	
LUMO+2		-1.89	-1.67
LUMO+1	-1.85	-2.66	-1.85
LUMO	-2.65	-3.42	-3.39
HOMO	-6.46	-5.88	-5.85
HOMO-1		-6.47	-7.26

**Table 2.6:** The wavelengths  $\lambda$ , oscillator strengths  $f$ , and dominant orbital characters for the 10 lowest-energy calculated vertical electronic transitions of [Re(Phbpy)(py)(CO)<sub>3</sub>]<sup>+</sup>.

$\lambda$ [nm]	$f$	Primary Transition Character	%	Secondary Transition Character	%
394.7	0.040	HOMO→LUMO	70	HOMO-1→LUMO	28
383.4	0.117	HOMO-1→LUMO	67	HOMO→LUMO	24
369.7	0.044	HOMO-2→LUMO	91	HOMO-1→LUMO	4
317.2	0.208	HOMO-3→LUMO	76	HOMO-5→LUMO	8
308.3	0.142	HOMO→LUMO+1	56	HOMO-3→LUMO	14
304.3	0.019	HOMO-1→LUMO+1	39	HOMO-4→LUMO	21
302.2	0.016	HOMO-4→LUMO	36	HOMO-1→LUMO+1	33
301.3	0.046	HOMO→LUMO+2	39	HOMO-5→LUMO	22
295.8	0.200	HOMO-5→LUMO	35	HOMO-1→LUMO+2	26
295.5	0.089	HOMO-1→LUMO+2	33	HOMO→LUMO+2	16

**Table 2.7:** The calculated vibronic absorption maximum peak wavelengths  $\lambda$  of the first three electronic transitions, and the vertical wavelengths  $\lambda$ , oscillator strengths  $f$ , and dominant orbital characters for the 10 lowest-energy calculated electronic transitions of the reduced PDI<sup>-</sup> radical.

$\lambda_{\text{vibronic}}$ [nm]	$\lambda$ [nm]	$f$	Primary Transition Character	%	Secondary Transition Character	%
974.4	844.3	0.032	$\beta$ HOMO→LUMO	74	$\alpha$ LUMO→LUMO+1	26

688.4	668.6	0.052	$\alpha$ LUMO $\rightarrow$ LUMO+2	97	N/A	0
717.1	621.4	0.885	$\alpha$ LUMO $\rightarrow$ LUMO+1	72	$\beta$ HOMO $\rightarrow$ LUMO	24
	532.5	0.001	$\alpha$ LUMO $\rightarrow$ LUMO+3	97	N/A	0
	462.7	0.000	$\alpha$ LUMO $\rightarrow$ LUMO+4	39	$\beta$ HOMO $\rightarrow$ LUMO+2	18
	442.2	0.000	$\beta$ HOMO $\rightarrow$ LUMO+1	33	$\alpha$ HOMO $\rightarrow$ LUMO+1	29
	419.7	0.000	$\alpha$ LUMO $\rightarrow$ LUMO+4	48	$\beta$ HOMO $\rightarrow$ LUMO+2	13
	400.2	0.000	$\beta$ HOMO-1 $\rightarrow$ LUMO	92	$\beta$ HOMO-1 $\rightarrow$ LUMO+1	4
	399.0	0.000	$\beta$ HOMO-2 $\rightarrow$ LUMO	92	$\beta$ HOMO-2 $\rightarrow$ LUMO+1	4
	394.3	0.000	$\beta$ HOMO-3 $\rightarrow$ LUMO	52	$\beta$ HOMO-4 $\rightarrow$ LUMO	26

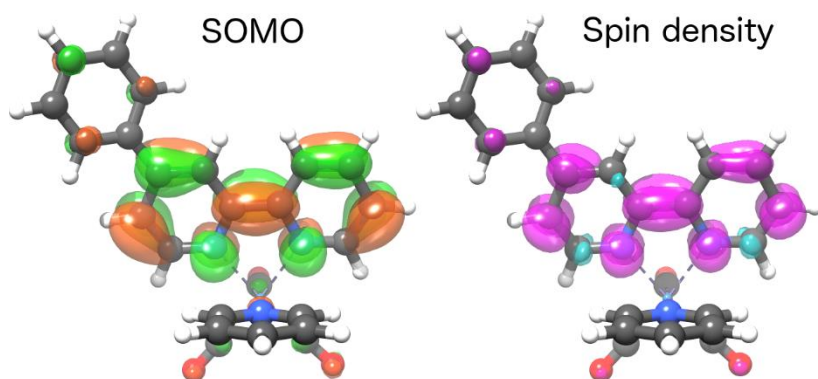


**Figure 2.26:** Calculated SOMO (isovalue=0.03) and spin density (isovalue=0.002, magenta for spin up and teal for spin down) of the  $\text{Re}(\text{Phbpy})(\text{CO})_3(\text{PyPh})$  doublet anion, calculated with B3LYP/Def2TZVP//Def2SVP showing that the reducing electron density is largest on the bpy, with some density extending onto the 4-phenyl group.

## 2.8.4 Excited State Equilibrium

### Determination of $\text{PDI}^{1-*}$ – $\text{PDI}^0$ equilibrium constant

The extinction coefficient for  $\text{PDI}^{1-*}$  was determined by examination of the transient absorption spectra of  $\text{PDI}^{1-}$  (Figure 2.2 in main text). The known extinction coefficient for the bleach at 798 nm ( $\epsilon = 49600 \text{ M}^{-1} \text{ cm}^{-1}$ )<sup>45</sup> was used to determine the transient concentration of

$\text{PDI}^{1-*}$  at a number of time points. That concentration was then used to determine the extinction coefficient of  $\text{PDI}^{1-*}$  at 460 nm and 526 nm ( $\epsilon_{460} = 25800 \text{ M}^{-1} \text{ cm}^{-1}$ ,  $\epsilon_{526} = 3300 \text{ M}^{-1} \text{ cm}^{-1}$ ). The extinction coefficients of  $\text{PDI}^0$  at those wavelengths were obtained from the literature<sup>45</sup> ( $\epsilon_{460} = 19300 \text{ M}^{-1} \text{ cm}^{-1}$ ,  $\epsilon_{526} = 80000 \text{ M}^{-1} \text{ cm}^{-1}$ ). The concentration of each species at a given timepoint can be expressed as the following system of equations:

$$A_{460} = [\text{PDI}^{1-*}] \times \epsilon_{460, \text{PDI}^{1-*}} + [\text{PDI}^0] \times \epsilon_{460, \text{PDI}^0}$$

$$A_{526} = [\text{PDI}^{1-*}] \times \epsilon_{526, \text{PDI}^{1-*}} + [\text{PDI}^0] \times \epsilon_{526, \text{PDI}^0}$$

This system can be solved to give the following expressions for  $[\text{PDI}^{1-*}]$  and  $[\text{PDI}^0]$ :

$$[\text{PDI}^{1-*}] = \frac{A_{460} \times \epsilon_{526, \text{PDI}^0} - A_{526} \times \epsilon_{460, \text{PDI}^0}}{\epsilon_{460, \text{PDI}^{1-*}} \times \epsilon_{526, \text{PDI}^0} - \epsilon_{526, \text{PDI}^0} \times \epsilon_{460, \text{PDI}^0}}$$

$$[\text{PDI}^0] = \frac{A_{460} \times \epsilon_{526, \text{PDI}^{1-*}} - A_{526} \times \epsilon_{460, \text{PDI}^{1-*}}}{\epsilon_{526, \text{PDI}^0} \times \epsilon_{460, \text{PDI}^0} - \epsilon_{460, \text{PDI}^{1-*}} \times \epsilon_{526, \text{PDI}^0}}$$

These expressions were applied to the spectra derived from the SVD of the transient absorption data to derive the equilibrium constants for the  $\text{PDI}^{1-*} \rightleftharpoons \text{PDI}^0$  excited-state electron transfer reaction.

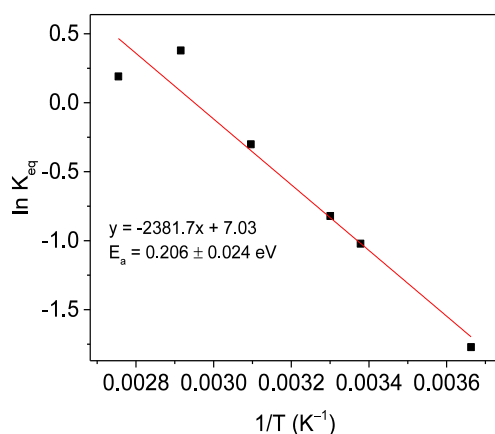


**Figure 2.27:** Plot of  $\ln K_{\text{eq}}$  vs.  $1/T$  derived from the  $[\text{PDI}^0]:[\text{PDI}^{1-*}]$  ratio in the SVD spectra of variable-temperature TA experiments on  $\text{PDI}^{1-}$ -Phbpy-Re-Py.

## **Chapter 3 Photodriven Electron from the Highly Reducing Excited State of Naphthalene Diimide Radical Anion to a CO<sub>2</sub> Reduction Catalyst within a Molecular Triad**

J. F. Martinez, N. T. La Porte, C. M. Mauck and M. R. Wasielewski, *Faraday Discuss.*, 2017, **198**, 235  
**DOI:** 10.1039/C6FD00219F - Reproduced by permission of The Royal Society of Chemistry

### 3.1 Introduction

Over the past several decades, many research groups have focused a great deal of effort on the electron transfer photosensitization of carbon dioxide reduction catalysts.<sup>116-117</sup> The work carried out in these groups has at turns focused on optimizing turnover frequency, catalyst durability, selectivity for CO<sub>2</sub> reduction products, or other factors. For the most part, the photosensitizers used in these systems have been polypyridyl or polypyrrole complexes of low-abundance second and third row transition metals, for the reason that these chromophores offer a reasonable balance of excited state lifetimes, reducing power, and visible light absorption. Typical organic chromophores with the power to reduce typical CO<sub>2</sub> reduction catalysts absorb in the blue or UV spectral regions, making them of little use for artificial photosynthesis. Recently, though, our group and others have reported donor-acceptor systems that make use of the radical anions of chemically-robust naphthalenediimide (NDI) and perylenediimide (PDI) derivatives as highly reducing chromophores that absorb in the red to near infrared.<sup>49-50, 74-75, 118-120</sup>

The NDI radical anion (NDI<sup>•-</sup>) is easily produced by mild chemical or electrochemical reduction (−0.5 V vs. SCE). Photoexcitation of NDI<sup>•-</sup>, even at its longest wavelength absorption band at 785 nm,<sup>45</sup> produces its excited doublet state (\*NDI<sup>•-</sup>), which is a strong photoreductant, possessing an excited-state oxidation potential of about −2.1 V vs. SCE, making it an extremely attractive chromophore for photosensitizing difficult-to-reduce substrates. However, in donor-acceptor systems reported earlier,<sup>120</sup> the free energy for back electron transfer, coupled with the increased electronic coupling associated with short donor-acceptor distances, has resulted in lifetimes for the charge-shifted state that are relatively short, up to tens of nanoseconds at most.

In the present report, we describe a covalent molecular triad system in which photoexcitation of an NDI<sup>•-</sup> chromophore produces NDI<sup>•-\*</sup> that serves as a powerful photoreductant to initially

reduce a 9,10-diphenylanthracene (DPA) acceptor. This is followed by thermal electron transfer from  $\text{DPA}^{\cdot-}$  to a  $\text{Re}(\text{dmb})(\text{CO})_3$  carbon dioxide reduction catalyst where dmb is 4,4'-dimethyl-2,2'-bipyridine. By employing an intermediate acceptor whose reduction potential is substantially more negative than the reduction potential of the metal complex, forward electron transfer occurs via a series of two rapid short-distance steps while back electron transfer must occur via a single long distance step. The result is that the back electron transfer lifetime is lengthened substantially, to longer than 40 microseconds. Sufficiently long lifetimes for the highly reduced intermediates involved in  $\text{CO}_2$  reduction by metal complexes are a necessary condition for efficient catalysis, given the need for small molecules to diffusively encounter these intermediates. This triad motif is appropriate for integration into organic or organometallic systems in which it is desirable to deliver electrons at highly reducing potentials using long-wavelength light typical of solar irradiation, and where back-electron transfer is a concern.

## **3.2 Experimental Details**

### **3.2.1 Synthesis and Materials**

Dichloromethane,  $\text{CH}_3\text{CN}$ , and MeOH used for synthesis were obtained from Fisher Scientific and used as received. DMF used for synthesis and spectroscopic experiments was dried on a commercial system (GlassContour, Laguna Beach, CA). For spectroscopy, DMF was further transferred under argon into a  $\text{N}_2$ -filled glovebox (MBraun Unilab) for use and storage. Commercially available reagents were purchased from Sigma-Aldrich or Oakwood Chemicals and used as received. Compounds were reduced in the glovebox using tetrakisdiaminoethylene (TDAE) from Tokyo Chemical Industries. UV/Vis/NIR absorbance spectroscopy was performed on a Shimadzu UV-1601 spectrometer at 298 K.

$^1\text{H}$  NMR spectra were recorded on a Bruker Avance 500 TCI Cryoprobe Spectrometer. Chemical shifts are recorded in ppm ( $\delta$ ) in  $\text{CDCl}_3$  (internal reference set to  $\delta$  7.26 ppm).  $^{13}\text{C}$  NMR (126 MHz) spectra were recorded using a Bruker Avance III QNP Cryoprobe with simultaneous decoupling of  $^1\text{H}$  nuclei and externally referenced to TMS set to 0 ppm. All spectra were recorded at 298 K. High resolution mass spectrometry (ESI-MS) were performed by Northwestern University's Integrated Molecular Structure Education and Research Center.

### 3.2.2 Steady State Spectroscopy

UV-vis spectra were acquired on a Shimadzu UV-1800 spectrophotometer at room temperature. The samples were normalized to the greatest peak.

### 3.2.3 Electrochemistry

Electrochemical measurements were performed using a CH Instruments Model 660A electrochemical workstation. A single-compartment cell was used for all cyclic voltammetry experiments with a 1.0 mm diameter glassy carbon disk working electrode, a platinum wire counter electrode, a silver wire pseudoreference electrode, and 0.1 M tetrabutylammonium hexafluorophosphate as the supporting electrolyte in DMF. The ferrocene/ferrocenium redox couple (0.45 V vs SCE)<sup>79</sup> was used as an internal standard. TBAPF<sub>6</sub> was recrystallized twice from ethanol prior to use. Electrochemical cells were shielded from light during experiments. All solutions were continuously purged with argon before and during the cyclic voltammetry experiments. Py-DPA-NDI (**5**) and  $[\text{Re}(\text{dmb})(\text{CO})_3(\text{Py-DPA-NDI})]^+\text{PF}_6^-$  (**6**) were prepared in concentrations of 0.5 mM for cyclic voltammetry experiments.

### 3.2.4 Femtosecond Transient Absorption Spectroscopy

Femtosecond transient absorption experiments were performed employing a regeneratively amplified Ti:sapphire laser system operating at 828 nm and a 1 kHz repetition rate as previously described.<sup>80-81</sup> The output of the amplifier was frequency-doubled to 414 nm using a BBO crystal and that light was used to pump a laboratory-built collinear optical parametric (OPA) amplifier<sup>82</sup> for visible-light excitation or a commercial non-collinear optical parametric amplifier (TOPAS-White, Light-Conversion, LLC.) for NIR excitation. Approximately 1-3 mW of the fundamental was focused onto a sapphire disk to generate the visible white-light probe spanning 430-850 nm, or into a 5 mm quartz cuvette containing a 1:1 mixture of H<sub>2</sub>O:D<sub>2</sub>O to generate a UV/visible white light probe spanning 385-750 nm, or onto a proprietary medium (Ultrafast Systems, LLC) to generate the NIR white-light probe spanning 850-1620 nm. The total instrument response function was 300 fs.

Experiments were performed at a randomized pump polarization to suppress contributions from orientational dynamics. Spectral and kinetic data were collected with a CMOS or InGaAs array detector for visible and NIR detection, respectively, and a 8 ns pump-probe delay track (customized Helios, Ultrafast Systems, LLC). Transient spectra were averaged for at least 3 seconds. All spectra were acquired in DMF solution. Samples had an absorbance of 0.2-0.7 at the excitation wavelength and were irradiated in 2 mm quartz cuvettes with 0.4-0.8  $\mu$ J/pulse focused to  $\sim$ 0.2 mm diameter spot. Samples were stirred to avoid effects of local heating or sample degradation. The samples were prepared in the glovebox and degassed by multiple freeze-pump-thaw cycles prior to analysis.

### 3.2.5 Nanosecond Transient Absorption Spectroscopy

Nanosecond transient absorption experiments were performed using the femtosecond excitation beam described above and a commercial spectrometer (Eos, Ultrafast Systems, LLC) utilizing a photonic crystal fiber ultra-broadband probe source. The pump polarization was randomized to suppress rotational dynamics. Samples were stirred to avoid effects of local heating or sample degradation.

### 3.2.6 Femtosecond Transient Mid-IR Absorption Spectroscopy

Femtosecond transient mid-IR absorption spectroscopy was performed using a commercial Ti:sapphire oscillator/amplifier (Solstice 3.5W, Spectra-Physics) to pump two optical parametric amplifiers (TOPAS-C, Light Conversion), one which provided a 100 fs, 2  $\mu$ J excitation pulse at 705 or 605 nm and the other which provided 100 fs probe pulses from 2150–1800  $\text{cm}^{-1}$ . The overall instrument response was 0.3 ps. The spectra were acquired with a liquid N<sub>2</sub>-cooled dual channel (2 x 64) MCT array detector that is coupled to a Horiba iHR320 monochromator as part of a Helios-IR spectrometer (Ultrafast Systems, LLC) with a 300 l/mm grating (3  $\text{cm}^{-1}$  resolution). Samples were prepared in DMF contained in a liquid demountable cell (Harrick Scientific) with CaF<sub>2</sub> windows and a 500  $\mu$ m or 630  $\mu$ m Teflon spacer. The sample cell was mounted on a motorized stage and rastered during acquisition to reduce sample degradation.

### 3.2.7 Kinetic Fitting

Singular Value Decomposition (SVD) analysis of transient absorption spectra was performed in MATLAB<sup>121</sup> using home written programs. The 2-dimensional spectra was deconvoluted by SVD to produce an orthonormal set of basis spectra which describe the wavelength dependence of the species and a corresponding set of orthogonal vectors which describes the time

dependent amplitude of the basis spectra.<sup>114</sup> For most complexes, a species associated first order kinetic model<sup>122</sup> was fit to a linear combination of the time dependent amplitude vectors and the same linear combination of basis spectra was used to construct the spectra for the chemical species. Species-associated spectra were obtained from that fit using a home-written program that has been described previously.<sup>123</sup> Briefly, the kinetic analysis is based a global fit to selected single-wavelength kinetics. Several kinetic traces at different wavelengths were chosen and fitted globally to a kinetic model. The MATLAB program solves the differential equations, then convolutes them with the instrument response function, before employing a least-squares fitting to find the parameters which result in matches to the same functions for all selected wavelengths. Once these parameters are established, they are fed directly into the differential equations, which were solved for the populations of the states in the model. Finally, the raw data matrix (with all the raw data) is deconvoluted with the populations as functions of time to produce the spectra associated with each species.

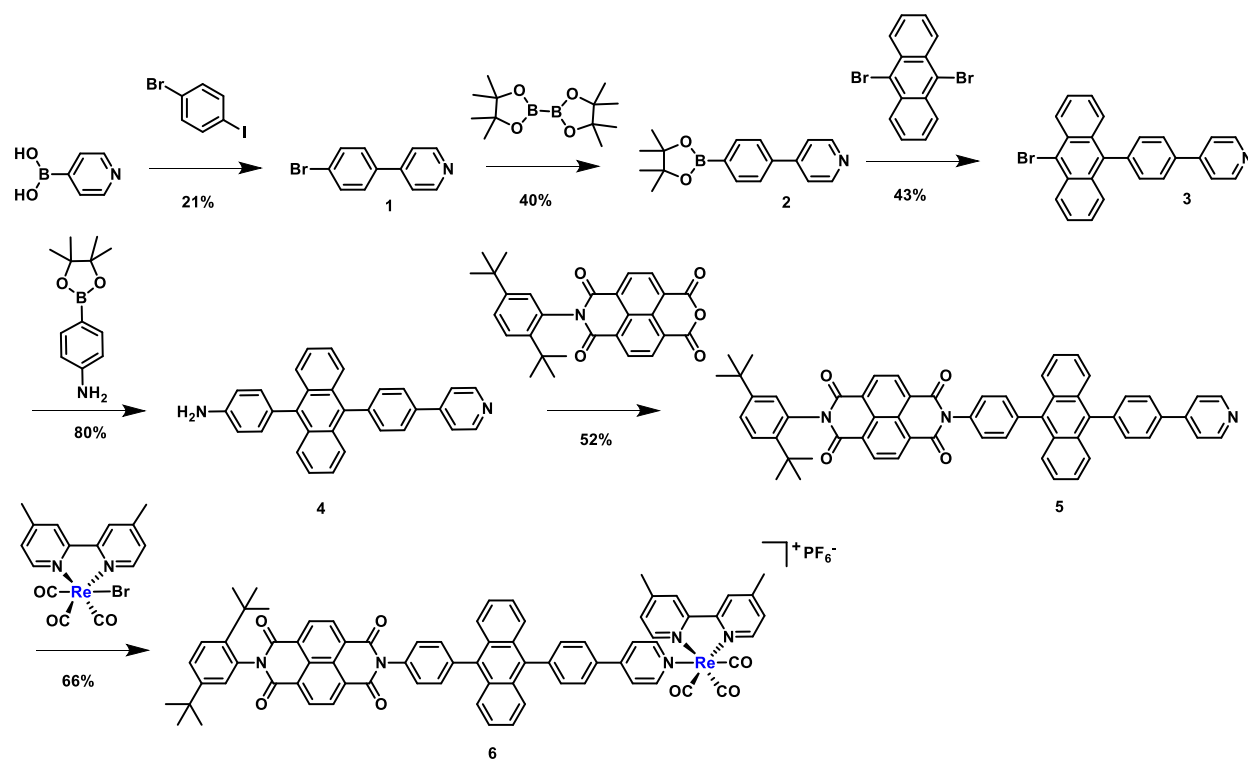
### **3.2.8 Computational Methodology**

Geometries were optimized using density functional theory (DFT) with Q-Chem Version 4.3<sup>83</sup> using the B3P86 functional and LANL2DZ ECP and basis set for Re-containing molecules,<sup>84</sup> and the B3LYP functional and 6-31G\* basis set for purely organic molecules.

## **3.3 Results**

### **3.3.1 Synthesis**

The synthesis of compounds Py-DPA-NDI (**5**) and  $[\text{Re}(\text{dmb})(\text{CO})_3(\text{Py-DPA-NDI})]^+\text{PF}_6^-$  (**6**) are illustrated in Scheme 3.1 and detailed in the section 3.7.  $\text{Re}(\text{dmb})(\text{CO})_3\text{Br}$  was prepared as previously reported.<sup>102</sup> All syntheses were carried out under an atmosphere of  $\text{N}_2$ . The full Py-DPA-NDI ligand (**5**) was built by first Suzuki coupling 4-pyridine boronic acid with 1-bromo-4-iodobenzene to form **1**, which was then converted into a pinacol boronic ester by standard Miyaura borylation to give **2**. Boronic ester **2** was then Suzuki coupled with 9,10-dibromoanthracene to



**Scheme 3.1:** Synthetic scheme for Py-DPA-NDI (**5**) and  $[\text{Re}(\text{dmb})(\text{CO})_3(\text{Py-DPA-NDI})]^+\text{PF}_6^-$  (**6**).

yield **3**. Compound **3** was then Suzuki coupled to 4-aminophenylboronic acid pinacol ester to form **4**. Condensation of *N*-(2,5-di-*t*-butyl)naphthalene-1,4-dicarboximide-5,8-dicarboxyanhydride<sup>120</sup> with **4** led to the desired ligand **5**. Finally, heating  $\text{Re}(\text{dmb})(\text{CO})_3\text{Br}$  and **5** in the presence of  $\text{AgPF}_6$  gave complex **6**. It is noted that employment of this stepwise procedure of building the ligand from

the pyridine backbone allows for easier purification with minimal need of column chromatography.

### 3.3.2 Electrochemistry

Cyclic voltammetry experiments were performed on **5** and **6** in order to determine the reduction potentials of each compound and the free energy changes for sequential electron transfer. Cyclic voltammograms of ligand **5** and complex **6** are shown in Figure 3.1. Redox potentials for

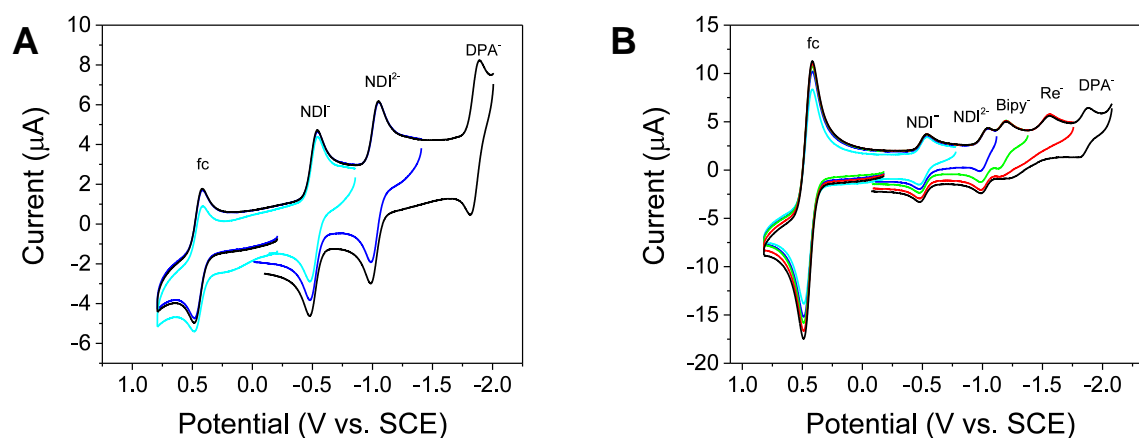


**Figure 3.1:** Cyclic voltammograms of 0.5 mM DMF solutions of (A) **5** and (B) **6**, recorded at  $100 \text{ mV s}^{-1}$  at room temperature with 0.1 M TBAPF<sub>6</sub> as supporting electrolyte. Potentials are reported versus SCE (Fc/Fc<sup>+</sup> occurs at 0.45 V vs SCE).

each complex are shown in Table 3.1.

**Table 3.1:** Redox potentials (vs. SCE using a Fc/Fc<sup>+</sup> reference at 0.45 V vs SCE).

	NDI <sup>0/-</sup>	NDI <sup>-2-</sup>	dmb <sup>0/-</sup>	Re <sup>1/0</sup>	anth <sup>0/-</sup>
Ligand <b>5</b>	-0.51	-1.02	-	-	-1.86
Complex <b>6</b>	-0.51	-1.02	-1.16	-1.56	-1.86

Compound **5** displays three, well-separated, reversible reduction processes. Initial reduction of **5** leads to the first and second reduction of the NDI component of the ligand at  $-0.51$  V and  $-1.02$  V, respectively. This is in good agreement with previous work that integrates NDI and Re complexes.<sup>120</sup> The third reduction at  $-1.86$  V corresponds to the reduction of the DPA component of the ligand.<sup>124</sup>

Compound **6** displays five different, well-separated reduction processes. Initial reduction of **6** begins similarly as with the free ligand, with the first and second reduction of the NDI portion of the complex occurring again at  $-0.51$  V and  $-1.02$  V, respectively. These reductions are followed by the one electron quasi-reversible reduction of the bipyridine ligand at  $-1.16$  V, and a subsequent one electron irreversible reduction of the rhenium center,  $-1.56$  V. These potentials and their degree of reversibility match previous reported findings.<sup>102</sup> The final reduction at  $-1.86$  V corresponds to the reduction of DPA, as was seen in the free ligand. The electrochemical data shown in Table 3.1 reveal that the attachment of the **5** ligand to the Re center has a negligible effect on the reduction potentials of the ligand, indicating that the electronic communication between **5** and the  $\text{Re(dmb)(CO)}_3$  complex is relatively weak.

### 3.3.3 Steady-State Spectroscopy

The normalized steady-state electronic absorption spectra of **5** and **6** are shown in Figure 3.2. The NDI absorptions dominate the spectrum of the unreduced compounds, with peaks at 381 nm and 360 nm and a shoulder at 345 nm. These absorptions overlap strongly with those of DPA, which cannot easily be distinguished from those of NDI in the spectra. In complex **6**, the  $\text{Re(dmb)(CO)}_3$  MLCT absorption band is broad and underlies the absorptions due to DPA and NDI in the region below 400 nm. When equimolar TDAE is added to each compound, their spectra

change dramatically, with the  $\text{NDI}^{\bullet-}$  absorptions appearing at 471 nm, 605 nm, 700 nm, and 785

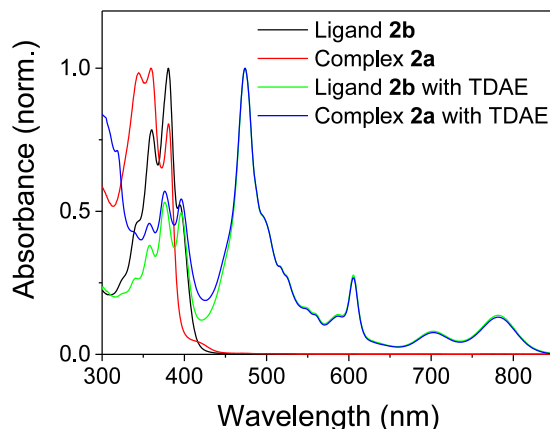


**Figure 3.2:** Electronic absorption spectra of ligand **5** and complex **6** in DMF with and without the TDAE reductant added.

nm, while the DPA absorptions become visible at 396 nm, 376 nm, 357 nm, and 340 nm. Once again, in complex **6** the  $\text{Re}(\text{dmb})(\text{CO})_3$  MLCT band underlies the absorptions below 400 nm.

### 3.3.4 Transient Absorption Spectroscopy

To probe the intramolecular electron transfer behavior of ligand **5** and complex **6**, transient absorption spectroscopy in the visible/NIR and mid-IR regions was performed. The fsTA spectra, the species-associated spectra for each decay component, and the multiple-wavelength kinetics and fits are shown in Figure 3.3. Excitation of  $\text{NDI}^{\bullet-}$  in ligand **5** at 700 nm results in instantaneous bleaching of the ground-state absorptions of  $\text{NDI}^{\bullet-}$  at 471 nm, 700 nm, and 785 nm, the appearance of a broad absorption spanning the region 600-780 nm, and a negative feature due to stimulated emission at 925 nm. These features match the transient spectrum of  $\text{NDI}^{\bullet-}$  itself. Fitting of the visible/NIR TA data at wavelengths corresponding to the bleach, induced absorption, and stimulated emission features gives an  $\text{NDI}^{\bullet-}$  state lifetime of  $\tau = 27.3 \pm 0.6$  ps.

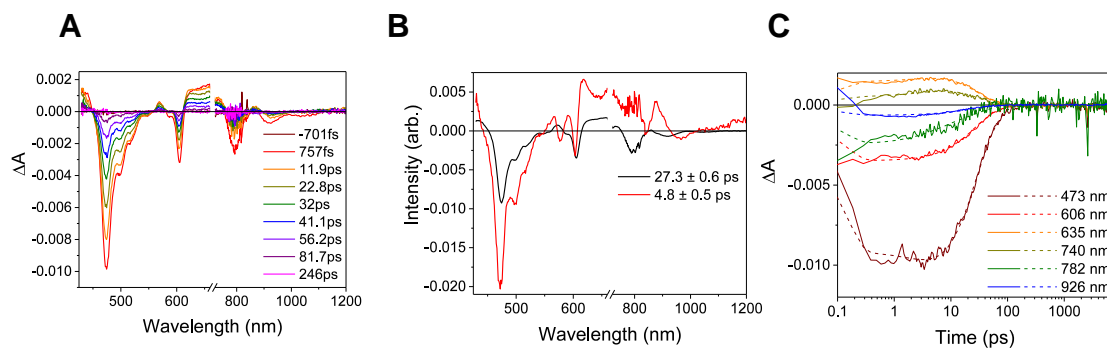


**Figure 3.3:** Transient absorption data for ligand **5** in DMF ( $\lambda_{\text{ex}} = 700$  nm). (A) Transient absorption spectra; (B) Species-associated spectra; (C) multiple-wavelength kinetic traces and fits.

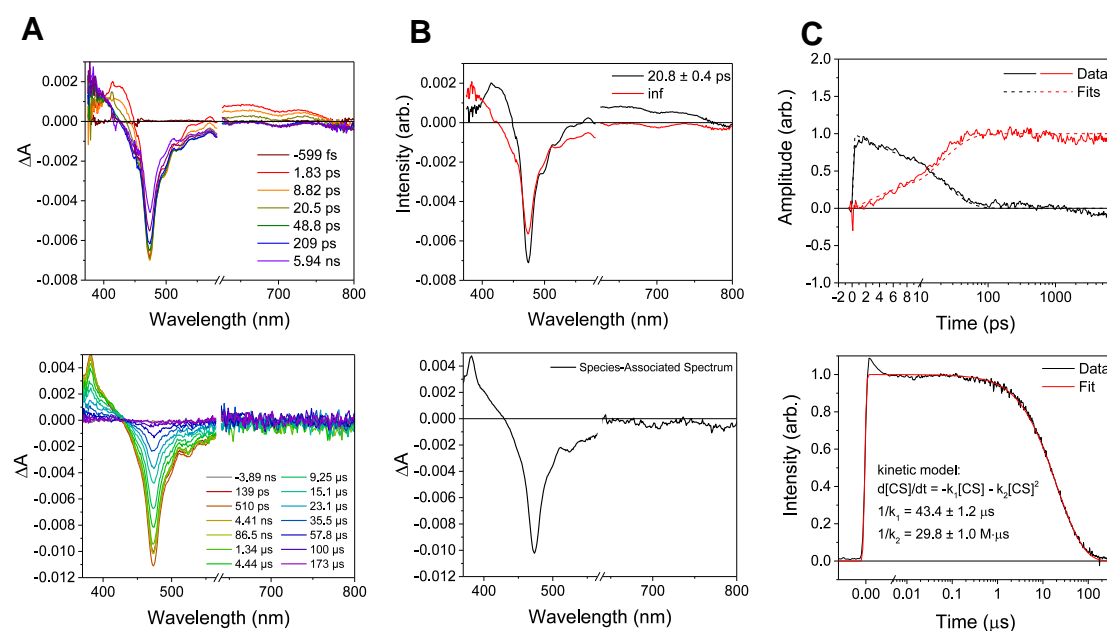


**Figure 3.4:** Transient absorption spectra for complex **6** in DMF ( $\lambda_{\text{ex}} = 605$  nm). (A) Transient absorption spectra. (B) Species-associated spectra. (C) Singular value decomposition kinetic traces and fits to the kinetic data based on the species-associated fits and lifetimes shown.

The  $\text{NDI}^*$  features appear to decay back to the ground state, however a better fit to the kinetic data is obtained by adding an intermediate component with a  $\tau = 4.7 \pm 0.5$  ps lifetime. The species-associated spectrum of this component contains the same ground state bleach features as

the initial component but lacks the stimulated emission features and has strong induced absorption features in the range 600-900 nm. Absorption in this region is characteristic of  $\text{DPA}^{-\bullet}$ ,<sup>125</sup> indicating that the  $^*\text{NDI}^{\bullet}$  state is quenched by electron transfer to the appended DPA moiety, which rapidly undergoes back electron transfer to regenerate the ground state. Excitation of complex **6** at 605 nm results in initial appearance of the same bleaches, induced absorptions, and stimulated emission features observed for ligand **5**.<sup>126</sup> The transient absorption spectra, species-associated spectra for each decay component, and kinetic data with fits are shown in Figure 3.4. Fitting of the visible/NIR TA data using singular value decomposition gives an  $\text{NDI}^{\bullet}$  lifetime of  $\tau = 20.8 \pm 0.4$  ps. As the  $\text{NDI}^{\bullet}$  features decay, an induced absorption at 382 nm appears with the same time constant. This absorption corresponds to the absorption of  $\text{NDI}^0$ , the product of oxidative quenching of  $\text{NDI}^{\bullet}$ . That feature and the  $\text{NDI}^{\bullet}$  bleach decay via a combination of first- and second-order kinetics with lifetimes of  $43.4 \pm 1.2$   $\mu\text{s}$  and  $29.8 \pm 1$   $\text{M}\cdot\mu\text{s}$ , respectively (details of the kinetic model used to fit the data will be discussed below). It was not possible to fit an intermediate component corresponding to the  $\text{NDI}^0\text{-DPA}^{\bullet}\text{-Re}^{\text{I}}(\text{dmb})(\text{CO})_3$  state, indicating that that this intermediate is very short-lived.

### 3.3.5 Transient mid-IR Spectroscopy

Complex **6** was also probed in the mid-IR region, where the frequencies of the CO stretches in the range 1850-2100  $\text{cm}^{-1}$  give a reliable indication of the ligand and electronic environment of the metal center.<sup>64, 102, 104, 127-128</sup> Femtosecond transient mid-IR (fsIR) spectra and kinetic traces at selected energies are shown below in Figure 3.5. The ground-state absorptions at 1928  $\text{cm}^{-1}$  and 2046  $\text{cm}^{-1}$  bleach with a  $\tau = 14.8 \pm 0.2$  ps time constant and remain bleached for the entirety of the 8 ns experimental window. Induced absorptions appear at 1885  $\text{cm}^{-1}$  and 2020  $\text{cm}^{-1}$  with the

same kinetics, which are shifted to lower energy by 43 and 26  $\text{cm}^{-1}$ , respectively, relative to the

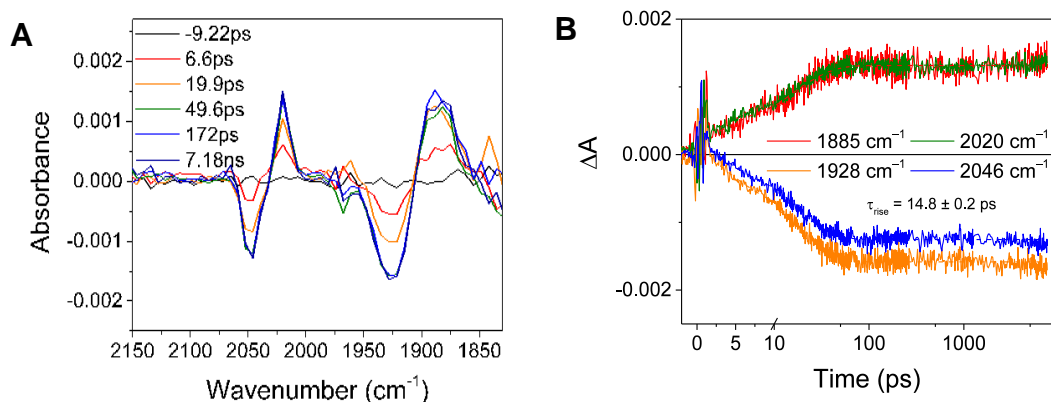


**Figure 3.5:** (A) Time-resolved IR spectra and (B) global multiple-wavelength kinetic traces and fits for complex **6** in DMF ( $\lambda_{\text{ex}} = 605$  nm).

ground state bleaches. This shift has been previously observed by our group and many others in photo- and electrochemical experiments in which  $\text{Re}(\text{dmb})(\text{CO})_3\text{L}$  complexes are reduced by one electron to form  $\text{Re}(\text{dmb}^{\bullet-})(\text{CO})_3\text{L}$ .<sup>43, 105-107, 120</sup>

### 3.4 Discussion

#### 3.4.1 Design of the Triad System

Complex **6** was designed with modular synthesis in mind, allowing for relatively easy modification of chromophore, primary acceptor, and metal center. As a consequence, ligand **5**, which serves as the source of high energy photochemical reducing equivalents can be easily attached to any metal center that accepts a pyridyl ligand, examples of which are numerous in the literature.

The individual components comprising triad **6** were chosen for the following reasons. It has been shown that visible light excitation of  $\text{NDI}^{\bullet-}$  gives its excited doublet state that is a powerful reductant,<sup>45, 74</sup> and it has been shown to effectively reduce  $\text{Re}(\text{bpy})(\text{CO})_3\text{X}$  complexes.<sup>120</sup> Catalysts having this architecture have been shown to reduce carbon dioxide at potentials that are

lower than the reduction potential of DPA.<sup>102</sup> This allows for exergonic electron transfer to occur in the sequence  ${}^*NDI^{\bullet} \rightarrow DPA \rightarrow \text{Re catalyst}$ , with the reverse process  $\text{Re catalyst} \rightarrow DPA$  being strongly endergonic, ultimately facilitating formation of a long-lived reduced state on the catalyst. Additionally,  $\text{Re(dmb)(CO)}_3$  and DPA are reduced at potentials more negative than those of NDI. This way NDI can be selectively reduced using TDAE ( $E_{1/2} = -0.6 \text{ V vs SCE}$ ) to  ${}^*NDI^{\bullet}$  without reducing any other components in the complex. The choices of NDI, DPA, and  $\text{Re(dmb)}$  not only have favorable reduction potentials as mentioned, but have distinct spectroscopic tags in the visible, near-IR, and mid-IR regions that allow for the entire electron transfer process to be monitored.

### 3.4.2 Electron Transfer Energetics

Based on the redox potentials shown above, the Gibbs free energy for the excited-state electron transfer reactions of ligand **5** can be estimated using the following equation:

$$\Delta G_{ET} = (E_{ox} - E_{red}) - E_{00}$$

where  $E_{ox}$  and  $E_{red}$  are the oxidation and reduction potentials of the donor and acceptor respectively, and  $E_{00}$  is the energy of the  ${}^*RDI^{n-}$  excited state. There is no electrostatic work term for this reaction because the reaction is a charge shift, not a charge separation.

The Gibbs free energy for the excited-state electron transfer reaction of complex **6** can be estimated using the following equation, which accounts for the electrostatic work term associated with bringing a negative charge closer to the positively charged Re center:

$$\Delta G_{ET} = (E_{ox} - E_{red}) - E_{00} + \frac{e^2}{r_{DPA,Re}\epsilon_s} - \frac{e^2}{r_{NDI,Re}\epsilon_s}$$

where  $E_{ox}$  and  $E_{red}$  are the oxidation and reduction potentials of the donor and acceptor respectively,  $E_{00}$  is the energy of the  ${}^*NDI^{n-}$  excited state<sup>45</sup>,  $e$  is the elementary charge,  $r_{anth,Re}$  and

$r_{\text{NDI,dmb}}$  are the DPA-Re and NDI-Re distances (calculated from centroid to centroid using DFT-optimized geometries), and  $\epsilon_s$  is the solvent dielectric constant.

The Gibbs free energy for the thermal forward and back electron transfer reactions can be estimated using the following equation, which accounts for the change in distance between the negative charge and the positively charged Re center:

$$\Delta G_{ET} = (E_{ox} - E_{red}) + \frac{e^2}{r_{A,Re}\epsilon_s} - \frac{e^2}{r_{D,Re}\epsilon_s}$$

where  $r_{A,Re}$  and  $r_{D,Re}$  are the donor-Re and acceptor-Re distances (calculated from centroid to centroid using DFT-optimized geometries) and all other constants are identical to those in the previous equation. Donor-acceptor distances calculated from optimized structures are shown in Table 3.2 below. From the equations above, the Gibbs free energies for each electron transfer step are shown in Table 3.3 below.

**Table 3.2:** Donor-acceptor distances in complex **2** calculated from the DFT-optimized geometries.

Moiety	distance to Re (Å)
NDI	23.0
anthracene	12.3
dmb	2.8

**Table 3.3:** Driving force for electron transfer reactions in ligand **5** and complex **6**.

compound	process	$\Delta G$ (eV)
<b>5</b>	$\text{NDI}^{*\bullet} \rightarrow \text{DPA}$	-0.26
<b>5</b>	$\text{DPA}^{\bullet-} \rightarrow \text{NDI}^0$	-1.34
<b>6</b>	$\text{NDI}^{*\bullet} \rightarrow \text{DPA}$	-0.27
<b>6</b>	$\text{DPA}^{\bullet-} \rightarrow \text{dmb}$	-0.76
<b>6</b>	$\text{DPA}^{\bullet-} \rightarrow \text{NDI}^0$	-1.33
<b>6</b>	$\text{dmb}^{\bullet-} \rightarrow \text{NDI}^0$	-0.57

### 3.4.3 Electron Transfer within Ligand **5** and Complex **6**

The forward and back electron transfer reactions in ligand **5** are intramolecular processes, and fit to a straightforward model in which the  $\text{NDI}^{*\bullet}$  excited state transfers an electron to DPA followed by decay of  $\text{DPA}^{\bullet-}$  back to ground state. Because the decay of  $\text{NDI}^0\text{-DPA}^{\bullet-}$  ( $\tau_{\text{ET}} = 4.8$  ps) is faster than its growth ( $\tau_{\text{ET}} = 27.3$  ps), spectral signatures of  $\text{DPA}^{\bullet-}$  are not readily visible in the raw transient absorption data. However, fitting the data to the proposed model results in the two species-associated spectra in Figure 3.3, which both exhibit negative features corresponding to bleaches of the ground state at 471 nm, 700 nm, and 785 nm, and the first species-associated spectrum contains features of the  $^*\text{NDI}^{\bullet}$  excited state as indicated by absorptions spanning 600-780 nm, and stimulated emission at 925 nm, while the second species-associated spectrum displays features attributable to  $\text{DPA}^{\bullet-}$  as indicated by the absorptions in the range 600-900 nm. The quantum yield of electron transfer to the DPA acceptor can be estimated by comparing the intrinsic  $^*\text{NDI}^{\bullet}$  excited state lifetime ( $\tau = 141$  ps for NDI bearing two aryl substituents) with its lifetime in **5**, which gives an 81% quantum yield.

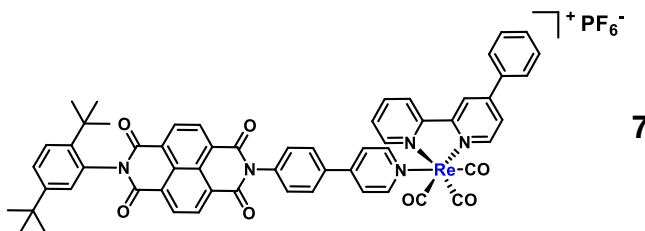
When ligand **5** is attached to a  $\text{Re}(\text{dmb})(\text{CO})_3$  center through its pyridine nitrogen atom, the electron transfer behavior changes dramatically, as shown in Figure 3.4. The decay of the  $^*\text{NDI}^-$  features is still rapid ( $\tau = 20.8$  ps), but again no features attributable to  $\text{DPA}^-$  can be detected. The slight decrease in quenching time constant is likely due to the presence of the positively charged Re center, which increases  $\Delta G$  by approximately 0.015 eV. No recovery of the ground state features is observed on the picosecond timescale, indicating that back electron transfer from  $\text{DPA}^-$  to  $\text{NDI}^0$  is not kinetically competitive with forward electron transfer from  $\text{DPA}^-$  to dmb. Since the presence of a charged Re center does not have a strong effect on the  $^*\text{NDI}^- \rightarrow \text{DPA}$  electron transfer rate, it is not expected to affect the  $\text{DPA}^-$  to  $\text{NDI}^0$  back electron transfer rate significantly either. Since the time constant for the reaction  $\text{DPA}^-$  to  $\text{NDI}^0$  in ligand **5** is observed to be  $\tau = 4.8$  ps, the  $\text{DPA}^- \rightarrow \text{dmb}$  electron transfer time constant must be much shorter, although, at present, we are not able to determine it.

The final charge-shifted state, as evidenced by the  $\text{NDI}^-$  ground state bleaches and  $\text{NDI}^0$  induced absorptions in the visible, and ground state bleaches and  $\text{Re}(\text{dmb}^+)(\text{CO})_3\text{L}$  induced absorptions in the mid-IR, persists into the microsecond time regime. The lifetime of the final charge-shifted state is long enough that intermolecular interactions, in which the  $\text{NDI}^0$  of one molecule is reduced by the  $\text{Re}(\text{dmb}^+)(\text{CO})_3$  moiety on a second molecule, are kinetically competitive with intramolecular back electron transfer. In order to correctly fit the kinetic data, a singular-value decomposition of the kinetic data was performed and fit to the following kinetic expression:

$$\frac{d[\text{CT}]}{dt} = -\left(\frac{1}{\tau_{\text{BET}2}} [\text{CS}] + \frac{1}{\tau_{\text{IM}}} [\text{CS}]^2\right) \quad (1)$$

where  $[CS]$  represents the concentration of the charge-shifted state,  $\tau_{\text{BET2}}$  represents the intramolecular back electron transfer lifetime, and  $\tau_{\text{IM}}$  represents the intermolecular electron transfer rate. Fitting the data to this expression results in the fit shown in Figure 3.4 (bottom right), with an intramolecular back electron transfer lifetime  $\tau_{\text{BET2}} = 43.3 \mu\text{s}$ .

This lifetime represents an increase of three orders of magnitude over the similar complex **7** previously investigated in our lab.<sup>120</sup> Complex **7** has a much shorter NDI-dmb distance (23.2 Å in complex **6** vs 14.5 Å in complex **7**) and lacks the intermediate DPA acceptor found in complex



**6**. Both the distance and the presence or absence of an intermediate acceptor play an important role in electron transfer kinetics. The forward electron transfer time constant increases from  $\tau = 1.5 \text{ ps}$  in complex **7** to  $\tau = 20.8 \text{ ps}$  in complex **6**, an approximate 30-fold increase. This increase is most likely attributable to the decreased free energy change for the excited state quenching reaction in complex **6**, for which  $\Delta G$  is only  $-0.27 \text{ eV}$ , compared to  $-1.11 \text{ eV}$  for complex **7**.

The increase in back electron transfer time constant from  $\tau = 29.7 \text{ ns}$  in complex **7** to  $\tau = 43.3 \mu\text{s}$  in complex **6** is a consequence of decreased electronic coupling as the donor-acceptor distance increases. Because the intermediate back electron transfer reaction  $\text{Re}(\text{dmb}^{\bullet-})(\text{CO})_3 \rightarrow \text{DPA}$  is an endergonic reaction, there is no intermediate acceptor for the back electron transfer reaction  $\text{Re}(\text{dmb}^{\bullet-})(\text{CO})_3 \rightarrow \text{NDI}^0$ . As a consequence, although the free energy change for the back electron transfer is similar in complexes **6** and **7**, the distance and therefore the lifetime of the  $\text{dmb}^{\bullet-}$  is much longer for complex **6**. An energy-level diagram for complex **6** is shown in Figure 3.6 (free energy changes for each reaction are shown in Table 3.3 above).

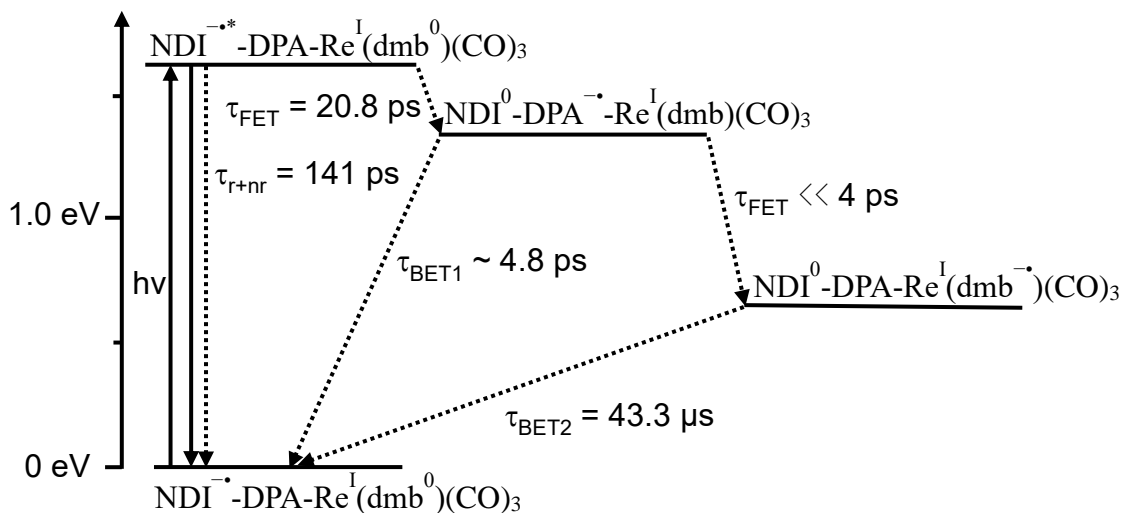


**Figure 3.6:** Energy-level diagram for complex **6**. Energies are obtained from Table 3.3.

### 3.5 Conclusions

In this report, we have described a complex consisting of a reduced NDI chromophore, a DPA primary electron acceptor, and  $\text{Re}(\text{dmb})(\text{CO})_3$  terminal electron acceptor. Upon excitation of the  $\text{NDI}^{\bullet-}$  chromophore, the terminal acceptor is reduced with a time constant of approximately 20 ps to the  $\text{Re}(\text{dmb}^{\bullet-})(\text{CO})_3$  state, the first step in activating that metal complex towards binding and reducing  $\text{CO}_2$ . The redox potential of the intermediate acceptor allows for rapid forward electron transfer to the metal center, but interposes a large barrier for back electron transfer, leading to a charge-shifted state that persists with a lifetime of more than 43  $\mu\text{s}$ .

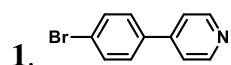
Because the  $\text{NDI}^{\bullet-}$ -DPA moiety comprises one ligand in the complex, we propose that it is immediately applicable to other metal complexes that require highly reducing electrons to be delivered photochemically. Moreover, the architectural motif of  $\text{NDI}^{\bullet-}$ -DPA as a chromophore and primary acceptor can be generalized to other donor-acceptor systems to allow for the production of long-lived, highly reduced states appropriate for a variety of difficult catalytic transformations.

For example, attachment of two such ligands to complexes requiring two electrons to carry out catalytic transformations, such as CO<sub>2</sub> to CO using Re(bpy)(CO)<sub>3</sub>, should allow the catalytic CO<sub>2</sub> reduction mechanism to be examined one step at a time with excellent time resolution to observe all relevant intermediates.

### 3.6 Acknowledgements

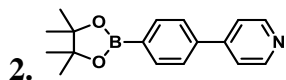
We thank Dr. Matthew D. Krzyaniak for assistance with fitting the kinetic data and Drs. Saman Shafaie and S. Habibi Goudarzi for collecting high-resolution mass spectrometric data. Dr. Yilei Wu synthesized *N,N*-dicyclohexyl-NDI, data for which are shown in the ESI. This work was supported by the Argonne-Northwestern Solar Energy Research (ANSER) Center, an Energy Frontier Research Center funded by the U.S. Department of Energy (DOE), Office of Science, Office of Basic Energy Sciences, under award number DE-SC0001059. C.M.M. was supported by a NSF Graduate Research Fellowship under grant no. DGE-1324585.

### 3.7 Synthetic Details

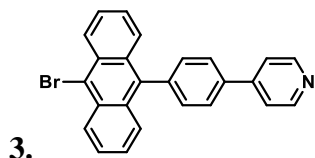


2.0 g (16.39 mmol) 4-pyridinylboronic acid, 6.94 g (24.59 mmol) 1-Bromo-4-iodobenzene, and 13.9 g (131.12 mmol) Na<sub>2</sub>CO<sub>3</sub> were combined in 300 mL THF and 100 mL DI H<sub>2</sub>O in a 500 mL two-necked roundbottom flask and sparged 30 minutes with N<sub>2</sub>. 0.9 g (0.8 mmol) Pd(PPh<sub>3</sub>)<sub>4</sub> was added under flow of N<sub>2</sub> and the solution sparged for an additional ten minutes, then refluxed overnight. The flask was cooled to room temperature, and the solvents were removed under reduced pressure. The remaining solid was suspended in 300 mL of DCM and poured over a silica plug. The product was then eluted using ethyl acetate. The solvent was evaporated under vacuum

to yield pure product. Yield: 0.86 g (22%).  $^1\text{H NMR}$  (500 MHz, Chloroform-*d*)  $\delta$  8.70 – 8.61 (m, 2H), 7.66 – 7.59 (m, 2H), 7.54 – 7.42 (m, 4H).

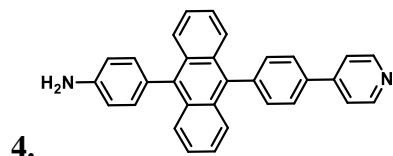


3.2 g (13.5 mmol) **1** and 4.3 g (16.9 mmol) bispinacolatoboron ( $\text{B}_2\text{pin}_2$ ) were combined with 4.0 g potassium acetate and 0.5 g (0.7 mmol)  $\text{Pd}(\text{dppf})\text{Cl}_2$  in a 500 mL two-neck round bottom flask fitted with a condenser. 300 mL dry dioxane was added into the flask and sparged 30 minutes with  $\text{N}_2$ . The solution was stirred at 100 °C overnight. The flask was cooled to RT and the solvent was under reduced pressure. The contents were suspended in 300 mL of DCM and pour over a silica plug. The product was eluted using ethyl acetate. The solvent was evaporated under reduced pressure and then sonicated in minimal pentane and gravity filtered. The solid was washed with cold pentane to yield pure product. Yield: 1.54 g (40%).  $^1\text{H NMR}$  (500 MHz, Chloroform-*d*)  $\delta$  8.69 – 8.64 (m, 2H), 7.95 – 7.90 (m, 2H), 7.67 – 7.62 (m, 2H), 7.55 – 7.50 (m, 2H), 1.37 (s, 12H).

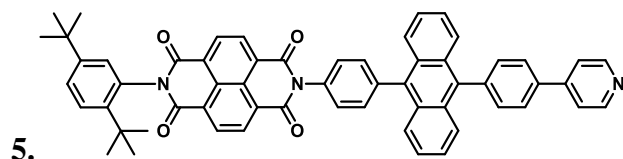


1.3 g (4.6 mmol) **2**, 15.54 g (46.0 mmol) 9,10-dibromoanthracene, and 3.9 g (37.0 mmol)  $\text{Na}_2\text{CO}_3$  were combined in 500 mL THF and 150 mL DI  $\text{H}_2\text{O}$  in a 1 L two-necked roundbottom flask and sparged 30 minutes with  $\text{N}_2$ . 0.3 g (0.23 mmol)  $\text{Pd}(\text{PPh}_3)_4$  was added under flow of  $\text{N}_2$  and the solution sparged for an additional ten minutes, then refluxed overnight. The flask was cooled to room temperature, and the solvents were removed under reduced pressure. The contents were suspended in 300 mL of DCM, poured over a silica plug and washed with DCM until the excess

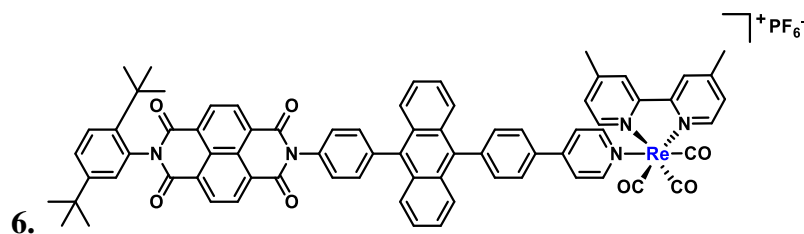
9,10-dibromoanthracene had been removed. Ethyl acetate was used to elute the product. The solvent was evaporated under reduced pressure and then sonicated in minimal DCM and gravity filtered. The product was washed with copious amounts of cold methanol to afford the pure product. Yield 0.8 g (43%).  $^1\text{H NMR}$  (500 MHz, Chloroform-*d*)  $\delta$  8.78 – 8.71 (m, 2H), 8.64 (d,  $J$  = 8.9 Hz, 2H), 7.91 – 7.85 (m, 2H), 7.72 – 7.65 (m, 4H), 7.65 – 7.58 (m, 2H), 7.58 – 7.52 (m, 2H), 7.43 – 7.39 (m, 2H).



0.8 g (2.0 mmol) **3**, 0.9 g (3.9 mmol) to 4-Aminophenylboronic acid pinacol ester, and 2.2 g (15.6 mmol)  $\text{Na}_2\text{CO}_3$  were combined in 500 mL THF and 150 mL DI  $\text{H}_2\text{O}$  in a 1 L two-necked roundbottom flask and sparged 30 minutes with  $\text{N}_2$ . 0.12 g (0.10 mmol)  $\text{Pd}(\text{PPh}_3)_4$  was added under flow of  $\text{N}_2$  and the solution sparged for an additional ten minutes, then refluxed overnight. The flask was cooled to room temperature, and the solvents were removed under reduced pressure. The contents were suspended in 300 mL of DCM and pour over a silica plug. The product was eluted using ethyl acetate. Ethyl acetate was removed under reduced pressure. The solid was then sonicated in copious amounts of MeOH and then gravity filtered. The solid remaining was then sonicated in minimal DCM and copious amounts of MeCN and then gravity filtered and collected. Yield 0.68 g (80%).  $^1\text{H NMR}$  (500 MHz, Chloroform-*d*)  $\delta$  8.77 – 8.73 (m, 2H), 7.93 – 7.88 (m, 2H), 7.86 – 7.82 (m, 2H), 7.73 – 7.68 (m, 4H), 7.63 – 7.59 (m, 2H), 7.37 – 7.33 (m, 4H), 7.28 – 7.26 (m, 2H), 6.95 – 6.92 (m, 2H), 3.87 (bs, 2H).



In an oven dried round bottom flask with a magnetic stirrer and reflux condenser, **4** (0.16 g, 0.427 mmol) and DtB-NIA (0.24 g, 0.53 mmol)<sup>129</sup> were dissolved in pyridine (50mL) and heated to 120 °C under N<sub>2</sub> overnight. The solution was cooled to room temperature and pyridine was removed in vacuo. The gooey residue was sonicated in ethanol until a solid precipitated, gravity filtered and collected. The solid was then dissolved in DCM and poured over silica plug. The product was eluted with ethyl acetate. The solvent was evaporated under reduced pressure and then sonicated in MeOH and filtered to afford the pure product. Yield 0.19 g (52%). **<sup>1</sup>H NMR** (500 MHz, Chloroform-*d*) δ 8.96 – 8.91 (m, 4H), 8.77 – 8.75 (m, 2H), 7.94 – 7.90 (m, 2H), 7.87 – 7.84 (m, 2H), 7.78 – 7.69 (m, 6H), 7.67 – 7.59 (m, 5H), 7.51 (dd, *J* = 8.6, 2.2 Hz, 1H), 7.46 – 7.39 (m, 4H), 7.05 (d, *J* = 2.1 Hz, 1H), 1.35 (s, 9H), 1.30 (s, 9H). **<sup>13</sup>C NMR** (126 MHz, CDCl<sub>3</sub>) δ 163.95, 163.37, 150.58, 148.18, 143.83, 140.25, 140.13, 137.46, 136.71, 136.33, 134.12, 132.59, 132.31, 132.11, 131.75, 131.72, 130.02, 129.95, 129.21, 128.83, 127.68, 127.58, 127.53, 127.49, 127.25, 127.21, 126.91, 126.76, 125.62, 125.56, 121.81, 100.13, 77.41, 77.16, 76.91, 35.75, 34.47, 31.91, 31.37, 26.15 **HRMS-ESI** (*m/z*): calculated C<sub>59</sub>H<sub>45</sub>N<sub>3</sub>O<sub>4</sub> [M+H]<sup>+</sup>: 860.3489, found 860.3493



In a nitrogen filled glove box, an oven dried pressure flask with a magnetic stirrer was filled with  $\text{Re(dmb)(CO)}_3\text{Br}$  (14 mg, 0.03 mmol), **5** (25 mg, 0.03 mmol),  $\text{AgPF}_6$  (7.8 mg, 0.04 mmol), and dichloromethane (40 mL). The pressure flask was capped and brought out of the glovebox and heated to  $80^\circ\text{C}$  overnight. The solution was cooled to room temperature and filtered through celite. The solvent was removed under reduced pressure and then sonicated in copious amounts of toluene, gravity filtered and collected. The compound was then sonicated in minimal MeOH, gravity filtered and collected. The compound was then dissolved in minimal dichloromethane and layered with diethyl ether. Upon filtering, a brown solid was obtained. Yield 0.03 g (66%).  $^1\text{H NMR}$  (500 MHz, Methylene Chloride- $d_2$ )  $\delta$  9.02 (d,  $J = 5.8$  Hz, 2H), 8.92 (d,  $J = 7.5$  Hz, 2H), 8.89 (d,  $J = 7.5$  Hz, 2H), 8.29 – 8.21 (m, 4H), 7.85 (dd,  $J = 10.2, 8.0$  Hz, 4H), 7.73 – 7.58 (m, 13H), 7.57 – 7.50 (m, 1H), 7.07 (d,  $J = 7.5$  Hz, 1H), 7.48 – 7.35 (m, 4H), 2.67 (s, 6H), 1.35 (s, 9H), 1.29 (s, 9H).  $^{13}\text{C NMR}$  (126 MHz,  $\text{CDCl}_3$ )  $\delta$  163.96, 163.35, 155.62, 154.93, 151.91, 151.67, 150.58, 143.83, 142.12, 140.06, 136.53, 136.05, 134.56, 134.12, 132.68, 132.56, 132.12, 131.74, 131.71, 129.95, 129.75, 129.47, 129.20, 128.81, 128.39, 128.16, 127.69, 127.57, 127.52, 127.47, 127.43, 127.27, 127.21, 127.18, 126.89, 126.78, 126.65, 125.70, 125.64, 124.65, 102.11, 77.41, 77.16, 76.91, 35.74, 34.46, 31.91, 31.36, 21.95. **HRMS-ESI** ( $m/z$ ): calculated  $\text{C}_{74}\text{H}_{57}\text{N}_5\text{O}_7\text{Re} [\text{M}-\text{PF}_6]^+$ : 1314.3816, found 1314.3865

## **Chapter 4 Electron Transfer from Photoexcited Naphthalene Diimide Radical Anion to Electrocatalytically Active $\text{Re}(\text{bpy})(\text{CO})_3\text{Cl}$ in a Molecular Triad**

Reproduced in part with permission from: Martinez, J. F.; La Porte, N. T.; Wasielewski, M. R., Electron Transfer from Photoexcited Naphthalene Diimide Radical Anion to Electrocatalytically Active  $\text{Re}(\text{bpy})(\text{CO})_3\text{Cl}$  in a Molecular Triad. Copyright: 2018, American Chemical Society.

## 4.1 Introduction

In the past several decades, many research groups have focused a great deal of effort on harnessing solar photons to power chemical reactions for artificial photosynthesis.<sup>27, 130-136</sup> A proven strategy is to synthesize supramolecular assemblies that can absorb light to produce long-lived charge-separated states using multi-step electron transfer processes. Natural photosynthesis provide the primary bio-inspiration for developing the molecular architectures necessary to achieve rapid charge separation as well as slow charge recombination.<sup>136-137</sup> For example, absorption of solar photons by chlorophylls in the photosystem II reaction center protein complex from green plants and cyanobacteria results in oxidation of the P680 special pair chlorophyll dimer, which in turn oxidizes an adjacent tyrosine. This tyrosine functions as a redox intermediate that transfers oxidizing equivalents to the water splitting  $\text{CaMn}_4$  cluster from  $\text{P680}^{\bullet+}$ .<sup>27, 138-139</sup> These naturally occurring processes demonstrate how nature effectively balances light absorption, charge separation, and catalysis, giving chemists a blueprint for developing artificial supramolecular systems, whether it be for water splitting or  $\text{CO}_2$  reduction.

The simplest supramolecular systems for  $\text{CO}_2$  reduction consist of a chromophore appended to a catalyst. The photoreaction is initiated either by reductive or oxidative quenching of the excited chromophore followed by a series of thermal electron transfer steps leading to the final photoproduct.<sup>31, 135, 140</sup> Sacrificial electron donors, such as triethylamine, triethanolamine (TEOA) or reduced nicotinamides, are typically employed either as primary reductive quenchers, or as thermal electron transfer reagents to re-reduce the oxidatively quenched chromophore.<sup>31, 141 27, 31, 140, 142-144</sup> Some of the most extensive studies involving the oxidative quenching mechanism have involved porphyrins and metalloporphyrins sensitizing  $\text{Re}(\text{diimine})(\text{CO})_3$  centers.<sup>43, 142, 145-149</sup> For example, the Perutz group reported the system  $[\text{Re}^{\text{I}}(\text{CO})_3(3\text{-picoline})\text{bpy-MTPP}][\text{OTf}]$ , where M

= Zn or Mg, OTf = trifluoromethanesulfonate, and TPP = tetraphenylporphyrin. Upon exciting the metalloporphyrin, the charge-separated species  $[\text{Re}^{\text{I}}(\text{CO})_3(3\text{-picoline})\text{bpy}^{\bullet-}\text{-MTPP}^{\bullet+}][\text{OTf}]$  is formed in  $\tau = 35\text{-}55$  ps. When triethylamine is present in solution, the back-electron transfer becomes irreversible, likely because the triethylamine is bound to the metalloporphyrin in its ground state and therefore rapidly reductively quenches the excited porphyrin, followed by thermal electron transfer to the rhenium center.<sup>145</sup> However, no  $\text{CO}_2$  reduction studies were reported on this persistent charge-separated species. More recently, it was demonstrated that the charge-separated species generated upon excitation of the Zn porphyrin in the dyad  $[\text{Re}^{\text{I}}(\text{CO})_3(3\text{-picoline})\text{dmb-carboxyamidyl-ZnTPP}][\text{OTf}]$  has a lifetime of 320 ps.<sup>147</sup>  $\text{CO}_2$  reduction studies were conducted with this complex, but no CO was detected without the TEOA sacrificial electron donor. TEOA likely inhibits back electron transfer, but these systems also potentially benefit greatly from a secondary effect of TEOA, in that it displaces the 3-picoline, and promotes  $\text{CO}_2$  insertion,<sup>150</sup> ultimately allowing the complex to undergo the catalytic cycle. In addition, there is significant photoreaction at the porphyrin during catalysis with TEOA, complicating the determination of the photocatalytic mechanism.

The majority of the efficient photocatalytic systems that have been reported for the reduction of  $\text{CO}_2$  in solution proceed via the reductive quenching mechanism because the excited state lifetimes of commonly used chromophoric metal complexes are long enough (on the order of hundreds of nanoseconds or microseconds) to be quenched by a sacrificial electron donor,<sup>140</sup> followed by thermal electron transfer from the reduced chromophore to the catalyst. Reductive quenching of the chromophore by a sacrificial donor shuts off the back electron transfer pathway and ensures that the electron remains on the catalyst until the next step in the catalytic cycle. For

example, Ishitani has developed systems such as  $\text{Ru}^{\text{II}}(\text{dmb})_3\text{-Re}^{\text{I}}(\text{dmb})(\text{CO})_2\text{X}_2$ , in which the Ru-based chromophore and Re-based catalysts are separated by an alkyl chain. This system is capable of producing charge-separated species, and reducing  $\text{CO}_2$  to  $\text{CO}$ .<sup>31, 53, 151-154</sup> The role of the sacrificial donor in enabling catalysis is underscored by the large variation in turnover number

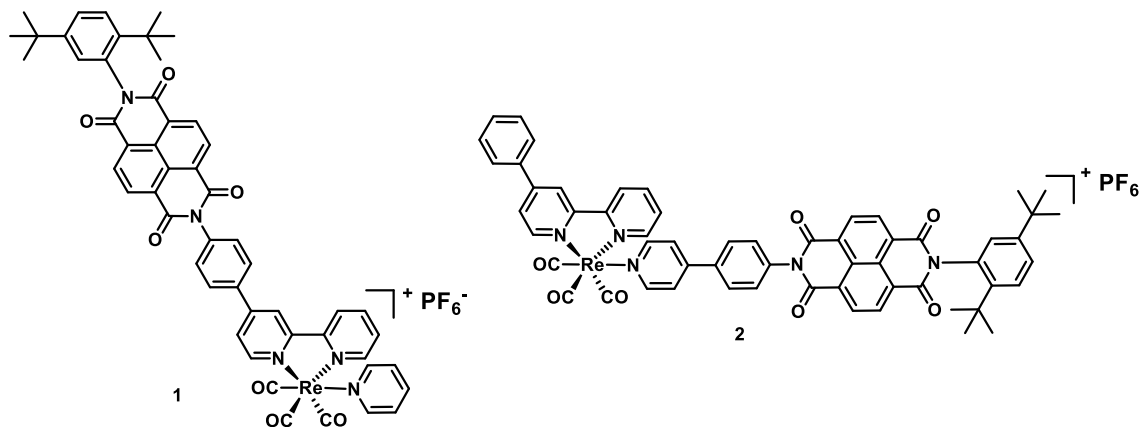


**Figure 4.1.**  $[\text{Re}(\text{bpy}\text{-NDI})(\text{CO})_3]^+ \text{PF}_6^-$  (**1**) and  $[\text{Re}(\text{bpy})(\text{CO})_3(\text{Py}\text{-}$

(TON) of  $\text{CO}$  produced by these compounds simply by changing sacrificial electron donors.<sup>53, 152</sup>

We have recently investigated the systems shown in Figure 4.1, where a naphthalenediimide radical anion (NDI) donor chromophore is appended covalently to  $\text{Re}(\text{bpy})(\text{CO})_3$  through either the bpy ligand (**1**) or more directly to the Re center via a pyridine ligand (**2**).<sup>155</sup> The NDI fragment is subsequently reduced either chemically or electrochemically to the radical anion  $\text{NDI}^{\cdot-}$ , generating the active species **1**<sup>-</sup> or **2**<sup>-</sup>. The  $\text{NDI}^{\cdot-}$  chromophore absorbs at wavelengths as long as 800 nm and has an excited state oxidation potential ( $-2.1$  V vs SCE) that rivals or exceeds those of metalorganic and organometallic chromophores. Photoexcitation of  $\text{NDI}^{\cdot-}$  results in  $^*\text{NDI}^{\cdot-}$ , which transfers an electron to the bpy ligand in  $\tau_{\text{CS}} < 2$  ps regardless of attachment geometry. However, back-electron transfer from the bpy ligand to the chromophore is three orders of magnitude longer with the chromophore attached to the Re center via a pyridine ligand ( $\tau_{\text{CR}} = 29.7$

$\pm 0.2$  ns) than through the bpy ( $\tau_{\text{CR}} = 31.8 \pm 0.8$  ps). In a subsequent report, we described a system containing an intermediate acceptor linked to the metal complex through the pyridine ligand (**3**), as shown in Figure 4.2.<sup>156</sup> By employing an intermediate acceptor, the back-electron transfer lifetime was lengthened to  $\tau_{\text{CR}} = 43 \pm 1$   $\mu\text{s}$ . The lifetime of  $\text{Re}(\text{bpy}^{\bullet-})(\text{CO})_3$  in **1**<sup>-</sup> is too short to carry out catalysis. While the corresponding lifetimes in **2**<sup>-</sup> and **3**<sup>-</sup> are most likely sufficiently long for catalysis, these compounds are unsuitable for that purpose because the pyridine ligand typically dissociates upon initial reduction of the metal complex. Indeed, dissociation at this site is crucial for the binding of  $\text{CO}_2$  to the metal complex.<sup>157</sup> Nonetheless, appending the chromophore through bpy or pyridine leads to ultrafast quenching of  $^*\text{NDI}^{\bullet-}$  to ultimately form  $\text{Re}(\text{bpy}^{\bullet-})(\text{CO})_3$  in the case of **1**<sup>-</sup> and **2**<sup>-</sup> or  $\text{Re}(\text{dmb}^{\bullet-})(\text{CO})_3$  in **3**<sup>-</sup>.

The incorporation of 9,10-diphenylanthracene (DPA) as an intermediate acceptor allows us to produce a long-lived charge-separated species while allowing efficient electron transfer.<sup>156</sup> The  $-2.1$  V oxidation potential available from  $^*\text{NDI}^{\bullet-}$  chromophore is capable of reducing DPA.<sup>45, 156</sup> By covalently attaching the NDI–DPA fragment to the bpy ligand on the Re center, we ensure the ligand cannot be displaced during catalysis. Ultimately, by using an electrode to produce the chromophoric  $\text{NDI}^{\bullet-}$  donor during bulk photoelectrolysis experiments, one can avoid the use of sacrificial electron donors that complicate many reaction mechanisms.<sup>158</sup>

In the present report, we describe the synthesis, electrochemistry, photophysics and electrocatalysis of a molecular triad utilizing the NDI–DPA moiety covalently linked to bpy to form complex **4**, depicted in Scheme 4.1. Cyclic voltammetry of the triad in CO<sub>2</sub>-saturated solution

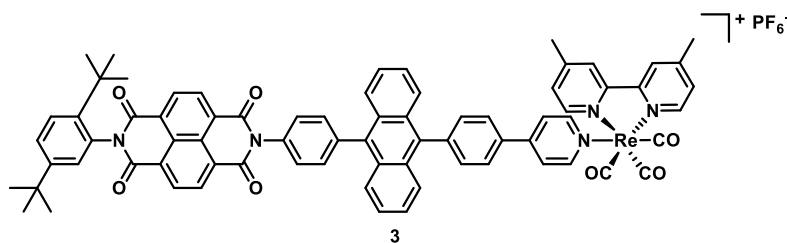


**Figure 4.2:**  $[\text{Re}(\text{dmb})(\text{CO})_3(\text{Py-DPA-NDI})]^+ \text{PF}_6^-$  (Complex **3**)

showed a 5.5-fold increase in the current at the potential corresponding to reduction of the rhenium center under CO<sub>2</sub>, illustrating its electrocatalytic activity. Photophysical experiments on **4**<sup>-</sup> using transient absorption spectroscopy demonstrated that <sup>\*</sup>NDI<sup>-</sup> serves as a powerful photoreductant, initially reducing the DPA acceptor followed by thermal electron transfer from DPA<sup>-</sup> to the Re(bpy)(CO)<sub>3</sub> carbon dioxide reduction catalyst. By employing an intermediate acceptor whose reduction potential is substantially more negative than the reduction potential of the metal complex, forward electron transfer occurs by a series of two rapid short-distance steps, while back electron transfer must occur via a single long-distance step. The result is that the back-electron transfer lifetime is lengthened substantially to 24 ns.

## 4.2 Experimental Details

### 4.2.1 Materials

Dichloromethane, acetone, CH<sub>3</sub>CN, and MeOH used for synthesis were obtained from Fisher Scientific and used as received. DMF used for synthesis and spectroscopic experiments was dried on a commercial system (GlassContour, Laguna Beach, CA). For spectroscopy, DMF was

further transferred under argon into a N<sub>2</sub>-filled glovebox (MBraun Unilab) for use and storage. Carbon dioxide (Research Grade) was obtained from Airgas and used without further purification. Commercially available reagents were purchased from Sigma-Aldrich or Oakwood Chemicals and used as received. Compounds were reduced in the glovebox using tetrakis(dimethylamino)ethylene (TDAE) from Tokyo Chemical Industries. Yttrium(III) hexafluoroacetylacetonate was obtained from Fisher Scientific. UV/Vis/NIR absorbance spectroscopy was performed on a Shimadzu UV-1601 spectrometer at 298 K.

#### **4.2.2 Electrochemistry**

Electrochemical measurements were performed using a CH Instruments Model 660A electrochemical workstation. A single-compartment cell was used for all cyclic voltammetry experiments with a 1.0 mm diameter glassy carbon disk working electrode, a platinum wire counter electrode, a silver wire pseudoreference electrode, and 0.1 M tetrabutylammonium hexafluorophosphate as the supporting electrolyte in DMF. The ferrocene/ferrocenium redox couple (0.45 V vs SCE)<sup>79</sup> was used as an internal standard. TBAPF<sub>6</sub> was recrystallized twice from ethanol prior to use. Electrochemical cells were shielded from light during experiments. All solutions were continuously purged with argon before and during the cyclic voltammetry experiments. Solutions of bpy–DPA–NDI (**5**) and Re(bpy–DPA–NDI)(CO)<sub>3</sub>Cl (**4**) were prepared in concentrations of 0.5 mM for cyclic voltammetry experiments.

#### **4.2.3 Femtosecond Transient Vis/NIR Absorption Spectroscopy**

Femtosecond transient absorption experiments were performed employing a regeneratively amplified Ti:sapphire laser system operating at 828 nm and a 1 kHz repetition rate as previously described.<sup>80-81</sup> The output of the amplifier was frequency-doubled to 414 nm using a BBO crystal

and the 414 nm pulses were used to pump a laboratory-built collinear optical parametric (OPA) amplifier for visible-light excitation<sup>82, 159</sup> or a commercial non-collinear optical parametric amplifier (TOPAS-White, Light-Conversion, LLC.) for NIR excitation. Approximately 1-3 mW of the fundamental was focused into a sapphire disk to generate the visible white-light probe spanning 430-850 nm, into a 5 mm quartz cuvette containing a 1:1 mixture of H<sub>2</sub>O:D<sub>2</sub>O to generate a UV/visible white light probe spanning 385-750 nm, or into a proprietary medium (Ultrafast Systems, LLC) to generate the NIR white-light probe spanning 850-1620 nm. The total instrument response function was 300 fs. Experiments were performed at a randomized pump polarization to suppress contributions from orientational dynamics. Spectral and kinetic data were collected with a CMOS or InGaAs array detector for visible and NIR detection, respectively, and a 8 ns pump-probe delay track (customized Helios, Ultrafast Systems, LLC). Transient spectra were averaged for at least 3 seconds. Gaps in the spectra shown are due to either scattering of the pump or idler beam, or regions not covered by the detectors. Samples prepared in DMF had an absorbance of 0.2-0.7 at the excitation wavelength and were irradiated in 2 mm quartz cuvettes with 0.4-0.8  $\mu$ J/pulse focused to  $\sim$ 0.2 mm diameter spot. Samples were stirred to avoid effects of local heating or sample degradation. The samples were prepared in the glovebox and degassed by multiple freeze-pump-thaw cycles prior to analysis.

#### **4.2.4 Nanosecond Transient Absorption Spectroscopy**

Nanosecond transient absorption experiments were performed using the femtosecond excitation beam described above and a commercial spectrometer (Eos, Ultrafast Systems, LLC) utilizing a photonic crystal fiber ultra-broadband probe source. The pump polarization was

randomized to suppress rotational dynamics. Samples were stirred to avoid effects of local heating or sample degradation.

#### **4.2.5 Femtosecond Time-Resolved mid-IR Spectroscopy**

Femtosecond transient mid-IR absorption (fsIR) spectroscopy was performed using a commercial Ti:sapphire oscillator/amplifier (Solstice 3.5W, Spectra-Physics) to pump two optical parametric amplifiers (TOPAS-C, Light Conversion), one which provided a 100 fs, 605 nm excitation pulse and the other provided 100 fs pulses at 2150-1800  $\text{cm}^{-1}$ . The overall instrument response was 300 fs. The spectra were acquired with a liquid  $\text{N}_2$ -cooled dual channel (2 x 64) MCT array detector that is coupled to a Horiba HR320 monochromator as part of a Helios-IR spectrometer (Ultrafast Systems, LLC). Samples with a maximum optical density of 1.5 at the excitation wavelength were prepared in DMF contained in a liquid demountable cell (Harrick Scientific) with 2.0 mm thick  $\text{CaF}_2$  windows and a 500  $\mu\text{m}$  Teflon spacer. During data acquisition, the cell was mounted and rastered on a motorized stage to prevent sample degradation.

#### **4.2.6 Computational Methods**

Geometries were optimized using density functional theory (DFT) with Q-Chem Version 4.3<sup>160</sup> using the B3P86 functional and LANL2DZ ECP and basis set for Re-containing molecules.<sup>84</sup>

#### **4.2.7 Characterization**

$^1\text{H}$  NMR spectra were recorded on a Bruker Avance 500 TCI Cryoprobe Spectrometer. Chemical shifts are recorded in ppm ( $\delta$ ) in  $\text{CDCl}_3$  (internal reference set to  $\delta$  7.26 ppm).  $^{13}\text{C}$  NMR (126 MHz) spectra were recorded using a Bruker Avance III QNP Cryoprobe with simultaneous decoupling of  $^1\text{H}$  nuclei and externally referenced to TMS set to 0 ppm. All spectra were recorded

at 298 K. ESI-MS were performed by Northwestern University's Integrated Molecular Structure Education and Research Center.

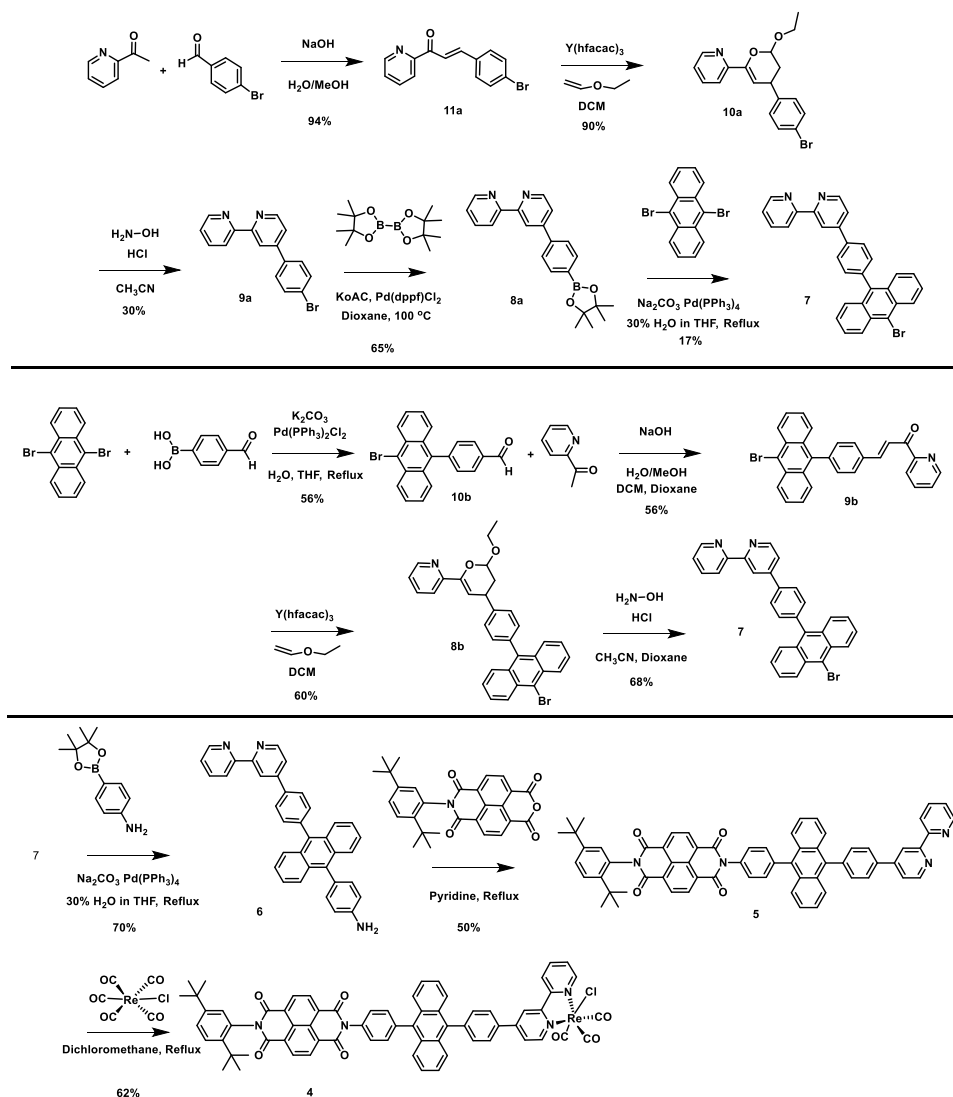
## 4.3 Results

### 4.3.1 Design and Synthesis of the Triad System

In the context of electron transfer dynamics, the individual components comprising triad **4** were chosen for the following reasons: it has been shown that visible light excitation of  $\text{NDI}^{\bullet-}$  gives its excited doublet state that is a powerful reductant,<sup>45</sup> which has been shown to readily reduce  $\text{Re}(\text{bpy})(\text{CO})_3$  complexes.<sup>155-156</sup> Catalysts having this architecture have been shown to reduce carbon dioxide at potentials that are lower than the reduction potential of DPA.<sup>31, 102</sup> This allows for exergonic electron transfer to occur in the sequence  $^*\text{NDI}^{\bullet-} \rightarrow \text{DPA} \rightarrow \text{Re}(\text{bpy})$ , with the reverse process  $\text{Re}(\text{bpy})^{\bullet-} \rightarrow \text{DPA}$  being strongly endergonic, ultimately facilitating formation of a long-lived reduced state on the catalyst. Additionally,  $\text{Re}(\text{bpy})(\text{CO})_3\text{Cl}$  and DPA are reduced at potentials more negative than those of NDI, allowing NDI to be selectively reduced to  $\text{NDI}^{\bullet-}$  using TDAE ( $E_{1/2} = -0.5$  V vs SCE) without reducing any other components in the complex. Finally, NDI, DPA, and  $\text{Re}(\text{bpy})(\text{CO})_3\text{Cl}$  each have distinct spectroscopic tags in the visible, near-IR, and mid-IR regions that allow for monitoring the entire electron transfer process.

Compounds  $\text{bpy-DPA-NDI}$  (**5**) and  $\text{Re}(\text{bpy-DPA-NDI})(\text{CO})_3\text{Cl}$  (**4**) were synthesized as illustrated in Scheme 4.1 and detailed in the 4.7. Two different routes were employed to prepare the building block **7**. In route 1, compound **7** was synthesized by aldol condensation of 2-acetylpyridine with 4-bromobenzaldehyde forming the hetero-diene product **11a**. The conversion of **11a** to the dihydropyran **10a** was catalyzed by yttrium(III) hexafluoroacetylacetonate ( $\text{Y}(\text{hfacac})_3$ ) with excess ethyl vinyl ether in DCM at room temperature.<sup>161</sup> Compound **10a** was

then heated in the presence of  $\text{H}_2\text{NOH}\cdot\text{HCl}$  to form **9a**, which was then converted into a pinacol boronic ester by standard Miyaura borylation to give **8a**.<sup>162</sup> Boronic ester **8a** was reacted with 9,10-dibromoanthracene under Suzuki reaction conditions to yield **7**. In route 2, compound **7** was synthesized by first coupling 9,10-dibromoanthracene with (4-formylphenyl)boronic acid under Suzuki reaction conditions to form **10b**. Compound **10b** was then converted into compound **9b** via Suzuki reaction conditions to form **10b**. Compound **10b** was then converted into compound **9b** via



**Scheme 4.1:** Synthetic scheme for bpy–DPA–NDI (**5**) and  $\text{Re}(\text{bpy}\text{--}\text{DPA}\text{--}\text{NDI})(\text{CO})_3\text{Cl}$  (**4**)

an aldol condensation. Conversion of **9b** to the dihydropyran **8b** was catalyzed by  $Y(\text{hfacac})_3$ . Compound **8b** was then heated with  $\text{H}_2\text{NOH}\cdot\text{HCl}$  to form **7**.

Compound **7** was coupled to 4-aminophenylboronic acid pinacol ester under Suzuki conditions to form **6**. Condensation of *N*-(2,5-di-*t*-butyl) naphthalene-1,4-dicarboximide-5,8-dicarboxyanhydride<sup>155</sup> with **6** gave the desired ligand **5**. Finally, heating  $\text{Re}(\text{CO})_5\text{Cl}$  and **5** in the dark under an inert atmosphere gave complex **4**.

### 4.3.2 Electrochemistry

Compound **5** displays four, well-separated, reversible reduction processes under cyclic voltammetry (Figure 4.3). Initial reduction of **5** leads to the first and second reduction of the NDI component of the ligand at  $-0.51$  V and  $-1.03$  V, respectively (Table 4.1). The third reduction at  $-1.90$  V corresponds to the reduction of the DPA component of the ligand. These redox potentials are in good agreement with previous work that integrates NDI and DPA.<sup>156</sup> The fourth reduction corresponds to the reduction of uncoordinated bipyridine.<sup>163</sup>

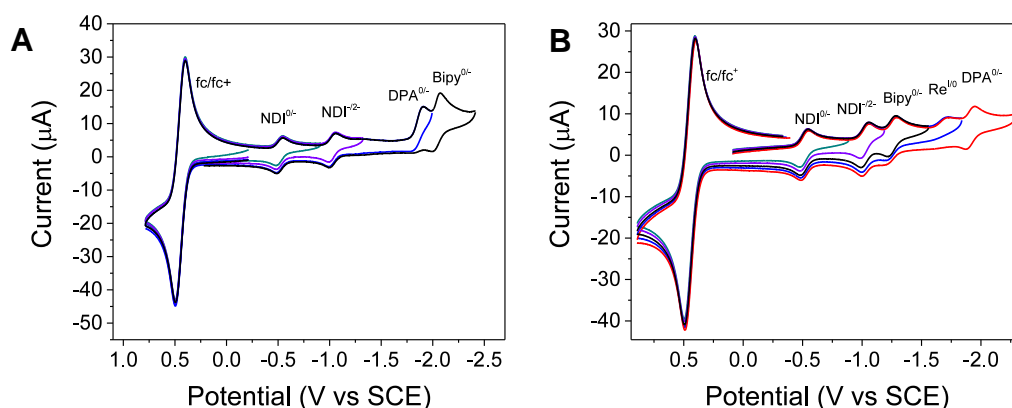


**Figure 4.3:** Cyclic voltammograms of 0.5 mM DMF solutions of (A) **5** and (B) **4**, recorded at  $100 \text{ mV s}^{-1}$  at room temperature with 0.1 M TBAPF<sub>6</sub> as supporting electrolyte. Potentials are reported versus (Fc/Fc<sup>+</sup> occurs at 0.45 V vs. SCE)

Cyclic voltammetry on compound **4** displays five different, well-separated reduction processes. The initial reduction of **4** is very similar to that of the free ligand, with the first and second reduction of the NDI portion of the complex occurring again at  $-0.51$  V and  $-1.03$  V, respectively. These reductions are followed by the one-electron quasi-reversible reduction of the bpy ligand at  $-1.26$  V, and a subsequent one-electron irreversible reduction of the Re center,  $-1.72$  V.<sup>164</sup> These potentials and their degree of reversibility match previously reported findings.<sup>102, 156</sup> The final reduction at  $-1.90$  V corresponds to the reduction of DPA, at an identical potential to the reduction of DPA in the free ligand. The identical reduction potentials for the NDI and DPA portions of compound **4** indicated negligible electronic coupling between those components of the ligand and the metal complex. The shift to a lower reduction potential of the bpy is expected upon coordination to the metal center.<sup>102, 155-156</sup>

**Table 4.1:** Redox potentials (vs. SCE using a Fc/Fc<sup>+</sup> reference at 0.45 V vs SCE).

	NDI <sup>0/-</sup>	NDI <sup>-2-</sup>	bpy <sup>0/-</sup>	Re <sup>I/0</sup>	DPA <sup>0/-</sup>
Ligand <b>5</b>	-0.51	-1.03	-2.03	-	-1.90
Complex <b>4</b>	-0.51	-1.03	-1.26	-1.72	-1.90

### 4.3.3 Electrocatalysis

The electrocatalytic properties of **4** (0.5 mM in DMF) were studied in a single-compartment cell with a glassy carbon working electrode, Pt counter electrode, and a Ag/AgCl reference electrode (potentials were then converted to SCE). The DMF solution was sparged for fifteen

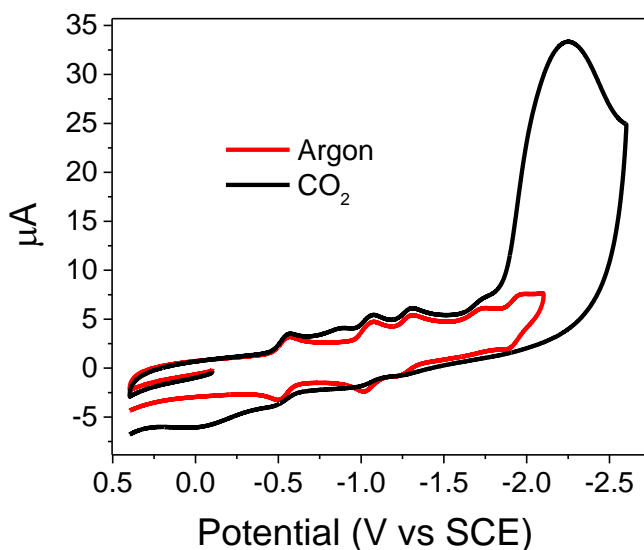


**Figure 4.4:** Cyclic voltammograms of a 0.5 mM solution of complex **4** in 0.1 M TBAPF<sub>6</sub> in DMF under argon (red), saturated with CO<sub>2</sub> (black). Scan rate: 100 mV s<sup>-1</sup>, glassy carbon electrode, Ag/AgCl reference electrode, platinum wire counter electrode

minutes with carbon dioxide to yield a saturated solution (0.20 M).<sup>165</sup> When the potential was swept negative, a large increase in current was observed upon the fourth reduction of the complex (Figure 4.4), while the first three reduction waves of the ligand were largely unchanged in the presence of CO<sub>2</sub>. Complex **4** at the fourth reduction peak showed a 5.5-fold increase in peak current at a scan rate of 100 mV/s (Figure 4.4). The fourth reduction of complex **4** corresponds to the reduction of the Re center (following the reduction of bpy and the two NDI reductions) and forms the expected electrocatalytically active species, Re<sup>0</sup>(bpy<sup>-</sup>-DPA-NDI)(CO)<sub>3</sub>, that can bind and ultimately reduce CO<sub>2</sub>.<sup>102, 157</sup> This mechanistic pathway for CO<sub>2</sub> reduction is consistent with that

proposed for other  $\text{Re}^{\text{I}}(\text{bpy})(\text{CO})_3$  complexes.<sup>102, 157</sup> Moreover, in the absence of added acid,  $\text{CO}_2$  reduction catalysis with complex **4** likely proceeds in a similar fashion as other reported  $\text{Re}(\text{bpy})(\text{CO})_3\text{Cl}$  catalysts to form CO, through deprotonation of the electrolyte via Hoffman degradation or deprotonation of the solvent that allows the complex to undergo the catalytic cycle.<sup>166</sup>

#### 4.3.4 Electron Transfer Energetics

Based on the redox potentials shown above, the Gibbs free energy for the excited state electron transfer reactions of complex **4**<sup>-</sup> can be estimated using the following equation:

$$\Delta G_{\text{ET}} = (E_{\text{ox}} - E_{\text{red}}) - E_{00} \quad (1)$$

where  $E_{\text{ox}}$  and  $E_{\text{red}}$  are the oxidation and reduction potentials of the donor and acceptor respectively, and  $E_{00}$  is the energy of the  $^*\text{NDI}^-$  excited state. There is no electrostatic work term for this reaction because the reaction is a charge shift, not a charge separation. In addition, there is no solvation correction term because the experiments are performed in the same solvent as the electrochemical data is obtained. The Gibbs free energy for the thermal forward and back electron transfer reactions can be estimated using the following equation

$$\Delta G_{\text{ET}} = (E_{\text{ox}} - E_{\text{red}}) \quad (2)$$

From the equations above, the Gibbs free energies for each electron transfer step are shown in Table 4.2 below.

**Table 4.2:** Free energy changes for electron transfer reactions in complex  $4^-$ .

compound	process	$\Delta G$ (eV)
$4^-$	*NDI $^{\cdot-}$ $\rightarrow$ DPA	-0.24
$4^-$	DPA $^{\cdot-}$ $\rightarrow$ Re(bpy)	-0.64
$4^-$	DPA $^{\cdot-}$ $\rightarrow$ NDI $^0$	-1.37
$4^-$	Re(bpy $^{\cdot-}$ ) $\rightarrow$ NDI $^0$	-0.73

### 4.3.5 Steady-State Photophysical Characterization

The normalized steady-state electronic absorption spectra of **4** are shown in Figure 5. In complex **4**, the Re(bpy)(CO) $_3$ Cl MLCT absorption band is broad and underlies the absorptions due to DPA and NDI in the region below 400 nm. When equimolar TDAE is added to complex **4** to form  $4^-$ , the NDI absorptions disappear while the NDI $^{\cdot-}$  absorptions appear at 471 nm, 605 nm, 700 nm, and 785 nm,<sup>45</sup> additionally the DPA absorptions become visible at 396 nm, 376 nm, 357 nm, and 340 nm. Once again, in the chemically reduced complex  $4^-$ , the Re(bpy)(CO) $_3$ Cl MLCT band underlies the absorptions below 400 nm.

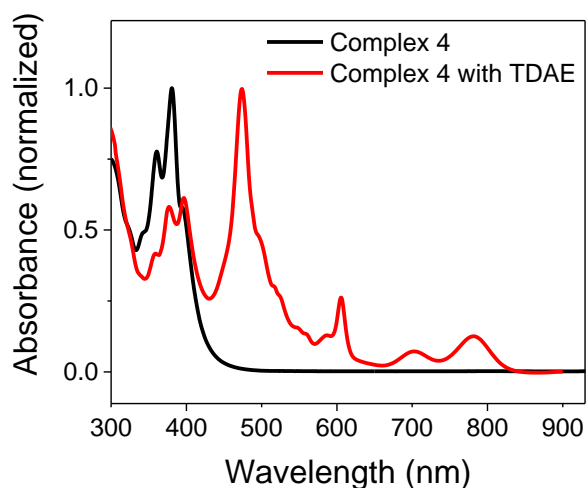


**Figure 4.5:** Electronic absorption spectra of complex **4** in DMF with and without the TDAE reductant added.

### 4.3.6 Femto/nanosecond Transient Absorption Spectroscopy

The intramolecular electron transfer behavior of complex  $4^-$  was probed using transient absorption spectroscopy in the visible/NIR and mid-IR regions. The fsTA spectra, the species-associated spectra for each decay component, and the multiple-wavelength kinetics and fits are shown in Figure 4.6. Excitation of complex  $4^-$  at 605 nm results in instantaneous bleaching of the ground-state absorptions of  $\text{NDI}^-$  at 473 nm, and the appearance of a broad absorption spanning the region 600–780 nm. These features match the transient spectrum of  $^*\text{NDI}^-$  itself. Fitting of the visible/NIR TA data using singular value decomposition gives an  $^*\text{NDI}^-$  lifetime of  $\tau = 14.5 \pm 0.2$  ps. As the  $^*\text{NDI}^-$  features decay, an induced absorption at 382 nm appears with the same time constant. This absorption corresponds to the absorption of  $\text{NDI}^0$ , the product of oxidative quenching of  $^*\text{NDI}^-$ . That feature and the  $^*\text{NDI}^-$  bleach decay via first-order kinetics with a lifetime of  $\tau = 24.5 \pm 0.2$  ns. No spectral features attributable to the DPA radical anion<sup>125</sup> are observed, indicating that the  $\text{Re}(\text{bpy}-\text{DPA}^--\text{NDI}^0)(\text{CO})_3\text{Cl}$  state is very short-lived. Attempts to

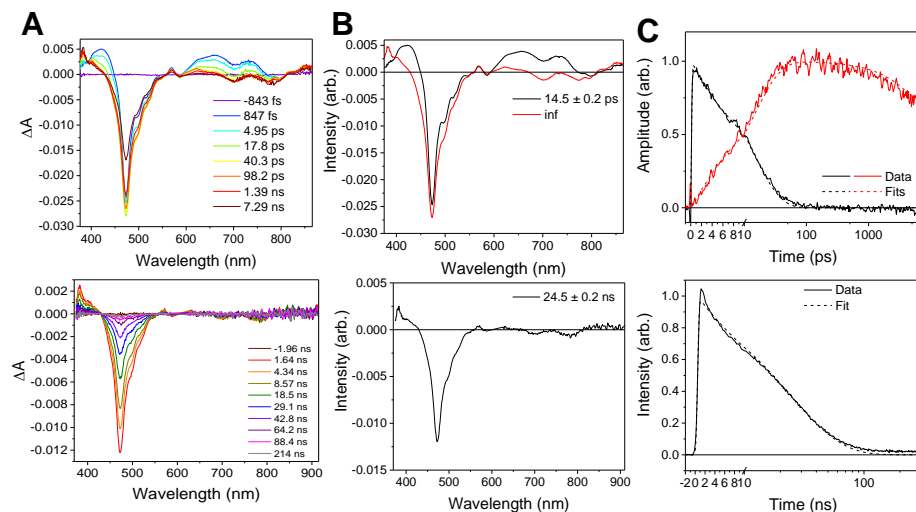


**Figure 4.6:** Femtosecond (top row) and nanosecond (bottom row) transient absorption data for complex  $4^-$  in DMF ( $\lambda = 605$  nm) (A) Transient absorption spectra; (B) species-associated spectra; (C) multiple-wavelength kinetic traces and fits.

fit the data using a model that contained a short-lived component corresponding to that state were unsuccessful, indicating that the transient population of that state is negligible.

#### 4.3.7 Time-resolved mid-IR Spectroscopy

In order to unambiguously assign the species with the 24.5 ns lifetime, complex  $4^-$  was also probed using femtosecond transient mid-IR (fsIR) spectroscopy. In this region, the CO

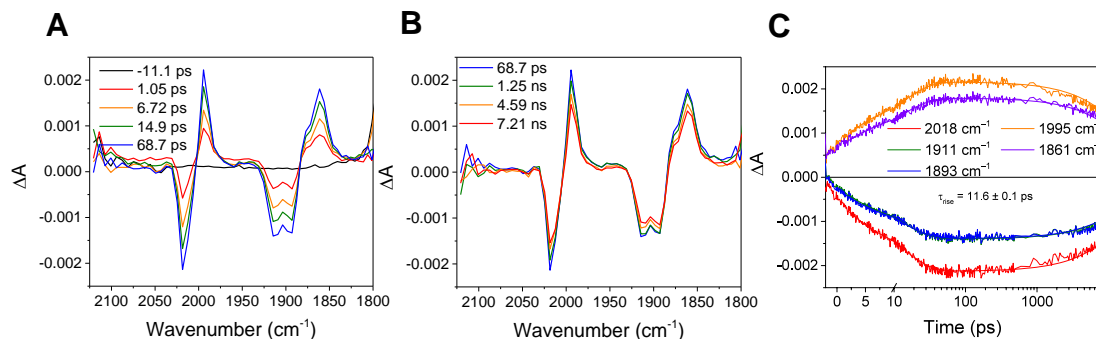


**Figure 4.7:** (A,B) Time-resolved IR spectra and (C) global multiple-wavelength kinetic traces and fits for complex  $4^-$  in DMF ( $\lambda = 605$  nm).

stretching frequencies of the carbonyl ligands on the Re (in the range  $1850\text{--}2100$   $\text{cm}^{-1}$ ) are

diagnostic of the ligand and electronic environment.<sup>102</sup> FsIR spectra and kinetic traces at selected energies are shown below in Figure 4.7. The ground-state absorptions at 1892 cm<sup>-1</sup>, 1910 cm<sup>-1</sup>, and 2018 cm<sup>-1</sup> bleach with a  $\tau = 11.6 \pm 0.1$  ps time constant, and remain bleached for the entirety of the 8 ns experimental window. Induced absorptions appear at 1861 cm<sup>-1</sup> and 1994 cm<sup>-1</sup> with the same kinetics. The induced absorption at 1861 cm<sup>-1</sup> is an overlap and shifting of the 1892 cm<sup>-1</sup> and 1910 cm<sup>-1</sup> bands, while the induced absorption at 1994 cm<sup>-1</sup> is a shift of the 2018 cm<sup>-1</sup> band. These shifts have been previously observed by our group and others in photo- and electrochemical experiments in which Re(bpy)(CO)<sub>3</sub>L complexes are reduced by one electron to form Re(bpy<sup>-</sup>)(CO)<sub>3</sub>L.<sup>102, 155-156</sup>

## 4.4 Discussion

### 4.4.1 Electron Transfer Dynamics

The forward and back electron transfer reactions in complex **4<sup>-</sup>** are intramolecular processes, beginning with the rapid decay of the <sup>\*</sup>NDI<sup>-</sup> excited state ( $\tau_{\text{obs}} = 14.5 \pm 0.2$  ps, corresponding to a rate of  $1.6 \times 10^{11}$  s<sup>-1</sup>). The <sup>\*</sup>NDI<sup>-</sup> excited state transfers an electron to the DPA component of the triad, but no features attributable to DPA<sup>-</sup> can be detected following the decay of the <sup>\*</sup>NDI<sup>-</sup> excited state. Additionally, no recovery of the ground state features is observed on the picosecond timescale, indicating that back electron transfer from DPA<sup>-</sup> to NDI<sup>0</sup> is not kinetically competitive with forward electron transfer from DPA<sup>-</sup> to bpy. This behavior was seen in a similar triad system previously investigated by us,<sup>156</sup> where the NDI–DPA component of the triad was attached to a Re complex via a pyridine ligand (complex **3<sup>-</sup>**) instead of a bpy ligand (complex **4<sup>-</sup>**), no features attributable to DPA<sup>-</sup> were seen following the formation of <sup>\*</sup>NDI<sup>-</sup>. The previous investigation of the Py–DPA–NDI<sup>-</sup> ligand demonstrated that <sup>\*</sup>NDI<sup>-</sup> can be oxidatively quenched by appended

DPA to form  $\text{DPA}^{\bullet-}$ , but since the decay of  $\text{NDI}^0\text{-DPA}^{\bullet-}$  ( $\tau_{\text{ET}} = 4.8$  ps) was faster than its growth ( $\tau_{\text{ET}} = 27.3$  ps), spectral signatures of  $\text{DPA}^{\bullet-}$  were not readily visible in the raw transient absorption data; this is likely the same in complex  $\mathbf{4}^-$ . The quantum yield of electron transfer to the DPA acceptor in complex  $\mathbf{4}^-$  can be estimated by comparing the intrinsic  $^*\text{NDI}^-$  excited state lifetime ( $\tau = 141$  ps for NDI bearing two aryl substituents)<sup>155</sup> with its lifetime in  $\mathbf{4}$ , which gives an approximately 90% quantum yield.

The final charge-shifted state in complex  $\mathbf{4}^-$  persists well into the nanosecond time regime, as evidenced by the ground state bleaches and induced absorptions in both the visible and mid-IR spectral regions. UV-visible spectra taken before and after the transient experiments confirm the photostability of  $\mathbf{4}^-$  under irradiation. This lifetime represents an increase of three orders of magnitude over the analogous dyad  $\mathbf{1}$  ( $\tau = 31.8 \pm 0.8$  ps) investigated previously by us.<sup>102, 155-156</sup> This dramatic increase in lifetime is most likely a result of the diminished electronic coupling between the donor and acceptor, which is exponentially distance dependent. Thus, the longer NDI-bpy distance in  $\mathbf{4}$  relative to  $\mathbf{1}$ , 23.2 Å vs. 14.5 Å, respectively, is consistent with the much slower electron transfer rate observed for  $\mathbf{4}^-$ .

#### 4.4.2 Comparison of Electron Transfer Dynamics to Previous Complexes

The exponential distance dependence of the electronic coupling matrix element for electron transfer is once again evident when one notes that the lifetime of the charge-shifted state in  $\mathbf{4}^-$  is about three orders of magnitude shorter than that of complex  $\mathbf{3}^-$  ( $43 \pm 1$  μs) investigated previously by us,<sup>156</sup> where the NDI-DPA moiety is attached to the rhenium center via a pyridine instead of a bpy as in complex  $\mathbf{4}^-$ . While the electron in the final charge separated state of both complexes resides on their respective bipyridine ligands (bpy for complex  $\mathbf{4}^-$  and 4,4'-dimethyl-2,2'-bipyridine

(dmb) for complex **3**<sup>-</sup>), complex **4**<sup>-</sup> has a shorter distance between the NDI and bpy ligand in comparison to the distance between NDI and dmb. (20.6 Å in **4** vs. 23.2 Å in **3**). Since electron transfer most likely occurs through the covalent bonds as is usually the case for linked donor-acceptor systems, one must also consider the nature of the bonding that occurs between the donor and acceptor. As the structures of **3** and **4** clearly show, there are large differences in the number and type of bonds connecting the donor and acceptor in these systems. The electron transfer pathways and rates for complex **4**<sup>-</sup> are depicted graphically in a Jablonski diagram in Figure 4.8.

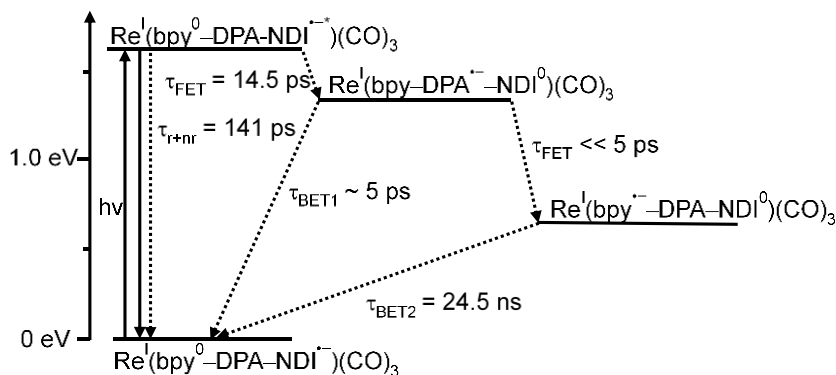


**Figure 4.8:** Energy-level diagram for  $\text{Re}(\text{bpy-DPA-NDI}^{\bullet-})(\text{CO})_3\text{Cl}$  (**4**<sup>-</sup>)

## 4.5 Conclusions

The data presented here clearly show that upon excitation of  $\text{NDI}^{\bullet-}$ , the final charge separated state is  $\text{Re}^{\text{I}}(\text{bpy}^{\bullet-}\text{-DPA-NDI}^0)(\text{CO})_3\text{Cl}$ . Earlier reports by various workers have postulated that the analogous 19-electron species  $\text{Re}^{\text{I}}(\text{dmb})^{\bullet-}(\text{CO})_3\text{Cl}$  could be responsible for initiating  $\text{CO}_2$  binding.<sup>167-168</sup> Additionally, the 17-electron species  $\text{Re}^0(\text{bpy})(\text{CO})_3$ ,  $\text{Re}^{\text{I}}(\text{bpy}^{\bullet-})(\text{CO})_3$ ,<sup>104, 158, 169-170</sup> or alternatively, the 18-electron species  $\text{Re}^0(\text{bpy}^{\bullet-})(\text{CO})_3$  are plausible nucleophiles for initiating  $\text{CO}_2$  binding.<sup>169</sup> In the absence of time-resolved mid-IR spectroscopy at times longer than a few nanoseconds, it was not possible to determine when the chloride ion dissociates upon single

electron reduction of the metal center within complex **4**<sup>-</sup>. The mechanism for photocatalytic CO<sub>2</sub> reduction by Re<sup>I</sup>(bpy)(CO)<sub>3</sub>Cl has been studied by a variety of techniques including UV-visible absorption spectroscopy, cold-spray ionization spectrometry, H<sup>1</sup> C<sup>13</sup> NMR, mass spectrometry, electron spin resonance, infrared spectroscopy, ultrafast spectroscopy, but remains to be completely elucidated because the multiple products that form complicate the analysis.<sup>27, 104, 150,</sup>

171-177

In this report, we have described a complex consisting of a reduced NDI chromophore, a DPA primary electron acceptor, and Re(bpy)(CO)<sub>3</sub>Cl terminal electron acceptor, which under typical electrocatalytic conditions demonstrates electrochemical reduction of CO<sub>2</sub> without the specific addition of a proton source. Having confirmed that complex **4** can activate CO<sub>2</sub>, the photophysics of chemically reduced complex **4**<sup>-</sup> were probed using transient spectroscopy. Upon excitation of the NDI<sup>-</sup> chromophore, the terminal acceptor is reduced with a time constant of approximately 15 ps to the Re(bpy<sup>-</sup>)(CO)<sub>3</sub>Cl state, the first step in activating that metal complex towards binding and reducing CO<sub>2</sub>. The redox potential of the intermediate acceptor allows for rapid forward electron transfer to the metal center, but interposes a large barrier for back electron transfer, leading to a charge-shifted state that persists with a lifetime of more than 24 nanoseconds. The quantum yield of the electron transfer step is approximately 90%, indicating a highly efficient process for the reduction of the metal center using visible light.

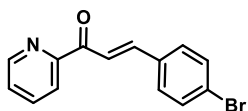
This work provides several important realizations for integrating donor-acceptor assemblies with CO<sub>2</sub> reduction catalysts. One important finding is that the extension of the bpy to form a triad does not interfere with the electrocatalytic performance of the complex. Second, by incorporating an appropriate intermediate acceptor not only is the lifetime of the charge separated species lengthened, but the 90% electron transfer quantum yield demonstrates that this design ensures that

most photons absorbed by the system are being utilized for the reduction of the metal center. Third, NDI can easily be modified so that complex **4** can be attached to an electrode surface,<sup>178</sup> allowing for quick regeneration of NDI<sup>-</sup> to inhibit back electron transfer, thereby rendering the lifetime of the charge-separated state sufficiently long to allow a second electron transfer from <sup>\*</sup>NDI<sup>-</sup> to the Re complex that can result in CO<sub>2</sub> binding to start the catalytic cycle. These and other modifications are currently being pursued.

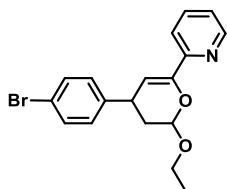
#### 4.6 Acknowledgements

We thank Dr Matthew D. Krzyaniak for assistance with fitting the kinetic data and Drs. Saman Shafaie and S. Habibi Goudarzi for collecting high-resolution mass spectrometric data. This work was supported by the Argonne Northwestern Solar Energy Research (ANSER) Center, an Energy Frontier Research Center funded by the U.S. Department of Energy (DOE), Office of Science, Office of Basic Energy Sciences, under Award No. DE-SC0001059. This publication was made possible by NPRP Grant No. 9-174-2-092 from the Qatar National Research Fund (a member of Qatar Foundation). The findings achieved herein are solely the responsibility of the authors. NMR and MS measurements in this work were performed at the IMSERC at Northwestern University, which has received support from the Soft and Hybrid Nanotechnology Experimental (SHyNE) Resource (NSF NNCI-1542205); the State of Illinois and International Institute for Nanotechnology (IIN).

#### 4.7 Synthetic Details

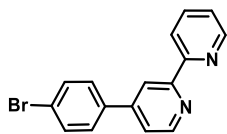


**3-(4-bromo-phenyl)-1-pyridin-2-yl-propenone (11a).** 2-Acetylpyridine (12.1g, 0.1mol) was added to 300mL of MeOH while stirring exposure to air. 40mL of 1M NaOH was added and stirred for 5 minutes. 4-Bromobenzaldehyde (18.5g, 0.1mol) was then added slowly, within moments a precipitate formed. After 1.5 hours, the reaction was removed from the stir plate, filtered, washed with H<sub>2</sub>O and MeOH, and the precipitate was collected (26.8g, 94%). <sup>1</sup>H NMR (500 MHz, Chloroform-*d*) 8.71 (d, *J* = 5 Hz, 1H), 8.28 (d, *J* = 16 Hz, 1H), 8.16 (d, *J* = 8 Hz, 1H), 7.85 (m, 2H), 7.56 (d, *J* = 8 Hz, 2H), 7.52 (d, *J* = 8 Hz, 2H), 7.47 (dd, *J* = 7, 4 Hz, 1H).

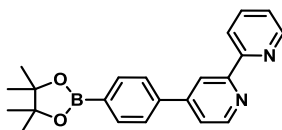


**2-[4-(4-bromo-phenyl)-6-ethoxy-5,6-dihydro-4H-pyran-2-yl]-pyridine (10a).** 3-(4-bromo-phenyl)-1-pyridin-2-yl-propenone (2.00g, 6.96 mmol) and 4 Å molecular sieves (2.00g, *ca.* equal to mass of hetero-diene) and ethyl vinyl ether (10 equiv) were added to a round bottom with 100mL of dichloromethane. Then yttrium (III) hexafluoroacetylacetonate (0.25g, 0.35mmol, 5 mol%) was added and then the round bottom was sealed with a rubber septum. The reaction was allowed to stir for 48 hours. the solvent was filtered through celite using a medium pore glass frit. The celite was washed with diethyl ether and the organic solvent evaporated under reduced pressure to give an oil. The product was then extracted using ethyl acetate and water (3x100mL). Ethyl acetate was removed under reduced pressure. The compound was then purified further via chromatography on silica gel (dichloromethane) yielding a colorless oil (2.50g, 99%). <sup>1</sup>H NMR (500 MHz, Chloroform-*d*) 8.51 (ddd, *J* = 5, 2, 1 Hz, 1H), 7.63 (m, 2H), 7.35 (dd, *J* = 7, 2 Hz, 2H), 7.13 (m,

3H), 6.16 (dd,  $J = 3, 1$  Hz, 1H), 5.21 (dd,  $J = 9, 2$  Hz, 1H), 4.05 (dq,  $J = 9, 7$  Hz, 1H), 3.75 (m, 1H), 3.65 (dq,  $J = 9, 7$  Hz, 1H), 2.30 (dd,  $J = 13, 7$  Hz, 1H), 1.92 (m, 1H), 1.24 (t,  $J = 8$  Hz, 1H).

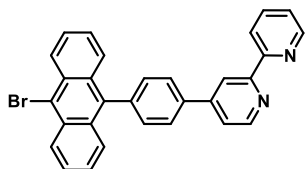


**4-(4-bromo-phenyl)-[2,2']bipyridinyl (9a).** 2-[4-(4-bromo-phenyl)-6-ethoxy-5,6-dihydro-4H-pyran-2-yl]-pyridine (2.50g, 6.96mmol) and  $\text{H}_2\text{NOH}\cdot\text{HCl}$  (4.83g, 69.64mmol), and acetonitrile (150 mL) were added to round bottom flask under air and heated to reflux. The reaction was allowed to stir for 12 hours and cooled to room temperature. The acetonitrile was removed under reduced pressure. A saturated aqueous solution of  $\text{NaOH}/\text{NaCl}$  (200mL) and dichloromethane (200mL) were added to the solid and the mixture stirred vigorously until all the solid dissolved. The product was then extracted with dichloromethane (3x100 mL), and evaporated using a rotary evaporator. The crude mixture was then dissolved in dichloromethane and purified via column chromatography on silica gel (MeOH:DCM 7%). The fractions were collected and the solvent was then removed using a rotary evaporator, sonicated in minimal MeOH, and filtered to yield the product (0.76g, 35%).  $^1\text{H NMR}$  (500 MHz, Chloroform-*d*) 8.72 (d,  $J = 5$  Hz, 1H), 7.80 (d,  $J = 4$  Hz, 1H), 8.65 (d,  $J = 1$  Hz, 1H), 8.46 (d,  $J = 8$  Hz, 1H), 7.85 (td,  $J = 8, 2$  Hz, 1H), 7.62 (m, 4H), 7.50 (dd,  $J = 5, 1$  Hz, 1H), 7.34 (ddd,  $J = 8, 5, 1$  Hz, 1H).



**4-(4-boronicester-phenyl)-[2,2']bipyridinyl (8a).** 4-(4-bromo-phenyl)-[2,2']bipyridinyl (8.0g, 25.8mmol), bis(pinacolato)diboron (6.52g, 25.8mmol), and potassium acetate (20.25g, 206.4mmol) were added to dioxane (300mL) and magnetic stirrer in a two-neck round bottom

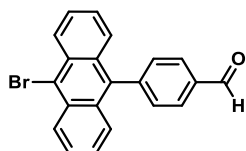
flask fitted with a condenser. The flask was evacuated and backfilled three times with N<sub>2</sub>. The flask was stirred at 100°C overnight and then cooled to room temperature. Then 200 ml of dichloromethane was added to the mixture and filtered through filter paper. DCM and dioxane were then rotovapped off and the crude mixture was then sonicated in hexanes and filtered through celite. The solvent was then removed under reduced pressure and the product was collected (8.3g, 90%). <sup>1</sup>H NMR (500 MHz, Chloroform-*d*) δ 8.78 – 8.63 (m, 3H), 8.45 (dt, *J* = 7.9, 1.1 Hz, 1H), 7.94 (d, *J* = 8.1 Hz, 2H), 7.85 (td, *J* = 7.7, 1.8 Hz, 1H), 7.80 – 7.76 (m, 2H), 7.57 (dd, *J* = 5.1, 1.8 Hz, 1H), 7.34 (ddd, *J* = 7.5, 4.7, 1.2 Hz, 1H), 1.38 (s, 12H).



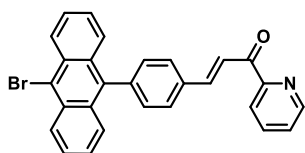
**4-(9-bromoanthracene-10-phenyl)-[2,2']bipyridinyl (7).** 4-(4-boronic-ester-phenyl)-[2,2']

bipyridinyl (2.88g, 8.04mmol), 9,10-dibromoanthracene (13.35g, 40.0mmol), and Na<sub>2</sub>CO<sub>3</sub> (6.8g, 64.3mmol) were combined in 500 mL THF and 100 mL DI H<sub>2</sub>O in a 1 L two-necked round bottom flask and sparged 30 minutes with N<sub>2</sub>. Pd(PPh<sub>3</sub>)<sub>4</sub> (0.93g, 0.80mmol) was added under flow of N<sub>2</sub> and the solution sparged for an additional ten minutes, then refluxed overnight. The flask was cooled to room temperature. The mixture was then extracted using dichloromethane and rotovapped under reduced pressure. The contents were then suspended in 300 mL of DCM, poured over a silica plug and washed with DCM until the excess 9,10-dibromoanthracene had been removed. DCM:MeOH (75:25) was then used to elute the product. The solvent was evaporated under reduced pressure and then sonicated in minimal MeOH and gravity filtered. Then sonicated in minimal acetone and filtered. The product was collected as an off-yellow

solid. (0.68g, 17%)  $^1\text{H NMR}$  (500 MHz, Chloroform-*d*)  $\delta$  8.85 – 8.80 (m, 2H), 8.74 (dt,  $J = 4.5$ , 1.2 Hz, 1H), 8.64 (d,  $J = 8.9$  Hz, 2H), 8.51 (dt,  $J = 8.1$ , 1.2 Hz, 1H), 8.02 – 7.98 (m, 2H), 7.88 (td,  $J = 7.7$ , 1.8 Hz, 1H), 7.73 – 7.68 (m, 3H), 7.62 (ddd,  $J = 8.9$ , 6.4, 1.2 Hz, 2H), 7.58 – 7.54 (m, 2H), 7.42 (ddd,  $J = 8.9$ , 6.5, 1.1 Hz, 2H), 7.36 (ddd,  $J = 7.6$ , 4.7, 1.2 Hz, 1H).

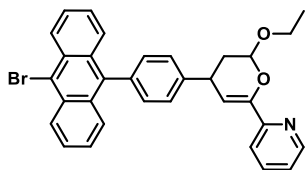


**9-bromoanthracene-10-formyl (10b).** 9,10-dibromoanthracene (9.21g, 27mmol), 4-formylphenylboronic acid (1.35g, 9mmol) were suspended in 150mL THF under  $\text{N}_2$  in a two-neck round bottom flask with a magnetic stir bar and a reflux condenser. Then 10mL of 2M  $\text{K}_2\text{CO}_3$  was added with  $\text{Pd}(\text{PPh}_3)_2\text{Cl}_2$  (0.31g, 0.9mmol) were added and the system was purged for 15 minutes. The flask was stirred at  $80^\circ\text{C}$  overnight and then cooled to room temperature, and the solvents were removed under pressure. The contents were then suspended in acetone and gravity filtered. The solvent was evaporated under reduced pressure and the remaining solid was purified via column chromatography on silica, (DCM:Hexanes 1:4). (1.83g, 56%).  $^1\text{H NMR}$  (500 MHz, Chloroform-*d*)  $\delta$  10.20 (s, 1H), 8.64 (dt,  $J = 9.1$ , 1.0 Hz, 2H), 8.12 (dd,  $J = 7.9$ , 1.4 Hz, 2H), 7.64 – 7.58 (m, 4H), 7.55 (dt,  $J = 8.9$ , 1.0 Hz, 2H), 7.40 (ddd,  $J = 8.8$ , 6.4, 1.2 Hz, 2H).

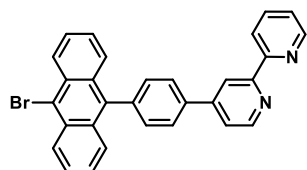


**3-(9-bromoanthracene-10-phenyl)-1-pyridin-2-yl-propenone (9b).** 2-Acetylpyridine (0.23g, 1.92mmol) was dissolved in MeOH (20mL) with a magnetic stir bar inside a round bottom flask

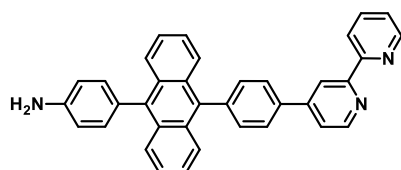
opened to air. 9-bromoanthracene-10-formyl (0.50g, 1.38 mmol) was suspended in DCM (20mL) and dioxane (20mL). 4M NaOH (10mL) was added to the solution and allowed to stir overnight at room temperature. 40mL of MeOH was added and the solution was gravity filtered to afford the product. (0.34g, 56%).  $^1\text{H NMR}$  (500 MHz, Chloroform-*d*)  $\delta$  8.78 (dt,  $J = 4.7, 1.3$  Hz, 1H), 8.63 (d,  $J = 8.9$  Hz, 2H), 8.47 (d,  $J = 16.0$  Hz, 1H), 8.25 (dt,  $J = 7.9, 1.1$  Hz, 1H), 8.10 (d,  $J = 16.1$  Hz, 1H), 7.96 (d,  $J = 7.9$  Hz, 2H), 7.92 (td,  $J = 7.7, 1.7$  Hz, 1H), 7.66 (d,  $J = 8.8$  Hz, 2H), 7.61 (ddd,  $J = 9.1, 6.5, 1.2$  Hz, 2H), 7.52 (ddd,  $J = 7.6, 4.7, 1.2$  Hz, 1H), 7.50 – 7.46 (m, 2H), 7.40 (m, 2H).



**2-[4-(9-bromoanthracene-10-phenyl)-6-ethoxy-5,6-dihydro-4H-pyran-2-yl]-pyridine (8b).** 3-(9-bromoanthracene-10-phenyl)-1-pyridin-2-yl-propenone (0.36g, 0.78mmole), ethyl vinyl ether (0.55g, 7.66mmol), and yttrium (III) hexafluoroacetylacetonate (0.03g, 0.04mmol) were dissolved in 30mL of dry DCM in a round bottom flask with a magnetic stir bar. Then 4Å molecular sieves (0.35g) were added and the solution was capped with a rubber septum and allowed to stir for 2 days. The solution was then filtered through celite using DCM. The solvent was removed and the product was used without further purification. (0.41g, 60%).  $^1\text{H NMR}$  (500 MHz, Chloroform-*d*)  $\delta$  8.60 (d,  $J = 8.7$  Hz, 3H), 7.76 – 7.66 (m, 4H), 7.59 (ddd,  $J = 8.8, 6.5, 1.2$  Hz, 2H), 7.52 (d,  $J = 7.8$  Hz, 2H), 7.41 – 7.37 (m, 2H), 7.35 – 7.32 (m, 2H), 7.24 (d,  $J = 7.1$  Hz, 1H), 6.36 (dd,  $J = 3.1, 1.1$  Hz, 1H), 5.39 (s, 1H), 4.15 (s, 1H), 4.02 (ddd,  $J = 9.8, 6.8, 2.9$  Hz, 1H), 3.77 (dt,  $J = 14.2, 7.1$  Hz, 1H), 2.55 (s, 1H), 2.24 (s, 1H), 1.34 (s, 3H).

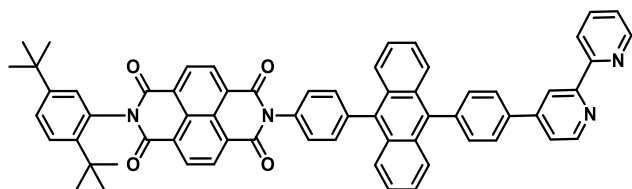


**4-(9-bromoanthracene-10-phenyl)-[2,2']bipyridinyl (7).** 2-[4-(9-bromoanthracene-10-phenyl)-6-ethoxy-5,6-dihydro-4*H*-pyran-2-yl]-pyridine (0.41g, 0.76mmol) was dissolved in MeCN (100mL) and dioxane (50mL) in a 250mL two-necked round bottom flask.  $\text{H}_2\text{NOH}\cdot\text{HCl}$  (0.54g, 7.66mmol) was added to the suspension and purged with  $\text{N}_2$ . The solution was then heated to  $100^\circ\text{C}$  overnight and cooled to room temperature. The solvents were removed under reduced pressure. A saturated aqueous solution of NaOH/NaCl (200mL) and dichloromethane (200mL) were added to the solid and stirred for 2 hours. The product was then extracted with dichloromethane and the solvent removed under reduced pressure. The crude mixture was then sonicated in MeOH and gravity filtered leaving behind the pure product. (0.25g, 68%).  $^1\text{H NMR}$  (500 MHz, Chloroform-*d*)  $\delta$  8.85 – 8.80 (m, 2H), 8.74 (dt,  $J = 4.5, 1.2$  Hz, 1H), 8.64 (d,  $J = 8.9$  Hz, 2H), 8.51 (dt,  $J = 8.1, 1.2$  Hz, 1H), 8.02 – 7.98 (m, 2H), 7.88 (td,  $J = 7.7, 1.8$  Hz, 1H), 7.73 – 7.68 (m, 3H), 7.62 (ddd,  $J = 8.9, 6.4, 1.2$  Hz, 2H), 7.58 – 7.54 (m, 2H), 7.42 (ddd,  $J = 8.9, 6.5, 1.1$  Hz, 2H), 7.36 (ddd,  $J = 7.6, 4.7, 1.2$  Hz, 1H).



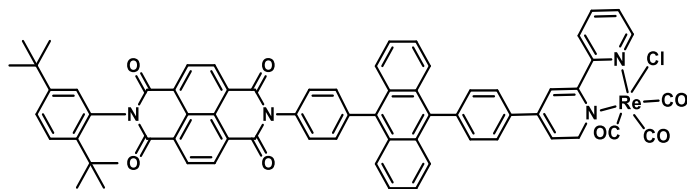
**4-(9-(aniline)anthracene-10-phenyl)-[2,2']bipyridinyl (6).** 4-(9-bromoanthracene-10-phenyl)-[2,2']bipyridinyl (0.68g, 1.40mmol), 4-Aminophenylboronic acid pinacol ester (0.61g,

2.80mmol), and  $\text{Na}_2\text{CO}_3$  (1.2g, 11.2mmol) were combined in 100 mL THF and 50 mL DI  $\text{H}_2\text{O}$  in a 250mL two-necked round bottom flask and sparged 30 minutes with  $\text{N}_2$ .  $\text{Pd}(\text{PPh}_3)_4$  (0.16g, 0.14mmol) was added under flow of  $\text{N}_2$  and the solution sparged for an additional ten minutes, then refluxed overnight. The flask was cooled to room temperature, and the solvents were removed under reduced pressure. The mixture was then sonicated in copious amounts of diethyl ether and filtered through celite. DCM was then added afterwards to elute the product. DCM was removed under reduced pressure. Then the crude mixture was sonicated in copious amounts of methanol and then gravity filtered to yield the product. (0.49g, 70%)  $^1\text{H NMR}$  (500 MHz, Chloroform-*d*)  $\delta$  8.86 (d,  $J = 1.7$  Hz, 1H), 8.82 (d,  $J = 5.0$  Hz, 1H), 8.76 – 8.73 (m, 1H), 8.52 – 8.50 (m, 1H), 8.04 – 8.01 (m, 2H), 7.91 – 7.80 (m, 3H), 7.75 – 7.70 (m, 3H), 7.66 – 7.62 (m, 2H), 7.39 – 7.33 (m, 6H), 7.28 (s, 1H), 6.95 – 6.91 (m, 2H), 3.87 (s, 2H).



**4-(9-(DtB-NDI-phenyl)anthracene-10-phenyl)-[2,2']bipyridinyl (5).** In an oven dried round bottom flask with a magnetic stirrer and reflux condenser, 4-(9-(aniline)anthracene-10-phenyl)-[2,2']bipyridinyl (0.09g, 0.18mmol), and N-(2,5-di-*t*-butyl) naphthalene-1,4-dicarboximide-5,8-dicarboxyanhydride (DtB-NIA) (0.11g, 0.234mmol), were dissolved in pyridine (100 mL) and heated to reflux under  $\text{N}_2$  overnight. The solution was cooled to room temperature and pyridine was removed in vacuo. The mixture was then dissolved in DCM and ran through a silica plug with copious of DCM until excess DtB-NIA was removed. Then the product was eluted using DCM:MeOH (10:1). The solution was then evaporated using a rotary evaporator. The residue was

sonicated in methanol, gravity filtered, and collected. The solid was then sonicated in acetone, gravity filtered, and collected. Yield (0.07g, 38%). **<sup>1</sup>H NMR** (500 MHz, Chloroform-*d*) δ 8.96 – 8.92 (m, 4H), 8.88 (d, *J* = 1.9 Hz, 1H), 8.83 (d, *J* = 5.0 Hz, 1H), 8.77 – 8.74 (m, 1H), 8.52 (dt, *J* = 8.0, 1.1 Hz, 1H), 8.05 (d, *J* = 8.1 Hz, 2H), 7.91 – 7.85 (m, 3H), 7.78 (dd, *J* = 7.5, 1.9 Hz, 2H), 7.73 (dd, *J* = 6.6, 4.1 Hz, 3H), 7.68 – 7.59 (m, 5H), 7.51 (dd, *J* = 8.6, 2.2 Hz, 1H), 7.47 – 7.40 (m, 4H), 7.37 (ddd, *J* = 7.5, 4.7, 1.2 Hz, 1H), 7.05 (s, 1H), 1.35 (s, 9H), 1.30 (s, 9H). **<sup>13</sup>C NMR** (126 MHz, CDCl<sub>3</sub>) δ 163.96, 163.37, 156.99, 156.31, 150.58, 149.99, 149.42, 149.27, 143.84, 140.18, 137.76, 137.17, 136.88, 136.27, 134.11, 132.62, 132.38, 132.38, 132.22, 132.13, 131.75, 131.71, 130.02, 129.98, 129.21, 128.82, 127.69, 127.59, 127.49, 127.46, 127.23, 127.17, 126.99, 126.89, 125.62, 125.56, 124.04, 121.76, 121.44, 119.38, 35.75, 34.47, 31.92, 31.37. **HRMS-ESI** (*m/z*): calculated C<sub>64</sub>H<sub>48</sub>N<sub>4</sub>O<sub>4</sub> [M + H]<sup>+</sup>: 937.3676, found 937.3766



#### 4-(9-(DtB-NDI-phenyl)anthracene-10-phenyl)-[2,2']bipyridinyl (4)

**(NDI-DPA-BpyRe(CO)<sub>3</sub>Cl)**. In the dark, and in a nitrogen filled glove box, an oven dried pressure flask with a magnetic stirrer was filled with compound 4-(4-bromoanthracene-phenyl)-[2,2']bipyridinyl (0.07g, 0.08mmol), pentacarbonylchlororhenium(I) (0.06g, 0.17mmol), and dichloromethane (25 mL). The pressure flask was capped, completely wrapped in aluminum foil, and brought out of the glovebox and heated to 80 °C overnight in the dark. The solution was cooled to room temperature and returned to the glovebox. Heptane was added to the mixture until the product precipitated out. The solution was then filtered. The solid was washed with minimal

acetone and collected. Yield (0.06g, 62%). **<sup>1</sup>H NMR** (500 MHz, Chloroform-*d*)  $\delta$  9.18 (d,  $J = 5.7$  Hz, 1H), 9.15 (dd,  $J = 5.5, 1.6$  Hz, 1H), 8.96 – 8.92 (m, 4H), 8.52 (d,  $J = 1.9$  Hz, 1H), 8.39 (d,  $J = 8.1$  Hz, 1H), 8.17 – 8.11 (m, 1H), 8.00 – 7.96 (m, 2H), 7.89 (td,  $J = 5.9, 2.7$  Hz, 3H), 7.77 – 7.70 (m, 6H), 7.63 (dd,  $J = 8.4, 6.5$  Hz, 4H), 7.51 (dd,  $J = 8.6, 2.2$  Hz, 1H), 7.49 – 7.41 (m, 4H), 7.05 (s, 1H), 1.35 (s, 9H), 1.30 (s, 9H). **<sup>13</sup>C NMR** (126 MHz, CDCl<sub>3</sub>)  $\delta$  163.95, 163.39, 156.25, 156.06, 153.63, 151.67, 150.60, 143.83, 142.34, 139.97, 139.68, 139.05, 136.79, 135.85, 135.32, 134.24, 132.96, 132.55, 132.11, 131.76, 131.73, 130.03, 129.85, 129.22, 129.12, 128.92, 128.89, 128.33, 128.14, 127.68, 127.59, 127.52, 127.38, 127.19, 126.92, 126.60, 125.84, 125.72, 125.14, 123.24, 121.19, 35.75, 34.47, 31.91, 31.37. **HRMS-ESI** ( $m/z$ ): calculated C<sub>67</sub>H<sub>48</sub>ClN<sub>4</sub>O<sub>7</sub>Re [M]<sup>+</sup>: 1242.2769, found 1242.2774, [M + NH<sub>4</sub><sup>+</sup>]<sup>+</sup> 1260.3113, found 1260.3113, [M + Na<sup>+</sup>]<sup>+</sup> 1265.2667, found 1265.2682.

## 4.8 Supplementary Details

### 4.8.1 Transient Absorption SVD/global fitting

#### Processing / Fitting of Time-Resolved Optical Spectroscopy Data.

*Femtosecond Spectroscopy*: Prior to kinetic analysis, the fsTA & fsIR data are background/scatter-subtracted and chirp-corrected, and the visible and NIR data sets are spectrally merged (Surface Xplorer 4, Ultrafast Systems, LLC).

#### Global Analysis.

The kinetic analysis was performed using home written programs in MATLAB<sup>179</sup> and was based on a global fit to kinetic vectors following singular value decomposition. The time-resolution is given as  $w = 250$  fs (full width at half maximum, FWHM); the assumption of a

uniform instrument response across the frequency domain and a fixed time-zero ( $t_0$ ) are implicit in global analysis.

*Singular Value Decomposition.* Factoring of the two-dimensional (signal vs time & frequency) data set by Singular Value Decomposition (SVD) is performed as implemented in the MATLAB software package.<sup>179</sup> This factoring produces an orthonormal set of basis spectra that describe the wavelength dependence of the species and a corresponding set of orthogonal vectors that describe the time-dependent amplitudes of the basis spectra.<sup>180</sup> These kinetic vectors are then fit using the global analysis method described below.

*Multiple-Wavelength Global Fitting.* The kinetic data from multiple different wavelengths are fit using the global analysis described below. Each wavelength is given an initial amplitude that is representative of the spectral intensity at time  $t_0$ , and varied independently to fit the data. The time/rate constants and  $t_0$  are shared between the various kinetic data and are varied globally across the kinetic data in order to fit the model(s) described below.

*Species-Associated Fitting.* We globally fit the dataset to a specified kinetic model and use the resultant populations to deconvolute the dataset and reconstruct species-associated spectra.

*1<sup>st</sup> order model:*

We use a first-order kinetic model with rate matrix  $K$ :

$$\underline{\underline{K}} = \begin{pmatrix} -k_{A \rightarrow B} & 0 \\ k_{A \rightarrow B} & -k_{B \rightarrow g} \end{pmatrix} \quad (\text{Eqn. S4.1})$$

The MATLAB program numerically solves the differential equations through matrix methods,<sup>181</sup> then convolutes the solutions with a Gaussian instrument response function with width

$w$  (FWHM), before employing a least-squares fitting using a Levenberg-Marquardt or Simplex method to find the parameters which result in matches to the kinetic data.

*Spectral Reconstruction.* Once the fit parameters are established, they are fed directly into the differential equations, which were solved for the populations of the states in model—i.e.,  $A(t)$  and  $B(t)$ . Finally, the raw data matrix (with all the raw data) is deconvoluted with the populations as functions of time to produce the spectra associated with each species.

**Chapter 5 Substituent Location Dependence of Photoinduced Electron Transfer Lifetimes to  $\text{Re}(\text{bpy})(\text{CO})_3\text{X}$  from a Naphthalene Diimide Radical Anion Donor: Effects of Electronic Coupling and Gibbs Free Energy**

## 5.1 Introduction

Natural photosynthesis utilizes solar photons to initiate and drive the conversion of solar energy into chemical energy. Many research groups have focused a great deal of time into understanding, mimicking, and improving upon the natural photosynthetic pathways, giving rise to artificial photosynthesis. One of the most critical components of natural photosynthesis that is replicated in artificial photosynthesis are photoinduced electron-transfer (ET) reactions. These photoinitiated processes are needed to produce charge-separated (CS) states that carry out redox processes important to bond formation reactions.<sup>182-183</sup> Precise control of the rates of formation and decay of charge separated species in these supramolecular artificial photosynthesis systems is important to maximize the utility of photogenerated CS states.

Natural photosynthesis provides the primary bioinspiration for developing the molecular architectures necessary to achieve rapid charge separation as well as slow charge recombination. For example, absorption of solar photons by chlorophylls in the photosystem II reaction center protein complex in green plants results in oxidation of the P680 special pair chlorophyll dimer, which in turn oxidizes an adjacent tyrosine. This tyrosine functions as a redox intermediate that transfers oxidizing equivalents to the water splitting CaMn<sub>4</sub> cluster from P680<sup>\*+</sup>.<sup>13-14</sup> These naturally occurring processes demonstrate the importance of balancing energetics, distances, and electronic coupling in order to produce CS species to conduct catalysis, whether it be for CO<sub>2</sub> reduction or water splitting. Quite often the rate for electron transfer for these CS states in donor acceptor systems that mimic nature can be modelled by the Marcus equation:

$$k_{ET, \text{ Marcus}} = \frac{2\pi|H_{if}|^2}{\hbar\sqrt{4\pi\lambda k_B T}} \exp\left(-\frac{(\Delta G^\circ + \lambda)^2}{4\lambda k_B T}\right) \quad (1)$$

where  $\Delta G^\circ$  is the standard free energy change for the ET reaction,  $\lambda$  is the reorganization energy,  $H_{if}$  is the electronic coupling between the donor and acceptor,  $T$  is the temperature and  $k_b$  is Boltzmann's constant.

As the rising concentration of  $\text{CO}_2$  in the atmosphere continues to plague us with global warming issues, one approach to mitigate its effects is to utilize the solar spectrum to transform carbon dioxide into fuel, much like how plants utilize sunlight to transform  $\text{CO}_2$  into glucose.<sup>13</sup> One of the most utilized transition metal complexes for homogenous catalytic transformation of  $\text{CO}_2$  is *fac*- $\text{Re}(\text{bpy})(\text{CO})_3\text{X}$  ( $\text{bpy} = 2,2'$ -bipyridine), where  $\text{X}$  can range from a wide variety of monodentate coordinating ligands.<sup>31, 63, 65</sup> The photocatalytic ability of rhenium polypyridyl complexes for  $\text{CO}_2$  photoreduction was first studied in the 1980's by Lehn, Ziessel, and Hawecker where they were able to demonstrate that the complex reduces  $\text{CO}_2$  with high efficiency and high selectivity towards formation of  $\text{CO}$ .<sup>184</sup> Because of the high product selectivity and high  $\text{CO}_2$  reduction efficiency of these complexes, researchers have explored different avenues to improve their catalytic rate and stability. To improve photo- and electro- catalytic performance, researchers turned to tuning the steric hindrance and redox potentials of the complex through substitution on the bipyridine, most commonly at the 4 position,<sup>22, 63, 104</sup> less commonly at the 5 position,<sup>185-186</sup> and rarely at the 6 position. Modification of the  $\text{X}$  ligand has also been pursued. As Kubiak demonstrated by studying a plethora of substituents at the 4,4' bipyridine position as well as by changing the  $\text{X}$  ligand,  $\text{Re}(4,4'\text{-R-bpy})(\text{CO})_3\text{X}$  ( $\text{R} = \text{OCH}_3, \text{CH}_3, \text{tBu}, \text{H}, \text{CN}, \text{CF}_3$ ;  $\text{X} = \text{Cl}, \text{Br}, \text{Py}(\text{OTf}), \text{or } \text{CH}_3\text{CN}(\text{OTf}), \text{OTF} = \text{trifluoromethanesulfonate}$ ), substituents on the 4,4' position of the bipyridine ring alter the first redox potential of archetypal  $\text{Re}(4,4'\text{-R-bpy})(\text{CO})_3\text{X}$  complexes while changing the  $\text{X}$  ligand affects both first and second redox potentials.<sup>63</sup> Whereas the electron-donating ability of the 4,4' substituent determined the first redox potential and stability of the

corresponding catalyst,<sup>63</sup> complexes who had the same 4,4' substituents, but different X ligands reported the same electrocatalytic ability towards CO<sub>2</sub> reduction. With regards to photocatalytic CO<sub>2</sub> reduction activity, Ishitani illustrated that while maintaining the 4,4' substituent constant and by changing the X ligand through a series of different coordinating phosphine ligands made the first reduction of Re(bpy)(CO)<sub>3</sub>X more difficult, which in turn resulted in better photocatalytic CO<sub>2</sub> reduction activity.<sup>31</sup>

As demonstrated, different substituents on the bipyridine ring and different coordinating ligands have effects on the redox potentials and stability of Re(bpy)(CO)<sub>3</sub>X, which in turn have different effects on photo- and electrocatalysis of CO<sub>2</sub>. We therefore sought to see how the different position of a photosensitizer around a bipyridine ligand in conjunction with a different X ligand could improve the charge separation lifetimes as the lifetimes and energetics of charge separated species are intrinsically related to photocatalytic CO<sub>2</sub> reduction performances.<sup>187-188</sup> To the best of our knowledge, no systematic study has been conducted on photoinduced electron transfer reactions from a chromophore to Re(bpy)(CO)<sub>3</sub>X through the 4, 5, and 6 positions of bipyridine.

Bipyridine substituted at the 4 position is by far the most commonly studied location for a chromophore. Ishitani developed supramolecular Re(bpy)(CO)<sub>3</sub>X systems by covalently attaching Ru-based chromophores to Re(bpy)-based catalysts at the 4-bipyridine position to form Ru<sup>II</sup>(dmb)<sub>3</sub>-Re<sup>I</sup>(dmb)(CO)<sub>2</sub>L<sub>1</sub>L<sub>2</sub>.<sup>31</sup> The perutz group developed metalloporphyrins that link through the 4-position on bipyridine to form [Re<sup>I</sup>(CO)<sub>3</sub>(3-picoline)-4-bpy-MTPP][OTf], where M = Zn or Mg, OTf, and TPP = tetraphenylporphyrin.<sup>43</sup> Recently, quarterpyridine (qpy), which can be viewed as two bipyridines linked to one another via the 5-position on bipyridine, was utilized as a binding ligand to form the [(bpy)<sub>2</sub>Ru<sup>II</sup>]-[qpy]-[Re(CO)<sub>3</sub>Cl] dinuclear complexes.<sup>186</sup> Electron

transfer to  $\text{Re}(\text{bpy})(\text{CO})_3\text{X}$  via the 6- position of bipyridine is rare, and no direct electron transfer through a bridge has been demonstrated. Instead, Gray and Grubbs demonstrated that by linking phenothiazine (PTZ) via a tris(meta-phenylene-ethynylene) bridge to form  $\text{Re}(\text{PTZ-Tris}(\text{Meta-Phenylene-Ethynylene})\text{-6-bpy})(\text{CO})_3\text{Py}$ , had a 20 Å distance through space between the PTZ and  $\text{Re}(\text{bpy})(\text{CO})_3\text{Py}$ . This complex was capable of folding in on itself to form a structural conformer that brought the PTZ donor within 7 Å of the  $\text{Re}(\text{bpy})(\text{CO})_3\text{Py}$  which could undergo through-space electron transfer when the MLCT of Re was excited with a 400 nm laser pulse and subsequently quenched by the PTZ donor.<sup>189</sup>

In light of these scattered examples of electron transfer to  $\text{Re}(\text{bpy})(\text{CO})_3\text{X}$  through the 4, 5, 6-positions of bipyridine in  $\text{Re}(\text{bpy})(\text{CO})_3\text{X}$  complexes, we started to systematically investigate the electron transfer rates from chromophores to  $\text{Re}(\text{bpy})(\text{CO})_3\text{X}$ , a key component for the development of artificial photosystems where the CS states are generated via photoreduction processes. We recently demonstrated the utility of naphthelenediimide (NDI) and perylenediimide (PDI) radical anions as chromophores bound through the 4-position of bipyridine in  $[\text{Re}(\text{bpy})(\text{CO})_3\text{Py}][\text{PF}_6]$  complexes.<sup>190</sup>  $\text{NDI}^-$  and  $\text{PDI}^-$  are all-organic super-reductant chromophores formed through mild reduction using TDAE or with a platinum electrode, with an excited-state oxidation potential of -2.1 V vs SCE, exceeding that of currently utilized metalorganics and organometallic chromophores. These chromophores offer several other advantageous properties as well: their absorption spectra span the entire visible region and extend into the near-infrared region; they can be easily coupled using well-developed synthetic techniques to many organic and organometallic electron acceptors; and their extremely negative excited-state oxidation potentials make them able to reduce extremely thermodynamically demanding substrates

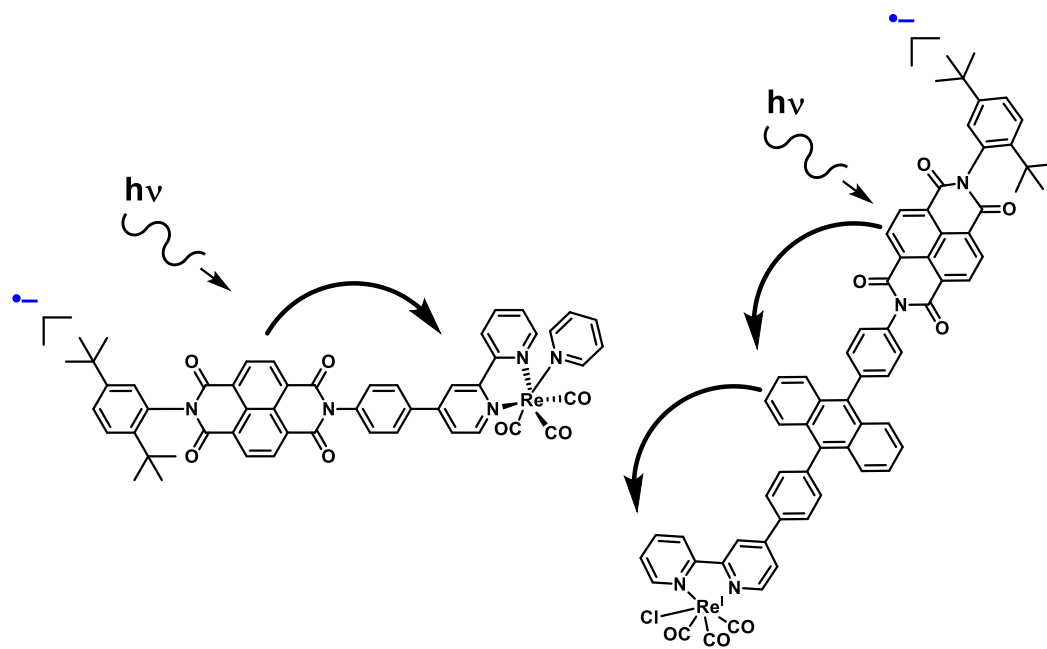


**Figure 5.1:** Photoinduced Electron transfer from  $\text{NDI}^{\bullet-}$  to  $\text{Re}(\text{bpy})(\text{CO})_3$  via various attachment motifs and distances.

like  $\text{Re}(\text{bpy})(\text{CO})_3\text{X}$  and successive intermediates in its catalytic cycle. As shown in Figure 5.1, our previous work demonstrated that attaching NDI to the 4-position of bipyridine with a phenyl spacer to form  $[\text{Re}(4\text{-bpy-NDI})(\text{CO})_3\text{Py}][\text{PF}_6]$  and photoexciting the chemically generated  $\text{NDI}^{\bullet-}$  leads to charge separation from  $^*\text{NDI}^{\bullet-}$  to  $[\text{Re}(\text{bpy})(\text{CO})_3\text{Py}][\text{PF}_6]$  with a charge separated time constant of  $\tau_{\text{CS}} = 0.4 \pm 0.3$  ps to form  $[\text{Re}(\text{bpy}^{\bullet-})(\text{CO})_3\text{Py}][\text{PF}_6]$ , with charge recombination back to the ground state occurring with a lifetime of  $\tau_{\text{CR}} = 31.8 \pm 0.8$  ps. By including an intermediate acceptor between the  $\text{NDI}^{\bullet-}$  and  $\text{Re}(\text{bpy})(\text{CO})_3\text{X}$ , the lifetime of the charge-separated state was extended further. This was accomplished by coupling NDI to diphenylanthracene (DPA) which in turn was coupled to the bipyridine. Transient absorption experiments showed that upon excitation of the  $\text{NDI}^{\bullet-}$ ,  $\text{Re}(4\text{-bpy}^{\bullet-}\text{-DPA-NDI})(\text{CO})_3\text{Cl}$  had a lifetime of the charge-separated state of  $\tau_{\text{CR}} = 24.5 \pm 0.2$  ns. Given these results, we sought to extend charge separation lifetimes in

Re(bpy<sup>-</sup>-NDI)(CO)<sub>3</sub>X complexes through investigation of different substitution locations on bipyridine. We also sought to explore the influence of the X ligand, given that these substitutions both affect the photo- and electrocatalytic properties of Re(bpy)(CO)<sub>3</sub>X complexes. These results can be extended to understand and improve CS states formed during photocatalysis of Re(bpy)(CO)<sub>3</sub>X supramolecular structures. Outside the scope of Re(bpy)(CO)<sub>3</sub>X, bipyridine is one of the most widely used ligands, illustration of the effect of substituent position on charge separation and recombination rates will impact rational design of donor-acceptor complexes employing bipyridine ligands.

In the present report, we describe the synthesis, electrochemistry, time-resolved UV/Vis/Near-IR/Mid-IR spectroscopy, and calculated electronic coupling of molecular dyads with NDI covalently attached through a phenyl bridge to the 4, 5, and 6 positions of bipyridine to form Re(bpy-Ph-NDI)(CO)<sub>3</sub>X (Re(bpy-NDI)(CO)<sub>3</sub>X) complexes, depicted in Scheme 5.1. Chemical reduction of Re(bpy-NDI)(CO)<sub>3</sub>X with tetrakis(dimethylamino)ethylene (TDAE) leads to the selective reduction of the NDI component<sup>45, 74, 190</sup> to form Re(bpy-NDI<sup>-</sup>)(CO)<sub>3</sub>X (**1<sup>-</sup>-6<sup>-</sup>**). Transient absorption spectroscopy on complexes **1<sup>-</sup>-6<sup>-</sup>** proceed with similar spectral features but with different kinetics. Selective excitation of NDI<sup>-</sup> at 605 nm first yields the excited state \*NDI<sup>-</sup> which undergoes oxidative quenching to transfer an electron to Re(bpy)(CO)<sub>3</sub>X, leading to the formation of Re(bpy<sup>-</sup>)(CO)<sub>3</sub>X. Forward electron transfer ( $\tau_{FET}$ ) occurs in approximately one picosecond while back electron transfer ( $\tau_{BET}$ ) occurs in tens of picoseconds, with the trend  $\tau_{BET_3} > \tau_{BET_2} > \tau_{BET_1}$  and  $\tau_{BET_6} > \tau_{BET_5} > \tau_{BET_4}$ . Charge separation lifetimes in the analogous cationic complexes demonstrate that by when the substituent location of NDI<sup>-</sup>-Ph fragment is kept constant,  $\Delta G_{BET}$  dictates the  $\tau_{BET}$ , resulting in pyridine substituted complexes with longer  $\tau_{BET}$

than their neutral counterparts:  $\tau_{BET_6} > \tau_{BET_3}$ ,  $\tau_{BET_5} > \tau_{BET_2}$ , and  $\tau_{BET_4} > \tau_{BET_1}$ . Instead, by changing the substituent location of NDI<sup>-</sup>-Ph around bipyridine but keeping same X ligand,  $\Delta G_{BET}$  does not dictate the  $\tau_{BET}$  but instead the electronic couplings ( $|H_{if}(\varphi)|$ ).

Electronic couplings  $|H_{if}(\varphi)|$  were computed for the back-ET reaction  $[\text{Re}(\text{bpy})(\text{CO})_3\text{X}^{\bullet-}][\text{NDI}] \rightarrow [\text{Re}(\text{bpy})(\text{CO})_3\text{X}][\text{NDI}^{\bullet-}]$  which illustrated that  $|H_{if}^B|$  decreases as the NDI<sup>-</sup>-Ph moves from the 4 to the 5 to the 6 positions of bipyridine with the trend  $H_1 > H_2 > H_3$  and  $H_4 > H_5 > H_6$ . These results correlate with the observed trends in the lifetimes of the respective charge separated species. Thus, electronic coupling  $|H_{if}^B|$  between the NDI<sup>-</sup>-Ph substituent and  $\text{Re}(\text{bpy})(\text{CO})_3\text{Cl}$  at the 4, 5, and 6 position of bipyridine is the key factor governing the rate of electron transfer.

## 5.2 Experimental Details

### 5.2.1 Materials.

Dichloromethane, acetone, acetonitrile, and methanol used for synthesis were obtained from Fisher Scientific and used as received. Dimethylformamide (DMF) used for synthesis and spectroscopic experiments was dried on a commercial system (GlassContour, Laguna Beach, CA). For spectroscopy, DMF was further transferred under argon into a N<sub>2</sub>-filled glovebox (MBraun Unilab) for use and storage. Commercially available reagents were purchased from Sigma-Aldrich or Oakwood Chemicals and used as received. Compounds were reduced in the glovebox using tetrakisdiaminoethylene (TDAE) from Tokyo Chemical Industries. UV/Vis/NIR absorbance spectroscopy was performed on a Shimadzu UV-1601 spectrometer at 298 K.

### 5.2.2 Electrochemistry.

Electrochemical measurements were performed using a CH Instruments Model 660A electrochemical workstation. A single-compartment cell was used for all cyclic voltammetry experiments with a 1.0 mm diameter glassy carbon disk working electrode, a platinum wire counter electrode, a silver wire pseudoreference electrode, and 0.1 M tetrabutylammonium hexafluorophosphate as the supporting electrolyte in DMF. The ferrocene/ferrocenium redox couple (0.45 V vs SCE)<sup>79</sup> was used as an internal standard. TBAPF<sub>6</sub> was recrystallized twice from ethanol prior to use. Electrochemical cells were shielded from light during experiments. All solutions were continuously purged with argon before and during the cyclic voltammetry experiments. Solutions of rhenium complexes were prepared in concentrations of 0.5 mM for cyclic voltammetry experiments.

### 5.2.3 Femtosecond Transient Vis/NIR Absorption Spectroscopy.

Femtosecond transient absorption experiments were performed employing a regeneratively amplified Ti:sapphire laser system operating at 828 nm and a 1 kHz repetition rate as previously described.<sup>80-81</sup> The output of the amplifier was frequency-doubled to 414 nm using a BBO crystal and that light was used to pump a laboratory-built collinear optical parametric (OPA) amplifier for visible-light excitation<sup>159</sup> or a commercial non-collinear optical parametric amplifier (TOPAS-White, Light-Conversion, LLC.) for NIR excitation. Approximately 1-3 mW of the fundamental was focused onto a sapphire disk to generate the visible white-light probe spanning 430-850 nm, onto a 5 mm quartz cuvette containing a 1:1 mixture of H<sub>2</sub>O:D<sub>2</sub>O to generate a UV/visible white light probe spanning 385-750 nm, or onto a proprietary medium (Ultrafast Systems, LLC) to generate the NIR white-light probe spanning 850-1620 nm. The total instrument response function

was 300 fs. Experiments were performed at a randomized pump polarization to suppress contributions from orientational dynamics. Spectral and kinetic data were collected with a CMOS or InGaAs array detector for visible and NIR detection, respectively, and a 8 ns pump-probe delay track (customized Helios, Ultrafast Systems, LLC). Transient spectra were averaged for at least 3 seconds. Gaps in the spectra shown are due to either scattering of the pump or idler beam, or regions not covered by the detectors. Samples prepared in DMF had an absorbance of 0.2-0.7 at the excitation wavelength and were irradiated in 2 mm quartz cuvettes with 0.4-0.8  $\mu\text{J}/\text{pulse}$  focused to  $\sim 0.2$  mm diameter spot. Samples were stirred to avoid effects of local heating or sample degradation. The samples were prepared in the glovebox and degassed by multiple freeze-pump-thaw cycles prior to analysis.

#### **5.2.4 Nanosecond transient absorption spectroscopy.**

Nanosecond transient absorption experiments were performed using the femtosecond excitation beam described above and a commercial spectrometer (Eos, Ultrafast Systems, LLC) utilizing a photonic crystal fiber ultra-broadband probe source. The pump polarization was randomized to suppress rotational dynamics. Samples were stirred to avoid effects of local heating or sample degradation.

#### **5.2.5 Femtosecond time-resolved mid-IR spectroscopy.**

Femtosecond transient mid-IR absorption (fsIR) spectroscopy was performed using a commercial Ti:sapphire oscillator/amplifier (Solstice 3.5W, Spectra-Physics) to pump two optical parametric amplifiers (TOPAS-C, Light Conversion), one which provided a 100 fs, 605 nm excitation pulse and the other provided 100 fs pulses at 2150-1800  $\text{cm}^{-1}$ . The overall instrument response was 300 fs. The spectra were acquired with a liquid  $\text{N}_2$ -cooled dual channel (2 x 64) MCT

array detector that is coupled to a Horiba HR320 monochromator as part of a Helios-IR spectrometer (Ultrafast Systems, LLC). Samples with a maximum optical density of 1.5 at the excitation wavelength were prepared in DMF contained in a liquid demountable cell (Harrick Scientific) with 2.0 mm thick CaF<sub>2</sub> windows and a 500 μm Teflon spacer. During data acquisition, the cell was mounted and rastered on a motorized stage to prevent sample degradation.

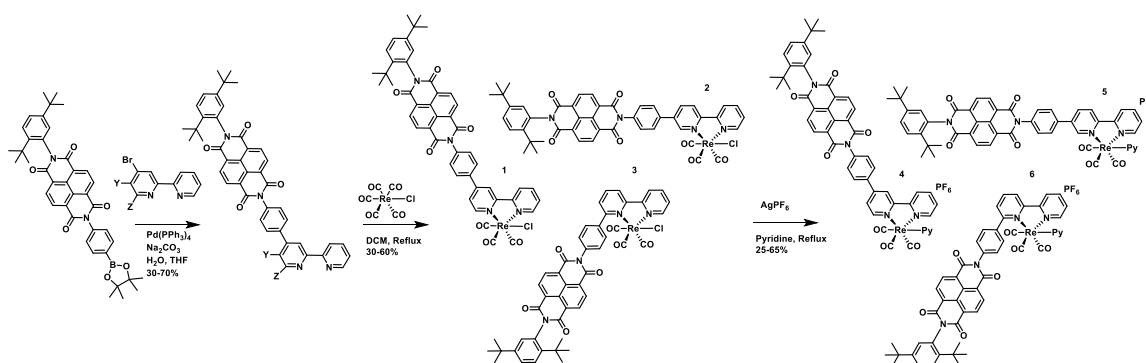
### 5.2.6 Computational methods.

DFT calculations were performed using a combination of Gaussian 09 and QChem 5.0. Geometry optimizations and TDDFT calculations were performed at B3LYP/6-31G+(d) level of theory in the presence of polarizable continuum DMF solvent implemented using the C-PCM solvation model in Gaussian 09. A double zeta effective core potential basis (LANL2DZ) was used for the Re atom in all the above-mentioned calculations. To reduce computational cost the *t*-butyl groups were replaced by methyl groups, since the *t*-butyl substituent does not affect the spectroscopic properties of such complexes. To consider thermal fluctuations, multiple configurations were obtained by performing constrained optimizations keeping a dihedral  $\varphi$  between the NDI and Re(bpy)(CO)<sub>3</sub>X<sup>−</sup> parts of the complexes fixed at different values in increments of 30°. The constrained optimizations were done in Gaussian 09 at B3LYP/Def2SVP level of theory in a SMD dielectric continuum of DMF. Electronic couplings  $|H_{if}(\varphi)|$  were computed using the direct diabatic-state method implemented in QChem 5.0 at HF/Def2TZVP level of theory. A C-PCM dielectric continuum solvent model of DMF was used in all the coupling calculations.

## 5.3 Results

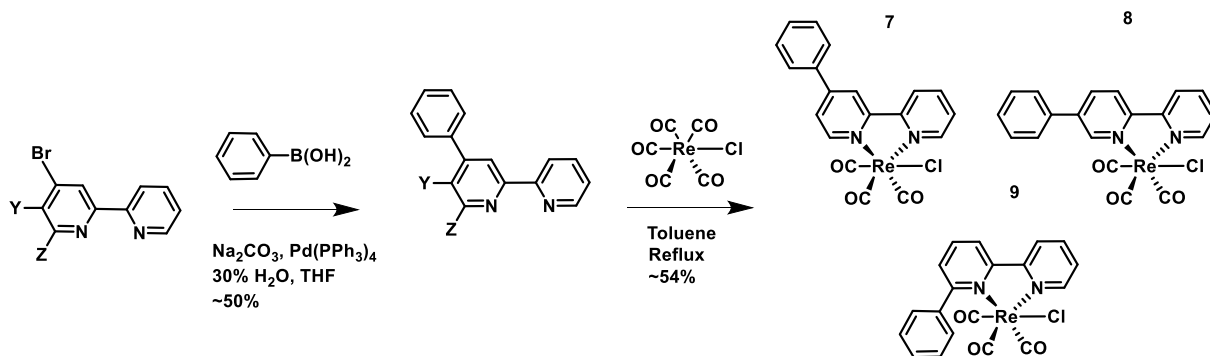
### 5.3.1 Synthesis

Complexes **1** ( $\text{Re}(\text{4-bpy-NDI})(\text{CO})_3\text{Cl}$ ), **2** ( $\text{Re}(\text{5-bpy-NDI})(\text{CO})_3\text{Cl}$ ), **3** ( $\text{Re}(\text{6-bpy-NDI})(\text{CO})_3\text{Cl}$ ) and **4** ( $[\text{Re}(\text{4-bpy-NDI})(\text{CO})_3\text{Py}][\text{PF}_6]$ ), **5** ( $[\text{Re}(\text{5-bpy-NDI})(\text{CO})_3\text{Py}][\text{PF}_6]$ ), **6** ( $[\text{Re}(\text{6-bpy-NDI})(\text{CO})_3\text{Py}][\text{PF}_6]$ ) were prepared as illustrated in Scheme 5.1 and detailed in 5.7. The NDI-Ph-Bpin<sup>191</sup> was Suzuki coupled<sup>192</sup> with the corresponding 4-, 5-, or 6-bromo-2,2'-bipyridine to form the corresponding 4-, 5-, or 6-phenyl-NDI-2,2'-bipyridine. Each ligand was then refluxed in dry dichloromethane under nitrogen with pentacarbonylchlororhenium(I) to form **1**, **2**, and **3**, respectively. Complexes **1**, **2**, and **3**, were then heated to 80°C in pyridine with silver hexafluorophosphate to yield their respective pyridine complexes, **4**, **5**, and **6**.



**Scheme 5.1:** Synthetic scheme for  $\text{Re}(\text{4-, 5-, 6-(bpy-NDI})(\text{CO})_3\text{Cl}$  (**1**, **2**, **3**) and  $[\text{Re}(\text{4-, 5-, 6-bpy-NDI})(\text{CO})_3\text{Py}][\text{PF}_6]$  (**4**, **5**, **6**)

Model complexes **7**, **8**, and **9** were synthesized as illustrated in Scheme 5.2 and detailed in 5.7. The corresponding 4-, 5-, or 6-bromo-2,2'-bipyridine was Suzuki coupled with phenylboronic acid. Each ligand was then refluxed in dry dichloromethane under nitrogen with pentacarbonylchlororhenium(I) to form **7**, **8**, and **9**, respectively.



**Scheme 5.2:** Synthetic scheme for  $\text{Re}(4\text{-}, 5\text{-}, 6\text{-Ph-bpy})(\text{CO})_3\text{Cl}$  (**7**, **8**, **9**)

### 5.3.2 Electrochemistry

Cyclic voltammetry experiments were conducted on complexes **1-6** to measure the effect of including a NDI-phenyl substituent on the redox potentials as well to estimate the Gibbs free energy of photoinduced electron transfer from NDI to the corresponding bound rhenium complex shown in Figure 5.2. The redox potentials are tabulated in Table 5.1 and Table 5.2. Cyclic voltammetry experiments were conducted on complexes **7-9** to understand the influence of solely the phenyl substituent on the redox properties of each rhenium complex. Cyclic voltammetry redox

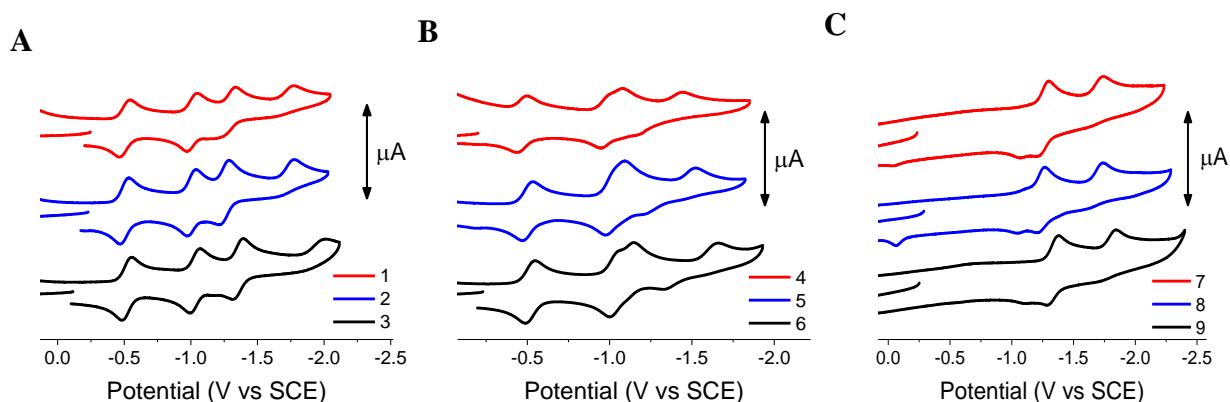


**Figure 5.2:** Cyclic voltammograms of 0.5 mM DMF solutions of complexes **1-3** (A), **4-6** (B), and **7-9** (C), recorded at  $100 \text{ mVs}^{-1}$  at room temperature with 0.1 M  $\text{TBAPF}_6$  as supporting electrolyte. Potentials are reported versus ( $\text{Fc}/\text{Fc}^+$  occurs at 0.45 V vs SCE in DMF).

potentials for each complex are shown in Figure 5.2. The redox potentials are tabulated in Table 5.3.

For complexes **1-3**, where the rhenium complex has a bound chloride ligand, the voltammogram first displays two reductions near  $-0.51$  V and  $-1.01$  V. These reversible processes are the formation of the radical anion of NDI ( $\text{NDI}^{\bullet-}$ ) and the dianion of NDI ( $\text{NDI}^{2-}$ ). These reductions are followed by the one electron reduction of the bipyridine ligand ( $\text{bpy}^{\bullet-}$ ) between  $-1.25$  V and  $-1.36$  V. A subsequent one electron irreversible reduction of the rhenium center follows  $\text{Re-Cl}^{I/0}$ , coinciding with the loss of the chloride ligand. For complexes **1** and **2** the reduction of the rhenium center occurs at  $-1.77$  V while in complex **3** this reduction occurs at  $-2.01$  V, a 240mV difference.

**Table 5.1:** Redox potentials of complexes **1-3** vs SCE ( $\text{Fc}/\text{Fc}^+$  reference at 0.45 V vs SCE in DMF)

Complex #	$\text{NDI}^{0/-}$	$\text{NDI}^{-/2-}$	$\text{bpy}^{0/-}$	$\text{Re-Cl}^{I/0}$
Complex <b>1</b>	$-0.51$	$-1.02$	$-1.34$	$-1.77$
Complex <b>2</b>	$-0.50$	$-1.01$	$-1.29$	$-1.77$
Complex <b>3</b>	$-0.52$	$-1.01$	$-1.39$	$-2.01$

For complexes **4-6**, where the rhenium complex has a bound pyridine ligand and is positively charged, the voltammogram first displays two reductions near  $-0.50$  V and  $-1.01$  V. These reversible reduction processes correspond to the formation of  $\text{NDI}^{\bullet-}$  and  $\text{NDI}^{2-}$ , respectively. These reductions are followed by the one electron reduction of the bipyridine ligand between  $-1.08$  V and  $-1.15$  V. A subsequent one electron irreversible reduction of the rhenium center follows. For complexes **4** and **5** this reduction occurs at  $-1.45$  V and  $-1.52$  V, respectively, while in complex **6** this reduction occurs at  $-1.67$  V.

**Table 5.2:** Redox potentials of complexes **4-6** vs SCE (Fc/Fc<sup>+</sup> reference at 0.45 V vs SCE in DMF)

Complex #	NDI <sup>0/-</sup>	NDI <sup>-/2-</sup>	bpy <sup>0/-</sup>	Re-py <sup>I/0</sup>
Complex <b>4</b>	-0.49	-1.00	-1.08	-1.47
Complex <b>5</b>	-0.50	-1.01	-1.10	-1.52
Complex <b>6</b>	-0.52	-1.03	-1.15	-1.67

Complexes **7-10** display two reduction peaks, the first reduction corresponds to the reduction of the coordinated bipyridine (bpy<sup>•-</sup>) while the second reduction corresponds to reduction of the rhenium center (Re-Cl<sup>I/0</sup>), coinciding with the loss of the chloride ligand. On the reverse scan, there is a small anodic peak that appears in each complex that is slightly more positive than the bpy<sup>0/-</sup> anodic wave. This anodic wave represents the reoxidation of the radicals [Re(R-bpy<sup>0/-</sup>)(CO)<sub>3</sub>(DMF)]; formed by the labile radical anions by dissociation of Cl<sup>-</sup> from their respective complex and rapid coordination of the solvent ligand.<sup>65</sup>

**Table 5.3.** Redox potentials of complexes **7-10** vs SCE (Fc/Fc<sup>+</sup> reference at 0.45 V vs SCE in DMF)

Complex #	bpy <sup>0/-</sup>	Re-Cl <sup>I/0</sup>
Complex <b>7</b>	-1.31	-1.75
Complex <b>8</b>	-1.27	-1.74
Complex <b>9</b>	-1.40	-1.86
Complex <b>10</b>	-1.35	-1.80

### 5.3.3 Electron Transfer Energetics

Based on the redox potentials shown above, the Gibbs free energy for the excited state electron transfer reactions of complex  $\mathbf{1}^- - \mathbf{6}^-$  can be estimated using the following equation:

$$\Delta G_{\text{ET}} = E(\text{NDI}^{\bullet-}/\text{NDI}) - E(\text{A}^{\bullet-}/\text{A}) - E_{\text{D}_1}(*\text{NDI}^{\bullet-}) \quad (2)$$

where  $E(\text{NDI}^{\bullet-}/\text{NDI})$  is the reduction potential of NDI and  $E(\text{A}^{\bullet-}/\text{A})$  is the reduction potential of the complex of interest, and  $E_{\text{D}_1}$  is the energy of the  $*\text{NDI}^{\bullet-}$  excited state, assuming electron transfer occurs from the  $\text{D}_1$  state. The  $\text{D}_1 \leftarrow \text{D}_0$  transition of  $\text{NDI}^{\bullet-}$  absorbs at 785 nm, making  $E_{\text{D}_1} = 1.58$  eV. There is no electrostatic work term for this reaction because the reaction is a charge shift, not a charge separation. In addition, there is no solvation correction term because the FsTA and electrochemical experiments are performed in the same high polarity solvent. The Gibbs free energy for the thermal forward and back electron transfer reactions can be estimated using the following equation:

$$\Delta G_{\text{ET}} = E(\text{A}^{\bullet-}/\text{A}) - E(\text{NDI}^{\bullet-}/\text{NDI}) \quad (3)$$

From the equations above, the Gibbs free energies for each electron transfer step are shown in Table 5.4 below.

**Table 5.4:** Free energy changes for electron transfer reactions in complex **1<sup>-</sup>** - **6<sup>-</sup>**.

compound	process	$\Delta G$ (eV)
<b>1<sup>-</sup></b>	*NDI <sup>-</sup> $\rightarrow$ Re(4-bpy)Cl	-0.78
<b>2<sup>-</sup></b>	*NDI <sup>-</sup> $\rightarrow$ Re(5-bpy)Cl	-0.82
<b>3<sup>-</sup></b>	*NDI <sup>-</sup> $\rightarrow$ Re(6-bpy)Cl	-0.69
<b>4<sup>-</sup></b>	*NDI <sup>-</sup> $\rightarrow$ Re(4-bpy)Py	-0.45
<b>5<sup>-</sup></b>	*NDI <sup>-</sup> $\rightarrow$ Re(5-bpy)Py	-0.50
<b>6<sup>-</sup></b>	*NDI <sup>-</sup> $\rightarrow$ Re(6-bpy)Py	-0.52
<b>1<sup>-</sup></b>	Re(4-bpy <sup>*-</sup> )Cl $\rightarrow$ NDI <sup>0</sup>	-0.83
<b>2<sup>-</sup></b>	Re(5-bpy <sup>*-</sup> )Cl $\rightarrow$ NDI <sup>0</sup>	-0.79
<b>3<sup>-</sup></b>	Re(6-bpy <sup>*-</sup> )Cl $\rightarrow$ NDI <sup>0</sup>	-0.92
<b>4<sup>-</sup></b>	Re(4-bpy <sup>*-</sup> )Py $\rightarrow$ NDI <sup>0</sup>	-0.63
<b>5<sup>-</sup></b>	Re(5-bpy <sup>*-</sup> )Py $\rightarrow$ NDI <sup>0</sup>	-0.60
<b>6<sup>-</sup></b>	Re(6-bpy <sup>*-</sup> )Py $\rightarrow$ NDI <sup>0</sup>	-0.63

### 5.3.4 Steady-State Spectroscopy

Complexes **1-6** all exhibit very similar steady-state spectroscopic features in both the UV/Vis/NIR and mid-IR regions. Representative steady-state spectra for complex **3** are shown in Figure 5.3, and the full set of spectra are given in Figures 5.18-5.29.

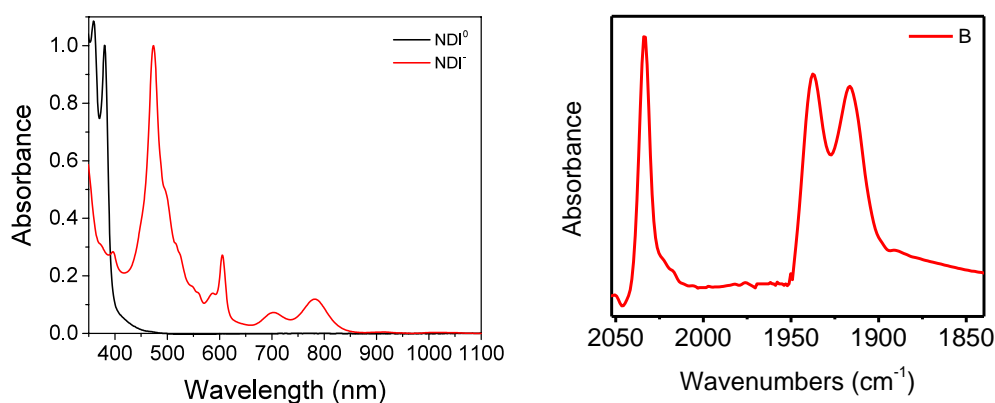


**Figure 5.3:** UV/Visible/NIR (left) and mid-IR (right) steady-state spectra of **3** in DMF without (black) and with excess TDAE (red). The mid-IR spectrum is identical in the presence or absence of TDAE.

Before reduction by TDAE, the electronic absorption spectra exhibit the strong narrow absorbance bands characteristic of neutral NDI at 381 nm and 361 nm.<sup>45</sup> Underneath these absorbances and tailing into the visible region is the broad MLCT absorbance of the  $\text{Re}(\text{bpy})(\text{CO})_3\text{L}$  fragment, which peaks in the 340–360 nm region depending on the complex. In general, Cl-substituted complexes **1-3** have MLCT bands whose peaks are redder than the Py-substituted **4-6**.<sup>193</sup> In addition to this variation, complexes **2** and **5**, substituted at the 5-bpy position, have MLCT bands that tail further into the visible region, giving solutions of these complexes a distinctly more orange color than solutions of the other complexes. Upon reduction, the neutral NDI peaks disappear and are replaced by peaks at 471 nm, 605 nm, 700 nm and 795 nm characteristic of the NDI radical anion.<sup>45</sup> The MLCT absorbance remains unchanged.

In the mid-IR, three peaks are observed in the carbonyl stretching region; with the two lower-energy peaks sometimes overlapping and forming one broad peak. These correspond to the symmetric (high-energy, around 2000–2050  $\text{cm}^{-1}$ ) and asymmetric (lower-energy, around 1850–1950  $\text{cm}^{-1}$ ) stretches of the CO ligands.<sup>194</sup> Py-ligated complexes have stretches that are shifted to higher energy relative to the analogous complex with a  $\text{Cl}^-$  ligand, reflective of the lower electron density on the Re center weakening the Re–C backbonding and strengthening the  $\text{C}\equiv\text{O}$  bond. As expected, reduction of the NDI fragment does not affect these vibrational peaks.

### 5.3.5 Time-Resolved Visible, Near-infrared, and Mid-infrared Spectroscopy

The forward- and back-electron transfer kinetics upon excitation of the NDI radical anion in **1<sup>-</sup>-6<sup>-</sup>** were probed using a combination of femtosecond time-resolved visible/NIR (fsTA) and time-resolved mid-IR (fsIR) spectroscopy. The oxidation state of the NDI moiety was monitored in the visible/NIR region, while the oxidation state of the  $\text{Re}(\text{bpy})(\text{CO})_3\text{X}$  fragment was monitored

in the mid-IR. A representative set of fsTA and fsIR spectra, acquired on complex **6**<sup>+</sup>, are shown in Figure 5.4 and Figure 5.5 together with the kinetic analysis of the data. Data for all six complexes is included in Figures 5.18-5.29.

The fsTA data were analyzed using Singular Value Decomposition (SVD) as described in many of our previous papers.<sup>190</sup> SVD produces a set of kinetic and spectral basis vectors that are fit to a specified kinetic model, and which are then fit using a least-squares fitting algorithm to determine the lifetimes for each kinetic component. These kinetic components are then used to calculate species-associated spectra (SAS) for each decay lifetime. For all six compounds **1**<sup>+</sup>-**6**<sup>+</sup>, the fsTA data were fit to an A→B→G(round) model, where A represents the excited state of NDI<sup>+</sup> and B represents the NDI<sup>0</sup>-Re(bpy<sup>+</sup>)(CO)<sub>3</sub>X charge-shifted state. The kinetics of forward- and back-electron transfer as determined by analysis of the fsTA data are shown in Table 5.5. The quantum yield of forward electron transfer was estimated by comparing the forward intrinsic \*NDI<sup>+</sup> excited state lifetime ( $\tau = 141$  ps) with its lifetime in each complex.<sup>45</sup> Now, because the IR spectrum is insensitive to the oxidation or excitation state of the NDI moiety, the fsIR data were analyzed using multiple-wavelength global fitting procedure that fit the kinetics of the B→G(round) process only. While it would theoretically be possible to determine the A→B kinetics by fitting the rise time of the signals corresponding to state B, that rise time, as discussed

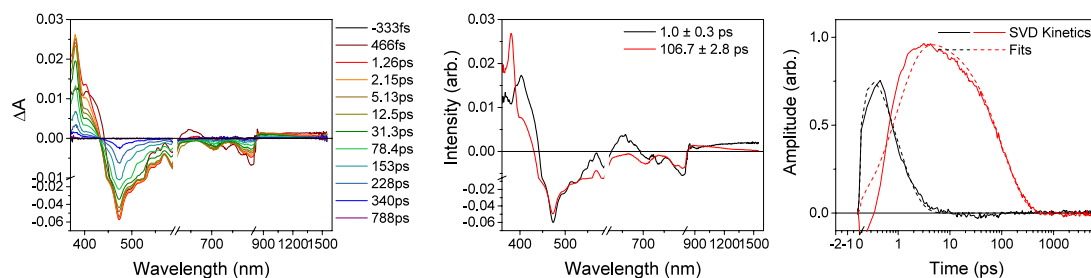


**Figure 5.4:** *Left:* fsTA spectrum of  $\text{Re}(6\text{-bpy-NDI}^{\cdot-})(\text{CO})_3\text{Cl}$  in DMF with excess TDAE ( $\lambda_{\text{ex}} = 605$  nm). *Center:* Species-associated spectra obtained from global analysis of TA data using Singular Value Decomposition (SVD) kinetic traces. Best-fit lifetimes of each spectral component are given in the legend. *Right:* Kinetic traces (solid) and fits (dashed) obtained by SVD of fsTA data. Best-fit lifetimes are given in the legend for the species-associated spectra.

below, occurs within the 1-2 ps instrument response of the fsIR apparatus and cannot be accurately fit, Figure 5.5.

**Table 5.5:** Forward- and back-electron transfer lifetimes for complexes  $\mathbf{1}^{\cdot-}$ - $\mathbf{6}^{\cdot-}$  in DMF with excess TDAE ( $\lambda_{\text{ex}} = 605$  nm), calculated from analysis of fsTA spectra.

Complex	X	$\tau_{FET}$ (ps)	$k_{FET}$ ( $\text{s}^{-1}$ )	$\tau_{BET}$ (ps)	$k_{BET}$ ( $\text{s}^{-1}$ )	$\Phi_{FET}$
$\mathbf{1}^{\cdot-}$		$1.2 \pm 0.3$	$8.3 \times 10^{11}$	$9.5 \pm 0.7$	$1.1 \times 10^{11}$	0.99
$\mathbf{2}^{\cdot-}$	$\text{Cl}^-$	$1.1 \pm 0.3$	$9.1 \times 10^{11}$	$10.0 \pm 0.4$	$1.0 \times 10^{11}$	0.99
$\mathbf{3}^{\cdot-}$		$1.3 \pm 0.3$	$7.7 \times 10^{11}$	$17.8 \pm 0.3$	$5.6 \times 10^{10}$	0.99
$\mathbf{4}^{\cdot-}$		$0.4 \pm 0.3$	$2.5 \times 10^{12}$	$32 \pm 1$	$3.1 \times 10^{10}$	0.99
$\mathbf{5}^{\cdot-}$	Py	$1.5 \pm 0.3$	$6.7 \times 10^{11}$	$59 \pm 4$	$1.7 \times 10^{10}$	0.99
$\mathbf{6}^{\cdot-}$		$1.0 \pm 0.3$	$1.0 \times 10^{12}$	$107 \pm 2$	$9.4 \times 10^9$	0.99

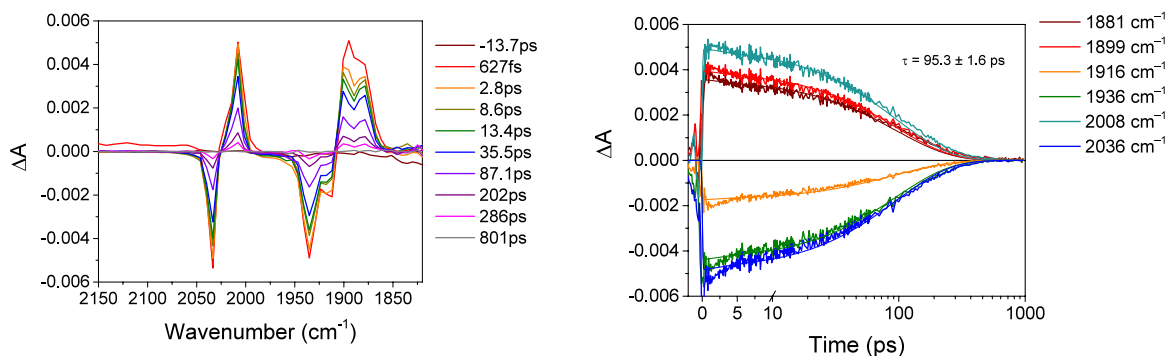


**Figure 5.5:** *Left:* fsIR spectrum of  $\text{Re}(6\text{-bpy-NDI}^-)(\text{CO})_3\text{Py}$  in DMF with excess TDAE ( $\lambda_{\text{ex}} = 605 \text{ nm}$ ). *Right:* Kinetic traces and fits to the lifetime shown of the fsIR at the given frequencies.

### 5.3.6 NMR Spectroscopy

$^1\text{H}$ ,  $^{13}\text{C}$ , COSY, HSQC, and  $^{13}\text{C}$  DEPT-135 NMR spectra were recorded on a Bruker Avance 500 TCI Cryoprobe Spectrometer. Synthesis of complexes **7-9** allowed for more detailed correlations between broadening and peaks observed in the  $^1\text{H}$  NMR for complexes **1-6**, Figures 5.7-5.8 and 5.15-5.17.

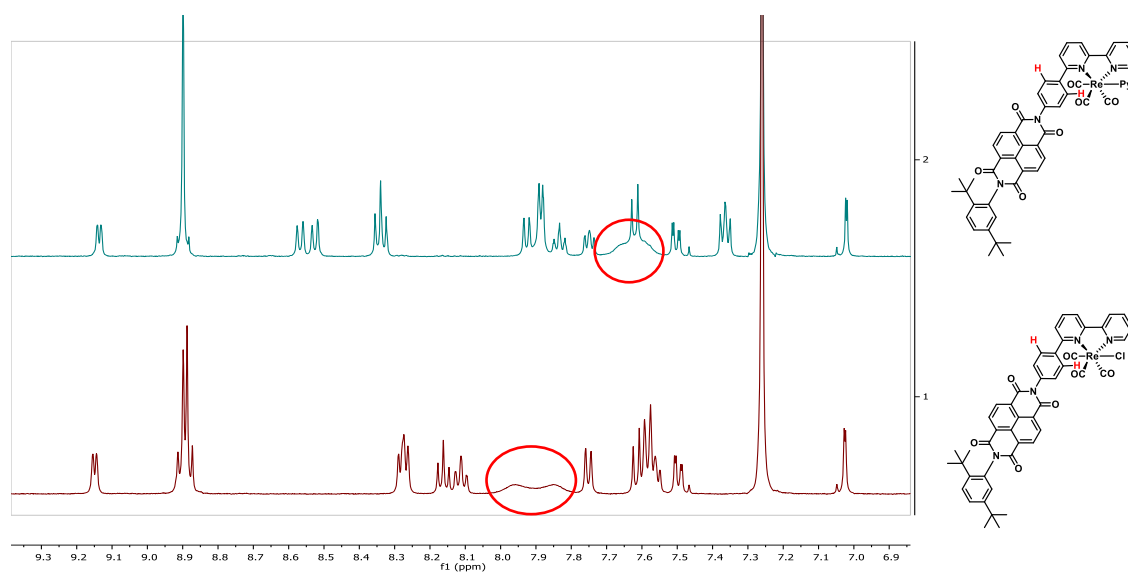


**Figure 5.6:**  $^1\text{H}$ -NMR of complexes **6** (top) and **3** (bottom), respectively. Broadening of two protons on their respective phenyl substituent are circled.

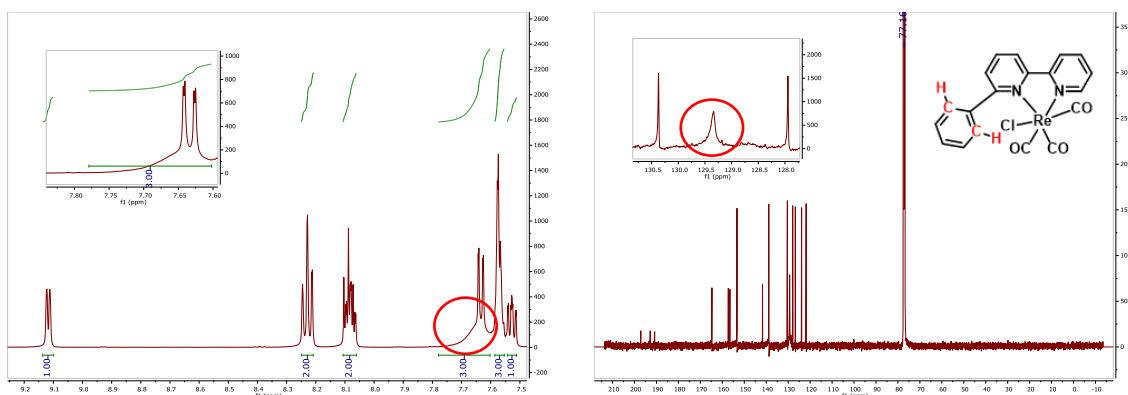


**Figure 5.7:**  $^1\text{H}$ -NMR (left) and  $^{13}\text{C}$ -NMR (right) of complex **9**. Broadening of two protons and carbons on the phenyl substituent are illustrated.

### 5.3.8 X-Ray Crystallography

Single crystals of complex **9** suitable for X-ray diffraction were obtained by vapor diffusion between a solution of the compound in dichloromethane and a diethyl ether reservoir. The crystal was mounted on MiTeGen MicroLoops with Paratone oil and data were collected at 100 K on a Bruker Prospector system equipped with the micro-focused X-ray tube and MX optics. The structures were solved using SHELXS and refined using SHELXT. Structure have been deposited in the Cambridge Structural Database (CCDC Nos. 1856229). Crystal data and structure refinement for complex **9** are shown in Table 5.6. Fractional Atomic Coordinates and Equivalent Isotropic Displacement Parameters for complex **9** are in Table 5.9.

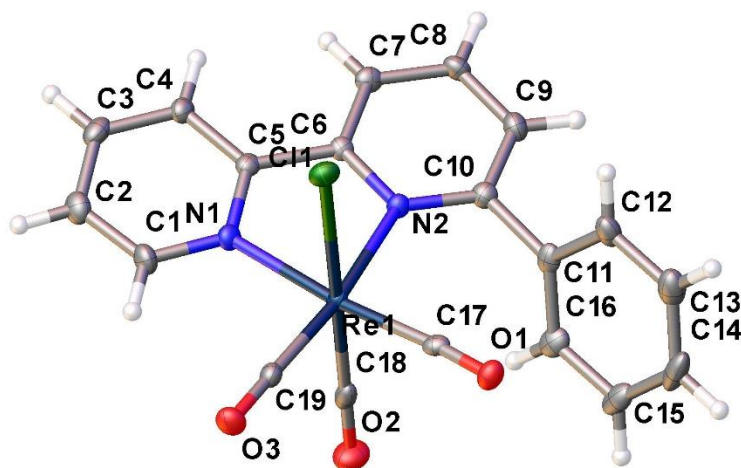


**Figure 5.8:** X-ray crystallographically derived molecular structure of complex **9**.

**Table 5.6:** Crystal data and structure refinement for complex **9**

Identification code	Complex <b>9</b>
Empirical formula	C <sub>19</sub> H <sub>12</sub> N <sub>2</sub> O <sub>3</sub> ClRe
Formula weight	537.96
Temperature/K	100.01
Crystal system	monoclinic
Space group	P2 <sub>1</sub> /c
a/Å	7.0735(12)
b/Å	14.576(2)
c/Å	16.991(3)
α/°	90
β/°	101.338(8)
γ/°	90
Volume/Å <sup>3</sup>	1717.6(5)
Z	4
ρ <sub>calc</sub> /cm <sup>3</sup>	2.08
μ/mm <sup>-1</sup>	15.467
F(000)	1024
Crystal size/mm <sup>3</sup>	0.314 × 0.134 × 0.091
Radiation	CuKα (λ = 1.54178)

2 $\Theta$ range for data collection/ $^{\circ}$	10.62 to 133.258
Index ranges	$-8 \leq h \leq 7$ , $-16 \leq k \leq 17$ , $-10 \leq l \leq 20$
Reflections collected	6832
Independent reflections	2926 [ $R_{\text{int}} = 0.0322$ , $R_{\text{sigma}} = 0.0405$ ]
Data/restraints/parameters	2926/0/235
Goodness-of-fit on $F^2$	1.096
Final R indexes [ $I \geq 2\sigma(I)$ ]	$R_1 = 0.0316$ , $wR_2 = 0.0848$
Final R indexes [all data]	$R_1 = 0.0323$ , $wR_2 = 0.0856$
Largest diff. peak/hole / $e \text{ \AA}^{-3}$	1.87/-1.35

### 5.3.9 Computed Molecular Orbitals

**Table 5.7:** Computed geometry parameters for the investigated complexes.

Compound #	$d_{\text{Re-COeq}} / \text{\AA}$	$d_{\text{Re-COax}} / \text{\AA}$	$d_{\text{Re-X}} / \text{\AA}$	$\Theta_{\text{py-py}} / ^{\circ}$	$\Theta_{\text{py-ph}} / ^{\circ}$
1	1.930;1.929	1.920	2.513	0.033	-40.681
2	1.929;1.930	1.919	2.512	0.109	39.698
3	1.917;1.942	1.914	2.520	9.919	54.788
4	1.934;1.934	1.937	2.275	-0.803	-35.19
5	1.934;1.934	1.937	2.274	0.652	36.25
6	1.921;1.947	1.930	2.276	10.667	53.22
7	1.930;1.929	1.919	2.513	-0.393	-39.260
8	1.929;1.929	1.919	2.512	0.290	38.267
9	1.916;1.940	1.914	2.517	10.054	54.612

In the absence of crystal structure for most of the reported complexes, the optimization of the ground state geometry for the reported complexes revealed structural information fundamental for understanding some of the experimental properties. As reported in Table 5.7, the distance between the rhenium and both equatorial carbonyl ligands are approximately 1.93  $\text{\AA}$  for all the complexes

except for those with a substituent in position 6 to the bpy. In this case (complexes **3**, **6** and **9**) the Re-CO distance for the carbonyl pointing away from the substituted position 6, resulted shorter by 0.02 Å than the opposite equatorial carbonyl. On the other side, both axial ligands were not affected by the different bipyridyl ligands. We attribute the asymmetry between the two equatorial carbonyls to the strong distortion of the two pyridyl rings in the 6-substituted bpy ligands. The 4- and 5-substituted bipyridine show a quasi-coplanarity of the two rings, whereas the 6-substituted ligands present a dihedral angle of 10°. For the 6-substituted bipyridyl ligands also the dihedral angle between the substituted ring and the phenyl fragment result more distorted than for the 4 and 5 corresponding ligands, with  $\approx 54^\circ$  instead of  $\approx 38^\circ$ .

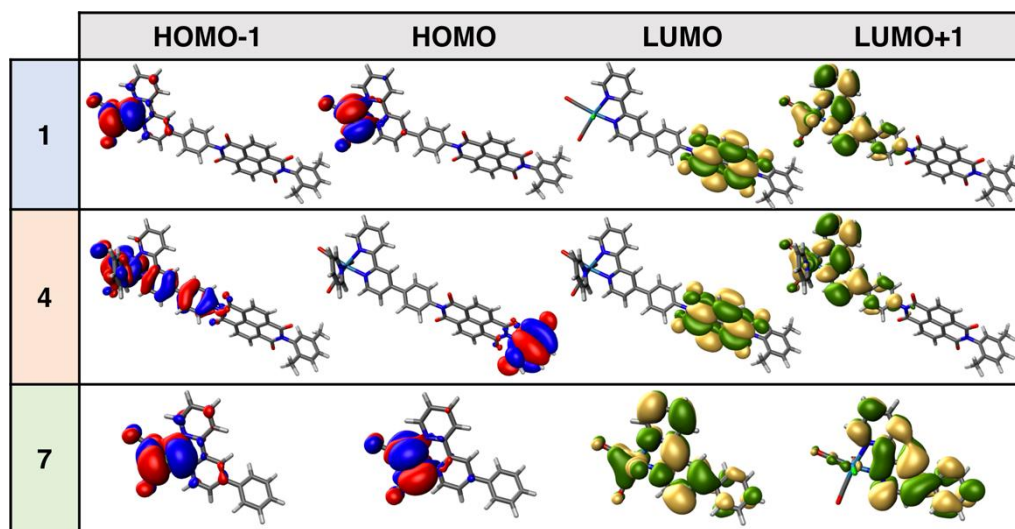


**Figure 5.9:** Optimized geometries and plots of HOMO-1, HOMO, LUMO and LUMO+1 orbitals for complexes **1**, **4** and **7**.

The frontier orbital distribution is depicted in Figure 5.9. For the same orbital, the localization doesn't change within the three sets of complexes, hence in Figure 5.9 we compared only the 4-substituted complexes **1**, **4** and **7**. For all the neutral investigated complexes, the HOMO

and HOMO-1 are predictably localized between the rhenium, the halogen and the three carbonyl ligands with minimum (HOMO-1) or no contribution (HOMO) arising from the ancillary ligand. For the cationic analogues, the energy of occupied MOs become stabilized enough to alter the distribution pattern seen in Figure 10 (complexes **1** and **7**). Therefore, the HOMO for the Pyridine substituted complexes resulted localized on the NDI substituent, whereas the bpy pyridyl rings contribute together with the metal and the carbonyls to the HOMO-1. In the NDI complexes **1-6** the LUMO is dominated by the NDI fragment whereas the LUMO+1 is bpy centered. Model complexes **7-9** have both LUMO and LUMO+1 localized on the bpy-Ph ligand.

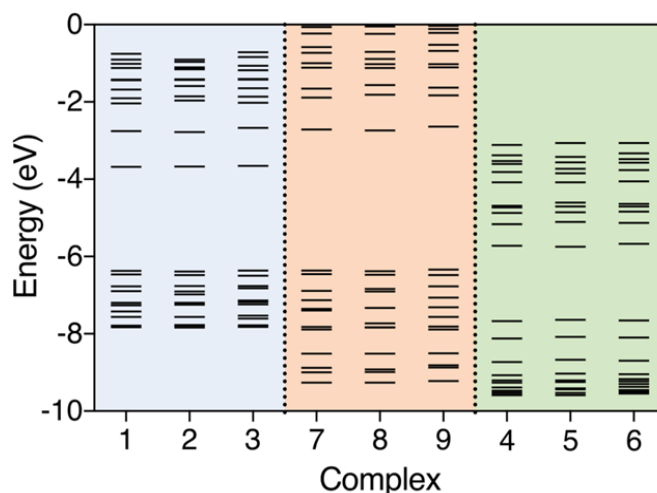


**Figure 5.10:** Calculated molecular orbital energy level diagram for complexes **1-9**. Model complexes **7-9** are displayed next to **1-3** to better appreciate the effect of the NDI fragment.

Kohn–Sham energy diagrams for the ten highest occupied and ten lowest unoccupied MOs for **1-9** are shown in Figure 5.10 and frontier orbital energies are summarized in Table 5.8. In agreement with the orbital distribution, the HOMO energies for the neutral complexes **1-3** and **7-9** lie at about -6.3 eV. Complexes **1-3** display almost identical LUMO energies supported by the

NDI centered localization. Similarly, LUMO+1 for complexes **1-3** and LUMO for **7-9** have similar energies due to the similar orbital distribution. The energies for the cationic species result shifted to lower energies than for the neutral complexes, this is attributed as an effect of the positive charge of these systems. Although, comparing the HOMO-LUMO gap between the neutral and the cationic complexes, the replacement of a  $\pi$ -donor (the halogen) with a  $\pi$ -accepting ligand (pyridine) induces a destabilization of the HOMO hence a narrower HOMO-LUMO gap.

**Table 5.8:** Calculated HOMO and LUMO energies for complexes **1-9**.

Complex	HOMO eV	LUMO eV	$\Delta_{\text{HOMO-LUMO}}$ eV	$\Delta_{\text{HOMO-LUMO}}$ nm nm
<b>1</b>	-6.373	-3.676	2.696	460
<b>2</b>	-6.385	-3.668	2.717	456
<b>3</b>	-6.359	-3.658	2.700	459
<b>4</b>	-7.674	-5.723	1.952	635
<b>5</b>	-7.640	-5.746	1.894	654
<b>6</b>	-7.654	-5.670	1.984	625
<b>7</b>	-6.362	-2.716	3.646	340
<b>8</b>	-6.378	-2.740	3.638	341
<b>9</b>	-6.339	-2.639	3.700	335

### 5.3.10 Thermally Averaged Electronic Coupling

Electronic coupling depends strongly on the relative orientation of the donor and acceptor, which can vary due to thermal fluctuations. Electronic couplings  $|H_{if}(\varphi)|$  were computed for the back-ET reaction  $[\text{Re}(\text{bpy})(\text{CO})_3\text{X}^{\bullet-}][\text{NDI}] \rightarrow [\text{Re}(\text{bpy})(\text{CO})_3\text{X}][\text{NDI}^{\bullet-}]$ . Thermally averaged coupling was obtained by taking the energetically feasible configurations of the complexes at room temperature (selected using a cutoff of 1 kcal/mol on the energies of the complexes, Figure 5.11

A and B) and Boltzmann averaging the electronic couplings  $|H_{if}(\varphi)|$  computed for those configurations were done using equation 4.

$$H_{if}^B = \frac{\sum_i |H_{if}(\varphi)| e^{-\frac{\Delta E_i(\varphi)}{kT}}}{\sum_i e^{-\frac{\Delta E_i(\varphi)}{kT}}} \quad (4)$$

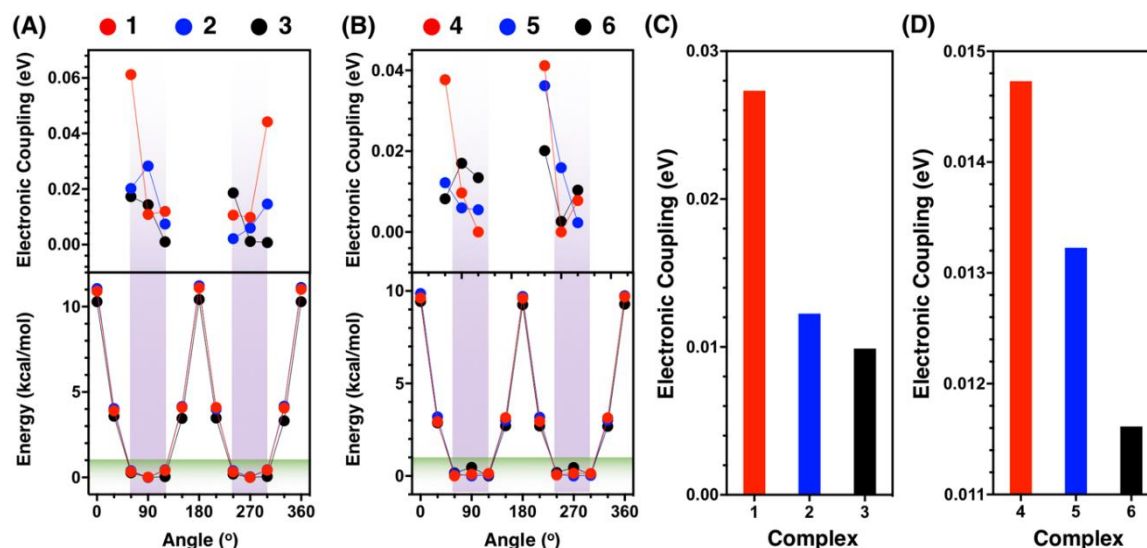


**Figure 5.11:** (A) (Bottom) Energies for different structures of complexes **1**, **2** and **3** obtained by scanning the dihedral between  $\text{Re}(\text{bpy})(\text{CO})_3\text{Cl}^-$  and NDI and (Top) Electronic couplings for the back-electron transfer for structures with energies  $< 1$  kcal/mol. (B) (Bottom) Energies for different structures of complexes **1**, **2** and **3** obtained by scanning the dihedral between  $\text{Re}(\text{bpy})(\text{CO})_3\text{Py}^-$  and NDI and (Top) Electronic couplings for the back-ET for structures with energies  $< 1$  kcal/mol. Boltzmann averaged electronic couplings  $|H_{if}^B|$  for back-ET complexes (C) **1**, **2** & **3** and (D) **4**, **5** & **6**.

## 5.4 Discussion

The electrochemical data shown in Tables 5.1-5.2 reveal that the attachment of the NDI-Ph to  $\text{Re}(\text{bpy})(\text{CO})_3\text{X}$  has a negligible effect on the reduction potentials of NDI. The first two reductions for complexes **1-6** are NDI localized and are similar to that of the free NDI chromophore.<sup>45</sup> Despite that, the two reduction potentials of  $\text{Re}(\text{bpy})(\text{CO})_3\text{X}$  are perturbed slightly

with an NDI-Ph bound. For example, in complexes **1-3** the bipyridine reductions are separated by 100 mV while the  $\text{Re-Cl}^{I/0}$  are separated by 240 mV. To obtain more insight into this disparity, we synthesized model rhenium complexes that do not have an NDI chromophore attached at the 4-, 5-, or 6- bipyridine position in order to isolate the effects the Ph- and NDI-Ph have on the reduction potentials of  $\text{Re}(\text{bpy})(\text{CO})_3\text{Cl}$ . In comparing complex **7** to the unsubstituted  $\text{Re}(\text{bpy})(\text{CO})_3\text{Cl}$  (complex **10**), the  $\text{bpy}^{0/-}$  and  $\text{Re-Cl}^{I/0}$  shift to more positive potentials. This is attributed to the extended conjugation from the bpy into the phenyl substituent, lowering the bpy  $\pi^*$ star orbital's energy and making the  $\text{bpy}^{0/-}$  reduction more facile. This is likely the same reason of the anodic shift for complex **8** when compared to complex **10**. This is expected because of greater electronic coupling and conjugation onto the phenyl from the bipyridine, shifting positive of the redox potentials. In contrast, in complex **9**, where the bipyridine is substituted at the 6-position with a phenyl, the  $\text{bpy}^{0/-}$  and  $\text{Re-Cl}^{I/0}$  reductions instead shift to more negative potentials. X-ray quality grown crystals of **9** illustrate the proximity of the phenyl substituent with respect to the metal center. Likely as the complex gets reduced once or twice, the complex must electrostatically repel this phenyl substituent, whereas complex **7** and **8** do not, incurring more difficult reductions for complex **9**. This is additionally supported by  $^1\text{H-NMR}$  and  $^{13}\text{C-NMR}$ , as the phenyl group on the complex **9** has broadened  $^1\text{H-NMR}$  and  $^{13}\text{C-NMR}$  peaks, indicating lack of free rotation, caused by the phenyl's close vicinity to the metal complex, while complexes **7** and **8** do not. This rationale can be extended to complexes **1-6**, where in the case of complex **3** and **6**, the metal complex must repel the phenyl that has a bulky NDI substituent also linked. This leads to more negative reduction potentials for the metal complex than their constitutional isomer counterparts, Table 5.1-5.3. Similar results have been seen before by Ishitani that constructed Ru-Re complexes that were separated by an alkyl bridge, when the length of the alkyl bridge was decreased from 6 to 4 to 2

carbons, they observed a through space interaction that changed the  $\text{Re}(\text{dmb})(\text{CO})_3\text{Cl}$  reduction potentials.<sup>31, 195</sup>

When comparing the reduction potentials of complexes **1-3** to complexes **4-6**, the third reductions ( $\text{bpy}^{0/-}$ ) are at more negative potentials; this reflects the destabilizing of the  $\text{bpy} \pi^*$  orbital by the chloride ligand due to the chloride's ability to be a  $\pi$ -donor in contrast to the pyridine ligand.<sup>65</sup> This effect, in addition to complexes **4-6** being positively charged, has a more drastic effect on the fourth reduction ( $\text{Re-X}^{I/0}$ ) where the metal based reductions shift by  $\sim 230\text{mV}$  more positive with a pyridine bound than in complexes **1-3** with a chloride bound. With respect to  $\Delta G_{\text{BET}}$  of complexes **1<sup>-</sup>-6<sup>-</sup>**, the reduction potentials of bipyridine are only of concern as we are interested in the reduction of  $\text{Re}(\text{bpy-NDI}^-)(\text{CO})_3\text{X}$  to  $\text{Re}(\text{bpy}^--\text{NDI}^0)(\text{CO})_3\text{X}$ . The electrochemical data in Tables 5.1-5.2 illustrate that by substituting the chloride ligand for pyridine,  $\Delta G_{\text{BET}}$  for  $\text{Re}(\text{bpy}^-)(\text{CO})_3\text{X} \rightarrow \text{NDI}^0$  is decreased by 200-300 mV between complexes **1-3** and their pyridine counterparts. This will have implication on the rate of back electron transfer that will be discussed later.

Whether the  $\text{NDI}^-$ -Ph substituent is at the 4, 5, or 6 position of bipyridine on  $\text{Re}(\text{bpy})(\text{CO})_3\text{X}$ , the same photophysical processes occur upon selective excitation at  $\lambda_{\text{ex}} = 605\text{ nm}$  of the  $\text{NDI}^-$  chromophore, albeit with different kinetics. At short times, the spectral features observed in the fsTA are instantaneous bleaches of the ground-state  $\text{NDI}^-$  features at 471 nm, 700 nm, and 795 nm and induced absorptions attributable to  $^*\text{NDI}^-$  at 403 nm and in the region 600–1500 nm overlapping the bleaches at 700 nm and 795 nm. As the fsTA spectrum evolves, the bleaches remain but the  $^*\text{NDI}^-$  induced absorptions decay. In their place, an induced absorption at 381 nm appears, characteristic of  $\text{NDI}^0$  (in some datasets an additional induced absorption at

361 nm is also visible, although this wavelength lies just at the edge of detectability in the fsTA apparatus and is not always observable). In the NIR, a broad induced absorption attributable to the  $\text{Re}(\text{bpy}^*)(\text{CO})_3\text{L}$  moiety is observed to grow in with the same kinetics as the growth of the  $\text{NDI}^0$  band(s). The strength and wavelength of that band varies with the site of substitution on the bpy and with the nature of X, although it always corresponds to  $\text{SOMO} \rightarrow \text{LUMO}+n$ , all orbitals of which are located on the bpy ligand. Because the conjugation of the bpy ligand extends partially onto the Ph substituent, shifting the location of substitution affects the relative energies of the bpy-centered orbitals and consequently the spectra of the reduced  $\text{Re}(\text{bpy})(\text{CO})_3\text{L}$  fragment.

The fsIR spectra are quite similar to those obtained from our previous experiments for similar rhenium complexes.<sup>190-191, 196-197</sup> Upon reduction, the ground-state absorptions are observed to bleach and induced absorptions at lower energies are observed to form. A shift to lower energy of the CO stretching frequencies is commonly observed when the bpy ligand on the Re is reduced, due to increased electron density on the Re center strengthening the  $\pi$ -backbonding to the CO and weakening the CO bond.<sup>104</sup> These induced absorptions are observed to decay with kinetics identical within experimental error to the kinetics of the  $\text{B} \rightarrow \text{G}(\text{round})$  process observed in the fsTA data. Due to a large coherence artifact that obscures the first  $\sim 2$  ns of fsIR data, kinetic fitting of these data, especially for complexes with shorter lifetimes for back-electron transfer, are less accurate than lifetimes obtained from fitting the fsTA data.

In comparing the  $\tau_{\text{BET}}$  in complexes with the same substituent position of the  $\text{NDI}^-$ -Ph chromophore but with different X ligands (e.g. complex  $\mathbf{1}^-$  vs complex  $\mathbf{4}^-$ ), we see that the rate of back electron transfer decreased. For example,  $\tau_{\text{BET}}$  for complex  $\mathbf{1}^-$  is  $9.5 \pm 0.7$  ps while the  $\tau_{\text{BET}}$  for complex  $\mathbf{4}^-$  is  $32 \pm 1$  ps. It is clear that by substituting Cl for pyridine, the Gibbs free energy for back electron transfer decreases as well, leading to a slower charge recombination

lifetime. This trend is consistent when comparing all the  $\tau_{BET}$  between complexes  $\mathbf{1}^{\bullet-}$ - $\mathbf{3}^{\bullet-}$  and their counterparts  $\mathbf{4}^{\bullet-}$ - $\mathbf{6}^{\bullet-}$ . In comparing  $\tau_{BET}$  for complexes with a different substituent location of the NDI<sup>-</sup>-Ph fragment but with the same X ligand (e.g. complexes  $\mathbf{1}^{\bullet-}$  vs  $\mathbf{2}^{\bullet-}$  vs  $\mathbf{3}^{\bullet-}$ ), we see that the  $\tau_{BET}$  is slower. In the set of complexes with a chloride bound, the complex with NDI<sup>-</sup>-Ph at the 6 position has a greater  $\Delta G_{BET}$  than the complexes with NDI<sup>-</sup>-Ph at the 4 or 5 position but a slower back electron transfer time constant ( $\tau_{BET} = 17.8 \pm 0.3$  for complex  $\mathbf{3}^{\bullet-}$  vs  $\tau_{BET} = 9.5 \pm 0.7$  ps for complex  $\mathbf{1}^{\bullet-}$ ). In the set of complexes with a pyridine bound ( $\mathbf{4}^{\bullet-}$ - $\mathbf{6}^{\bullet-}$ ), the  $\Delta G_{BET}$  for back electron transfer are quite similar. Despite that, the  $\tau_{BET}$  among the three complexes are quite different, with the time constant for back electron transfer being ~3 times longer in complex  $\mathbf{6}^{\bullet-}$  than in complex  $\mathbf{4}^{\bullet-}$ . It is clear that the substituent location of NDI<sup>-</sup>-Ph onto bipyridine plays a role in the  $\tau_{BET}$  when bound to the  $\text{Re}(\text{bpy})(\text{CO})_3\text{Cl}$ , but the slower charge recombination times cannot be rationalized via the energetics estimated by the  $\Delta G_{BET}$ . As seen in Figure 5.11 (C) and (D),  $|H_{if}^B|$  for back ET in  $\text{Re}(4-, 5-, 6\text{-bpy-NDI})(\text{CO})_3\text{Cl}$  shows the trend  $H_1 > H_2 > H_3$  resulting in the observed back-ET trend of  $\tau_{BET_1} < \tau_{BET_2} < \tau_{BET_3}$ . Likewise in  $[\text{Re}(4-, 5-, 6\text{-bpy-NDI})(\text{CO})_3\text{Py}][\text{PF}_6]$ , the computed trend of  $H_4 > H_5 > H_6$  results in the observed back-ET trend of  $\tau_{BET_4} < \tau_{BET_5} < \tau_{BET_6}$ . Thus, electronic coupling  $|H_{if}|$  between the NDI<sup>-</sup>-Ph substituent and  $\text{Re}(\text{bpy})(\text{CO})_3\text{Cl}$  at the 4, 5, and 6 position of bipyridine is the key factor governing the rate of electron transfer.

The decrease in electronic coupling is likely a through space interaction that forces the reduced metal complex  $\text{Re}(\text{bpy})(\text{CO})_3\text{X}$  to electrostatically repel the NDI-Ph (after electron transfer) or NDI<sup>-</sup>-Ph (before electron transfer) substituent due to their proximity in space. The shift of the bipyridine and  $\text{Re}^{I/0}$ -Cl reduction potentials to more negative potentials is evidence of

a through space interaction.<sup>54, 198</sup> Additionally, <sup>1</sup>H-NMR of complexes **3** and **6** and illustrate significant broadening of resonances assigned to two protons on the phenyl ring (Figure 5.6). No broadening of <sup>1</sup>H-NMR resonances occurred in the 4 or 5 positioned Re(bpy-NDI)(CO)<sub>3</sub>X complexes. Additionally, there is no broadening of protons in the bare ligands of any bipyridine ligand investigated in this study. To obtain better insight into the broadening of <sup>1</sup>H-NMR resonances, the model complex Re(6-Ph-bpy)(CO)<sub>3</sub>Cl (complex **9**) was investigated further. <sup>1</sup>H-NMR of complex **9** illustrated significant broadening of two phenyl protons (Figure 5.7), while the rest of the phenyl and bipyridine protons appear sharp, as with the case with Re(6-bpy-NDI)(CO)<sub>3</sub>Cl and Re(6-bpy-NDI)(CO)<sub>3</sub>Py. <sup>13</sup>C-NMR of complex **9** illustrate significant broadening to the carbon atoms attached to these protons while the remaining bipyridine and phenyl carbons are single sharp peaks. <sup>1</sup>H and <sup>13</sup>C NMR assignments were further confirmed via COSY, HSQC, and <sup>13</sup>Carbon DEPT-135 experiments (see 5.8.1). The broadening in the <sup>1</sup>H and <sup>13</sup>C NMR of complex **9** is associated with restricted rotation of the protons and carbons because of the phenyl's proximity to the metal center through space. To verify this interaction, crystals of **9** suitable for X-ray diffraction were grown by vapor diffusion of diethyl ether into solution of **9** dissolved in dichloromethane. The diffraction data revealed molecular structures like previously reported Re compounds<sup>185</sup> with an quasi-octahedral arrangement of ligands around a rhenium center (Figure 5.8), consistent with IR data that demonstrate that the carbonyl ligands adopt facial geometries. The distance from the carbons at the 8 and 9 positions of complex **9** are closest to the closest carbonyl in space, as indicated by the crystal structure, this interaction likely broadens the protons and carbons as they are perturbed. Previous work done on using 6-phenyl-2,2'-bipyridine (HL) as a coordinating ligand (N,N donor) to form Ru(HL)<sub>2</sub>Cl<sub>2</sub> illustrated significant broadening

of the phenyl substituents protons in  $^1\text{H-NMR}$  while the bipyridine protons appeared sharp.<sup>199</sup> Additionally, the HL ligand could be utilized as a C,N,N-donor in metal complexes that incorporated Rh. The phenyl substituent was found to form an organometallic (carbon-metal) bond and formed the cyclometallated complex  $\text{Rh-HL}(\text{MeCN})\text{Cl}_2$ , illustrating the HL's close proximity to the metal center.<sup>199</sup> The phenyl to metal complex through space interaction likely decouples the 6-NDI-Ph substituents from the  $\text{Re}(\text{bpy})(\text{CO})_3\text{X}$  in comparison to having the ligand at the 4 and 5 position of bipyridine as this interaction doesn't occur. This is supported by the DFT calculated optimized geometries of complexes **1-9**, as the dihedral angle between the substituted ring and the phenyl fragment are less distorted in the 4 and 5 corresponding ligands than the 6-substituent, with  $\approx 54^\circ$  instead of  $\approx 38^\circ$ .

This data illustrates that by altering the substitution on the bipyridine core, as well as changing the X ligand bound to the metal complex, can increase charge separation lifetimes in  $\text{Re}(\text{bpy}^{\text{N}}\text{-NDI}^{\text{O}})(\text{CO})_3\text{X}$  by an order of magnitude. These results will have immediate effects in the redesign of complexes that form donor-acceptor systems with  $\text{Re}(\text{bpy})(\text{CO})_3\text{X}$ . For example, in our previously reported complex  $\text{Re}(4\text{-bpy-DPA-NDI}^{\text{N}})(\text{CO})_3\text{Cl}$  (see Figure 5.1), where the triad is constructed through the 4 position of bipyridine. Simply by attaching NDI-DPA- to the 6 position of bipyridine instead of the 4 position, as well as changing the chloride ligand to pyridine, would we expect the charge separation lifetime to increase from  $\sim 25$  ns to  $\sim 250$  ns. This implementation will lengthen the complex's charge recombination lifetime and will allow the reduction of the complex to compete with reactions that proceed on the diffusional time scale, such as  $\text{CO}_2$  binding and catalysis.

## 5.5 Conclusion

In this study we described six new complexes that contained an  $\text{NDI}^{\bullet-}$  chromophore bound to  $\text{Re}(\text{bpy})(\text{CO})_3\text{X}$  via a phenyl bridge. By varying the position of the NDI-Ph substituent on bipyridine had varying degrees of effect on the reduction potentials of the  $\text{Re}(\text{bpy})(\text{CO})_3\text{X}$ . The complexes that had NDI-Ph at the 6 position of bipyridine had its two  $\text{Re}(\text{bpy})(\text{CO})_3\text{X}$  centered reductions shifted to more negative potentials while the complexes that had NDI-Ph positioned at the 4 or 5 position of bipyridine were shifted more positive. To isolate the effect between the NDI-Ph and Ph- had on the reduction potentials, three model complexes were synthesized that only had a phenyl substituent bound. X-ray crystallography coupled with  $^1\text{H}$  and  $^{13}\text{C}$  NMR illustrated that the 6 positioned Ph- on bipyridine was perturbed by the metal center complex and that likely upon one or two reductions of the metal complex forces the complex to coulombically repel the phenyl substituent while the 4 or 5 complexes do not. Instead, the complexes that had a phenyl on the 4 or 5 position had more positive reductions, indicating that the electron density is likely distributed onto the phenyl from the bipyridine due to conjugation. As a result, these model compounds showed the same trend for their respective  $\text{Re}(\text{bpy})(\text{CO})_3\text{X}$  reductions as the NDI-Ph complexes.

FsTA and fsIR experiments verified that upon selective excitation of the  $\text{NDI}^{\bullet-}$  at 605 nm, the covalently attached  $\text{Re}(\text{bpy})(\text{CO})_3\text{X}$  is reduced to  $\text{Re}(\text{bpy}^{\bullet-})(\text{CO})_3\text{X}$  in  $< 2$  ps. FsTA results illustrated that the  $\tau_{\text{BET}}$  increased when the chloride ligand was exchanged for a pyridine ligand, this could be affirmed by the  $\Delta G_{\text{BET}}$ . FsTA results additionally showed that when the  $\text{NDI}^{\bullet-}$ -Ph-chromophore substituent location was changed from 4  $\rightarrow$  5  $\rightarrow$  6 positions around the bipyridine on  $\text{Re}(\text{bpy})(\text{CO})_3\text{X}$ , that  $\tau_{\text{BET}}$  increased. While the  $\Delta G_{\text{BET}}$  were contradictory to the  $\tau_{\text{BET}}$ , we turned towards calculating the electronic coupling between the NDI chromophore and  $\text{Re}(\text{bpy}^{\bullet-})(\text{CO})_3\text{X}$

as the  $\tau_{BET}$  is proportional to the electronic coupling between the two fragments. These calculations demonstrated that the electronic coupling between the NDI and  $\text{Re}(\text{bpy NDI}^-)(\text{CO})_3\text{X}$  decreased from the 4  $\rightarrow$  5  $\rightarrow$  6 positions around the bipyridine, supporting the  $\tau_{BET}$  obtained by FsTA.

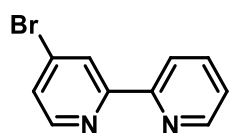
This work provides several important understandings for creating donor-acceptor based on the popular  $\text{Re}(\text{bpy})(\text{CO})_3\text{X}$   $\text{CO}_2$  reduction catalyst. One important finding is that incorporating a chromophore at the 4, 5, or 6 position of bipyridine does not affect the quantum yield of forward electron transfer. This ensures that in photocatalytic systems, each photon that is absorbed by the  $\text{NDI}^-$  is transferred to form  $\text{Re}(\text{bpy}^*)(\text{CO})_3\text{X}$ , the first intermediate in the catalytic cycle. Second, the attachment of the  $\text{NDI}^-$ -Ph to the 6 position of bipyridine does not negatively impact the reduction of the bipyridine, indicating that the potency for  $\text{CO}_2$  reduction by the singly reduced complex  $\text{Re}(\text{bpy}^*)(\text{CO})_3\text{X}$  is maintained, a fault seen in previous conjugated chromophores. Third, by incorporating the  $\text{NDI}^-$  chromophore at the 6 position of bipyridine and exchanging the Cl ligand to pyridine leads to an order of magnitude increase in  $\tau_{BET}$ . Finally, the photoinduced electron transfer recombination rates can be dictated either by the Gibbs free energy of back electron transfer or the electronic coupling between  $\text{Re}(\text{bpy}^*)(\text{CO})_3\text{Cl}$  and NDI. This systematic approach will impact the rational design of these complexes that aim to maximize charge recombination lifetimes, a vital component to photocatalytic  $\text{CO}_2$  reduction and artificial photosynthesis.

## 5.6 Acknowledgements

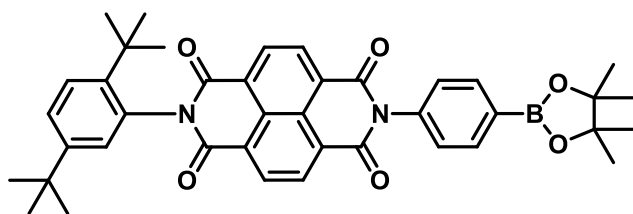
We thank Drs. Saman Shafaie for collecting high-resolution mass spectrometric data. This work was supported by the Argonne Northwestern Solar Energy Research (ANSER) Center, an

Energy Frontier Research Center funded by the U.S. Department of Energy (DOE), Office of Science, Office of Basic Energy Sciences, under Award No. DE-SC0001059. This publication was made possible by NPRP Grant No. 9-174-2-092 from the Qatar National Research Fund (a member of Qatar Foundation). The findings achieved herein are solely the responsibility of the authors. NMR and MS measurements in this work were performed at the IMSERC at Northwestern University, which has received support from the Soft and Hybrid Nanotechnology Experimental (SHyNE) Resource (NSF NNCI-1542205); the State of Illinois and International Institute for Nanotechnology (IIN). We are grateful to Yale HPC and the Research Computing Center in Texas A&M University at Qatar for where the calculations were conducted.

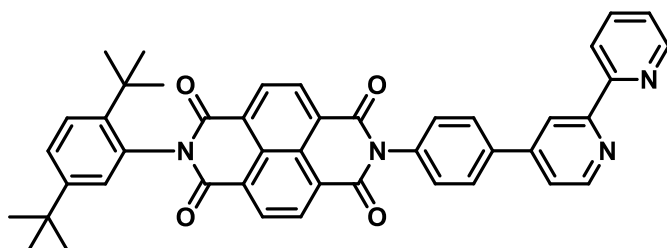
## 5.7 Synthetic Details



**4-bromo-2,2'-bipyridine** was prepared as was previously reported.<sup>191</sup>

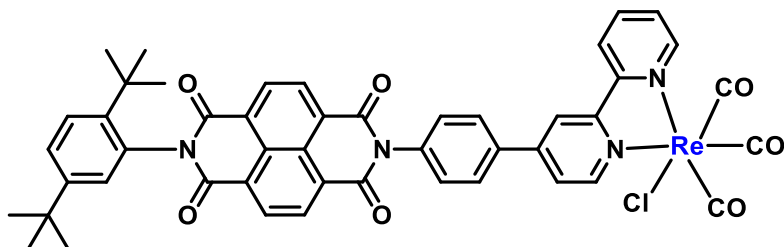


**DtB-NDI-PhBpin** was prepared as was previously reported.<sup>191</sup>



### DtB-NDI-4-Phbpy

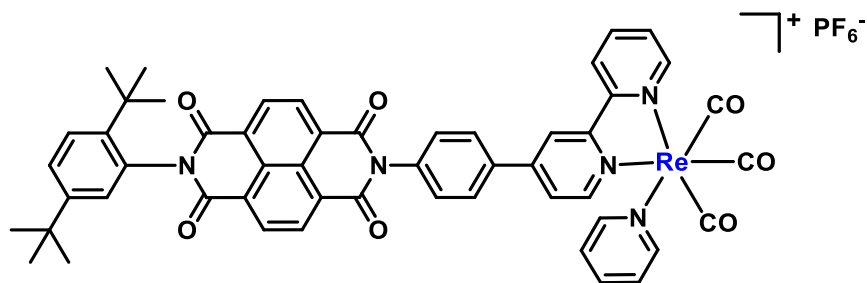
In an oven dried round bottom flask with a magnetic stirrer and reflux condenser, DtB-NDI-PhBpin (0.10 g, 0.15 mmol), 4-bromo-2,2'-bipyridyl (0.04 g, 0.18 mmol), and Na<sub>2</sub>CO<sub>3</sub> (0.127 g, 1.2 mmol) were dissolved in THF (33mL) and H<sub>2</sub>O (7mL) and put under N<sub>2</sub>. After 15 minutes of purging, fresh Pd[PPh<sub>3</sub>]<sub>4</sub> (8.7mg, 5% eq) was added via the second port and purged for 5 minutes. The solution was set to reflux overnight. The solution was cooled to room temperature and the solvent was removed under reduced pressure. The crude material was then dissolved in dichloromethane and ran through a celite plug. The solvent was removed under reduced pressure. The remaining solid was sonicated in minimal MeOH and allowed to sit overnight in a freezer. The solution was filtered and the light brown solid was collected (20%, 0.043g). <sup>1</sup>H NMR (500 MHz, Chloroform-*d*) δ 8.89 (s, 4H), 8.80 – 8.71 (m, 3H), 8.48 (dt, *J* = 8.0, 1.2 Hz, 1H), 7.99 (d, *J* = 8.3 Hz, 2H), 7.86 (td, *J* = 7.8, 1.8 Hz, 1H), 7.64 – 7.59 (m, 2H), 7.52 – 7.48 (m, 3H), 7.38 – 7.34 (m, 1H), 7.03 (d, *J* = 2.2 Hz, 1H), 1.34 (s, 9H), 1.29 (s, 9H).



### NDI-4-Phbpy-Re(CO)<sub>3</sub>-Cl

In a nitrogen filled glove box, an oven dried pressure flask with a magnetic stirrer was filled with compound **DtB-NDI-4-Phbpy** (0.1 g, 0.15 mmol), pentacarbonylchlororhenium(I) (0.065 g, 0.18 mmol), and dichloromethane (30 mL). The pressure flask was capped and brought out of the glovebox and heated to 80 °C overnight. The solution was cooled to room temperature and the

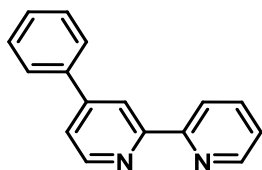
solvent was removed by reduced pressure. The solid was then column chromatographed on silica using a gradient between dichloromethane and Ethyl Acetate (100 → 98:2 → 85:15). The compound was then dissolved in minimal dichloromethane and layered with diethyl ether. Upon filtering, a bright yellow compound was obtained with sufficient purity to carry through to the next step. Yield: (0.03 g, 20%). **<sup>1</sup>H NMR** (500 MHz, Chloroform-*d*) δ 9.12 (td, *J* = 5.6, 1.1 Hz, 2H), 8.90 (s, 4H), 8.38 (d, *J* = 1.8 Hz, 1H), 8.35 – 8.30 (m, 1H), 8.10 (td, *J* = 7.6, 3.7 Hz, 1H), 7.93 – 7.87 (m, 2H), 7.75 (dt, *J* = 5.9, 1.9 Hz, 1H), 7.65 – 7.58 (m, 2H), 7.58 – 7.54 (m, 2H), 7.51 (dd, *J* = 8.6, 2.2 Hz, 1H), 7.03 (d, *J* = 2.2 Hz, 1H), 1.34 (s, 9H), 1.29 (s, 9H). **<sup>13</sup>C NMR** (126 MHz, CDCl<sub>3</sub>) δ 163.84, 163.12, 156.31, 155.84, 153.65, 153.53, 150.90, 150.62, 143.81, 139.08, 137.08, 132.02, 131.88, 131.70, 130.22, 129.24, 128.71, 127.67, 127.63, 127.53, 127.50, 127.38, 126.94, 126.80, 125.22, 123.37, 121.38, 35.75, 34.46, 31.91, 31.36. **HRMS-ESI** (*m/z*): calculated C<sub>47</sub>H<sub>36</sub>ClN<sub>4</sub>O<sub>7</sub>Re [M+NH<sub>4</sub>]<sup>+</sup>: 1008.2174, found 1008.2152



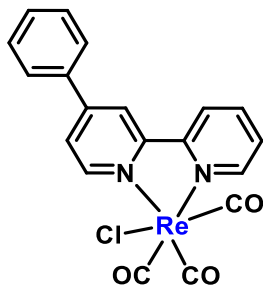
### [DtB-NDI-4-Phbpy-Re(CO)<sub>3</sub>-Py]PF<sub>6</sub>

In a nitrogen filled glove box, an oven dried pressure flask with a magnetic stirrer was filled with **DtB-NDI-4-Phbpy-Re-Cl** (30 mg, 0.030 mmol), AgPF<sub>6</sub> (8 mg, 0.033 mmol), pyridine (20 mL). The pressure flask was capped and brought out of the glovebox and heated to 80 °C overnight. The solution was cooled to room temperature and 50 mL of DCM was added. The solution was then

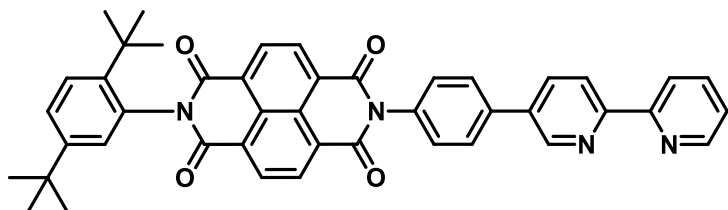
filtered. The solvent was removed under reduced pressure and then column chromatographed on silica using a gradient between dichloromethane and Acetone (100 → 90:10). The compound was then dissolved in minimal dichloromethane and layered with diethyl ether. Upon filtering, a bright yellow compound was obtained (16 mg, 42%). **<sup>1</sup>H NMR** (500 MHz, Chloroform-*d*) δ 9.10 – 9.03 (m, 2H), 8.86 (s, 4H), 8.77 – 8.69 (m, 2H), 8.32 (td, *J* = 7.9, 1.5 Hz, 1H), 8.16 (dt, *J* = 5.2, 1.5 Hz, 2H), 8.10 (d, *J* = 8.5 Hz, 2H), 7.91 (dd, *J* = 5.9, 1.9 Hz, 1H), 7.82 (tt, *J* = 7.7, 1.5 Hz, 1H), 7.72 (ddd, *J* = 7.4, 5.6, 1.1 Hz, 1H), 7.63 – 7.54 (m, 3H), 7.48 (dd, *J* = 8.6, 2.2 Hz, 1H), 7.42 – 7.35 (m, 2H), 7.01 (d, *J* = 2.2 Hz, 1H), 1.32 (s, 9H), 1.27 (s, 9H) **<sup>13</sup>C NMR** (126 MHz, CDCl<sub>3</sub>) δ 163.9, 162.9, 156.5, 155.9, 152.8, 152.8, 152.6, 151.7, 150.5, 143.8, 141.8, 140.1, 137.5, 136.0, 132.1, 131.7, 131.6, 130.3, 129.1, 129.1, 128.9, 127.6, 127.5, 127.5, 127.4, 126.9, 126.4, 126.2, 123.8, 35.7, 34.4, 31.9, 31.3 **HRMS-ESI** (*m/z*): calculated C<sub>52</sub>H<sub>41</sub>N<sub>5</sub>O<sub>7</sub>Re [M – PF<sub>6</sub>]<sup>+</sup>: 1034.2563, found 1034.2561



4-phenyl-2,2'-bipyridine was prepared as was previously reported.<sup>191</sup>



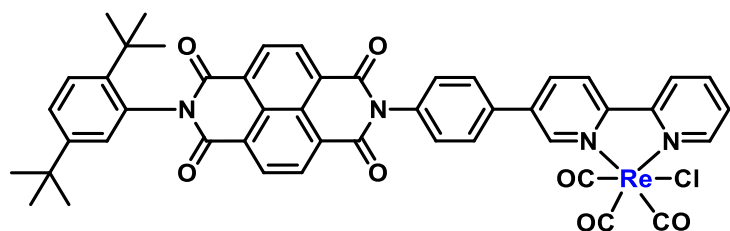
4-Phbpy-Re(CO)<sub>3</sub>-Cl was prepared as was previously reported.<sup>191</sup> **<sup>1</sup>H NMR** (500 MHz, Chloroform-*d*) δ 9.10 (d, *J* = 5.3 Hz, 1H), 9.07 (d, *J* = 5.8 Hz, 1H), 8.32 (d, *J* = 1.7 Hz, 1H), 8.30 (d, *J* = 8.3 Hz, 1H), 8.08 (td, *J* = 7.9, 1.6 Hz, 1H), 7.72 – 7.68 (m, 3H), 7.62 – 7.54 (m, 4H). **<sup>13</sup>C NMR** (126 MHz, CDCl<sub>3</sub>) δ 197.24, 189.67, 156.06, 155.99, 153.47, 153.42, 151.96, 138.98, 136.08, 130.95, 129.86, 127.36, 127.27, 125.11, 123.21, 121.14, 77.41, 77.16, 76.91, 53.57, 31.09, 29.86, 22.96. **HRMS-ESI** (*m/z*): calculated C<sub>19</sub>H<sub>12</sub>ClN<sub>2</sub>O<sub>3</sub>Re [[M]<sub>2</sub>+NH<sub>4</sub>]<sup>+</sup>: 1094.053, found 1094.049. [[M]<sub>2</sub>+Na]<sup>+</sup>: 1099.009, found 1099.008. [M+Na]<sup>+</sup>: 560.999 found, 560.994.



### DtB-NDI-5-Phbpy

In an oven dried round bottom flask with a magnetic stirrer and reflux condenser, DtB-NDI-PhBpin (0.81 g, 1.24 mmol), 5-bromo-2,2'-bipyridyl (0.29 g, 1.24 mmol), and Na<sub>2</sub>CO<sub>3</sub> (1.05 g, 9.92 mmol) were dissolved in THF (80mL) and H<sub>2</sub>O (27 mL) and put under N<sub>2</sub>. After 15 minutes of purging, fresh Pd[PPh<sub>3</sub>]<sub>4</sub> (0.14 g, 5% eq) was added via the second port and purged for 5 minutes. The solution was set to reflux overnight. The solution was cooled to room temperature

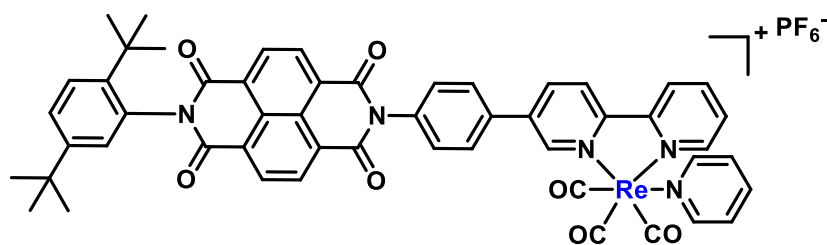
and the solvent was removed under reduced pressure. The remaining solid was washed with H<sub>2</sub>O and filtered. The solid on top of the filter paper was then washed with THF and filtered. The remaining solid was collected. (0.76 g, 90%). <sup>1</sup>H NMR (500 MHz, Chloroform-*d*) δ 9.01 (dd, *J* = 2.4, 0.8 Hz, 1H), 8.89 – 8.87 (m, *J* = 1.8 Hz, 4H), 8.73 (ddd, *J* = 4.9, 1.9, 0.9 Hz, 1H), 8.54 (dd, *J* = 8.2, 0.9 Hz, 1H), 8.47 (dt, *J* = 7.9, 1.1 Hz, 1H), 8.11 (dd, *J* = 8.2, 2.4 Hz, 1H), 7.91 – 7.83 (m, 3H), 7.62 (d, *J* = 8.6 Hz, 1H), 7.56 – 7.46 (m, 3H), 7.35 (ddd, *J* = 7.5, 4.7, 1.2 Hz, 1H), 7.03 (d, *J* = 2.2 Hz, 1H), 1.34 (s, 9H), 1.29 (s, 9H), 1.27 (d, *J* = 14.0 Hz, 1H).



### DtB-NDI-5-Phbpy-Re(CO)<sub>3</sub>-Cl

In a nitrogen filled glove box, an oven dried pressure flask with a magnetic stirrer was filled with compound **DtB-NDI-5-Phbpy** (0.30 g, 0.44 mmol), pentacarbonylchlororhenium(I) (0.25 g, 0.69 mmol), and dichloromethane (30 mL). The pressure flask was capped and brought out of the glovebox and heated to 80 °C overnight. The solution was cooled to room temperature and 150mL of N-heptane was added. Then dichloromethane was rotovapped from the solution. The remaining solution was then filtered and washed with N-heptane to yield the product. (0.40 g, 92%). <sup>1</sup>H NMR (500 MHz, Chloroform-*d*) δ 9.33 (s, 1H), 9.14 – 9.09 (m, 1H), 8.89 (s, 4H), 8.30 (d, *J* = 1.4 Hz, 2H), 8.24 (d, *J* = 8.0 Hz, 1H), 8.11 (td, *J* = 7.9, 1.6 Hz, 1H), 7.90 (d, *J* = 8.1 Hz, 2H), 7.65 – 7.54 (m, 4H), 7.50 (dd, *J* = 8.7, 2.3 Hz, 1H), 7.03 (d, *J* = 2.2 Hz, 1H), 1.34 (s, 9H), 1.29 (s, 9H). <sup>13</sup>C NMR (126 MHz, CDCl<sub>3</sub>) δ 163.87, 163.09, 155.62, 154.56, 153.48, 151.69, 150.58, 143.82,

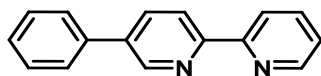
139.78, 139.09, 137.28, 136.40, 135.65, 132.07, 131.82, 131.67, 130.17, 129.20, 128.80, 127.66, 127.58, 127.52, 127.48, 127.25, 126.89, 123.30, 123.26, 35.74, 34.46, 31.90, 31.36. **HRMS-ESI** ( $m/z$ ): ( $m/z$ ): calculated  $C_{47}H_{36}ClN_4O_7Re$   $[M+NH_4]^+$ : 1008.2174, found 1008.2154



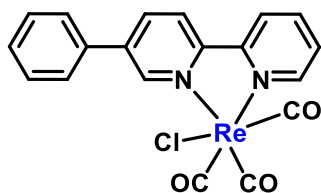
### [DtB-NDI-5-Phbpy-Re(CO)<sub>3</sub>-Py]PF<sub>6</sub>

In a nitrogen filled glove box, an oven dried pressure flask with a magnetic stirrer was filled with **DtB-NDI-5-Phbpy-Re-Cl** (0.20 g, 0.20 mmol), AgPF<sub>6</sub> (0.08 g, 0.33 mmol), pyridine (30 mL). The pressure flask was capped and brought out of the glovebox and heated to 80 °C overnight. The solution was cooled to room temperature and 100 mL of DCM was added. The solution was then filtered. The solvent was removed under reduced pressure and then column chromatographed on silica using a gradient between dichloromethane and Acetone (100 → 90:10). The compound was then dissolved in minimal dichloromethane and layered with diethyl ether. Upon filtering, a bright yellow compound was obtained (0.15 g, 65%). **<sup>1</sup>H NMR** (500 MHz, Chloroform-*d*) δ 9.25 (d,  $J = 2.3$  Hz, 1H), 9.10 – 9.05 (m, 1H), 8.90 (s, 4H), 8.70 (d,  $J = 8.5$  Hz, 1H), 8.64 (d,  $J = 8.2$  Hz, 1H), 8.56 (dd,  $J = 8.4, 2.1$  Hz, 1H), 8.34 (td,  $J = 8.0, 1.6$  Hz, 1H), 8.16 (dt,  $J = 5.2, 1.5$  Hz, 2H), 7.94 (d,  $J = 8.3$  Hz, 2H), 7.86 (tt,  $J = 7.7, 1.5$  Hz, 1H), 7.77 – 7.70 (m, 1H), 7.65 – 7.57 (m, 3H), 7.51 (dd,  $J = 8.6, 2.3$  Hz, 1H), 7.45 – 7.38 (m, 2H), 7.03 (d,  $J = 2.2$  Hz, 1H), 1.34 (s, 9H), 1.29 (s, 9H). **<sup>13</sup>C NMR** (126 MHz, CDCl<sub>3</sub>) δ 163.84, 163.11, 155.77, 154.62, 152.63, 151.68, 150.64, 150.59, 143.82, 141.82, 141.05, 140.24, 139.84, 136.82, 135.06, 132.05, 131.87, 131.67, 130.34, 129.22,

128.97, 128.72, 127.65, 127.57, 127.53, 127.49, 126.92, 126.82, 126.33, 126.28, 35.75, 34.47, 31.91, 31.36. **HRMS-ESI** ( $m/z$ ): calculated  $C_{52}H_{41}N_5O_7Re$   $[M - PF_6]^+$ : 1034.2563, found 1034.2563

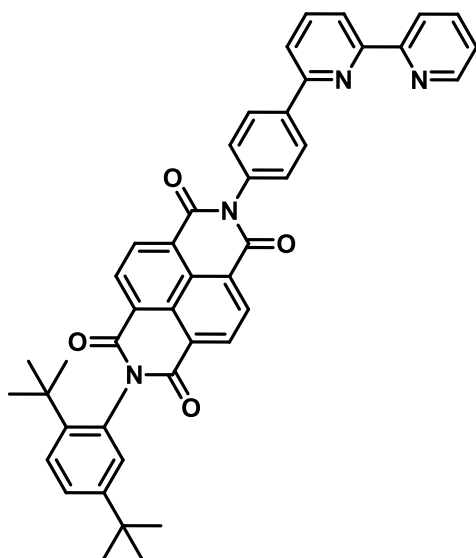


In an oven dried round bottom flask with a magnetic stirrer and reflux condenser, Phenylboronic acid (0.187, 1.534 mole), 5-Bromo-2,2'-bipyridine (0.30 g, 1.28 mmol), and  $Na_2CO_3$  (1.02 g, 9.60 mmol) were dissolved in THF (50 mL) and  $H_2O$  (15 mL) and put under  $N_2$ . After 15 minutes of purging, fresh  $Pd(PPh_3)_4$  (0.07 g, 5% eq) was added via the second port and purged for 5 minutes. The solution was set to reflux overnight. The solution was cooled to room temperature and the solvent was removed under reduced pressure. The crude material was dissolved in dichloromethane and ran through a celite plug. The solvent was removed under reduced pressure. The compound was not purified further and a conversion of 100% was assumed for further purposes.



In air with a reflux condenser attached to a round bottom flask with a magnetic stirrer was filled with **5-phenyl-2,2'-bipyridine** (xx g, mmol), pentacarbonylchlororhenium(I) (xx g, xxx mmol), and toluene (30 mL). The reaction was heated to reflux for 3 hours. The solution was cooled to room temperature and the solution was filtered. The solid was then washed with cold toluene to yield a bright yellow product.  **$^1H$  NMR** (500 MHz, Chloroform-*d*)  $\delta$  9.25 (t,  $J = 1.4$  Hz, 1H), 9.09

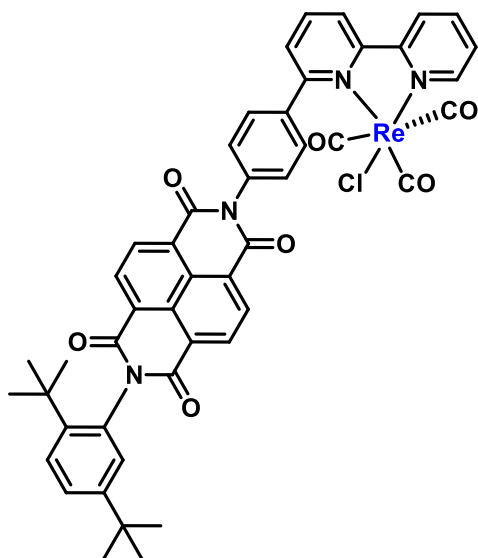
(ddd,  $J = 5.5, 1.6, 0.8$  Hz, 1H), 8.24 – 8.20 (m, 3H), 8.09 (td,  $J = 7.9, 1.6$  Hz, 1H), 7.69 – 7.66 (m, 2H), 7.59 – 7.53 (m, 4H).  $^{13}\text{C}$  NMR (126 MHz,  $\text{CDCl}_3$ )  $\delta$  155.77, 153.95, 153.41, 151.55, 140.76, 139.01, 136.94, 134.63, 130.12, 129.83, 127.48, 127.06, 123.14, 123.07, 77.41, 77.16, 76.91. **HRMS-ESI** ( $m/z$ ): calculated  $\text{C}_{19}\text{H}_{12}\text{ClN}_2\text{O}_3\text{Re}$   $[[\text{M}]_2+\text{NH}_4]^+$ : 1094.053, found 1094.046.  $[[\text{M}]_2+\text{Na}]^+$ : 1099.009, found 1099.004.  $[\text{M}+\text{Na}]^+$ : 560.999 found, 560.996.



### DtB-NDI-6-Phbpy

In an oven dried round bottom flask with a magnetic stirrer and reflux condenser, DtB-NDI-PhBpin (0.24 g, 0.037 mmol), 6-bromo-2,2'-bipyridyl (0.10 g, 0.43 mmol), and  $\text{Na}_2\text{CO}_3$  (0.32 g, 3.00 mmol) were dissolved in THF (80mL) and  $\text{H}_2\text{O}$  (27 mL) and put under  $\text{N}_2$ . After 15 minutes of purging, fresh  $\text{Pd}[\text{PPh}_3]_4$  (0.02 g, 5% eq) was added via the second port and purged for 5 minutes. The solution was set to reflux overnight. The solution was cooled to room temperature and the solvent was removed under reduced pressure. The product was extracted DCM and washed with  $\text{H}_2\text{O}$  (2 x 100 mL). The DCM was removed under reduced pressure. The remaining solid was

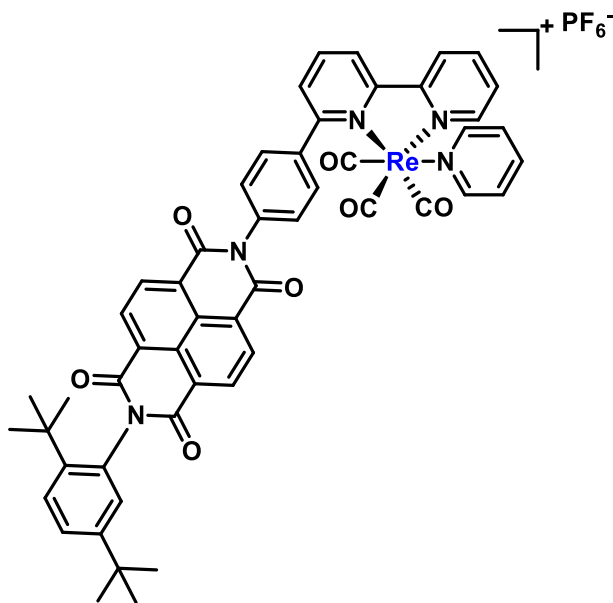
then sonicated in copious amounts of MeOH and filtered. The remaining solid was collected. (0.10 g, 63%).  $^1\text{H NMR}$  (500 MHz, Chloroform-*d*)  $\delta$  8.92 – 8.85 (m, 4H), 8.74 – 8.69 (m, 1H), 8.66 (d,  $J = 8.0$  Hz, 1H), 8.44 (d,  $J = 7.8$  Hz, 1H), 8.37 (d,  $J = 8.2$  Hz, 2H), 7.95 (t,  $J = 7.8$  Hz, 1H), 7.91 – 7.83 (m, 2H), 7.62 (d,  $J = 8.6$  Hz, 1H), 7.54 – 7.46 (m, 3H), 7.35 (ddd,  $J = 7.5, 4.8, 1.2$  Hz, 1H), 7.03 (d,  $J = 2.2$  Hz, 1H), 1.34 (s, 9H), 1.29 (s, 9H)



### DtB-NDI-6-Phbpy-Re(CO)<sub>3</sub>-Cl

In a nitrogen filled glove box, an oven dried pressure flask with a magnetic stirrer was filled with compound DtB-NDI-6-Phbpy (0.25 g, 0.36 mmol), pentacarbonylchlororhenium(I) (0.20 g, 0.54 mmol), and dichloromethane (30 mL). The pressure flask was capped and brought out of the glovebox and heated to 80 °C overnight. The solution was cooled to room temperature and was removing under reduced pressure. The remaining solution was then sonicated in copious amounts of MeOH and filtered, and then washed with pentanes to yield the product. (0.30 g, 85%).  $^1\text{H NMR}$  (500 MHz, Chloroform-*d*)  $\delta$  9.15 (d,  $J = 5.3$  Hz, 1H), 8.93 – 8.85 (m, 4H), 8.28 (td,  $J = 6.0, 2.9$  Hz, 2H), 8.20 – 8.07 (m, 2H), 7.96 (bs, 1H), 7.85 (bs, 1H), 7.75 (dd,  $J = 7.6, 1.2$  Hz, 1H), 7.62

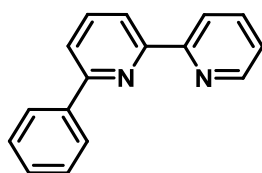
- 7.55 (m, 4H), 7.58 – 7.47 (m, 1H), 7.03 (d,  $J = 2.2$  Hz, 1H), 1.34 (s, 9H), 1.29 (s, 9H).  $^{13}\text{C}$  NMR (126 MHz,  $\text{CDCl}_3$ )  $\delta$  163.95, 163.74, 163.05, 157.12, 156.97, 153.42, 150.55, 143.86, 142.04, 139.09, 138.83, 136.57, 132.14, 131.77, 131.69, 129.18, 128.12, 127.69, 127.52, 127.47, 127.44, 127.07, 126.91, 126.86, 123.96, 122.18, 35.74, 34.45, 31.91, 31.36. **HRMS-ESI** ( $m/z$ ): calculated  $\text{C}_{47}\text{H}_{36}\text{ClN}_4\text{O}_7\text{Re}$  [ $\text{M}+\text{NH}_4$ ] $^+$ : 1008.2174, found 1008.2155



### [DtB-NDI-6-Phbpy-Re(CO) $_3$ -Py]PF $_6$

In a nitrogen filled glove box, an oven dried pressure flask with a magnetic stirrer was filled with **DtB-NDI-6-Phbpy-Re-Cl** (0.10 g, 0.10 mmol), AgPF $_6$  (0.03 g, 0.15 mmol), and pyridine (30 mL). The pressure flask was capped and brought out of the glovebox and heated to 80 °C overnight. The solution was cooled to room temperature and 100 mL of DCM was added. The solution was then filtered. The solvent was removed under reduced pressure and then column chromatographed on silica using a gradient between dichloromethane and ethyl acetate (100  $\rightarrow$  70:30). The compound was then dissolved in minimal dichloromethane and layered with diethyl ether. Upon filtering, a

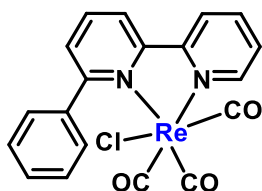
bright yellow compound was obtained (0.03 g, 26%). **<sup>1</sup>H NMR** (500 MHz, Chloroform-*d*)  $\delta$  9.14 (dd,  $J = 5.5, 1.5$  Hz, 1H), 8.90 (d,  $J = 1.3$  Hz, 4H), 8.60 – 8.50 (m, 2H), 8.38 – 8.30 (m, 2H), 7.96 – 7.82 (m, 5H), 7.75 (ddd,  $J = 6.9, 5.4, 1.3$  Hz, 1H), 7.67 (bs, 1H), 7.62 (d,  $J = 8.6$  Hz, 2H), 7.58 (bs, 1H), 7.50 (dd,  $J = 8.6, 2.2$  Hz, 1H), 7.40 – 7.33 (m, 2H), 7.02 (d,  $J = 2.2$  Hz, 1H), 1.34 (s, 9H), 1.29 (s, 9H). **<sup>13</sup>C NMR** (126 MHz, CDCl<sub>3</sub>)  $\delta$  163.84, 163.32, 163.05, 157.06, 156.29, 152.55, 151.61, 150.60, 143.82, 141.86, 141.53, 141.45, 140.20, 137.40, 132.05, 131.86, 131.71, 129.67, 129.21, 128.46, 127.64, 127.52, 127.48, 126.93, 126.83, 126.77, 124.75, 35.75, 34.46, 31.91, 31.36. **HRMS-ESI** ( $m/z$ ): calculated C<sub>52</sub>H<sub>41</sub>N<sub>5</sub>O<sub>7</sub>Re [M – PF<sub>6</sub>]<sup>+</sup>: 1034.2563, found 1034.2557



### 6-phenyl-2,2'-bipyridine

In an oven dried round bottom flask with a magnetic stirrer and reflux condenser, (0.33 g, 2.78 mmol), 6-bromo-2,2'-bipyridyl (0.5 g, 2.14 mmol), and Na<sub>2</sub>CO<sub>3</sub> (1.8 g, xx mmol) were dissolved in THF (80mL) and H<sub>2</sub>O (27 mL) and put under N<sub>2</sub>. After 15 minutes of purging, fresh Pd(PPh<sub>3</sub>)<sub>4</sub> (0.24 g, 10% eq) was added via the second port and purged for 5 minutes. The solution was set to reflux overnight. The solution was cooled to room temperature and the solvent was removed under reduced pressure. The product was extracted DCM and washed with H<sub>2</sub>O (2 x 100 mL). The DCM was removed under reduced pressure. The remaining solid was then sonicated in copious amounts of N-heptane and filtered through celite. The solution of N-heptane was then rotovapped to dryness. The solid was then column chromatographed on silica using dichloromethane and acetone (100 → 95:5). The fractions were then collected and rotovapped to dryness. The solid was then

sonicated in pentanes and put into the freezer. The product was then collected via vacuum filtration.



### 6-Phbpy-Re(CO)<sub>3</sub>-Cl

In air with a reflux condenser attached to a round bottom flask with a magnetic stirrer was filled with **6-phenyl-2,2'-bipyridine**, pentacarbonylchlororhenium(I) and toluene (30 mL). The reaction was heated to reflux for 3 hours. The solution was cooled to room temperature and the solution was filtered. The solid was then washed with cold methanol to yield a bright yellow product. **<sup>1</sup>H NMR** (500 MHz, Chloroform-*d*) δ 9.11 (d, *J* = 5.0 Hz, 1H, 6'-H), 8.25 – 8.20 (m, 2H, 3, 3'-H), 8.10 – 8.06 (m, 2H, 4, 4'-H), 7.66 (bs, 2H, 8, 9-H), 7.63 (dd, *J* = 7.7, 1.2 Hz, 1H, 5-H), 7.59 – 7.56 (m, 3H, 10, 11, 12-H), 7.55 – 7.51 (m, 1H, 5-H). **<sup>13</sup>C NMR** (126 MHz, CDCl<sub>3</sub>) δ 197.13 (CO), 192.84 (CO), 190.82 (CO), 164.73 (2-C), 157.28 (6-C), 156.55 (2'-C), 153.33 (6'-C), 141.71 (7-C), 138.83 (4'-C), 138.76 (4-C), 130.37 (10,11,12-C), 129.35 (5-C), 127.94 (bs, 8,9-C), 126.75 (5'-C), 123.88 (3-C), 121.82 (3'-C). **HRMS-ESI** (*m/z*): calculated C<sub>19</sub>H<sub>12</sub>ClN<sub>2</sub>O<sub>3</sub>Re [[M]<sub>2</sub>+NH<sub>4</sub>]<sup>+</sup>: 1094.053, found 1094.049. [[M]<sub>2</sub>+Na]<sup>+</sup>: 1099.009, found 1099.006. [M+Na]<sup>+</sup>: 560.999 found, 560.998.

## 5.8 Supplementary Details

### 5.8.1 NMR Characterization

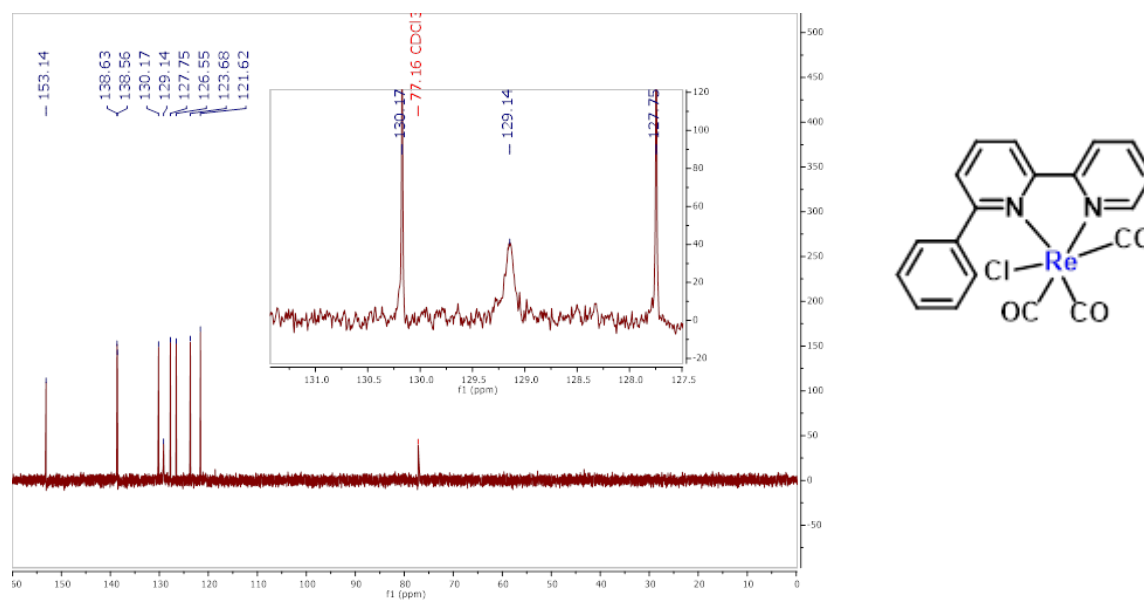


**Figure 5.12:**  $^{13}\text{C}$  Dept-135 experiment of complex **9**.

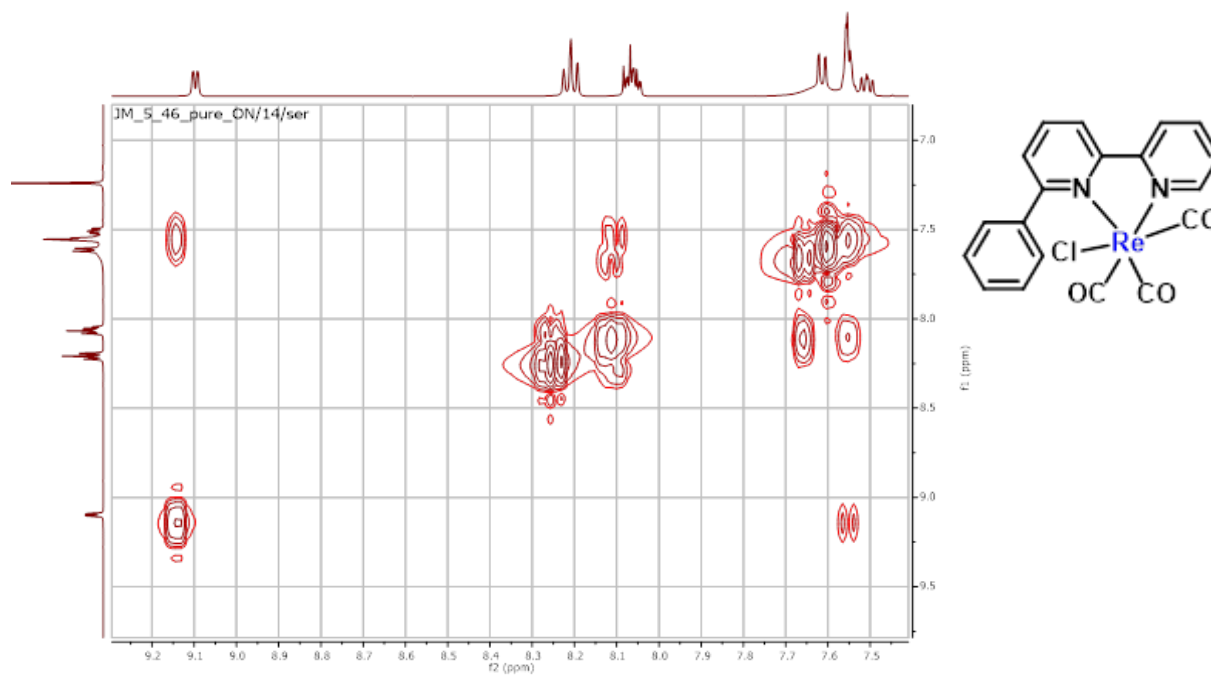


Figure 5.13: COSY NMR of complex 9.

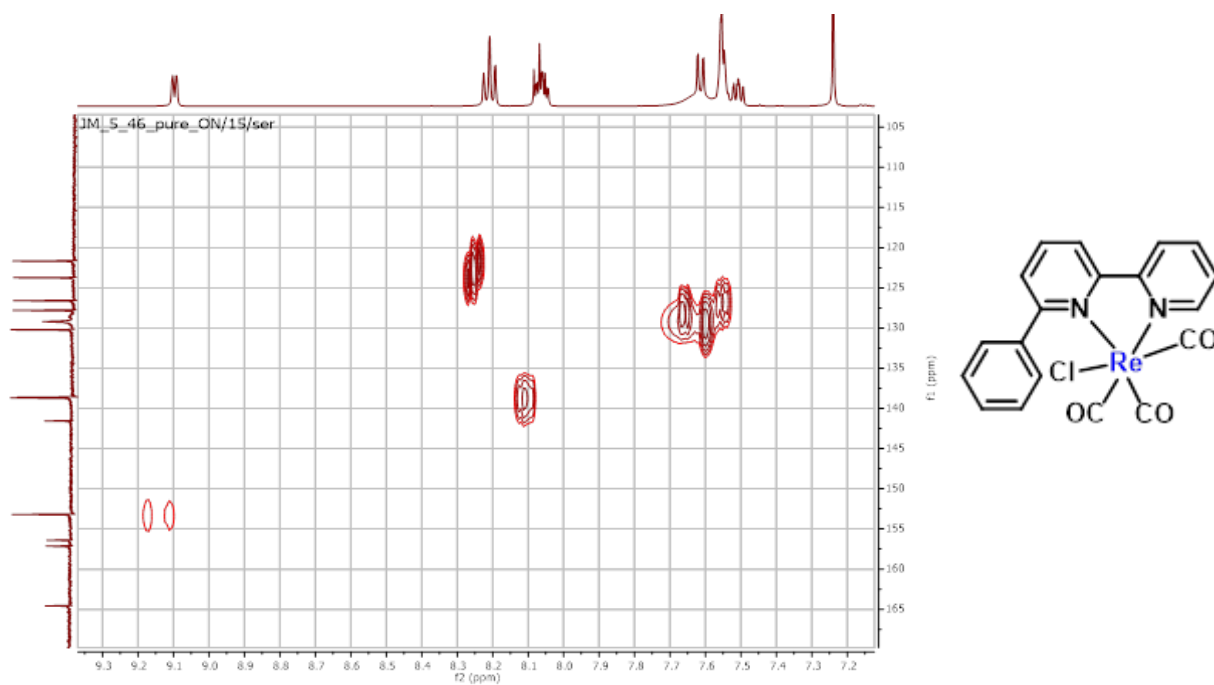
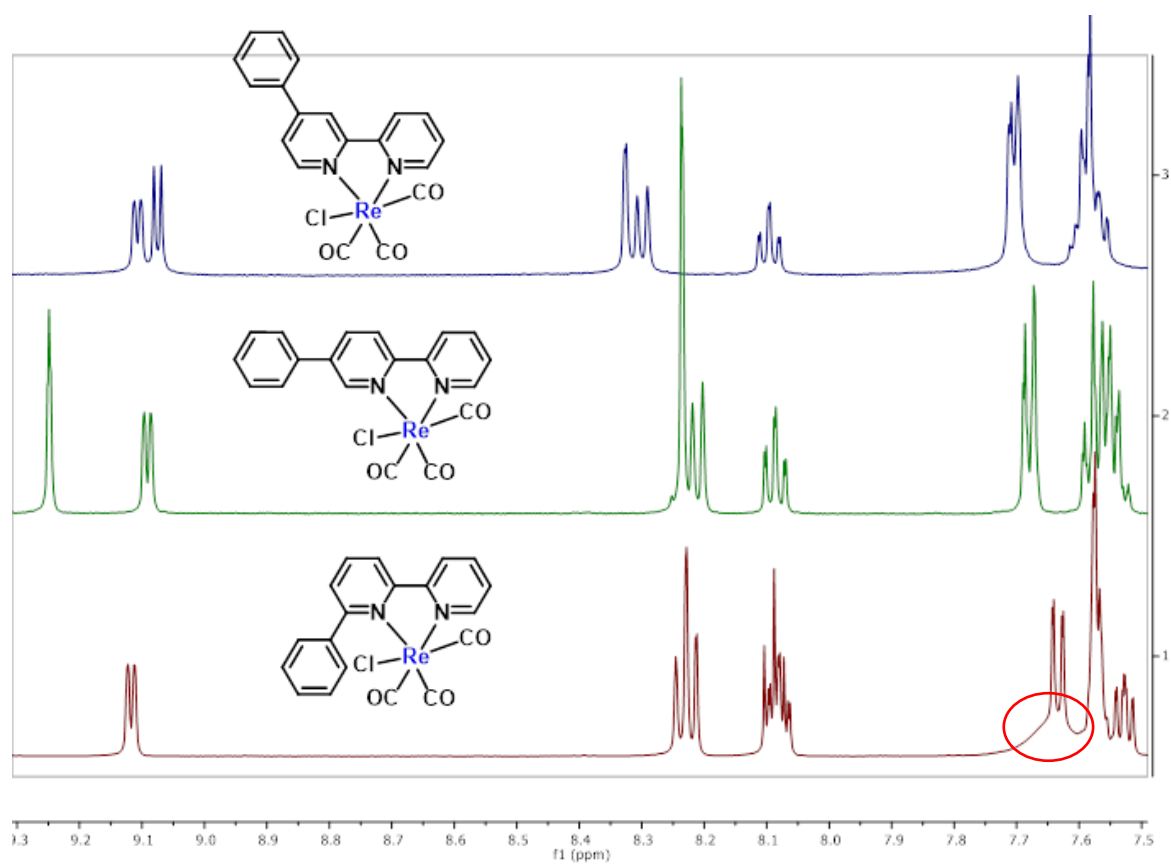
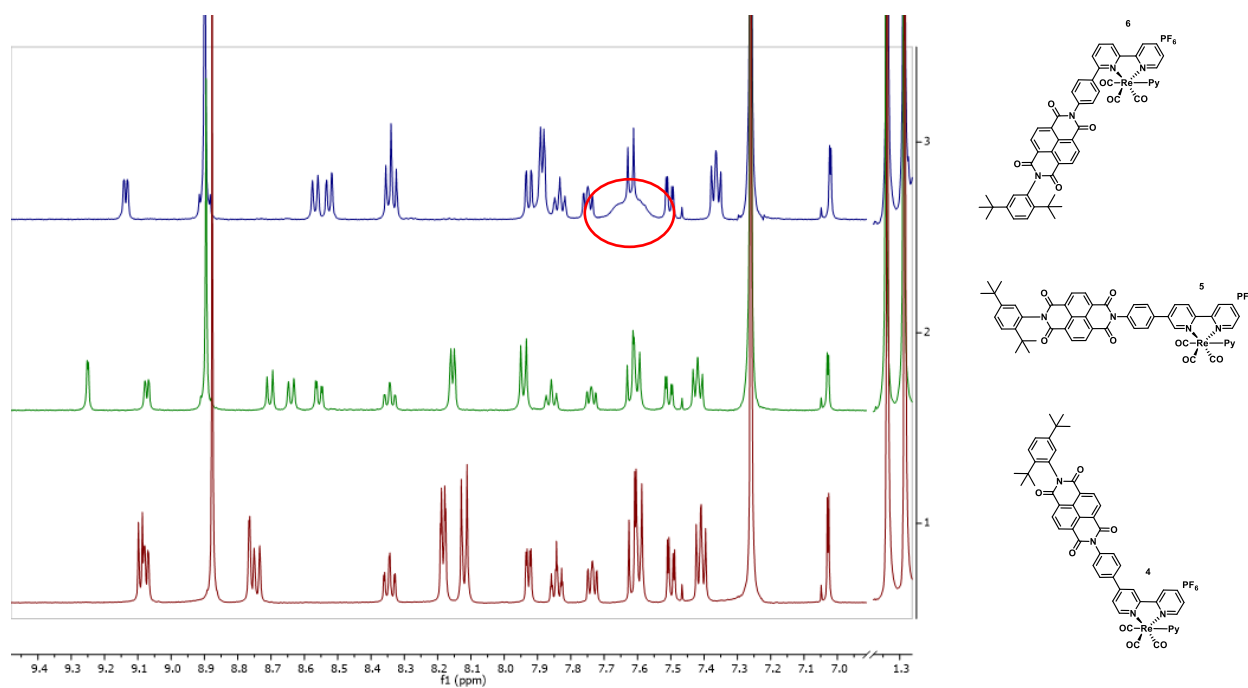


Figure 5.14: HSQC NMR of complex 9.



**Figure 5.15:**  $^1\text{H}$  NMRs of complexes **7-9**. No broadening of protons is found in complexes **7** or **8**. All taken in  $\text{CDCl}_3$



**Figure 5.16:**  $^1\text{H}$  NMRs of complexes **4-6**. No broadening of protons is found in complexes **4** or **5**. All taken in  $\text{CDCl}_3$  (7.26ppm)

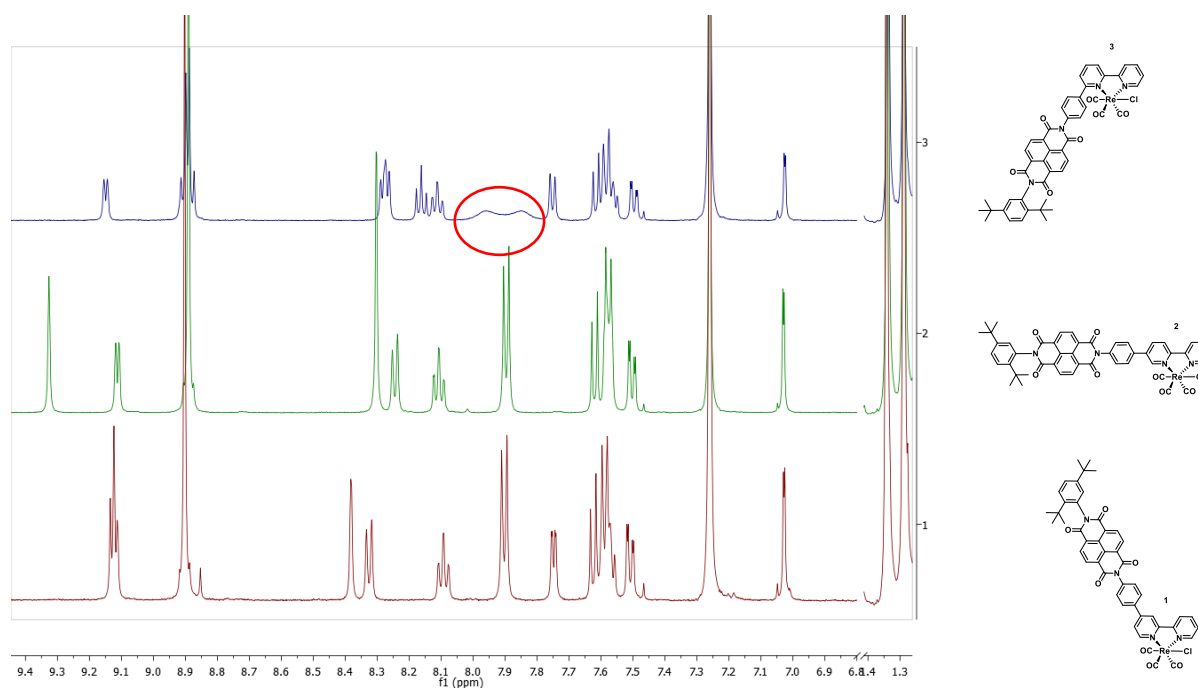


**Figure 5.17:**  $^1\text{H}$  NMRs of complexes **1-3**. No broadening of protons is found in complexes **1** or **2**. All  $^1\text{H}$  NMRs taken in  $\text{CDCl}_3$  (7.26ppm)

### 5.8.2 Fractional Atomic Coordinates and Equivalent Isotropic Displacement Parameters

**Table 5.9:** Fractional Atomic Coordinates ( $\times 10^4$ ) and Equivalent Isotropic Displacement Parameters ( $\text{\AA}^2 \times 10^3$ ) for complex **9**.  $U_{\text{eq}}$  is defined as 1/3 of the trace of the orthogonalised  $U_{\text{H}}$  tensor.

Atom	x	y	z	U(eq)
Re1	7033.6(2)	3953.3(2)	2709.1(2)	12.71(12)
Cl1	10387.5(13)	3634.2(7)	3401.2(5)	19.5(2)
O1	8181(5)	3890.9(19)	1047.5(18)	20.2(7)
O3	6057(4)	1936(2)	2337.3(17)	21.7(6)
O2	2860(4)	4385(3)	1893.9(18)	30.4(7)
N1	6545(6)	3976(2)	3933(2)	15.7(8)
N2	7728(5)	5375(2)	3137.5(18)	13.1(6)
C16	6239(8)	5964(3)	1310(3)	22.3(10)
C6	7817(5)	5500(3)	3943(2)	13.1(7)
C3	6661(7)	3968(3)	5575(3)	21.4(10)
C7	8401(6)	6318(3)	4329(3)	16.9(8)
C17	7776(7)	3957(2)	1668(3)	14.8(10)
C18	4403(7)	4252(3)	2218(2)	20.7(9)
C2	5897(6)	3230(3)	5104(3)	22.4(9)
C1	5863(6)	3257(3)	4288(2)	21.0(9)
C5	7224(5)	4707(3)	4385(2)	14.9(8)

C15	6086(8)	5943(3)	484(3)	28.1(11)
C4	7306(5)	4715(3)	5211(2)	16.7(8)
C19	6443(5)	2696(3)	2482(2)	15.7(8)
C12	9678(8)	6048(3)	1491(3)	23.3(10)
C11	8035(8)	6002(2)	1814(3)	17.8(10)
C13	9540(9)	6020(3)	666(3)	30.1(12)
C14	7753(11)	5964(3)	165(3)	34.9(14)
C9	8809(6)	6928(3)	3066(2)	19.4(8)
C10	8204(7)	6090(3)	2705(3)	17.1(10)
C8	8917(6)	7041(3)	3886(2)	18.6(8)

---

### 5.8.3 Time-Resolved Visible, Near-infrared, and Mid-infrared Spectroscopy

#### NDI-4Phbpy-ReCl

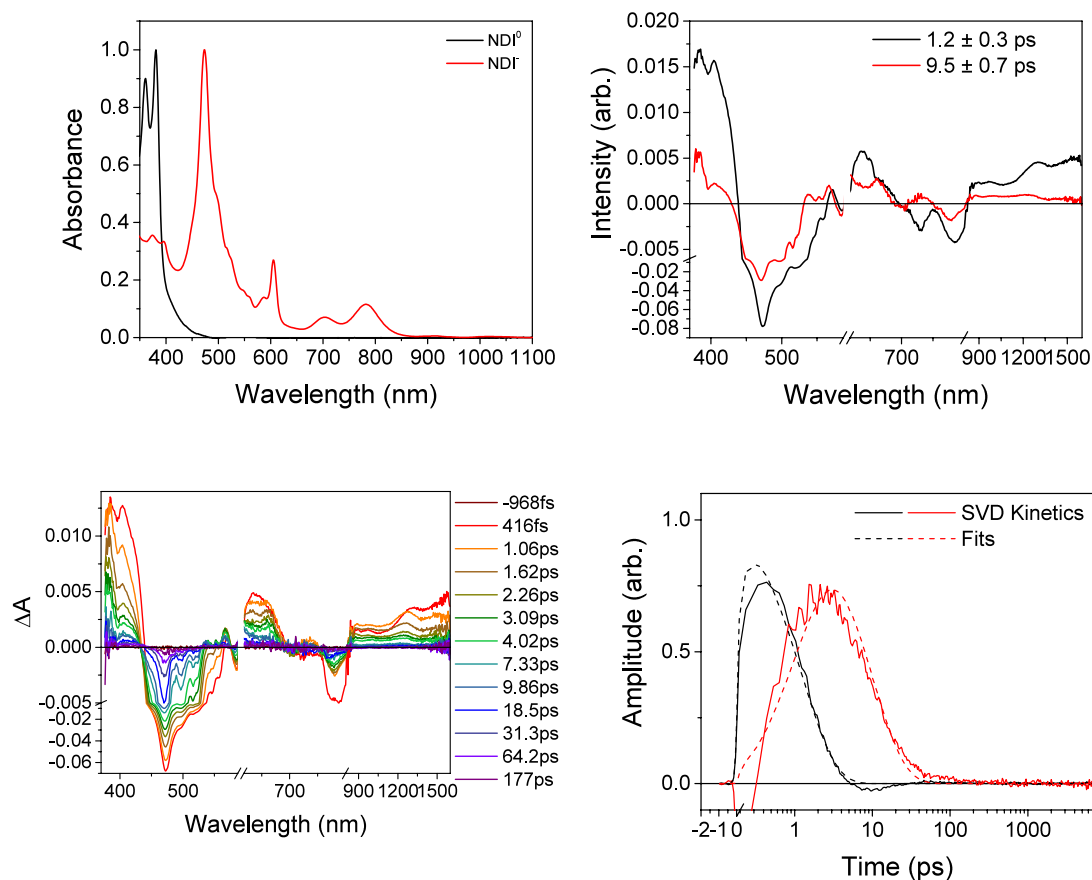


**Figure 5.18:** *Top left:* Electronic absorption spectrum of NDI-4Phbpy-ReCl in DMF without (black) and with (red) excess TDAE. *Bottom left:* fsTA spectrum of NDI-4Phbpy-ReCl in DMF with excess TDAE ( $\lambda_{\text{ex}} = 605$  nm). *Top right:* Species-associated spectra obtained from global analysis of TA data using Singular Value Decomposition (SVD) kinetic traces. Best-fit lifetimes of each spectral component are given in the legend. *Bottom right:* Kinetic traces (solid) and fits (dashed) obtained by SVD of fsTA data. Best-fit lifetimes are given in the legend for the species-associated spectra.

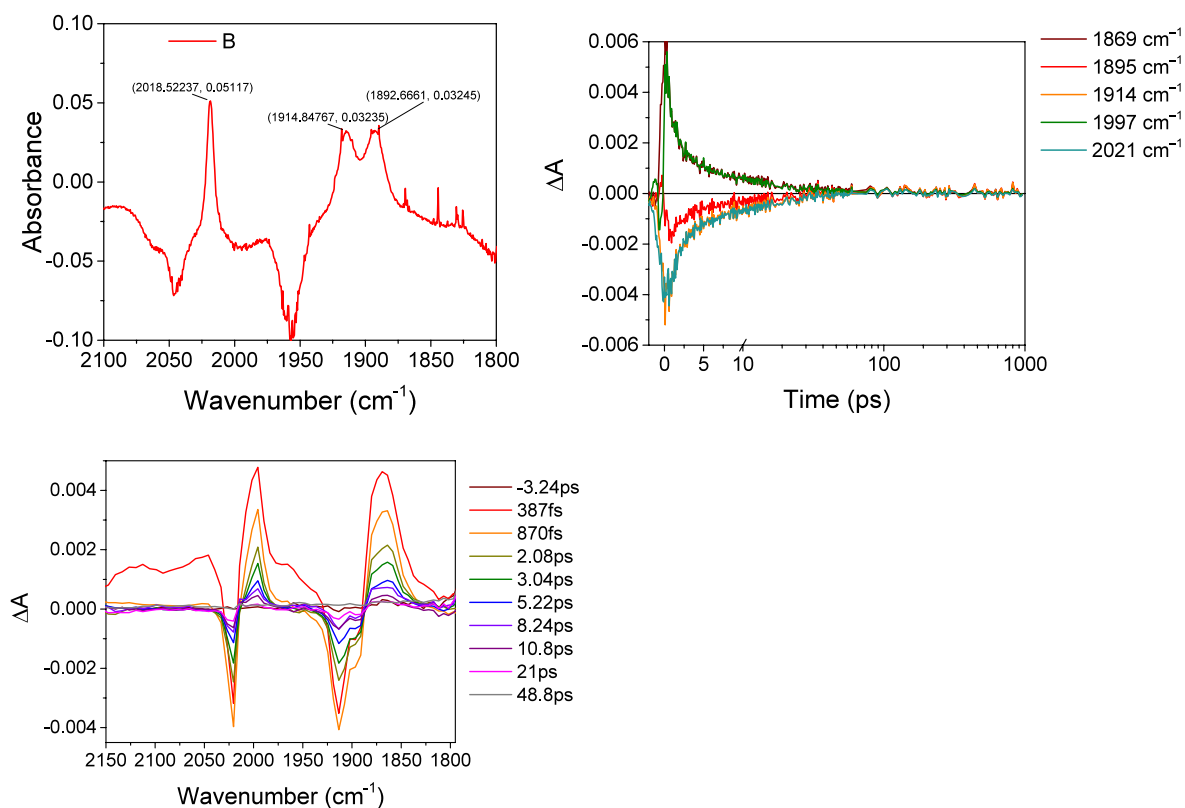


**Figure 5.19:** *Top left:* FTIR spectrum of NDI-4Phbpy-ReCl in DMF. *Bottom left:* fsIR spectrum of NDI-4Phbpy-ReCl in DMF with excess TDAE ( $\lambda_{\text{ex}} = 605 \text{ nm}$ ). *Top right:* Kinetic traces of the fsIR at the given frequencies.

## NDI-4Phbpy-RePy

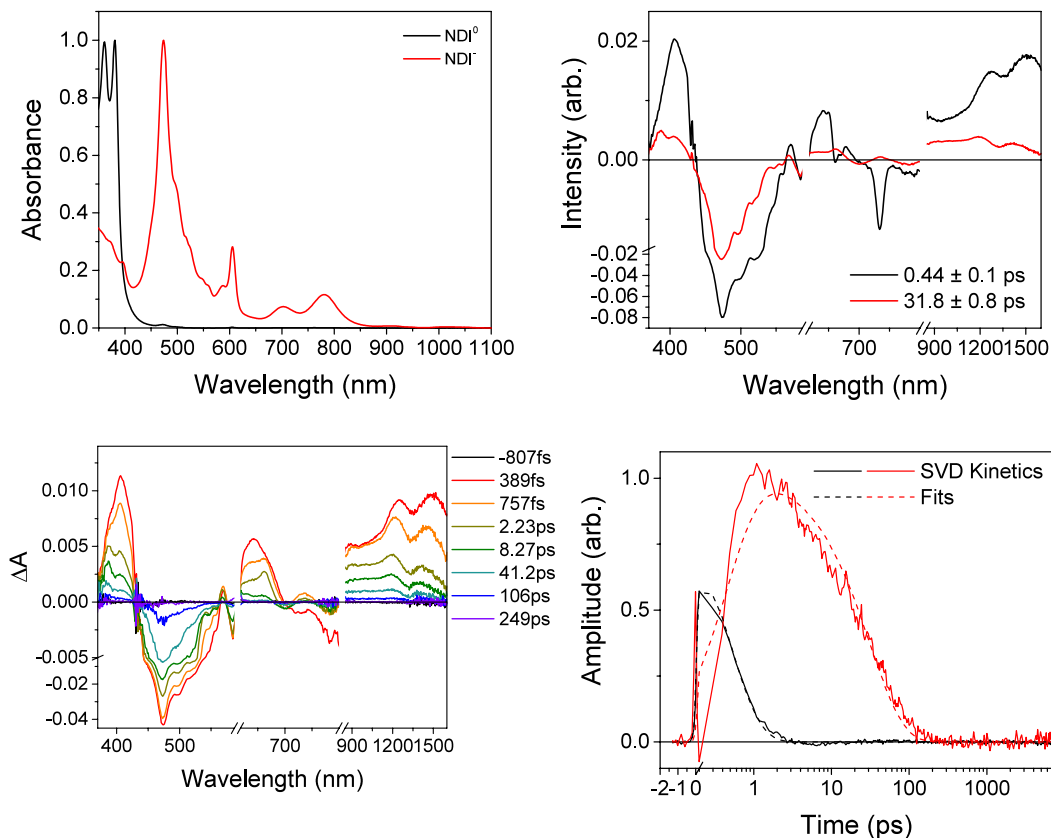


**Figure 5.20:** *Top left:* Electronic absorption spectrum of NDI-4Phbpy-RePy in DMF without (black) and with (red) excess TDAE. *Bottom left:* fsTA spectrum of NDI-4Phbpy-RePy in DMF with excess TDAE ( $\lambda_{\text{ex}} = 605$  nm). *Top right:* Species-associated spectra obtained from global analysis of TA data using Singular Value Decomposition (SVD) kinetic traces. Best-fit lifetimes of each spectral component are given in the legend. *Bottom right:* Kinetic traces (solid) and fits (dashed) obtained by SVD of fsTA data. Best-fit lifetimes are given in the legend for the species-associated spectra

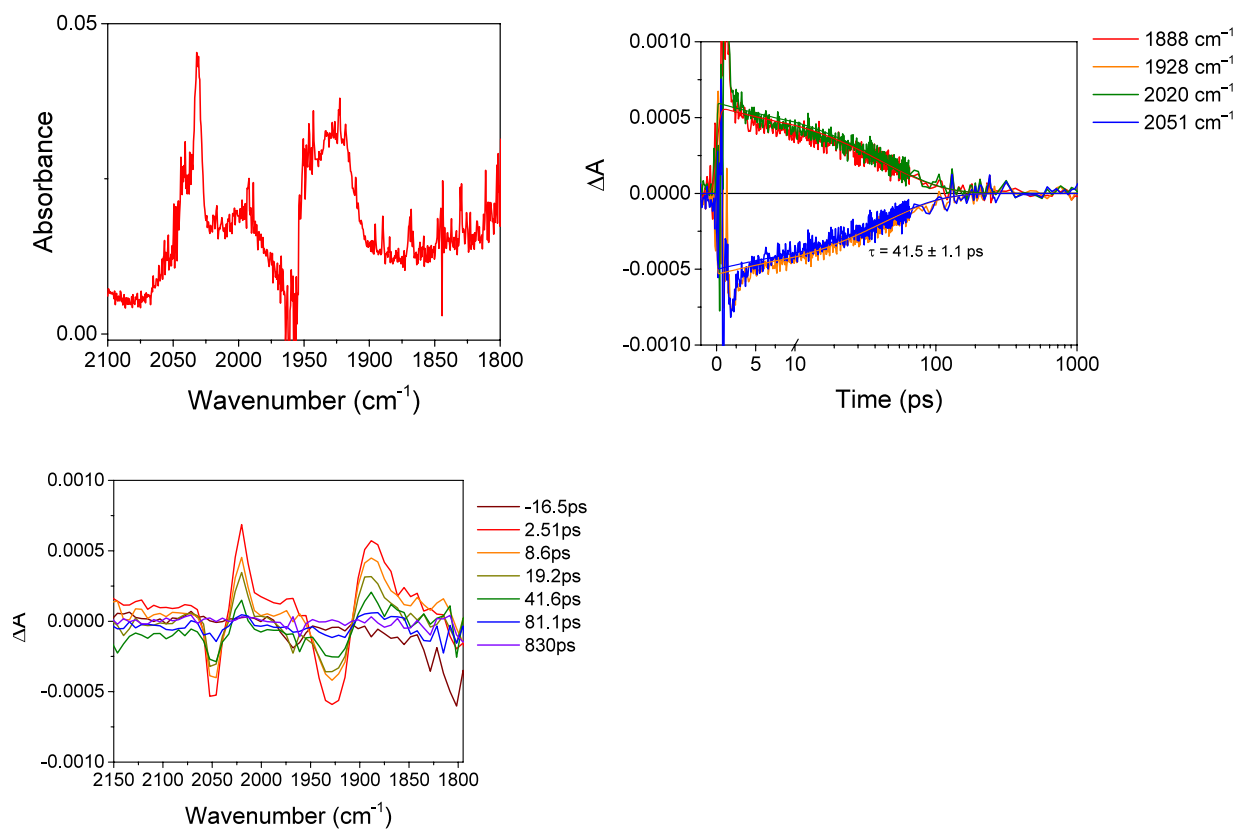


**Figure 5.21:** *Top left:* FTIR spectrum of NDI-4Phbpy-RePy in DMF. *Bottom left:* fsIR spectrum of NDI-4Phbpy-RePy in DMF with excess TDAE ( $\lambda_{ex} = 605$  nm). *Top right:* Kinetic traces and fits to the specified lifetime of the fsIR at the given frequencies.

## NDI-5Phbpy-ReCl

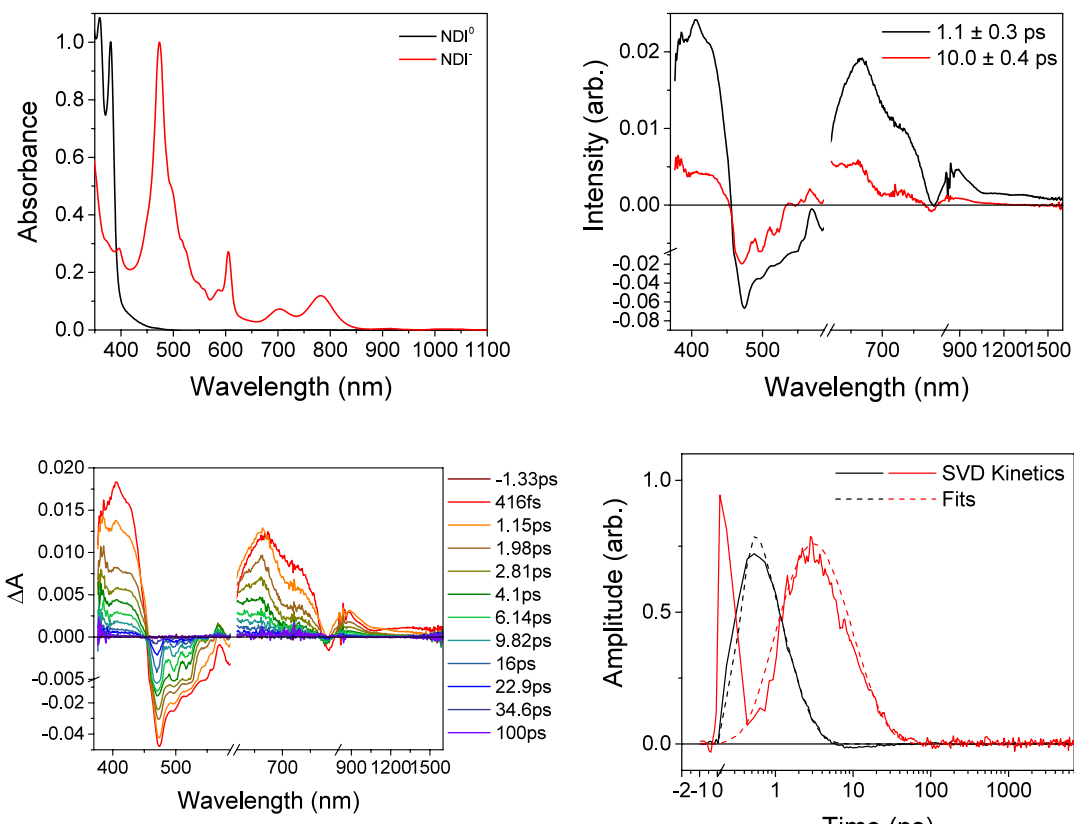


**Figure 5.22:** *Top left:* Electronic absorption spectrum of NDI-5Phbpy-ReCl in DMF without (black) and with (red) excess TDAE. *Bottom left:* fsTA spectrum of NDI-5Phbpy-ReCl in DMF with excess TDAE ( $\lambda_{\text{ex}} = 605$  nm). *Top right:* Species-associated spectra obtained from global analysis of TA data using Singular Value Decomposition (SVD) kinetic traces. Best-fit lifetimes of each spectral component are given in the legend. *Bottom right:* Kinetic traces (solid) and fits (dashed) obtained by SVD of fsTA data. Best-fit lifetimes are given in the legend for the species-associated spectra

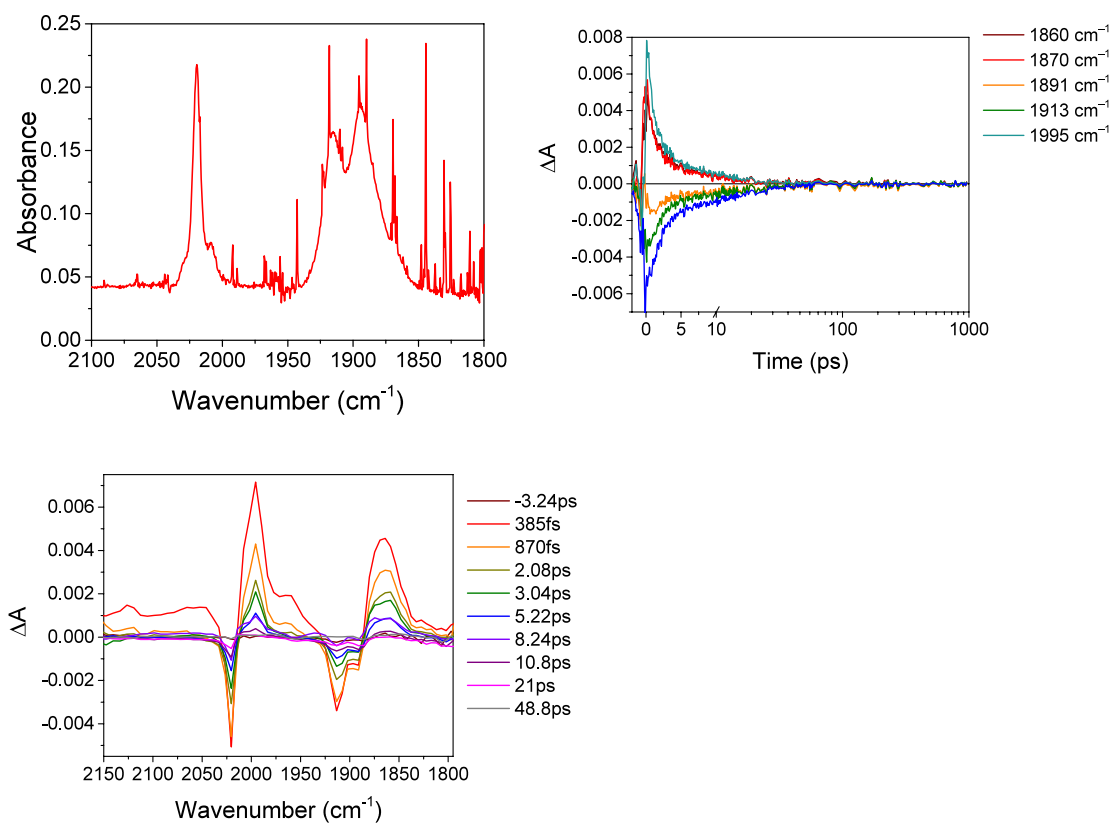


**Figure 5.23:** *Top left:* FTIR spectrum of NDI-5Phbpy-ReCl in DMF. *Bottom left:* fsIR spectrum of NDI-5Phbpy-ReCl in DMF with excess TDAE ( $\lambda_{\text{ex}} = 605$  nm). *Top right:* Kinetic traces of the fsIR at the given frequencies.

## NDI-5Phbpy-RePy

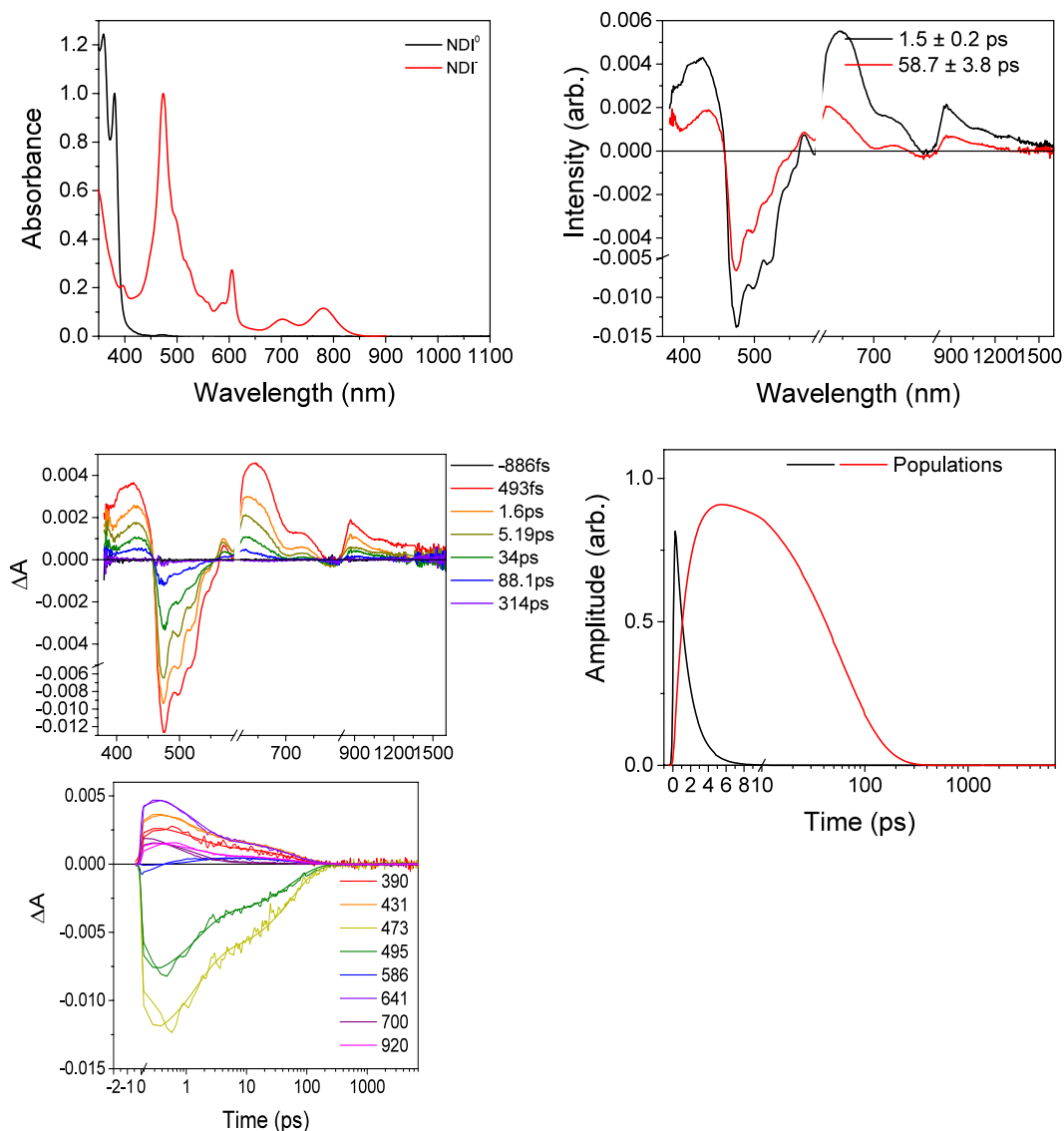


**Figure 5.24:** *Top left:* Electronic absorption spectrum of NDI-5Phbpy-RePy in DMF without (black) and with (red) excess TDAE. *Bottom left:* fsTA spectrum of NDI-5Phbpy-RePy in DMF with excess TDAE ( $\lambda_{\text{ex}} = 605 \text{ nm}$ ). *Top right:* Species-associated spectra obtained from analysis of TA data using kinetic traces at multiple wavelengths. Best-fit lifetimes of each spectral component are given in the legend. *Middle right:* Calculated populations of each spectral component over time using lifetimes given. *Bottom right:* Kinetic traces and fits at given wavelengths

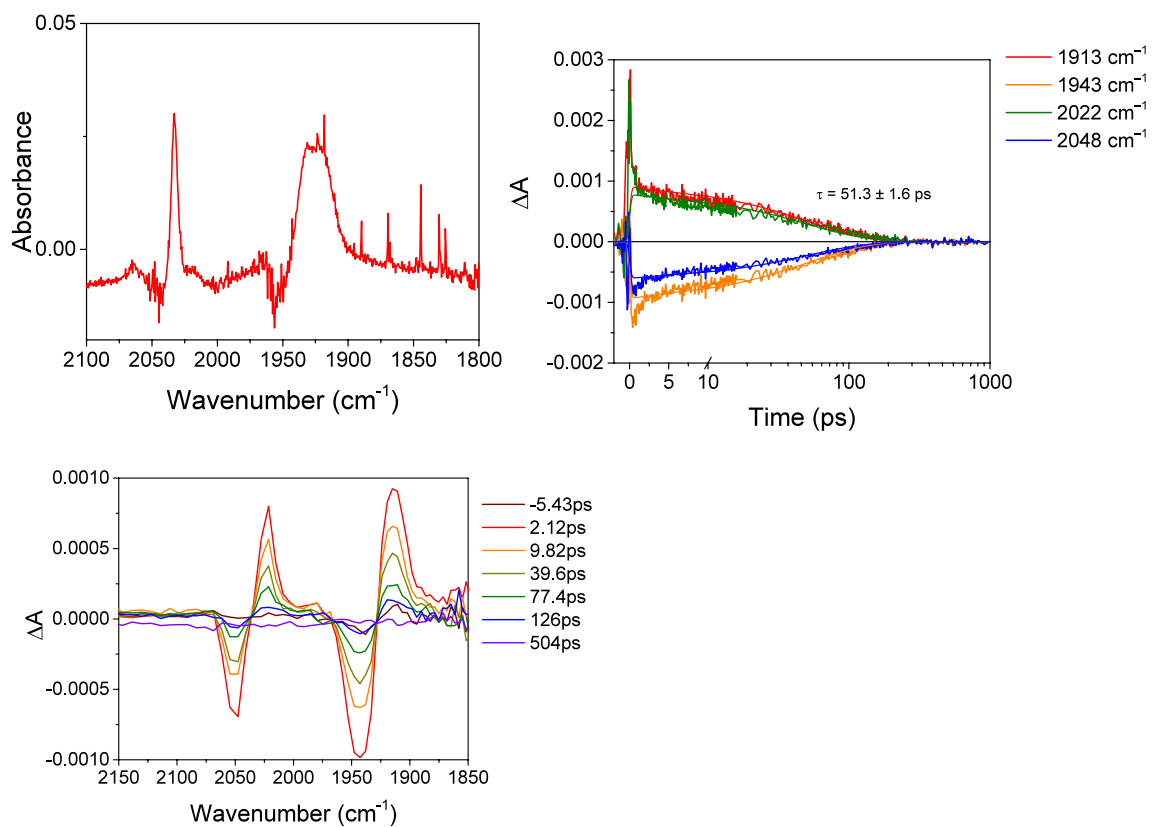


**Figure 5.25:** *Top left:* FTIR spectrum of NDI-5Phbpy-RePy in DMF. *Bottom left:* fsIR spectrum of NDI-5Phbpy-RePy in DMF with excess TDAE ( $\lambda_{\text{ex}} = 605$  nm). *Top right:* Kinetic traces and fits to the specified lifetime of the fsIR at the given frequencies.

## NDI-6Phbpy-ReCl

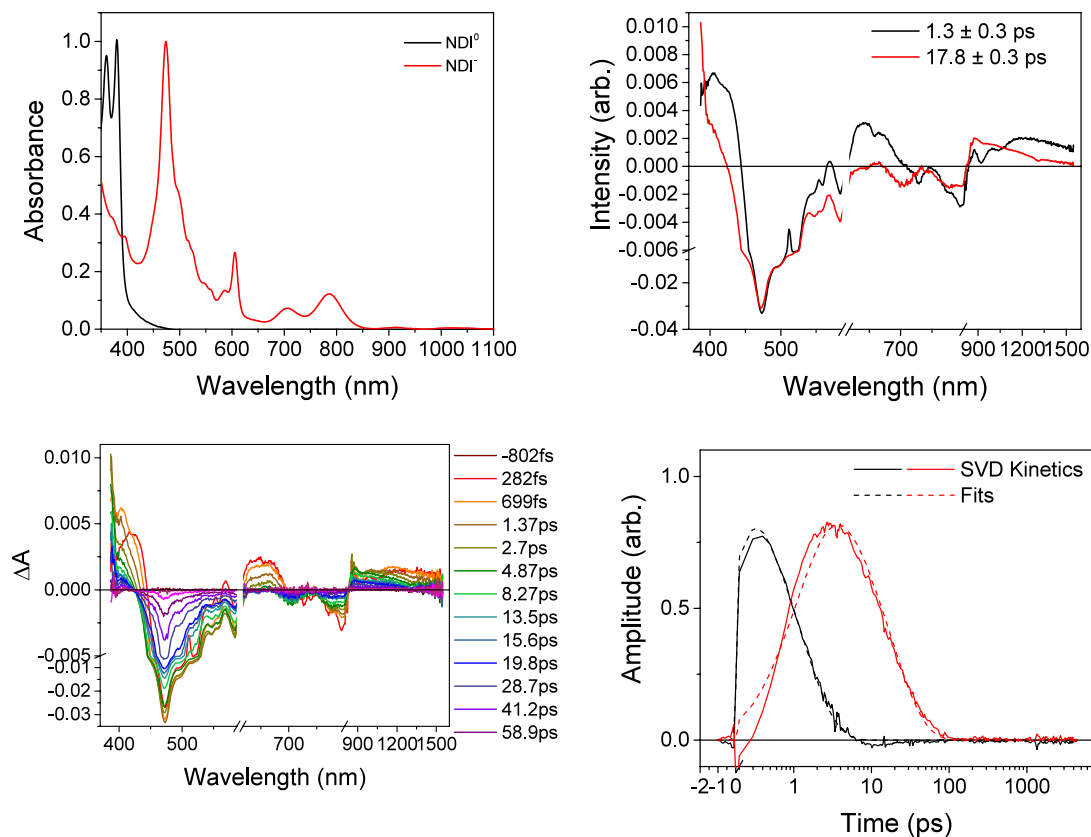


**Figure 5.26:** *Top left:* Electronic absorption spectrum of NDI-6Phbpy-ReCl in DMF without (black) and with (red) excess TDAE. *Bottom left:* fsTA spectrum of NDI-6Phbpy-ReCl in DMF with excess TDAE ( $\lambda_{\text{ex}} = 605$  nm). *Top right:* Species-associated spectra obtained from global analysis of TA data using Singular Value Decomposition (SVD) kinetic traces. Best-fit lifetimes of each spectral component are given in the legend. *Bottom right:* Kinetic traces (solid) and fits (dashed) obtained by SVD of fsTA data. Best-fit lifetimes are given in the legend for the species-associated spectra

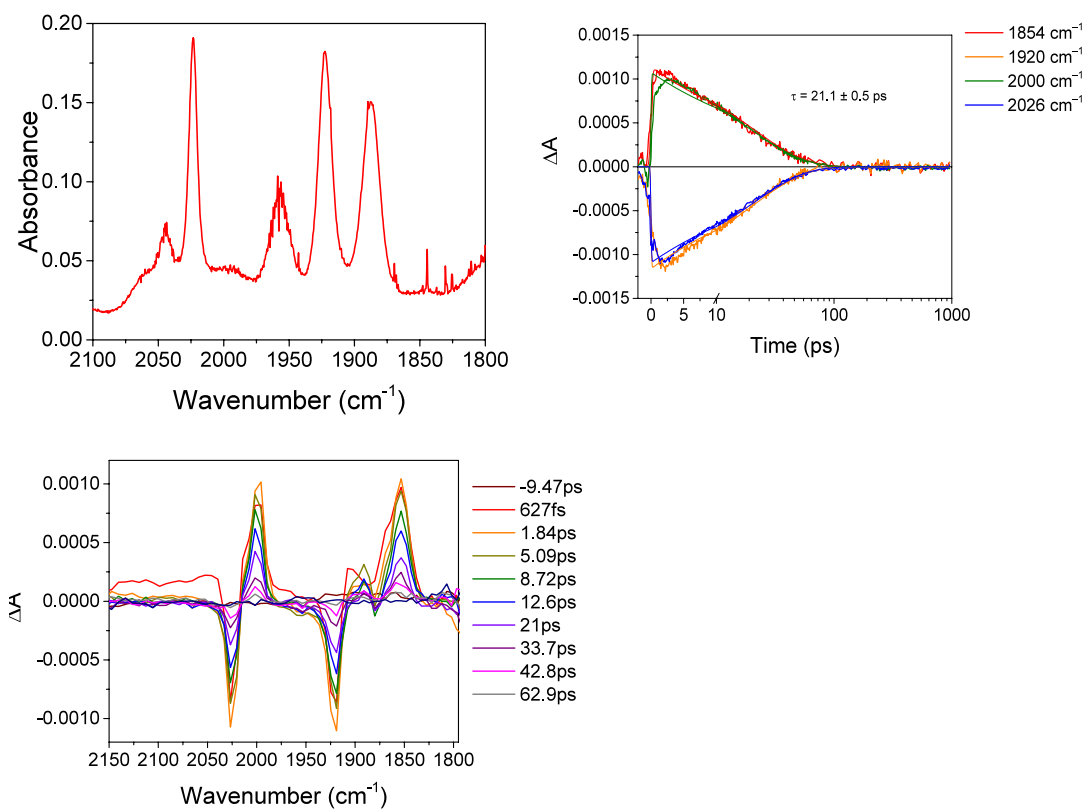


**Figure 5.27.** *Top left:* FTIR spectrum of NDI-6Phbpy-ReCl in DMF. *Bottom left:* fsIR spectrum of NDI-6Phbpy-ReCl in DMF with excess TDAE ( $\lambda_{ex} = 605$  nm). *Top right:* Kinetic traces of the fsIR at the given frequencies.

## NDI-6Phbpy-RePy

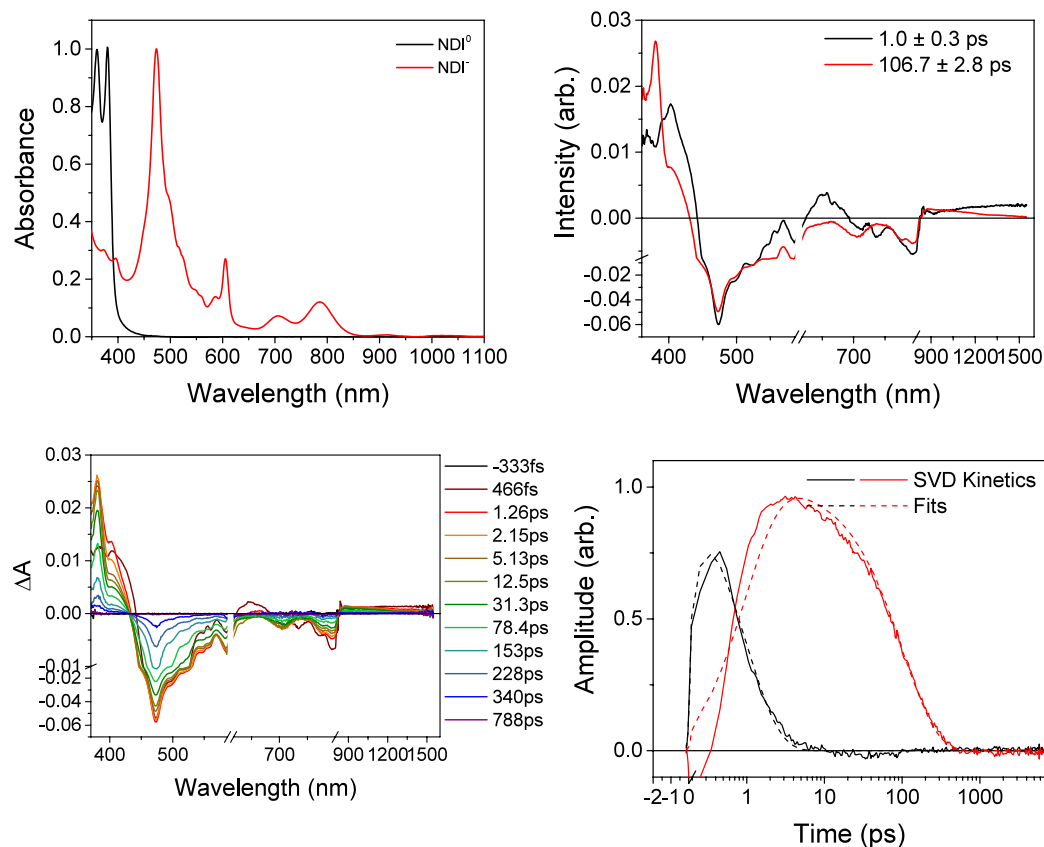


**Figure 5.28:** *Top left:* Electronic absorption spectrum of NDI-6Phbpy-RePy in DMF without (black) and with (red) excess TDAE. *Bottom left:* fsTA spectrum of NDI-6Phbpy-RePy in DMF with excess TDAE ( $\lambda_{\text{ex}} = 605$  nm). *Top right:* Species-associated spectra obtained from global analysis of TA data using Singular Value Decomposition (SVD) kinetic traces. Best-fit lifetimes of each spectral component are given in the legend. *Bottom right:* Kinetic traces (solid) and fits (dashed) obtained by SVD of fsTA data. Best-fit lifetimes are given in the legend for the species-associated spectra

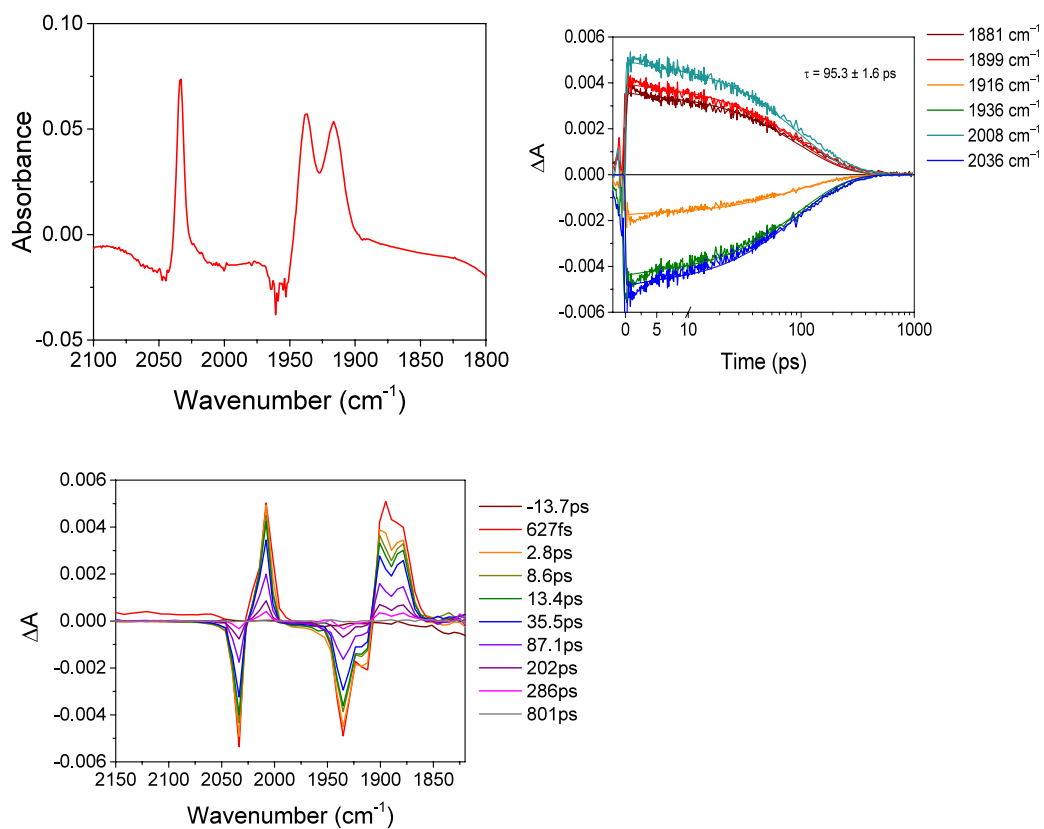


**Figure 5.29:** *Top left:* FTIR spectrum of NDI-6Phbpy-RePy in DMF. *Bottom left:* fsIR spectrum of NDI-6Phbpy-RePy in DMF with excess TDAE ( $\lambda_{\text{ex}} = 605$  nm). *Top right:* Kinetic traces and fits to the specified lifetime of the fsIR at the given frequencies.

**Chapter 6 Ten-thousand-fold Enhancement of Photoreduction Lifetime in Mn(bpy)(CO)<sub>3</sub>X Leading to Key Transient Intermediates via Substituent Location Dependence of a Naphthalene Diimide Radical Anion Chromophore**

## 6.1 Introduction

Over the past couple of decades,  $\text{Re}(\text{bpy})(\text{CO})_3\text{X}$  has established itself as a prominent electro- and photocatalyst for selective  $\text{CO}_2$  reduction.<sup>22-23, 31, 63, 65, 104, 151, 164, 184, 200-201</sup> However, the rarity, cost, and environmental ramifications of mining large quantities of rhenium is a major barrier to scaling up the usage of these catalysts. Recent research has pursued the substitution of Re with the more abundant transition metal Mn, yielding  $\text{Mn}(\text{bpy})(\text{CO})_3\text{X}$ , a similarly active electrocatalyst.<sup>25-26</sup>  $\text{Mn}(\text{bpy})(\text{CO})_3\text{X}$  has also been investigated as the acceptor in diffusional photocatalytic systems, but the mechanism of such systems is not well understood.<sup>68, 202-203</sup> The Mn-based catalysts are of considerable interest because they contain an earth-abundant first-row transition metal (manganese is 1.3 million times more abundant in the Earth's crust than rhenium) and facilitate  $\text{CO}_2$  reduction with similar catalytic activity as Re counterparts but at  $\sim 0.3$  V lower overpotential.<sup>26</sup> Since the Mn complexes offer the potential for scale-up, ongoing work has centered on elucidating the catalytic differences between the Re and Mn systems in order to optimize the Mn catalysts' properties.<sup>66, 68, 204</sup>

While the Mn catalysts appear analogous to the Re counterparts, the mechanism by which the precatalyst is converted to the active catalytic species differs,<sup>68</sup> which has implications for the electro- and photocatalytic mechanisms for  $\text{CO}_2$  reduction that remain to be elucidated. For example, the first reduction of  $\text{Mn}(\text{bpy})(\text{CO})_3\text{X}$  is considered metal center localized; this singly species releases the X ligand and quickly dimerizes to form a  $\text{Mn}^0\text{-Mn}^0$  complex. Upon a second reduction the electrocatalytically active species  $\text{Mn}(0)(\text{bpy}^{\bullet-})(\text{CO})_3$  is formed. There is evidence suggesting this species is the photo-catalytically active species as well. Recent work has shown that including bulky substituents at the 6,6' positions of bipyridine eliminates the propensity for

the  $\text{Mn}(\text{bpy})(\text{CO})_3\text{X}$  complexes to dimerize.<sup>205</sup> By contrast, in the Re complexes, the first reduction is bipyridine localized with the dimerization product on a much longer timescale.<sup>201</sup> The  $\text{Re}(\text{bpy})(\text{CO})_3\text{X}$  complex has a lower propensity to dimerize as the X ligand is much slower to dissociate upon one electron reduction. After a second reduction, the X ligand quickly dissociates to form  $[\text{Re}(0)(\text{bpy}^{\cdot-})(\text{CO})_3]^-$ ,<sup>201</sup> the electrocatalytically active species. The photocatalytically active species is not known for certain, but the six-coordinate one-electron reduced species  $\text{Re}(\text{bpy}^{\cdot-})(\text{CO})_3(\text{CO}_2\text{-TEOA})$  is thought to be a strong candidate.<sup>150</sup> With regards to activating  $\text{CO}_2$ , the  $\text{Mn}(\text{bpy})(\text{CO})_3\text{X}$  complexes generally require an external Brønsted acid while the  $\text{Re}(\text{bpy})(\text{CO})_3\text{X}$  complexes do not.<sup>26</sup>

Recently, the electrocatalytic mechanism for  $\text{CO}_2$  reduction by  $\text{Mn}(\text{bpy})(\text{CO})_3\text{X}$  has been studied while the photocatalytic mechanism has received less attention.<sup>66, 206</sup> To gain insight into the possible intermediates formed during electro- or photocatalysis, in 2014, Wishart and co-workers utilized pulse radiolysis with nanosecond time-resolved infrared (TRIR) spectroscopy to probe intermediates that could potentially be formed during reduction of  $\text{CO}_2$  by  $\text{Mn}(\text{bpy})(\text{CO})_3\text{X}$  complexes.<sup>202</sup> By starting with the derivative  $\text{Mn}(\text{tBu}_2\text{-bpy})(\text{CO})_3(\text{OCHO})$  ( $\text{tBu}_2\text{-bpy} = 4,4'\text{-tBu}_2\text{-2,2'\text{-bipyridine}}$ ) and generating solvated electrons via pulse radiolysis, they observed the simultaneous reduction of  $\text{Mn}(\text{tBu}_2\text{-bpy})(\text{CO})_3(\text{OCHO})$  to  $\text{Mn}(\text{tBu}_2\text{-bpy}^{\cdot-})(\text{CO})_3(\text{OCHO})$  and  $\text{Mn}(0)(\text{tBu}_2\text{-bpy})(\text{CO})_3$ . Though it is hypothesized that  $\text{Mn}(\text{tBu}_2\text{-bpy})(\text{CO})_3(\text{OCHO})$  converts into  $\text{Mn}(\text{tBu}_2\text{-bpy}^{\cdot-})(\text{CO})_3(\text{OCHO})$  which then converts into  $\text{Mn}(0)(\text{tBu}_2\text{-bpy})(\text{CO})_3$ , direct evidence of these transitions were not possible because the earliest response time of the TRIR detection system was  $\sim 40$  nanoseconds. The  $\text{Mn}(0)(\text{tBu}_2\text{-bpy})(\text{CO})_3$  then proceeds to dimerize with another  $\text{Mn}(0)(\text{tBu}_2\text{-bpy})(\text{CO})_3$  complex to form the  $\text{Mn}^0\text{-Mn}^0$  dimer complex. As these experiments were conducted under argon,  $\text{CO}_2$  activation was not studied and by 1.5 milliseconds, the solution

converts entirely to the  $\text{Mn}^0\text{-Mn}^0$  complex. These assignments were supported by DFT-calculated IR spectra, showing agreement with the spectra collected from pulse radiolysis-TRIR spectra. Other work done by Chardon-Noblat have showed that a Mn(II) hydroxycarbonyl intermediate could be formed from the  $\text{Mn}^0\text{-Mn}^0$  bound dimer under  $\text{CO}_2$  with a Brønsted acid, this was observed using electron paramagnetic resonance (EPR).<sup>69</sup> Kubiak also synthesized Mn complexes with bulky substituents that undergo a “slow catalysis” and a “fast catalysis” where the “slow catalysis” route is believed to proceed through a Mn(II) hydroxycarbonyl intermediate.<sup>205, 207</sup>

The first example of using  $\text{Mn}(\text{bpy})(\text{CO})_3\text{Br}$  complexes for photodriven  $\text{CO}_2$  reduction were reported in 2014 by Ishitani.<sup>203</sup> In a solution of DMF:TEOA (4:1, v:v) with  $\text{Mn}(\text{bpy})(\text{CO})_3\text{Br}$ ,  $[\text{Ru}^{\text{II}}(\text{dmbpy})_3]^{2+}$ , and 1-benzyl-1,4-dihydronicotinamide (BNAH), upon illumination with 480 nm light, formation of HCOOH and CO was observed. The photoreduction reaction with  $\text{CO}_2$  likely proceeds via a photoexcitation of the  $\text{Mn}^0\text{-Mn}^0$  dimer, formed after one-electron reduction via thermal electron transfer from the reduced photosensitizer. Since the  $[\text{Mn}(\text{bpy})(\text{CO})_3]_2$  can strongly absorb visible light, the induced homolysis of the  $\text{Mn}^0\text{-Mn}^0$  dimer can yield a reactive Mn radical catalytic intermediate,  $\text{Mn}(0)(\text{bpy})(\text{CO})_3$ , that is hypothesized to react with  $\text{CO}_2$  and initiate photocatalysis. Kubiak later studied  $\text{Mn}(\text{bpy})(\text{CO})_3\text{CN}$ , a precatalyst that is analogous to  $\text{Mn}(\text{bpy})(\text{CO})_3\text{Br}$  but instead avoids the dimer formation upon one electron reduction to form a stable  $\text{Mn}(0)(\text{bpy})(\text{CO})_3\text{CN}$  complex.<sup>204, 208</sup> Unlike the previous study that identified a  $\text{Mn}^0\text{-Mn}^0$  dimer upon one electron reduction, the singly reduced  $\text{Mn}(0)(\text{bpy})(\text{CO})_3\text{CN}$  underwent a disproportionation reaction which instead generated  $\text{Mn}(0)(\text{bpy}^{\cdot-})(\text{CO})_3$ , which is postulated to be the photoactive catalyst in this system that is seen in most electrocatalytic  $\text{CO}_2$  reduction systems.

While all of the photocatalytic systems utilizing  $\text{Mn}(\text{bpy})(\text{CO})_3\text{Br}$  that demonstrate the reduction of  $\text{CO}_2$  proceed via a diffusional system (reduced photosensitizer encountering a Mn complex in

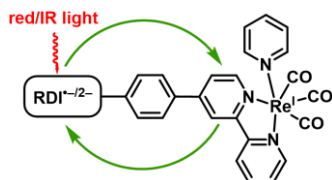


**Figure 6.2:** Photoexcitation of  $\text{RDI}^{2-}$  ( $\text{NDI}^{2-}$  or  $\text{PDI}^{2-}$ ) covalently attached to  $[\text{Re}(\text{bpy})(\text{CO})_3(\text{Py})][\text{PF}_6]$  forms the transiently observed species  $[\text{Re}(\text{RDI}^{0-}\text{bpy}^{\bullet-})(\text{CO})_3(\text{Py})][\text{PF}_6]$ .

solution via diffusion),<sup>66, 203, 206, 208-211</sup> covalently attaching a chromophore to  $\text{Mn}(\text{bpy})(\text{CO})_3\text{Br}$  to form dyad complexes allows for a more controlled observation of intermediates formed during the catalytic cycle.<sup>27, 190</sup> This is very important as many intermediates, formed during catalysis, complicate the photocatalytic mechanism,<sup>104, 172, 174-175, 184, 200, 212-213</sup> especially since some intermediates are formed transiently.<sup>202, 214-215</sup> Our recent work involved incorporating

$\text{NDI}^{2-}$  and  $\text{PDI}^{2-}$  chromophores to  $\text{Re}(\text{bpy})(\text{CO})_3\text{X}$  dyad complexes,<sup>191, 196-197, 216</sup> where X is a  $\text{Cl}^-$

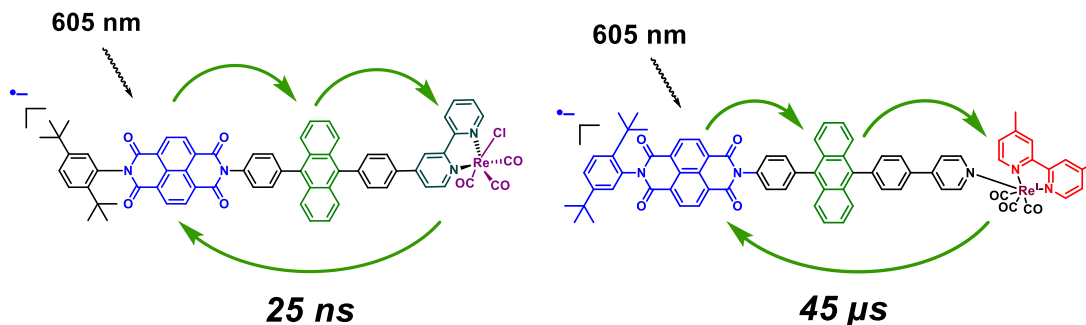


**Figure 6.1:** Photoexcitation of  $\text{NDI}^{2-}$  within a molecular triad covalently attached to  $[\text{Re}(\text{bpy})(\text{CO})_3(\text{Py})][\text{PF}_6]$  through a diphenyl anthracene intermediate acceptor to form the transiently observed species  $[\text{Re}(\text{bpy}^{\bullet-})(\text{CO})_3(\text{X})][\text{PF}_6]$ .

or pyridine ligand as shown in Figure 6.1. The  $\text{NDI}^{2-}$  or  $\text{PDI}^{2-}$  chromophores are all-organic chromophores that avoid the use of precious metal photosensitizers like  $[\text{Ru}(\text{R-bpy})_3]^{2+}$  or  $[\text{Ir}(\text{ppy})_2(\text{bpy})]^+$  and have higher excited state oxidation potentials.<sup>45, 140</sup> By utilizing femto- and nanosecond transient absorption spectroscopy coupled with TRIR spectroscopy, we observed that upon excitation of  $\text{NDI}^{2-}$  or  $\text{PDI}^{2-}$  with visible/NIR light,  $^*\text{NDI}^{2-}$  or  $^*\text{PDI}^{2-}$  transferred an electron

to the covalently attached  $\text{Re}(\text{bpy})(\text{CO})_3\text{X}$  to form  $\text{Re}(\text{bpy}^{\bullet-})(\text{CO})_3\text{X}$ . By incorporating the intermediate acceptor diphenylanthracene to form triad complexes (Figure 6.2) we were able to increase the charge recombination lifetimes into the nanosecond or microsecond regime while forming  $\text{Re}(\text{bpy}^{\bullet-})(\text{CO})_3\text{X}$ .<sup>196-197</sup> These complexes demonstrate the first step in the catalytic mechanism for the photo- or electrocatalysis of  $\text{CO}_2$ . As the analogous steps in the catalytic cycle for  $\text{Mn}(\text{bpy})(\text{CO})_3\text{X}$  intermediates have not been studied before the 40-nanosecond time window,<sup>202, 215</sup> we sought to utilize femto- and nanosecond time-resolved infrared spectroscopy to probe the transitions of the precatalyst to the proposed active catalyst(s). In particular, no clearly identified transition from  $\text{Mn}(\text{bpy})(\text{CO})_3\text{X}$  to  $\text{Mn}(\text{bpy}^{\bullet-})(\text{CO})_3\text{X}$  has been reported; we report the first direct evidence for the transition from  $\text{Mn}(\text{bpy})(\text{CO})_3\text{X}$  to  $\text{Mn}(\text{bpy}^{\bullet-})(\text{CO})_3\text{X}$ . Moreover, we report the first direct evidence for the transition from  $\text{Mn}(\text{I})(\text{bpy}^{\bullet-})(\text{CO})_3\text{X}$  to  $\text{Mn}(0)(\text{bpy})(\text{CO})_3$ . These processes proceed via photoreduction from a covalently attached  $\text{NDI}^{\bullet-}$  via a phenyl bridge. In complexes where  $\text{NDI}^{\bullet-}$  is attached to  $\text{Mn}(\text{bpy})(\text{CO})_3\text{X}$  via the 4- or 5-position of bipyridine, only the transition from  $\text{Mn}(\text{bpy})(\text{CO})_3\text{X}$  to  $\text{Mn}(\text{bpy}^{\bullet-})(\text{CO})_3\text{X}$  is observed. In the case where  $\text{NDI}^{\bullet-}$  is attached to  $\text{Mn}(\text{bpy})(\text{CO})_3\text{X}$  via the 6-position of bipyridine, the transition from  $\text{Mn}(\text{bpy})(\text{CO})_3\text{X} \rightarrow \text{Mn}(\text{bpy}^{\bullet-})(\text{CO})_3\text{X} \rightarrow \text{Mn}(0)(\text{bpy})(\text{CO})_3$  is observed upon selective photoexcitation of  $\text{NDI}^{\bullet-}$  ( $\lambda = 605$  nm). As a result, complexes with an NDI bound at the 6- position of the bipyridine ligand exhibit photoinduced charge-separated states  $\sim 10^5$  times longer than complexes with an NDI bound at the 4- or 5- position of the bipyridine.

## 6.2 Experimental Details

### 6.2.1 Materials

Dichloromethane (DCM), acetonitrile (MeCN), and N,N-dimethylformamide (DMF) used for synthesis and spectroscopic experiments was dried on a commercial system (GlassContour, Laguna Beach, CA). For spectroscopy, DMF and MeCN was further transferred under argon into a N<sub>2</sub>-filled glovebox (MBraun Unilab) for use and storage. Carbon dioxide (Research Grade) was obtained from Airgas and used without further purification. Commercially available reagents were purchased from Sigma-Aldrich or Oakwood Chemicals and used as received. Compounds were reduced in the glovebox using tetrakis(dimethylamino)ethylene (TDAE) from Tokyo Chemical Industries.

### 6.2.2 Steady-State Spectroscopy

UV–vis spectra were acquired on a Shimadzu UV-1800 spectrophotometer at room temperature. The samples were normalized to the greatest peak. FT-IR spectra were measured on a Shimadzu IRAffinity spectrophotometer in absorbance mode at 2 cm<sup>-1</sup> resolution. Samples were prepared in DMF or MeCN under an argon atmosphere, contained in a liquid demountable cell (Harrick Scientific) with 2.0 mm thick CaF<sub>2</sub> windows and 500 μm Teflon spacers.

### 6.2.3 Electrochemistry

Electrochemical measurements were performed using a CH Instruments Model 660A electrochemical workstation. A single-compartment cell was used for all cyclic voltammetry experiments with a 1.0 mm diameter glassy carbon disk working electrode, a platinum counter electrode, a silver wire pseudoreference electrode, and 0.1 M tetra-*n*-butylammonium hexafluorophosphate (TBAPF<sub>6</sub>) as the supporting electrolyte in DMF or MeCN. The ferrocene/ferrocenium redox couple (0.45 V vs SCE in DMF or 0.40 V vs SCE in MeCN)<sup>79</sup> was

used as an internal standard. TBAPF<sub>6</sub> was recrystallized twice from ethanol prior to use. Electrochemical cells were shielded from light during experiments and measurements done in the dark. All solutions were continuously purged with argon before and during the cyclic voltammetry experiments.

#### **6.2.4 Femtosecond Transient Vis/NIR Absorption Spectroscopy.**

Femtosecond transient absorption experiments were performed employing a regeneratively amplified Ti:sapphire laser system operating at 828 nm and a 1 kHz repetition rate as previously described.<sup>80-81</sup> The output of the amplifier was frequency-doubled to 414 nm using a BBO crystal and the 414 nm pulses were used to pump a laboratory-built collinear optical parametric (OPA) amplifier for visible-light excitation<sup>82, 159</sup> or a commercial non-collinear optical parametric amplifier (TOPAS-White, Light-Conversion, LLC.) for NIR excitation. Approximately 1-3 mW of the fundamental was focused into a sapphire disk to generate the visible white-light probe spanning 430-850 nm, into a 5 mm quartz cuvette containing a 1:1 mixture of H<sub>2</sub>O:D<sub>2</sub>O to generate a UV/visible white light probe spanning 385-750 nm, or into a proprietary medium (Ultrafast Systems, LLC) to generate the NIR white-light probe spanning 850-1620 nm. The total instrument response function was 300 fs. Experiments were performed at a randomized pump polarization to suppress contributions from orientational dynamics. Spectral and kinetic data were collected with a CMOS or InGaAs array detector for visible and NIR detection, respectively, and a 8 ns pump-probe delay track (customized Helios, Ultrafast Systems, LLC). Transient spectra were averaged for at least 3 seconds. Gaps shown in the spectra are due to either scattering of the pump or idler beam, or regions not covered by the detectors. Samples prepared in DMF had an absorbance of 0.2-0.7 at the excitation wavelength and were irradiated in 2 mm quartz cuvettes

with 0.4-0.8  $\mu\text{J}/\text{pulse}$  focused to  $\sim 0.2$  mm diameter spot. Samples were stirred to avoid effects of local heating or sample degradation. The samples were prepared in the glovebox. The fsTA data were corrected for group delay dispersion, or chirp, and scattered light prior to the kinetic analysis using Surface Xplorer (Ultrafast Systems, LLC). The kinetic analysis was performed using home-written programs in MATLAB<sup>121</sup> and was based on a global fit to selected single-wavelength kinetics. The time resolution is given as  $w = 300$  fs (full width at half-maximum); the assumption of a uniform instrument response across the frequency domain and a fixed time zero are implicit to global analysis. The data were globally fit either to specified kinetic models or a sum of exponentials. The data set was then deconvoluted with the resultant populations or amplitudes to reconstruct the species-associated or decay-associated spectra. Detailed descriptions of the kinetic models can be found in the Supporting Information.

### **6.2.5 Nanosecond transient absorption spectroscopy.**

Nanosecond transient absorption experiments were performed using the femtosecond excitation beam described above and a commercial spectrometer (Eos, Ultrafast Systems, LLC) utilizing a photonic crystal fiber ultra-broadband probe source. The pump polarization was randomized to suppress rotational dynamics. Samples were stirred to avoid effects of local heating or sample degradation.

### **6.2.6 Femtosecond time-resolved mid-IR spectroscopy.**

Femtosecond transient mid-IR absorption (fsIR) spectroscopy was performed using a commercial Ti:sapphire oscillator/amplifier (Solstice 3.5W, Spectra-Physics) to pump two optical parametric amplifiers (TOPAS-C, Light Conversion), one which provided a 100 fs, 605 nm excitation pulse and the other provided 100 fs pulses at 2150-1800  $\text{cm}^{-1}$ . The overall instrument

response was 300 fs. The spectra were acquired with a liquid N<sub>2</sub>-cooled dual channel (2 x 64) MCT array detector that is coupled to a Horiba HR320 monochromator as part of a Helios-IR spectrometer (Ultrafast Systems, LLC). Samples with a maximum optical density of 1.5 at the excitation wavelength were prepared in DMF or MeCN contained in a liquid demountable cell (Harrick Scientific) with 2.0 mm thick CaF<sub>2</sub> windows and a 500 μm Teflon spacer. During data acquisition, the cell was mounted and rastered on a motorized stage to prevent sample degradation.

### 6.2.7 Synthetic Characterization

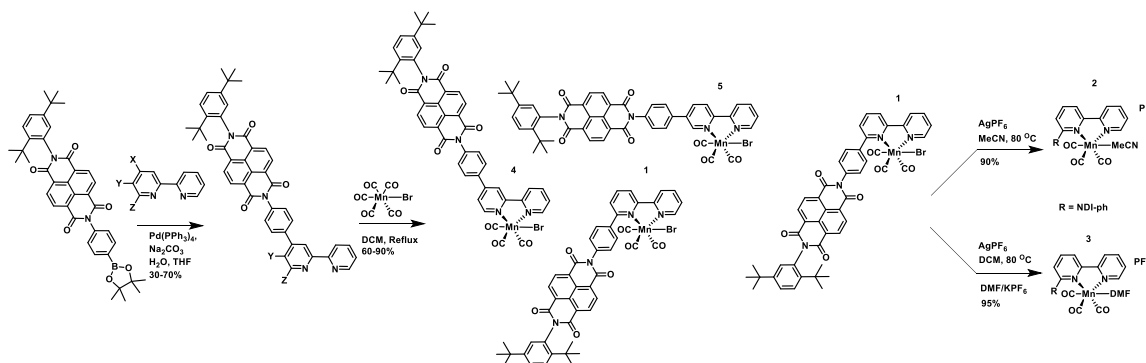
<sup>1</sup>H NMR spectra were recorded on a Bruker Avance 500 TCI Cryoprobe Spectrometer. Chemical shifts are recorded in ppm (δ) in CDCl<sub>3</sub>, MeCN-d<sub>3</sub>, DMF-d<sub>7</sub>, or CD<sub>2</sub>Cl<sub>2</sub>. <sup>13</sup>C NMR (126 MHz) spectra were recorded using a Bruker Avance III QNP Cryoprobe with simultaneous decoupling of <sup>1</sup>H nuclei and externally referenced to TMS set to 0 ppm. All spectra were recorded at 298 K. ESI-MS were performed by Northwestern University's Integrated Molecular Structure Education and Research Center.

## 6.3 Results

### 6.3.1 Synthesis

Complexes **1** (Mn(6-NDI-bpy)(CO)<sub>3</sub>Br), **2** ([Mn(6-NDI-bpy)(CO)<sub>3</sub>MeCN][PF<sub>6</sub>]), **3** ([Mn(6-NDI-bpy)(CO)<sub>3</sub>DMF][PF<sub>6</sub>]), **4** (Mn(4-NDI-bpy)(CO)<sub>3</sub>Br), **5** (Mn(5-NDI-bpy)(CO)<sub>3</sub>Br), were synthesized as illustrated in Scheme 6.1 and detailed in 6.7. NDI-ph-Bpin<sup>191</sup> was Suzuki coupled<sup>192</sup> with the corresponding 4, 5, or 6-bromo-2,2'-bipyridine to form the corresponding 4, 5, or 6-NDI-phenyl-2,2'-bipyridine (4-, 5-, or 6-NDI-bpy). The ligand was then refluxed in dry dichloromethane under argon with bromopentacarbonylmanganese(I) to form complexes **1**, **4**, or **5**. Complex **1** was then heated to 80°C in dry MeCN with silver hexafluorophosphate to form

complex **2**. Complex **1** was also heated to 80°C in dry DCM with silver hexafluorophosphate, stirred in dry DMF/KPF<sub>6</sub> to form complex **3**.



**Scheme 6.1:** Synthetic scheme for complexes **1-5**.

### 6.3.2 Electrochemistry

Electrochemical experiments were performed on all complexes **1-5**. Cyclic voltammograms on complexes **1-5** are shown in Figure 6.3 and Figure 6.4 with their reduction potentials summarized in Table 6.1.

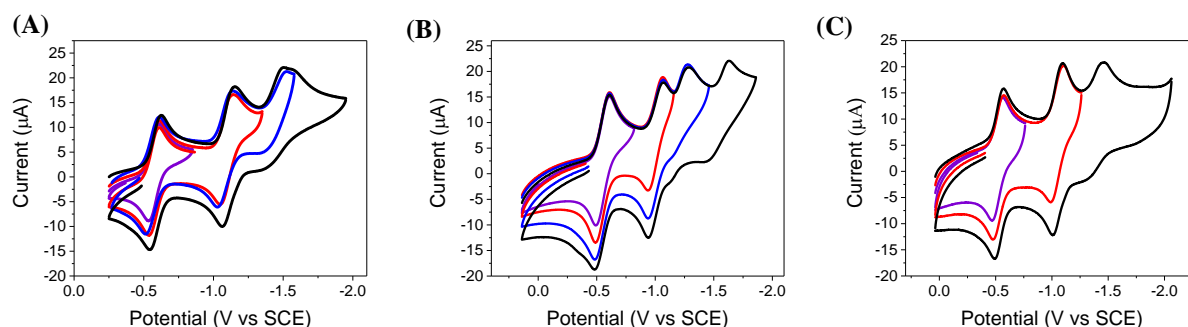


**Figure 6.3:** Cyclic voltammograms of 1.0 mM solutions of (A) **1** in DMF (B) **2** in MeCN (C) **3** in DMF, recorded at 100 mVs<sup>-1</sup> at room temperature with 0.1 M TBAPF<sub>6</sub> as supporting electrolyte.

Complex **1** displays four reduction waves under cyclic voltammetry conditions. The third and fourth reductions are not well separated one from another, these reductions occur at -1.51 and -1.54 V, respectively. Complex **2** displays four reduction waves under cyclic voltammetry

conditions. Initial reduction of **2** leads to the first and second reduction of the NDI component of the ligand at -0.51 and -1.01 V, respectively. The third and fourth reductions are well separated from one another, these reductions occur at -1.28 and -1.62 V, respectively. Complex **3** displays three reduction waves under cyclic voltammetry conditions. Initial reduction of **3** leads to the first and second reduction of the NDI component of the ligand at -0.53 and -1.06 V, respectively. The third reduction occur at -1.47 V. Sweeping more negative resulted in no further reduction peaks.

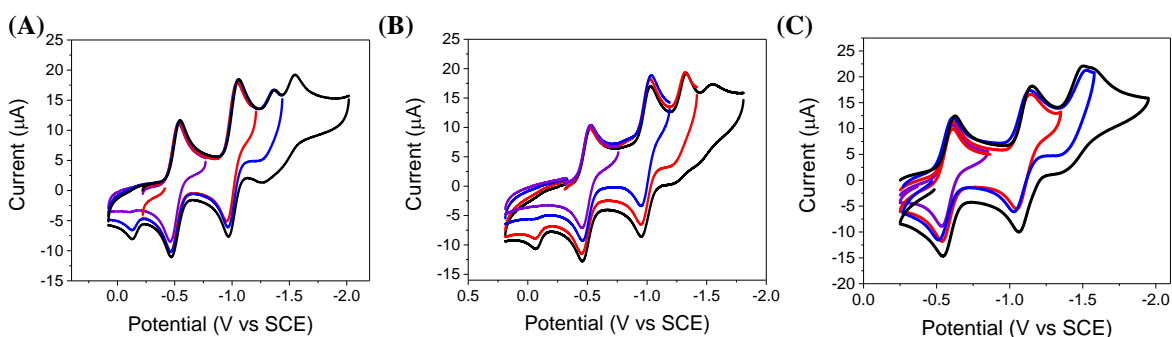


**Figure 6.4:** Cyclic voltammograms of 1.0 mM solutions in DMF of (A) **4** (B) **5** (C) **1**, recorded at  $100 \text{ mV s}^{-1}$  at room temperature with  $0.1 \text{ M TBAPF}_6$  as supporting electrolyte.

Complexes **4** and **5** display four separate reduction waves. Initial reduction of **4** leads to the first and second reduction of the NDI component of the ligand at -0.50 and -1.00 V, respectively. The third and fourth reductions are well separated one from another, these reductions occur at -1.36 and -1.55 V, respectively. On the reverse sweep there is an oxidation peak at -0.13 V. Initial reduction of **5** leads to the first and second reduction of the NDI component of the ligand at -0.50 and -1.01 V, respectively. The third and fourth reductions occur at -1.33 and -1.55 V, respectively. On the reverse sweep, there is an oxidation peak at -0.07 V.

**Table 6.1:** Redox potentials of complexes 1-5 vs SCE ( $\text{Fc}/\text{Fc}^+$  reference at  $0.45 \text{ V vs SCE}$  in DMF and  $0.40 \text{ V vs SCE}$  in MeCN).

	NDI <sup>0/-</sup>	NDI <sup>-2/-</sup>	Mn <sup>IV</sup> -X	bpy <sup>0/-</sup>
<b>1</b> <sup>a</sup>	-0.51	-1.00	-1.51	-1.57
<b>2</b> <sup>a</sup>	-0.55	-1.01	-1.28	-1.62
<b>3</b> <sup>b</sup>	-0.53	-1.06	-1.47	-1.47
<b>4</b> <sup>a</sup>	-0.50	-1.00	-1.36	-1.55
<b>5</b> <sup>a</sup>	-0.50	-1.01	-1.33	-1.55

a - measured in DMF, b - measured in MeCN

### 6.3.3 Electrocatalysis

The electrocatalytic properties of **1-5** (1.0 mM in DMF or MeCN) with TBAPF<sub>6</sub> electrolyte (0.1 M) were studied in a single-compartment cell with a glassy carbon working electrode, Pt counter electrode, and a silver reference electrode (potentials were then converted to SCE using ferrocene as an internal reference). The solutions were sparged for 15 min with carbon dioxide to yield a saturated solution (0.20 M or 0.28 M in DMF and MeCN, respectively).<sup>165</sup> When the potential was swept negative with an external proton source (MeOH), a large increase in current was observed upon the last reduction of the complex (Figure 6.5), while the first three reduction waves were largely unchanged in the presence of CO<sub>2</sub> and an external proton source. For complexes **4** and **5**, much higher concentrations of MeOH were needed to induce catalysis under CO<sub>2</sub>, see Figures 6.22-6.23

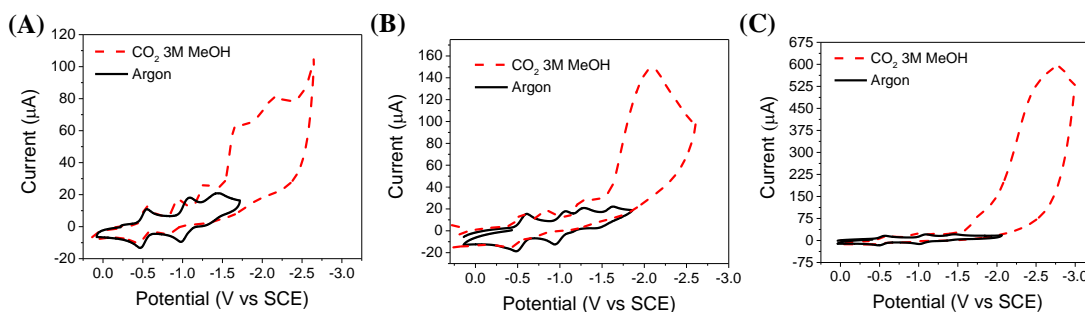


**Figure 6.5:** Cyclic voltammograms of a 1.0 mM solution of (A) complex **1** with 0.1 M TBAPF<sub>6</sub> in DMF, (B) complex **2** with 0.1 M TBAPF<sub>6</sub> in MeCN, (C) and complex **3** with 0.1 M TBAPF<sub>6</sub> in DMF under argon (black), saturated with CO<sub>2</sub> (dashed red line) with MeOH (3M). Scan rate: 100 mV s<sup>-1</sup>, glassy carbon electrode, platinum counter electrode, and silver reference wire.

To calculate the turnover frequency (TOF) of complexes **1-5**, Eq. (1) and (2), which describe the catalytic current (Eq. (1)) and the current response in the absence of catalyst substrate (Eq. (2)), can be used to estimate each complex's catalytic activity.<sup>217-218</sup> By dividing Eq. (2) by Eq. (1), the resulting equation can be reorganized to solve for TOF (Eq. (3)). Similar work has been done by Kubiak to calculate the TOFs and compare similar Mn(R-bpy)(CO)<sub>3</sub>X and Re(R-bpy)(CO)<sub>3</sub>X systems to one another.<sup>26, 205</sup>

$$i_p = 0.4463 \left( \frac{F}{RT} \right)^{1/2} n_p^{3/2} A D_c [C_p] v^{1/2} \quad (1)$$

$$i_{cat} = n_{cat} F A [C_{cat}] (D_c k_{cat} [S]^y)^{1/2} \quad (2)$$

$$TOF = k_{cat} [CO_2] = \frac{F v n_p^3}{RT} \left( \frac{0.4463}{n_{cat}} \right)^2 \left( \frac{i_{cat}}{i_p} \right)^2 \quad (3)$$

In these equations,  $i_p$  is the peak current in the absence of catalysis,  $i_{cat}$  is catalytic current,  $n_p$  is the number of electrons in the noncatalytic reaction (one for complexes **1-2** & **4-5**, and two for complex **3**),  $n_{cat}$  is the number of electrons in the catalytic transformation (CO<sub>2</sub> into CO requires two electrons),  $R$  is the universal gas constant,  $F$  is Faraday's constant,  $T$  is temperature in Kelvin,  $A$  is the surface area of the electrode,  $[C_{cat}]$  is the catalyst concentration under catalytic conditions

(at peak  $i_{cat}/i_p$ ),  $[C_p]$  is the catalyst concentration without substrate,  $D_c$  is the diffusion constant of the species prior to the catalytically active species,  $k_{cat}$  is the rate constant of the catalytic reaction,  $[S]$  is the substrate concentrations,  $y$  is the order of the substrates in the reactions ( $[\text{CO}_2]^1[\text{HX}]^2$  in this case), and  $v$  is scan rate (0.1 V/s). These equations assume that the catalytic reaction is under pseudo-first-order conditions, with an excess of substrate compared to the catalysts. Surface area cancels out because the same electrode was used for experiments under argon and  $\text{CO}_2$ , and in the current treatment  $D_c$  cancels out because we are assuming that the diffusion coefficient does not significantly change with the addition of the acid or  $\text{CO}_2$ . Using equations 1-3, we can calculate  $i_{cat}/i_p$  and TOF values for complexes **1-5** with added MeOH. For these calculations,  $i_p$  is determined as the peak current under argon with an amount of MeOH corresponding to peak  $i_{cat}$  conditions. Addition of MeOH to a 1.0 mM solution of **1-3** to form a 3.0 M MeOH solution under  $\text{CO}_2$  resulted in a peak  $i_{cat}/i_p = 3.9, 6.9,$  and  $28.5,$  respectively. These values correspond to a TOF = 2.9, 9.0, and  $1258.4 \text{ s}^{-1}$ , respectively. The  $i_{cat}/i_p$  and calculated TOF for complexes **1-5** are in Table 6.2. Scan rates and diffusion studies of complexes **1-5** are shown in Figure 6.16-6.20.

**Table 6.2:** Comparison of  $i_{cat}/i_p$  and TOF Values for complexes **1 – 5** with MeOH.

compound	[acid] (M)	$i_{cat}/i_p$	TOF ( $\text{s}^{-1}$ )
<b>1</b> <sup>a</sup>	3.0 MeOH	3.9	2.9
<b>2</b> <sup>b</sup>	3.0 MeOH	6.8	9.0
<b>3</b> <sup>a</sup>	3.0 MeOH	28.5	1258.4
<b>4</b> <sup>a</sup>	3.0 MeOH	~1.0	~0.0
<b>5</b> <sup>a</sup>	3.0 MeOH	~1.0	~0.0

a - measured in DMF, b - measured in MeCN. Solutions are saturated and under an atmosphere of  $\text{CO}_2$  with added MeOH.  $[\text{CO}_2]$  is approximately 0.28 M in dry MeCN, 0.20 M in dry DMF, 0.27 M in 3.0 M MeOH. Data are taken from voltammograms at a scan rate of  $100 \text{ mV s}^{-1}$  while under argon or  $\text{CO}_2$ .  $i_{cat}/i_p$  values include a correction for the concentration change of the catalyst.

### 6.3.4 Electron Transfer Energetics

Based on the redox potentials shown above, the Gibbs free energy for the excited state electron transfer reactions of complex  $\mathbf{1}^{\bullet-} - \mathbf{5}^{\bullet-}$  can be estimated using the following equation:

$$\Delta G_{\text{ET}} = E(\text{NDI}^{\bullet-}/\text{NDI}) - E(\text{A}^{\bullet-}/\text{A}) - E_{\text{D}_1}(*\text{NDI}^{\bullet-}) \quad (4)$$

where  $E(\text{NDI}^{\bullet-}/\text{NDI})$  is the reduction potential of NDI and  $E(\text{A}^{\bullet-}/\text{A})$  is the reduction potential of the complex of interest, and  $E_{\text{D}_1}$  is the energy of the  $*\text{NDI}^{\bullet-}$  excited state, assuming electron transfer occurs from the  $\text{D}_1$  state. The  $\text{D}_1 \leftarrow \text{D}_0$  transition of  $\text{NDI}^{\bullet-}$  absorbs at 785 nm, making  $E_{\text{D}_1} = 1.58$  eV. There is no electrostatic work term for this reaction because the reaction is a charge shift, not a charge separation. In addition, there is no solvation correction term because the fsTA and electrochemical experiments are performed in the same high polarity solvent. The Gibbs free energy for the thermal forward and back electron transfer reactions can be estimated using the following equation:

$$\Delta G_{\text{ET}} = E(\text{A}^{\bullet-}/\text{A}) - E(\text{NDI}^{\bullet-}/\text{NDI}) \quad (5)$$

From the equations above, the Gibbs free energies for each electron transfer step are shown in Table 6.3 below.

**Table 6.3:** Free energy changes for electron transfer reactions in complex **1<sup>-</sup>** - **5<sup>-</sup>**.

compound	process	$\Delta G$ (eV)
<b>1<sup>-</sup></b>	*NDI <sup>-</sup> → Mn(6-bpy)Br	-0.58
<b>2<sup>-</sup></b>	*NDI <sup>-</sup> → Mn(6-bpy)MeCN	-0.85
<b>3<sup>-</sup></b>	*NDI <sup>-</sup> → Mn(6-bpy)DMF	-0.64
<b>4<sup>-</sup></b>	*NDI <sup>-</sup> → Mn(4-bpy)Br	-0.72
<b>5<sup>-</sup></b>	*NDI <sup>-</sup> → Mn(5-bpy)Br	-0.75
<b>1<sup>-</sup></b>	Mn <sup>-</sup> (6-bpy)Br → NDI <sup>0</sup>	-1.00
<b>2<sup>-</sup></b>	Mn <sup>-</sup> (6-bpy)MeCN → NDI <sup>0</sup>	-0.73
<b>3<sup>-</sup></b>	Mn <sup>-</sup> (6-bpy)DMF → NDI <sup>0</sup>	-0.94
<b>4<sup>-</sup></b>	Mn(4-bpy <sup>-</sup> )Br → NDI <sup>0</sup>	-1.05
<b>5<sup>-</sup></b>	Mn(5-bpy <sup>-</sup> )Br → NDI <sup>0</sup>	-1.05

\*Grayed out ligands indicate loss of halide before charge recombination, ligand or solvent is expected to recoordinate.

### 6.3.5 Steady-State FTIR

The FTIR spectra of complexes **1-5** (Figure 6.6 and Figure 6.7) were collected in the solution phase. The  $\nu(\text{CO})$  were tabulated in Table 6.4. Complexes **1-5** show three characteristic  $\nu(\text{CO})$  stretches for facially coordinated tricarbonyl complexes. It is known that the energies of and separation between the two lower-energy bands depends on the axial ligand X.<sup>194</sup> Typically two well-developed bands are observed in complexes with halide- or O-coordinated ligands.<sup>194</sup> This is in agreement with the complex **1, 3-5** as the two lower bands are well separated by 16-29  $\text{cm}^{-1}$ . On the other hand, the two lower bands are generally merged into one broad band if X is N-coordinated like MeCN. This is in agreement with complex **2** with acetonitrile bound as the two lower bands are only separated by 8  $\text{cm}^{-1}$ .

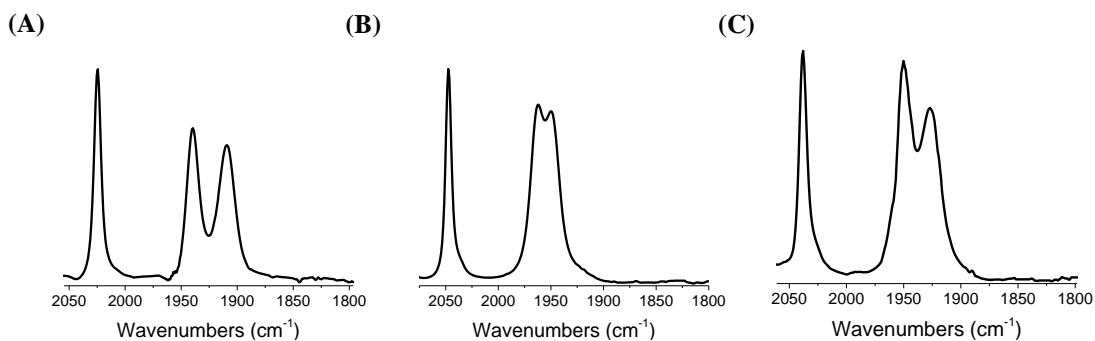


**Figure 6.6:** Resting state solution phase FTIR of complexes (A) **1** (DMF), (B) **2** (MeCN), and (C) **3** (DMF).

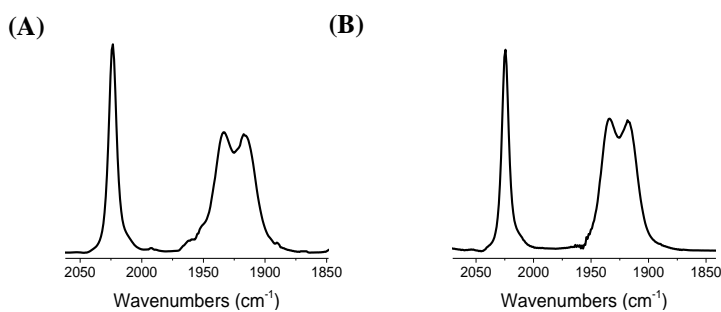


**Figure 6.7:** Resting state solution phase FTIR of complexes (A) **4** (DMF), (B) **5** (DMF)

**Table 6.4:** FTIR CO stretches of **1-5** complexes. Complexes **1, 3-5** were dissolved in DMF and complex **2** in MeCN

compound	A'(1)	A'(2)	A''
<b>1</b> <sup>a</sup>	2024	1939	1910
<b>2</b> <sup>b</sup>	2047	1959	1951
<b>3</b> <sup>a</sup>	2037	1949	1926
<b>4</b> <sup>a</sup>	2023	1932	1916
<b>5</b> <sup>a</sup>	2024	1933	1917

a - measured in DMF, b - measured in MeCN

### 6.3.6 Steady-State UV-Vis absorption

The normalized steady-state electronic absorption spectra of **1**, **2**, and **3** are shown in Figure 6.8. In complexes **1**, **2**, and **3**, the Mn(bpy)(CO)<sub>3</sub>X LMCT absorption band is broad and tails out

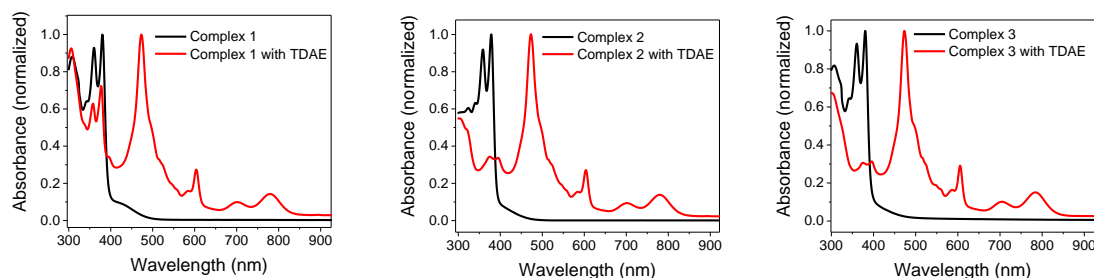


**Figure 6.8:** Electronic absorption spectra of complex **1** (DMF), **2** (MeCN), and **3** (DMF) with and without the TDAE reductant added.

to ~500 nm.<sup>203</sup> When TDAE is added to complex **1-3**, to form **1<sup>-</sup>-3<sup>-</sup>**, the NDI absorptions disappear while the NDI<sup>-</sup> absorptions appear at 471, 605, 700, and 785 nm.<sup>45</sup> In the chemically reduced complexes **1<sup>-</sup>-3<sup>-</sup>**, the Mn(bpy)(CO)<sub>3</sub>X LMCT band underlies the strong absorptions of NDI<sup>-</sup>. Complexes **4** and **5** and their chemically reduced counterparts exhibit similar steady electronic absorption spectra as **1-3** and their chemically reduced counterparts and are shown in Figure 6.21.

### 6.3.7 Transient Absorption Spectroscopy

The intramolecular electron transfer behavior of complexes **1<sup>-</sup>-5<sup>-</sup>** were investigated using pump-probe femtosecond transient absorption (fsTA) spectroscopy. Figures 6.9-6.11 display the fsTA spectra at selected time delays following selective photoexcitation of NDI<sup>-</sup> with a pump pulse centered at  $\lambda_{\text{ex}} = 605$  nm for each complex. Excitation of complex **1<sup>-</sup>-5<sup>-</sup>** at 605 nm results in instantaneous bleaching of the ground-state absorptions of NDI<sup>-</sup> at 473 nm, and the appearance of a broad absorption spanning the region 410 – 450 nm, corresponding to the induced absorptions of \*NDI<sup>-</sup>. As the \*NDI<sup>-</sup> features, visible only in the initial few timepoints (<1 ps delay times)

decay, induced absorptions at 362 and 382 nm appear; this absorption corresponds to the absorption of NDI<sup>0</sup>, signifying photoinduced electron transfer to the metal complex. For complexes **4**<sup>-</sup> and **5**<sup>-</sup>, the data were best fit to an A → GS kinetic model composing of a single exponential decay with time constants of  $\tau_{A \rightarrow GS} = 3.4 \pm 0.5$  ps and  $\tau_{A \rightarrow GS} = 3.6 \pm 0.1$  ps, respectively. The species-associated spectra corresponding to species A are shown in Figure 6.9. The transient kinetics at selected wavelengths and population dynamics are shown in Figures 6.27-6.28 For complexes **1**<sup>-</sup>-**3**<sup>-</sup>, the data were best fit to an A → B → GS kinetic model consisting of two exponential decays. The first time constant for complexes **1**<sup>-</sup>-**3**<sup>-</sup> was  $\tau_{A \rightarrow B} = 13.6 \pm 0.1$  ps,  $\tau_{A \rightarrow B} = 25.1 \pm 0.8$  ps, and  $\tau_{A \rightarrow B} = 30.7 \pm 0.3$  ps, respectively. The second time constant for each complex was  $\tau_{B \rightarrow GS} = 3.0 \pm 0.5$  ns,  $\tau_{B \rightarrow GS} = 39.9 \pm 0.7$  ns, and  $\tau_{B \rightarrow GS} = 27.8 \pm 0.2$  ns, respectively. The species-associated spectra corresponding to species A and B are shown in Figures 6.10-6.11. The transient kinetics at selected wavelengths and population dynamics are shown in Figures 6.29-6.31. Since the time constant for the charge shift reaction is on the same order as the IRF (~0.3 ps), these models neglect the initial charge shift reaction  $\text{Mn(I)(6-}^*\text{NDI}^- \text{-bpy)}(\text{CO})_3\text{X} \rightarrow \text{Mn(I)(6-NDI-bpy}^{\bullet-}\text{)}(\text{CO})_3\text{X}$  because it could not be extracted accurately. The lifetimes and rates for each species are shown in Table 6.5.

**Table 6.5:** Observed time constants and rates of electron transfer for complexes **1**<sup>-</sup> - **5**<sup>-</sup>

	$\tau_{A \rightarrow B}$	$k_{A \rightarrow B}$ (s <sup>-1</sup> )	$\tau_{B \rightarrow GS}$	$k_{B \rightarrow GS}$ (s <sup>-1</sup> )
<b>1</b> <sup>-</sup>	13.6 ± 0.1 ps	7.35 × 10 <sup>10</sup>	3.0 ± 0.5 ns	3.33 × 10 <sup>8</sup>
<b>2</b> <sup>-</sup>	25.1 ± 0.8 ps	3.98 × 10 <sup>10</sup>	39.9 ± 0.7 ns	2.51 × 10 <sup>7</sup>
<b>3</b> <sup>-</sup>	30.7 ± 0.3 ps	3.26 × 10 <sup>10</sup>	27.8 ± 0.2 ns	3.60 × 10 <sup>7</sup>
	$\tau_{A \rightarrow GS}$	$k_{A \rightarrow GS}$ (s <sup>-1</sup> )	—	—
<b>4</b> <sup>-</sup>	3.4 ± 0.5 ps	2.94 × 10 <sup>11</sup>		
<b>5</b> <sup>-</sup>	3.6 ± 0.1 ps	2.78 × 10 <sup>11</sup>		

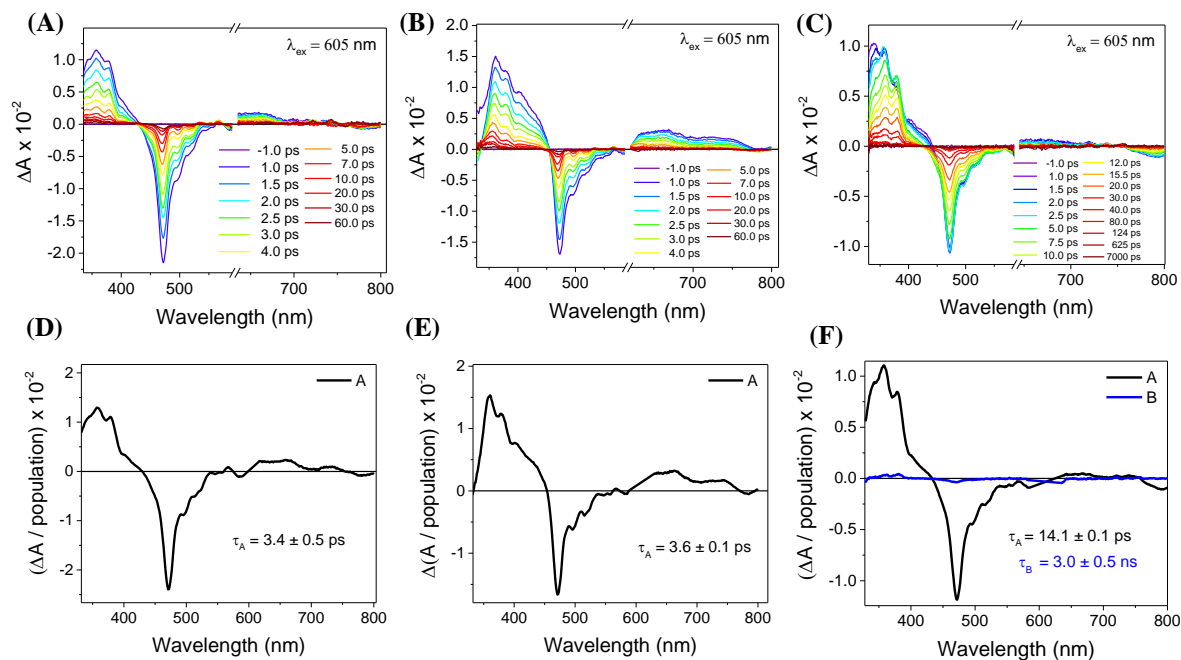


**Figure 6.9:** (top row) (A) fsTA spectra of complex  $4^-$  (B) fsTA spectra of complex  $5^-$  (C), fsTA spectra of complex  $1^-$ , (bottom row) (D) species-associate spectra for complex  $4^-$  (E) species-associate spectra for complex  $5^-$  (F) species-associate spectra for complex  $1^-$ .  $\lambda_{\text{ex}} = 605$  nm, solvent = DMF.

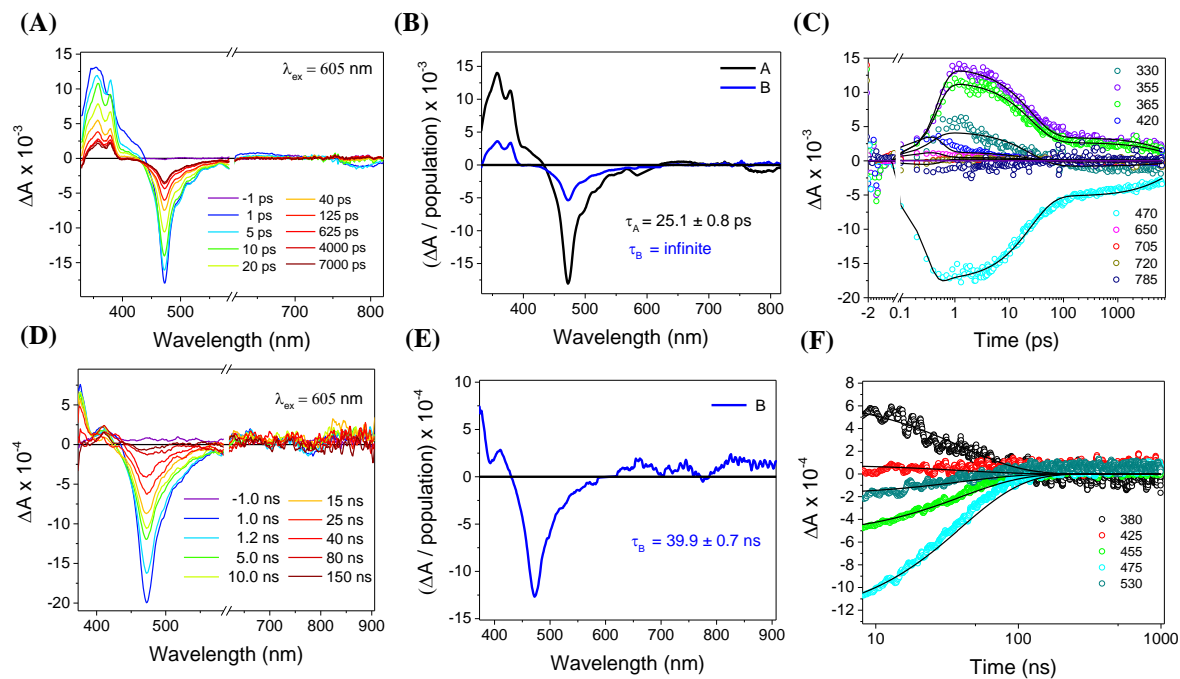


**Figure 6.10.** (top row) (A) fsTA spectra of complex  $2^{\bullet-}$  (B) species-associated spectra (C), transient kinetics at selected wavelengths, (bottom row) (D) nsTA spectra of complex  $2^{\bullet-}$  (E) species-associated spectra for complex  $2^{\bullet-}$  (F) nanosecond transient kinetics at selected wavelengths.  $\lambda_{\text{ex}} = 605$  nm, solvent = MeCN.

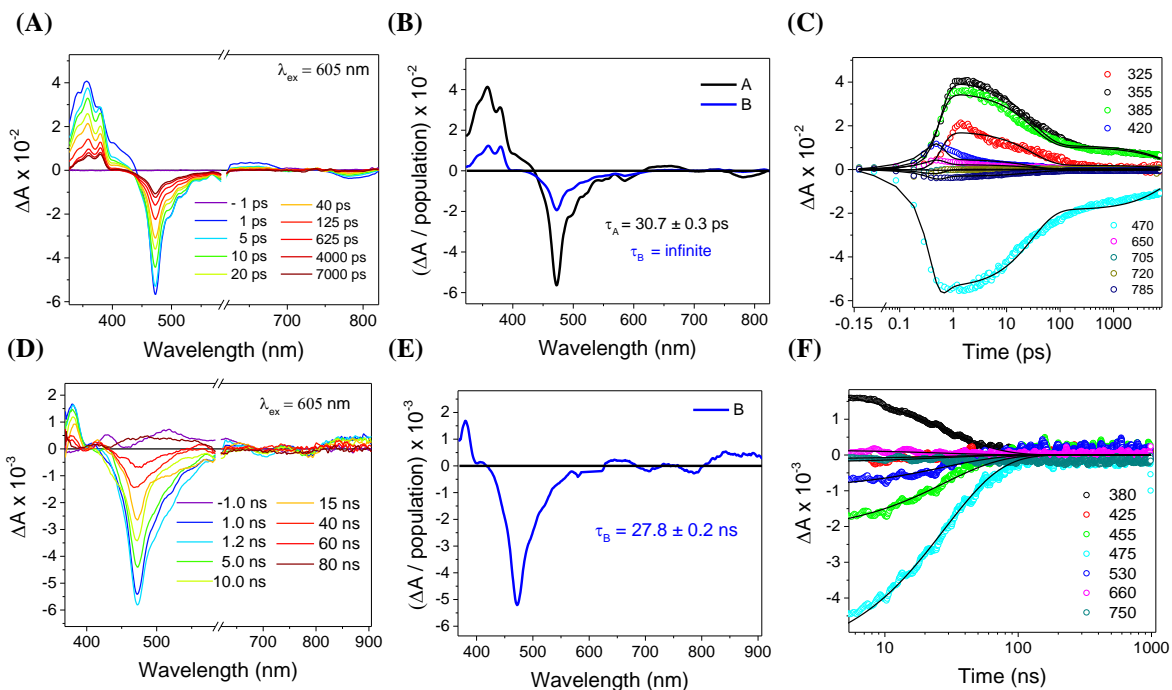


**Figure 6.11:** (top row) (A) fsTA spectra of complex  $3^{*-}$  (B) species-associated spectra (C), transient kinetics at selected wavelengths, (bottom row) (D) nsTA spectra of complex  $3^{*-}$  (E) species-associated spectra for complex  $3^{*-}$  (F) nanosecond transient kinetics at selected wavelengths.  $\lambda_{\text{ex}} = 605$  nm, solvent = DMF.

### 6.3.8 Time-resolved mid-IR Spectroscopy

In the femtosecond time-resolved mid-IR transient absorption (TRIR) experiments, the CO-stretching region of the  $\text{Mn}(\text{bpy})(\text{CO})_3\text{X}$  moiety ( $1850\text{--}2100\text{ cm}^{-1}$ ) were monitored. TRIR spectra and kinetic traces at selected energies are shown below in Figures 6.12–6.14. Complexes  $1^{*-}$ ,  $4^{*-}$ , and  $5^{*-}$  exhibited similar spectral features at early times, with only the kinetics differing from each complex, but at later times, complex  $1^{*-}$  displays a long-lived species. For example, in complexes  $1^{*-}$ ,  $4^{*-}$  and  $5^{*-}$ , at early times, the ground-state absorptions bleach while induced absorptions appear with the same kinetics. In complexes  $4^{*-}$  and  $5^{*-}$ , these induced shifts decay back to the ground state within picoseconds. In complex  $1^{*-}$  the induced absorptions at  $2003\text{ cm}^{-1}$

and  $1895\text{ cm}^{-1}$  decay, but instead of returning to the ground state, a new set of induced absorptions grow in at  $1859\text{ cm}^{-1}$  and  $1843\text{ cm}^{-1}$  with the same kinetics.

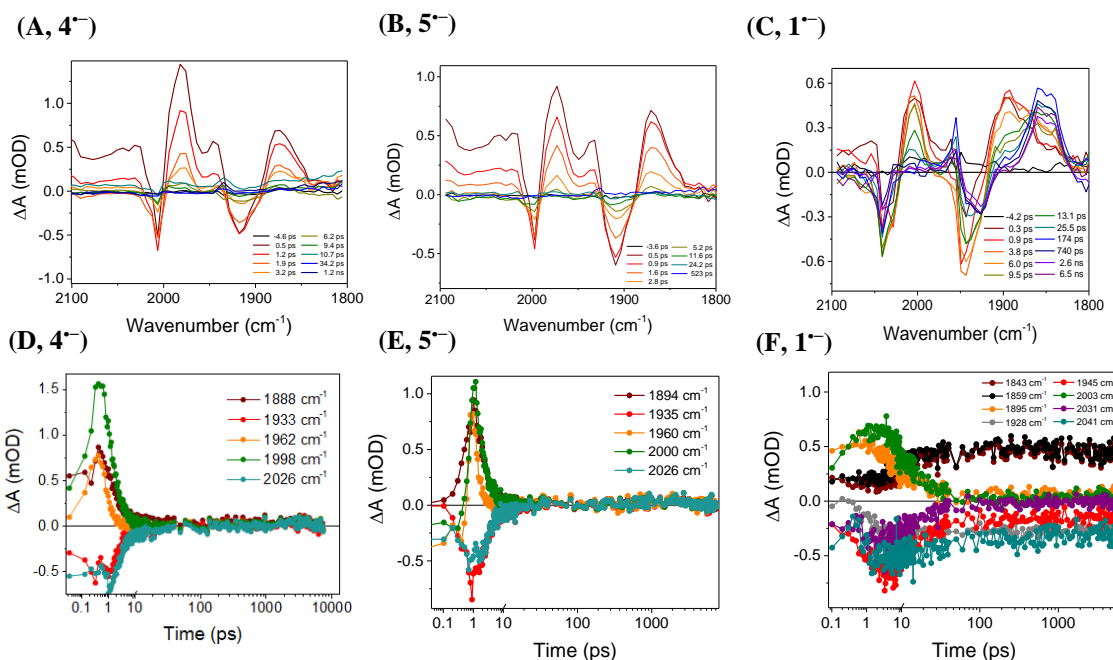


**Figure 6.12:** (top row) (A) TRIR spectra of complex  $4^{\bullet-}$  (B) TRIR spectra of complex  $5^{\bullet-}$  (C), TRIR spectra of complex  $1^{\bullet-}$ , (bottom row) (D) transient kinetics at selected  $\nu(\text{CO})$  of  $4^{\bullet-}$  (E) transient kinetics at selected  $\nu(\text{CO})$  of  $5^{\bullet-}$  (F) transient kinetics at selected  $\nu(\text{CO})$  of  $1^{\bullet-}$ .  $\lambda_{\text{ex}} = 605\text{ nm}$ , solvent = DMF.

Much like with complex  $1^{\bullet-}$ , complexes  $2^{\bullet-}$  and  $3^{\bullet-}$ , that also have the NDI bound to the 6-position of bipyridine, exhibited the same spectral features, with only the kinetics differing from complex to complex, Figures 6.11-6.12. For example, in complex  $3^{\bullet-}$ , the ground-state absorptions at  $2037\text{ cm}^{-1}$ ,  $1949\text{ cm}^{-1}$ , and  $1926\text{ cm}^{-1}$  bleach with new induced absorptions appearing at  $2008\text{ cm}^{-1}$  and  $1891\text{ cm}^{-1}$  with the same kinetics. These shifts shortly decay soon after and new induced absorptions grow in at  $1954\text{ cm}^{-1}$  and  $1845\text{ cm}^{-1}$  that persist for the remainder of the 8 ns time window. Complexes  $2^{\bullet-}$  and  $3^{\bullet-}$  were then fit for more accurate species given that the nanosecond transient absorption data illustrated a long lived second component. For complexes  $2^{\bullet-}$  and  $3^{\bullet-}$ , the

data were best fit to an  $A \rightarrow B \rightarrow GS$  kinetic model composing of a two exponential decays with time constants of  $\tau_{A \rightarrow GS} = 30.0 \pm 1.6$  ps and  $\tau_{A \rightarrow GS} = 11.0 \pm 0.5$  ps, respectively. The second species was fit to a  $\tau_{B \rightarrow GS} = \text{infinite}$  for both complexes.  $\tau_{B \rightarrow GS}$  is set to infinite as the TRIR time window is only 8 ns, accurate lifetimes are given via nanosecond transient absorption spectroscopy.

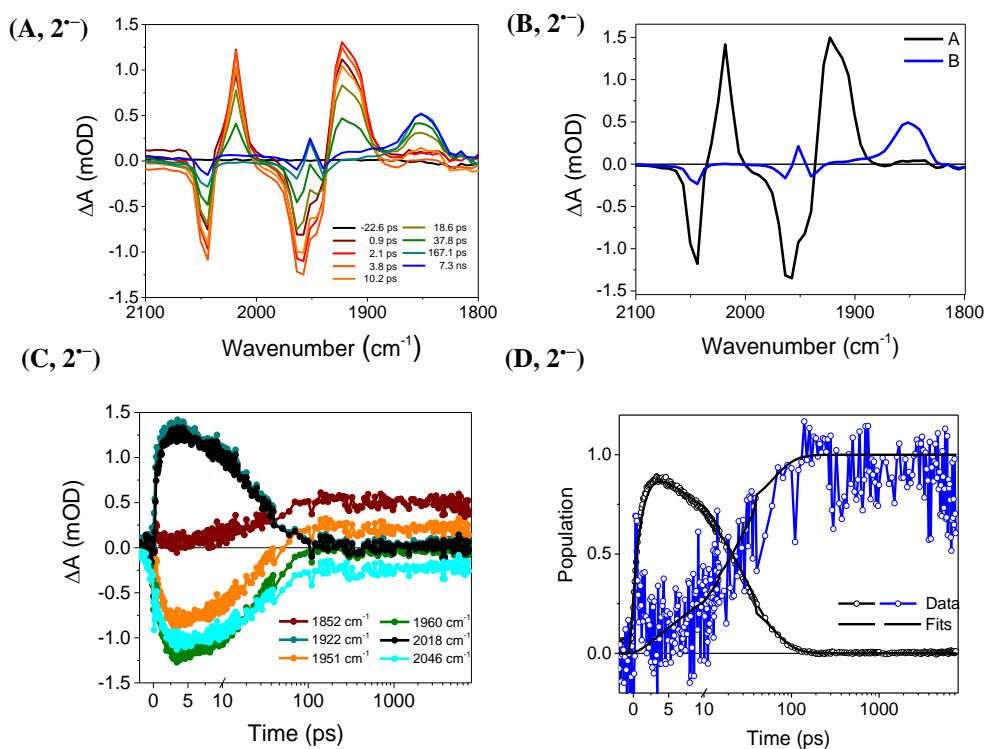


**Figure 6.13:** (top row) (A) TRIR spectra of complex  $2^-$  (B) species-associated spectra (bottom row) (C) transient kinetics at selected  $\nu(\text{CO})$  (D) Singular value decomposition kinetic traces and fits based on the species-associated fits and lifetimes shown.  $\lambda_{\text{ex}} = 605$  nm, solvent = MeCN.

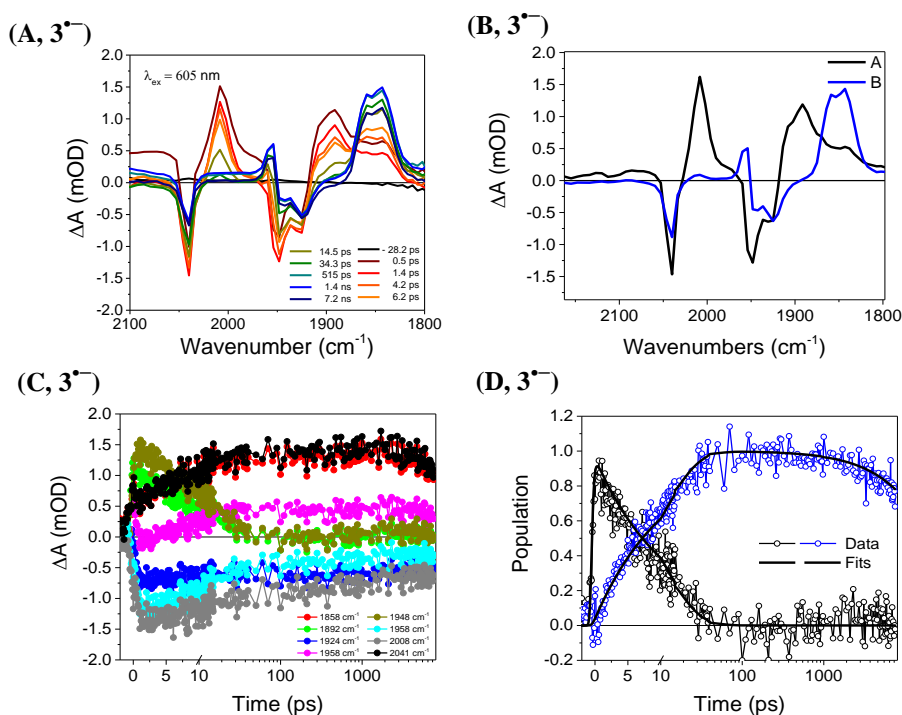


**Figure 6.14:** (top row) (A) TRIR spectra of complex  $3^{+}$  (B) species-associated spectra (bottom row) (C) transient kinetics at selected  $\nu(\text{CO})$  (D) Singular value decomposition kinetic traces and fits based on the species-associated fits and lifetimes.  $\lambda_{\text{ex}} = 605$  nm, solvent= DMF.

## 6.4 Discussion

In complex **1**, the last two reduction waves are close in potential and appear to be within 3 mV (Figure 6.3), whereas in the typical  $\text{Mn}(\text{bpy})(\text{CO})_3\text{Br}$  the same two reduction peaks are  $\sim 300$  mV apart. In the case of  $\text{Mn}(6,6'\text{-dimesityl-bpy})(\text{CO})_3\text{Br}$ , where bulky mesityl substituents at the 6,6' positions of bipyridine block dimerization leads to both reductions of the metal complex to occur at the same reduction potential. We expect the same as the phenyl substituent with an NDI attached is of significant bulk to block dimerization of two  $\text{Mn}(\text{bpy})(\text{CO})_3$  units. This is further evident on the reverse sweep in the cyclic voltammogram as the diagnostic oxidative cleavage of the dimer is not present. When MeOH is added to the solution while still under argon, the third and fourth reductions begin to become more distinct, with the  $\text{Mn}(\text{I})(\text{bpy}^{\cdot-})(\text{CO})_3$  becoming

slightly more positive, see Figure 6.26. This is expected as the protons stabilize the reductions. This also illustrates that complex **1** is not catalytic with regards to proton reduction as there is no increase in current in MeOH. As a result, we assign the last two reductions of complex **1** to be the formation of  $\text{Mn}(0)(6\text{-NDI}^{2-}\text{-bpy})(\text{CO})_3$  and ultimately  $\text{Mn}(0)(6\text{-NDI}^{2-}\text{-bpy}^{\cdot-})(\text{CO})_3$ . Complex **3** more strongly resembles  $\text{Mn}(6,6'\text{-dimesityl-bpy})(\text{CO})_3\text{Br}$ , where both bulky ligands lead to both reductions of the metal complex to occur simultaneously, Figure 6.3. Thus we assign the reduction peak at  $-1.47$  V to be the simultaneous reduction and formation of  $\text{Mn}(0)(6\text{-NDI}^{2-}\text{-bpy}^{\cdot-})(\text{CO})_3$  from  $\text{Mn}(\text{I})(6\text{-NDI}^{2-}\text{-bpy})(\text{CO})_3\text{DMF}$ . No diagnostic oxidative cleavage of the dimer was present in the cyclic voltammogram upon the reverse sweep after the reduction at  $-1.47$  V.

On the other hand, the cyclic voltammogram of complex **2** has two separate metal complex reductions which strongly resemble the CV of previously reported  $[\text{Mn}(\text{tBu}_2\text{-bpy})(\text{CO})_3\text{MeCN}][\text{OTf}]$ . While one might suspect that the CV of complex **2** would more closely resemble the previously reported  $[\text{Mn}(6,6'\text{-dimesityl-bpy})(\text{CO})_3\text{MeCN}]^+$ , with the bulky 6,6'-substituents, the  $\nu(\text{CO})$  of complex **2** instead illustrate a similar electron density around the metal complex to that of  $[\text{Mn}(\text{tBu}_2\text{-bpy})(\text{CO})_3\text{MeCN}][(\text{OTf})]$ , as the  $\nu(\text{CO})$  of  $[\text{Mn}(\text{tBu}_2\text{-bpy})(\text{CO})_3\text{MeCN}][\text{OTf}]$  and complex **2** are similar in the resting state. On the other hand, the previously reported  $\nu(\text{CO})$  of  $[\text{Mn}(6,6'\text{-dimesityl-bpy})(\text{CO})_3\text{MeCN}]^+$  match complexes **1** and **3**, illustrating a similar electron density of the metal complexes in their resting state. This is further evident as the reductions of  $[\text{Mn}(6,6'\text{-dimesityl-bpy})(\text{CO})_3\text{MeCN}]^+$ , complex **1**, and complex **3** all have both metal complex reductions occur simultaneously. Thus, we assign the reduction peak at  $-1.28$  V to be  $\text{Mn}(0)(6\text{-NDI}^{2-}\text{-bpy})(\text{CO})_3$  and the reduction peak at  $-1.62$  V to form  $\text{Mn}(0)(6\text{-NDI}^{2-}\text{-bpy}^{\cdot-})(\text{CO})_3$ . Complex **4** and **5** have all four well-separated reductions (Figure 6.4), much like complex **2** and the previously reported  $\text{Mn}(\text{tBu}_2\text{-bpy})(\text{CO})_3\text{Br}$ . However, unlike complex **2**,

complexes **4** and **5** have an oxidation wave that is observed in the CV of this complex. This wave is attributed to the oxidative cleavage of the  $\text{Mn}^0\text{-Mn}^0$  dimer formed upon the third reduction of the complex  $\text{Mn}(0)(\text{NDI}^{2-}\text{-bpy})(\text{CO})_3$ . Since the NDI-Ph- substituents are instead at the 4- and 5- position of bipyridine for complexes **4** and **5**, they do not inhibit dimerization to the same extent as NDI-Ph- at the 6-position of bipyridine.

In the presence of  $\text{CO}_2$  and MeOH, complexes **1-3** were demonstrated to be electrocatalytic (Figure 6.5). When the potential was swept negative, a large increase in current was observed upon the last reduction of the complex, while the earlier reduction waves were largely unchanged in the presence of  $\text{CO}_2$  or MeOH. The class of  $\text{Mn}(\text{bpy})(\text{CO})_3\text{X}$  catalysts is known to require an external proton source, while the analogous  $\text{Re}(\text{bpy})(\text{CO})_3\text{X}$  catalysts typically do not. The final reduction of these complexes likely corresponds to the second reduction of the metal complex and forms the expected electrocatalytically active species,  $\text{Mn}(0)(\text{bpy}^{\cdot-})(\text{CO})_3$ , that can bind and ultimately reduce  $\text{CO}_2$ . At increasing MeOH concentration, a snapshot of the difference in catalytic activity is seen between complexes **1-3** with the catalytic trend being complex **3** > complex **2** > complex **1**. Complexes **4** and **5** were not catalytic until much higher concentrations of MeOH were used and are shown in Figures 6.22-6.23.

The difference in  $\text{CO}_2$  reduction activity by complex **1** and complexes **4-5** is due to electronic effects. Complex **1**, in comparison to complexes **4** and **5**, has its third reduction (reduction of  $\text{Mn}(\text{I}) \rightarrow \text{Mn}(0)$  and formation of  $\text{Mn}(0)(6\text{-NDI}^{2-}\text{-bpy})(\text{CO})_3\text{Br}$ ) at a more negative potential, indicating more electron density on the metal complex. Thus, the doubly reduced metal complex component of complex **1** is a stronger nucleophile and more readily binds and activates  $\text{CO}_2$ . This is seen in similar  $\text{Re}(\text{bpy})(\text{CO})_3\text{X}$  or  $\text{Mn}(\text{bpy})(\text{CO})_3\text{X}$  complexes where making the

potentials of the metal complex more positive via changing the electronics on the bipyridine ring or changing the X ligand leads to a decrease in electro- or photocatalytic activity.<sup>31, 63</sup>

The difference in CO<sub>2</sub> reduction activity between complexes **1-3** is likely due to the electronic effects induced by the bound X, as the change in catalytic current is altered depending on the X ligand bound. Complex **3** illustrates the greatest catalytic TOF of 1258 s<sup>-1</sup> while complex **2** and complex **1** display lower TOFs (9 s<sup>-1</sup> and 3 s<sup>-1</sup>, respectively) at 3M MeOH. A notable difference between complex **3** and complexes **1** or **2** is that the final reductions of complex **3** are simultaneous, whereas the metal complex reductions in complexes **1** and **2** are separated to some degree. As seen by Kubiak, Mn(bpy)(CO)<sub>3</sub>X derivatives that have simultaneous reductions of the metal complex have greater TOFs than those that have separate reductions (2000 s<sup>-1</sup> for [Mn(6,6'-dimesityl-bpy)(CO)<sub>3</sub>(MeCN)]<sup>+</sup> vs 130 s<sup>-1</sup> for Mn(tBu<sub>2</sub>-bpy)(CO)<sub>3</sub>X or 94 s<sup>-1</sup> for [Re(tBu<sub>2</sub>-bpy)(CO)<sub>3</sub>MeCN]<sup>+</sup> with MeOH), this is similar to what's seen in comparing complexes **1-3**. Additionally, complex **3** (as well as complexes **1** and **2**) begin to produce CO<sub>2</sub> at the onset of its final reduction (with MeOH), which is in agreement with a doubly reduced metal complex, as Mn(0)(bpy<sup>-</sup>)(CO)<sub>3</sub> is commonly viewed as the electrocatalytic species. Under argon and MeOH, there is no current enhancement illustrating the complexes preference for CO<sub>2</sub> reduction instead of proton reduction, Figure 6.25-6.26.

Having confirmed that complexes **1<sup>-</sup>-5<sup>-</sup>** can activate CO<sub>2</sub>, the electron transfer dynamics were probed using transient spectroscopy. Time-resolved mid-IR (TRIR) spectroscopy has been used to observe facile differentiation among the various oxidation and ligand-field states of Re(bpy)(CO)<sub>3</sub>X complexes, and recently been shown to be useful for identifying various oxidation states of Mn(bpy)(CO)<sub>3</sub>X, albeit after 40 ns. Using TRIR spectroscopy, upon excitation of NDI<sup>-</sup> at 605 nm, we can determine the nature of the charge-shifted state produced with regard to the

bipyridine and Mn center, Figures 6.12-6.14. Excitation of complexes **1<sup>-</sup>-5<sup>-</sup>** lead to a bathochromic shift of 25-45 cm<sup>-1</sup> of the  $\nu(\text{CO})$ . Previous results from Wishart demonstrate that at 40 ns,<sup>202</sup> two products exist upon pulse-radiolysis, these CO stretches were corroborated via DFT and matched the  $\nu(\text{CO})$  stretches to Mn(I)(bpy<sup>-</sup>)(CO)<sub>3</sub>X, with the other set of  $\nu(\text{CO})$  corresponding to Mn(0)(bpy)(CO)<sub>3</sub>. Additionally, DFT calculations by Wishart of the  $\nu(\text{CO})$  for Mn(I)(bpy<sup>-</sup>)(CO)<sub>3</sub>MeCN match the  $\nu(\text{CO})$  observed during TRIR of Mn(I)(6-NDI<sup>-</sup>-bpy)(CO)<sub>3</sub>MeCN → Mn(I)(6-NDI<sup>0</sup>-bpy<sup>-</sup>)(CO)<sub>3</sub>MeCN. Thus, we assign the initial photoreduction of **1<sup>-</sup>-5<sup>-</sup>** to the formation of Mn(I)(6-NDI<sup>0</sup>-bpy<sup>-</sup>)(CO)<sub>3</sub>X. This is expected as complexes **1<sup>-</sup>-5<sup>-</sup>**, and their respective photoreduction products, maintain a Mn(I) metal center. Due to orbital overlap between the Mn(I) metal center and the bound bipyridine, the extra electron upon photoreduction resides largely in the  $\pi^*$  orbitals of the bpy ligand. This results in additional electron density on the Mn center and increased  $\pi$  back-bonding into the  $\pi^*(\text{CO})$  antibonding orbitals and weakening the CO bonds.<sup>68, 202</sup> Previous TRIR work done on the analogous Re(bpy)(CO)<sub>3</sub>X complex with a covalently attached NDI<sup>-</sup> or [Ru(bpy)<sub>3</sub>]<sup>2+</sup> have illustrated a similar bathochromic shift of the  $\nu(\text{CO})$  stretches that correspond to the formation of Re(bpy<sup>-</sup>)(CO)<sub>3</sub>X.<sup>188, 190</sup>

In complexes **4<sup>-</sup>-5<sup>-</sup>**, the initial induced  $\nu(\text{CO})$  depletes completely and returns to ground state, Figure 6.12. In complexes **1<sup>-</sup>-3<sup>-</sup>**, the initial induced absorptions deplete completely, and a second set of induced absorptions appear with a bathochromic shift of 25-45 cm<sup>-1</sup> of the  $\nu(\text{CO})$ , Figures 6.13-6.14. The second set of  $\nu(\text{CO})$  that were observed by Wishart *et al.* and corroborated with DFT, illustrated the formation of Mn(0)(bpy)(CO)<sub>3</sub>. Thus, we assign these new induced absorptions to the LMCT of Mn(I)(bpy<sup>-</sup>)(CO)<sub>3</sub>Br → Mn(0)(bpy)(CO)<sub>3</sub> and the simultaneous loss of the X ligand. This is expected as the electron that resides on the bipyridine can charge-shift to

the bound Mn(I) metal center. A similar mechanism is seen in the analogous  $\text{Re}(\text{bpy}^{\bullet-})(\text{CO})_3\text{X}$ , except in these complexes the transfer of the electron from bipyridine and the Re(I) metal center is extremely slow.<sup>65</sup> It is well known that upon the first reduction  $\text{Mn}(\text{I})(\text{bpy})(\text{CO})_3\text{X}$ , the X ligand quickly dissociates, and a  $\text{Mn}^0\text{-Mn}^0$  dimerized product is formed. As noted by the cyclic voltammetry experiments of complexes **1-3**, Figure 3, the NDI-Ph- substituent at the 6-position of bipyridine is sufficient to block dimerization; as a result we expect the  $\text{Mn}(0)(6\text{-NDI-bpy})(\text{CO})_3$  to return to  $\text{Mn}(\text{I})(6\text{-NDI}^{\bullet-}\text{-bpy})(\text{CO})_3\text{X}$  instead of forming the dimerized product. Recent pulse radiolysis and TRIR done by Rochford et al on  $\text{Mn}(6,6'\text{-dimesityl-bpy})(\text{CO})_3\text{X}$  demonstrated that at  $\sim 3 \mu\text{s}$ , the bulky complex does not form the dimerized product.<sup>215</sup>

As seen by the TRIR spectra, Figures 6.12-6.14, complexes **4<sup>•-</sup>** and **5<sup>•-</sup>** immediately return to ground state while complexes **1<sup>•-</sup>-3<sup>•-</sup>** proceed to form a new species as indicated by the shift in  $\nu(\text{CO})$  stretches. Looking at the fsTA spectra and the species-associated spectra for complexes **4<sup>•-</sup>** and **5<sup>•-</sup>**, Figure 6.9, we see that the charge separated species return back to ground state with lifetimes of  $\sim 3$  ps, while in complexes **1<sup>•-</sup>-3<sup>•-</sup>**, the charge separated species decay with lifetimes between 15-30 ps, Figures 6.9-6.11. Since the charge separated state persists for an order of magnitude longer in complexes **1<sup>•-</sup>-3<sup>•-</sup>** than in **4<sup>•-</sup>-5<sup>•-</sup>**, this must be ample time for the complex to favor a charge shift to the metal center instead of back electron transfer. The 6-position of bipyridine is likely more decoupled from NDI-Ph- than the 4- and 5- positions of bipyridine. This is evident in the cyclic voltammogram as the reduction of  $\text{Mn}(\text{I}) \rightarrow \text{Mn}(0)$  for complexes **1** and **3** is  $\sim 180$  mV more positive than for complexes **4** and **5**. This is due to the extended conjugation of the bound bipyridine with the phenyl substituent; similar electronic effects have been seen in the analogous  $\text{Re}(\text{I})(4\text{-NDI}^{\bullet-}\text{-bpy})(\text{CO})_3\text{X}$  complexes as well as many other  $\text{Re}(\text{I})(4\text{-R-bpy})(\text{CO})_3\text{X}$

complexes.<sup>22, 147, 190, 219</sup> However, when complex **2** is compared to *vs* complexes **4** and **5**, the reduction potentials for Mn(I)  $\rightarrow$  Mn(0) are similar, Table 6.1. This is because complex **2** has a MeCN (an N-bonding ligand) that is bound directly to Mn, making the complex cationic.<sup>26</sup> Such complexes have a more positive Mn(I)  $\rightarrow$  Mn(0) reduction than the neutral complex counterparts with Br<sup>-</sup> or the cationic complexes with O-bonding ligands. Likely through a combination of electronic effects and charge separated lifetimes caused through binding of the NDI-Ph- to the 6-position of bipyridine, complexes **1<sup>-</sup>**-**3<sup>-</sup>** go on to form the Mn(0)(bpy)(CO)<sub>3</sub> as observed in TRIR, unlike complexes **4<sup>-</sup>**-**5<sup>-</sup>**.

To support the TRIR observations, femto/nanosecond TA was employed to monitor the electron transfer dynamics from the viewpoint of the NDI chromophore, Figure 6.9. For complexes **4<sup>-</sup>** and **5<sup>-</sup>**, following excitation at  $\lambda_{\text{ex}} = 605$  nm, the photoinduced charge shift dynamics were fit to an A  $\rightarrow$  GS model, where A represents the photoinduced charge-shifted species Mn(I)(4-NDI<sup>0</sup>-bpy<sup>-</sup>)(CO)<sub>3</sub>Br or Mn(I)(5-NDI<sup>0</sup>-bpy<sup>-</sup>)(CO)<sub>3</sub>Br and GS represents the ground state, Mn(I)(4-NDI<sup>-</sup>-bpy)(CO)<sub>3</sub>Br or Mn(I)(5-NDI<sup>-</sup>-bpy)(CO)<sub>3</sub>Br. Observation of the induced absorptions of NDI<sup>0</sup> and concomitant growth of induced absorptions in the mid-IR characteristic of the bpy-localized reduction of the Mn(bpy)(CO)<sub>3</sub>Br moiety support the model of a single photoinduced electron transfer event to form species A. For complexes **1<sup>-</sup>**-**3<sup>-</sup>**, following excitation at  $\lambda_{\text{ex}} = 605$  nm, the photoinduced charge shift dynamics were fit to an A  $\rightarrow$  B  $\rightarrow$  GS model, where A represents the photoinduced species Mn(I)(6-NDI<sup>0</sup>-bpy<sup>-</sup>)(CO)<sub>3</sub>X, B represents the product of a second charge shift to form species Mn(0)(6-NDI<sup>0</sup>-bpy)(CO)<sub>3</sub>, and GS represents the ground state Mn(I)(6-NDI<sup>-</sup>-bpy)(CO)<sub>3</sub>X formed by back-electron transfer. As in **4<sup>-</sup>** and **5<sup>-</sup>**, for complexes **1<sup>-</sup>**-**3<sup>-</sup>**, observation of the induced absorptions of NDI<sup>0</sup> and concomitant growth of induced

absorptions in the mid-IR characteristic of a bpy-localized reduction of the Mn(Bpy)(CO)<sub>3</sub>Br moiety indicate that Mn(I)(6-NDI<sup>0</sup>-bpy<sup>•-</sup>)(CO)<sub>3</sub>X is species A. The observation of species B, Mn(0)(6-NDI<sup>0</sup>-bpy)(CO)<sub>3</sub>, is corroborated by a second component in the species-associated fitting along with a second set of induced absorptions seen by TRIR that have characteristics of a Mn-localized reduction. The results are summarized in the Jablonski diagram, Figure 6.15.

Complexes **4<sup>-</sup>**-**5<sup>-</sup>** display similar TRIR features reported by us in the analogous [Re(I)(4-NDI<sup>-</sup>-bpy)(CO)<sub>3</sub>(Pyridine)][PF<sub>6</sub>] complex, though in our earlier work with Re complexes the charge recombination lifetime for the photoreduction product, [Re(I)(4-NDI<sup>0</sup>-bpy<sup>•-</sup>)(CO)<sub>3</sub>(Pyridine)][PF<sub>6</sub>], as determined by fsTA, is approximately an order of magnitude longer ( $\tau_{CR} = 31.8 \pm 0.8$  ps) than in complexes **4<sup>-</sup>**-**5<sup>-</sup>** ( $\tau_{CR} = 3.4 \pm 0.5$  ps and  $\tau_{CR} = 3.6 \pm 0.1$  ps, respectively). These complexes exhibit charge recombination lifetimes that are too short to compete with diffusion-limited CO<sub>2</sub> binding. In our previous complexes where an intermediate acceptor was employed, the back-electron transfer lifetime was lengthened significantly. For example, [Re(I)(4-bpy)(CO)<sub>3</sub>(Pyridine-DPA-NDI<sup>-</sup>)][PF<sub>6</sub>] and Re(I)(4-NDI<sup>-</sup>-DPA-bpy)(CO)<sub>3</sub>Cl, the charge recombination lifetime for the photoreduction products are  $\tau_{CR} = 43.4 \pm 1.2$   $\mu$ s and  $\tau_{CR} = 24.5 \pm 0.2$  ns, respectively. While the CR lifetime in [Re(I)(4-bpy)(CO)<sub>3</sub>(Pyridine-DPA-NDI<sup>-</sup>)][PF<sub>6</sub>] is long enough to compete with diffusion-limited CO<sub>2</sub> binding, this compound is unsuitable for photocatalytic reduction of CO<sub>2</sub> because the pyridine ligand typically dissociates upon initial reduction of the metal complex. Like Re(I)(4-NDI<sup>-</sup>-DPA-bpy)(CO)<sub>3</sub>Cl, in complexes **2<sup>-</sup>**-**3<sup>-</sup>**, by nanosecond TA, the charge recombination lifetime for the photoreduction products are  $\tau_{CR} = 39.9 \pm 0.7$  ns and  $\tau_{CR} = 27.8 \pm 0.2$  ns, respectively. Simply by attaching the NDI-Ph to the 6-position of bipyridine and utilizing the difference in reduction pathways of Mn(bpy)(CO)<sub>3</sub>X, we

are able to achieve photoreduction lifetimes that can compete with diffusion-limited  $\text{CO}_2$  binding without creating a triad system. These photocatalytic experiments are currently underway in our lab.

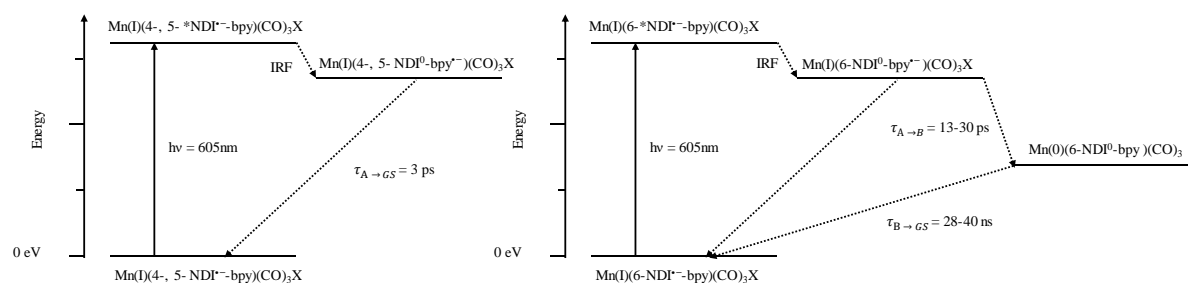


**Figure 6.15:** Jablonski diagram of  $1^{\bullet-}$  -  $5^{\bullet-}$  upon excitation ( $\lambda = 605 \text{ nm}$ ).

## 6.5 Conclusion

In this report, we have described a series of complexes that consist of a reduced NDI chromophore and a  $\text{Mn}(\text{bpy})(\text{CO})_3\text{X}$  terminal acceptor. By binding the NDI to the 4- or 5- position of the ligated bipyridine, excitation of the  $\text{NDI}^{\bullet-}$  with visible light led to reduction of the bpy ligand and formation of  $\text{Mn}(\text{bpy}^{\bullet-})(\text{CO})_3\text{X}$ . By binding the NDI to the 6- position of bipyridine, excitation of the  $\text{NDI}^{\bullet-}$  led to the formation of  $\text{Mn}(\text{bpy}^{\bullet-})(\text{CO})_3\text{X}$ , which charge shifted to the Mn metal center to ultimately form  $\text{Mn}(0)(\text{bpy})(\text{CO})_3$ . The reduced 4- and 5- Mn complexes persisted into the picosecond region while the 6-Mn complexes persisted into the nanosecond region. These assignments were corroborated with femto- and nanosecond time-resolved visible and mid-infrared spectroscopy. Additionally, these complexes demonstrate electrochemical reduction of  $\text{CO}_2$  under typical electrocatalytic conditions with the addition of a proton source. The TOF of the  $\text{Mn}(6\text{-NDI-bpy})(\text{CO})_3\text{X}$  was observed to increase from  $2.9 \text{ s}^{-1}$  to  $1258.4 \text{ s}^{-1}$  when the X ligand was exchanged from Br to DMF.

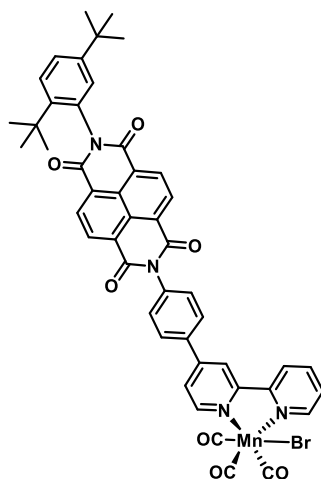
This is the first study that illustrates the mechanism for photoreduction of the  $\text{Mn}(\text{bpy})(\text{CO})_3\text{X}$   $\text{CO}_2$  reduction catalyst with a covalently attached chromophore. In the studies of the mechanism of photocatalytic  $\text{CO}_2$  reduction by Mn diimine complexes, reduction of the diimine and sequential electron transfer to the Mn center has been shown to be the step that initiates formation of a five-coordinate complex capable of binding  $\text{CO}_2$ .<sup>203</sup> By following the photoreduction mechanism via femto/nanosecond transient absorption and time-resolved IR, we are able to observe the transient species formed. This work demonstrates and elucidates the initial photosensitization of these complexes and the proceeding charge shift to the Mn center. Donor-acceptor assemblies are an effective strategy for observing early these intermediates and by taking advantage of the molecular dynamics can facilitate in long-lived species. Future work in our laboratory will investigate the photoelectrocatalytic properties of the 6-Mn complexes under a  $\text{CO}_2$  atmosphere as these complexes are on the timescale to compete with  $\text{CO}_2$  binding. Additionally towards modifying complexes such that they can be attached to an electrode surface,<sup>220</sup> allowing for generation and regeneration of the  $\text{NDI}^{\cdot-}$  via electrochemical processes, eliminating the need of sacrificial reagents in catalytic cycles.<sup>141</sup>

## 6.6 Acknowledgements

We thank Dr. Saman Shafaie for collecting high-resolution mass spectrometric data. This work was supported by the Argonne Northwestern Solar Energy Research (ANSER) Center, an Energy Frontier Research Center funded by the U.S. Department of Energy (DOE), Office of Science, Office of Basic Energy Sciences, under Award No. DE-SC0001059. This publication was made possible by NPRP Grant No. 9-174-2-092 from the Qatar National Research Fund (a member of Qatar Foundation). The findings achieved herein are solely the responsibility of the authors.

NMR and MS measurements in this work were performed at the IMSERC at Northwestern University, which has received support from the Soft and Hybrid Nanotechnology Experimental (SHyNE) Resource (NSF NNCI-1542205); the State of Illinois and International Institute for Nanotechnology (IIN).

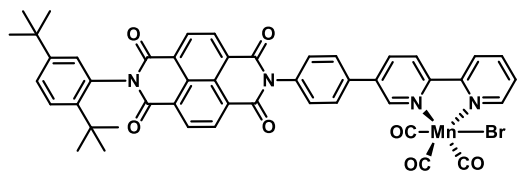
## 6.7 Synthetic Details



### Complex 4

In a nitrogen filled glove box, an oven dried pressure flask with a magnetic stirrer was filled with compound 4-NDI-phenyl-2,2'-bipyridine (1.00 g, 1.46 mmol), Bromopentacarbonylmanganese(I) (0.41 g, 1.50 mmol), and DCM (30 mL). The pressure flask was capped, wrapped in aluminum foil, and brought out of the glovebox and heated to 80 °C overnight. The solution was cooled to room temperature, and N-heptane was added to the solution, yielding a yellow precipitate. The DCM was removed by reduced pressure and the solution filtered to recover the yellow precipitate. All manipulations were done in the dark. Yield 1.02g, 78%. <sup>1</sup>H NMR (500 MHz, Chloroform-*d*) δ 9.31 (t, *J* = 5.1 Hz, 2H), 8.90 (s, 4H), 8.27 (d, *J* = 19.9 Hz, 2H), 7.99 (s, 1H), 7.88 (s, 2H), 7.72 (d, *J* = 5.7 Hz, 1H), 7.62 (d, *J* = 8.6 Hz, 1H), 7.59 – 7.48 (m, 4H),

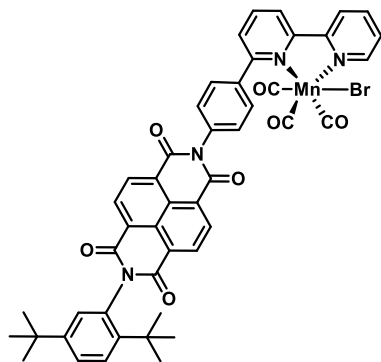
7.03 (d,  $J = 2.2$  Hz, 1H), 1.34 (s, 9H), 1.29 (s, 9H).  $^{13}\text{C}$  NMR (126 MHz,  $\text{CDCl}_3$ )  $\delta$  163.84, 163.14, 156.14, 155.68, 154.08, 153.93, 150.60, 150.09, 143.80, 138.34, 137.17, 136.79, 132.04, 131.85, 131.69, 130.06, 129.22, 128.69, 127.64, 127.53, 127.50, 126.93, 126.85, 126.43, 124.30, 122.56, 120.39, 35.75, 34.46, 31.91, 31.36. **HRMS-ESI (m/z):** calculated  $\text{C}_{47}\text{H}_{36}\text{BrMnN}_4\text{O}_7$   $[\text{M}+\text{Na}^+]^+$ : 925.1046, found  $[\text{M}+\text{Na}^+]^+$  925.1044.



### Complex 5

In a nitrogen filled glove box, an oven dried pressure flask with a magnetic stirrer was filled with compound 5-NDI-phenyl-2,2'-bipyridine (1.00 g, 1.46 mmol), Bromopentacarbonylmanganese(I) (0.41 g, 1.50 mmol), and DCM (30 mL). The pressure flask was capped, wrapped in aluminum foil, and brought out of the glovebox and heated to 80 °C overnight. The solution was cooled to room temperature, and N-heptane was added to the solution, yielding a yellow precipitate. The DCM was removed by reduced pressure and the solution filtered to recover the yellow precipitate. All manipulations were done in the dark. Yield 0.79g, 60%.  $^1\text{H}$  NMR (500 MHz, Chloroform-*d*)  $\delta$  9.53 (s, 1H), 9.31 (d,  $J = 5.3$  Hz, 1H), 8.90 (s, 4H), 8.20 (d,  $J = 34.3$  Hz, 3H), 8.03 (t,  $J = 7.6$  Hz, 1H), 7.92 (d,  $J = 7.1$  Hz, 2H), 7.62 (d,  $J = 8.6$  Hz, 1H), 7.60 – 7.54 (m, 3H), 7.50 (dd,  $J = 8.6, 2.2$  Hz, 1H), 7.03 (d,  $J = 2.3$  Hz, 1H), 1.34 (s, 9H), 1.29 (s, 9H).  $^{13}\text{C}$  NMR (126 MHz,  $\text{CDCl}_3$ )  $\delta$  163.87, 155.46, 154.49, 153.93, 152.11, 150.57, 143.81, 138.71, 138.40, 136.80, 136.26, 136.11, 132.06, 131.81, 131.64, 130.07, 129.19, 128.81, 127.66, 127.57,

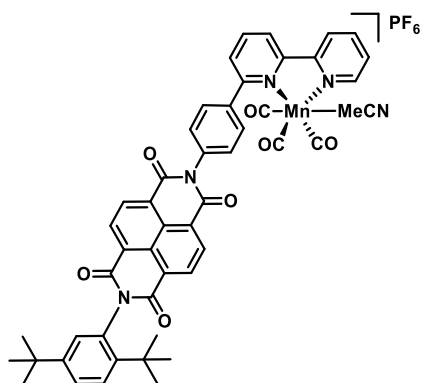
127.45, 126.90, 126.34, 122.64, 35.73, 34.44, 31.89, 31.78, 31.34, -6.88. **HRMS-ESI (m/z):** calculated  $C_{47}H_{36}BrMnN_4O_7$   $[M+Na^+]^+$ : 925.1046, found  $[M+Na^+]^+$  925.1050.



### Complex 1

In a nitrogen filled glove box, an oven dried pressure flask with a magnetic stirrer was filled with compound 6-NDI-phenyl-2,2'-bipyridine (1.00 g, 1.46 mmol), Bromopentacarbonylmanganese(I) (0.41 g, 1.50 mmol), and DCM (30 mL). The pressure flask was capped and brought out of the glovebox, wrapped in aluminum foil, and heated to 80 °C overnight. The solution was cooled to room temperature, and N-heptane was added to the solution, yielding a yellow precipitate. The DCM was removed by reduced pressure and the solution filtered to recover the yellow precipitate. All manipulations were done in the dark. Yield: 1.18g, 90%. **<sup>1</sup>H NMR** (500 MHz, Chloroform-*d*)  $\delta$  9.30 (d,  $J = 5.5$  Hz, 1H), 8.87 – 8.91 (m, 4H), 8.20 (d,  $J = 8.1$  Hz, 2H), 8.09 – 8.02 (m, 2H), 7.84 (s, 1H), 7.69 – 7.50 (m, 6H), 7.02 (d,  $J = 2.3$  Hz, 1H), 1.34 (s, 9H), 1.29 (s, 9H). **<sup>13</sup>C NMR** (126 MHz, CDCl<sub>3</sub>)  $\delta$  216.72, 164.99, 163.93, 163.04, 157.28, 156.67, 153.54, 150.53, 143.83, 142.52, 138.37, 138.25, 136.44, 132.12, 131.73, 131.67, 130.92, 130.40, 129.82, 129.16, 127.74, 127.67, 127.51, 127.46, 127.44, 127.05, 126.84, 125.87, 123.06, 121.28,

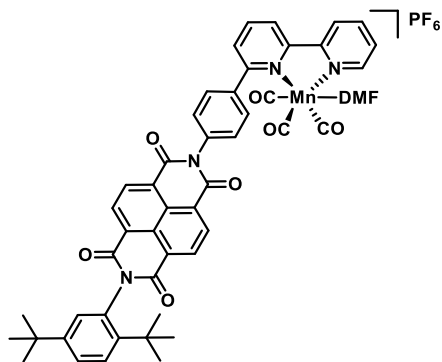
96.25, 35.73, 34.44, 31.89, 31.35. **HRMS-ESI (m/z):** calculated  $C_{47}H_{36}BrMnN_4O_7$   $[M+Na^+]^+$ : 925.1046, found  $[M+Na^+]^+$  925.1040.



## Complex 2

In a nitrogen filled glove box, an oven dried pressure flask with a magnetic stirrer was filled with compound  $Mn(6\text{-NDI-bpy})(CO)_3Br$  (0.05 g, 0.055 mmol),  $AgPF_6$  (0.015 g, 0.060 mmol), and acetonitrile (25 mL). The pressure flask was capped, wrapped in aluminum foil, brought out of the glovebox, and heated to 80 °C overnight. The solution was cooled to room temperature and filtered through Celite. Acetonitrile was removed under reduced pressure and the material was dissolved in minimal DCM and filtered through Celite once again. N-heptane was added to the filtrate and a bright yellow complex precipitated and was collected via filtration. All manipulations were done in the dark. Yield: 0.05g, 90%.  **$^1H$  NMR** (500 MHz, Acetonitrile- $d_3$ )  $\delta$  9.17 (s, 1H), 8.77 (s, 4H), 8.45 (s, 2H), 8.26 (s, 2H), 7.81 (s, 3H), 7.75 – 7.43 (m, 5H), 7.26 (s, 1H), 2.06 (s, 3H), 1.29 (s, 9H), 1.29 (s, 9H).  **$^{13}C$  NMR** (126 MHz,  $CD_3CN$ )  $\delta$  165.99, 165.29, 164.15, 158.13, 157.30, 155.10, 151.44, 145.17, 143.26, 141.20, 141.08, 138.66, 134.25, 132.02, 131.92, 131.07, 130.62, 130.05, 129.94, 129.08, 128.54, 128.34, 128.27, 127.24, 125.32, 123.50,

36.26, 35.06, 32.02, 31.49, 30.97. **HRMS-ESI (m/z):** calculated  $C_{49}H_{39}F_6MnN_5O_7P$   $[M-PF_6^+]^+$ : 864.2230, found  $[M-PF_6^+]^+$  864.2212.



### Complex 3

In a nitrogen filled glove box, an oven dried pressure flask with a magnetic stirrer was filled with compound  $Mn(6-NDI-bpy)(CO)_3Br$  (0.05 g, 0.055 mmol),  $AgPF_6$  (0.015 g, 0.060 mmol), and dichloromethane (15 mL). The pressure flask was capped, wrapped in aluminum foil, brought out of the glovebox, and heated to 80 °C overnight. The solution was cooled to room temperature and returned to the glovebox. DMF (15 mL) and  $KPF_6$  (0.011g, 0.06mmol) was added to the pressure flask and brought out of the glovebox and allowed to stir overnight at room temperature. The mixture was then filtered through Celite and the solvents removed under reduced pressure. The material was dissolved in minimal DCM and filtered through Celite once again. N-heptane was added to the filtrate. A yellow complex precipitated and was collected via filtration. All manipulations were done in the dark. Yield: 0.054g, 95%.  **$^1H$  NMR** (500 MHz, Methylene Chloride- $d_2$ )  $\delta$  9.21 (s, 1H), 8.87 (s, 4H), 8.44 – 8.36 (m, 2H), 8.32 – 8.22 (m, 2H), 8.01 – 7.80 (m, 2H), 7.75 – 7.60 (m, 4H), 7.58 – 7.42 (m, 2H), 7.05 (s, 1H), 1.34 (s, 9H), 1.27 (s, 9H).  **$^{13}C$  NMR** (126 MHz,  $CD_2Cl_2$ )  $\delta$  166.77, 165.07, 164.26, 163.32, 157.68, 156.90, 153.67, 153.34, 151.02, 144.57, 142.19, 140.85, 140.80, 137.70, 132.95, 131.81, 131.76, 129.49, 128.70, 128.03, 127.79,

127.29, 127.20, 126.92, 124.61, 122.42, 78.00, 77.74, 77.49, 54.27, 54.06, 53.84, 53.62, 53.41, 38.61, 35.90, 34.62, 32.94, 31.88, 31.34. **HRMS-ESI (m/z):** calculated  $C_{50}H_{43}F_6MnN_5O_8P [M-PF_6^+]^+$ : 896.2492, found  $[M-PF_6^+]^+$  896.2480.

### 6.8 Variable Scan Rates & Plots

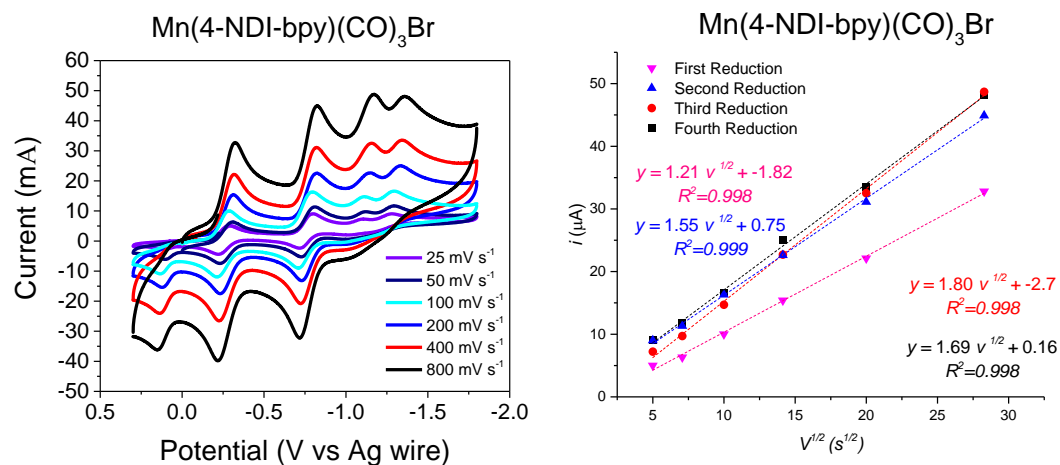


**Figure 6.16:** **A)** Cyclic voltammograms of 1.0 mM Complex **4** in *N,N*-DMF with 0.1 M TBAPF<sub>6</sub> solution under Argon saturation, showing response to variable scan rate. **B)** Variable scan rate plots of Complex **4**. Working electrode is glassy carbon (3 mm diameter), counter electrode is Pt, and pseudoreference is Ag wire.

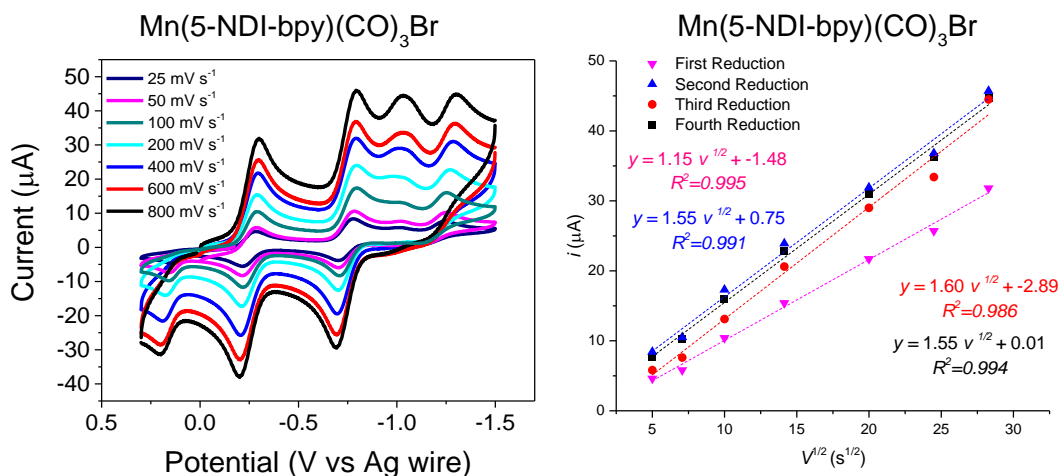


**Figure 6.17:** **A)** Cyclic voltammograms of 1.0 mM Complex **5** in N,N-DMF with 0.1 M TBAPF<sub>6</sub> solution under Argon saturation, showing response to variable scan rate. **B)** Variable scan rate plots of Complex **5**. Working electrode is glassy carbon (3 mm diameter), counter electrode is Pt, and pseudoreference is Ag wire.

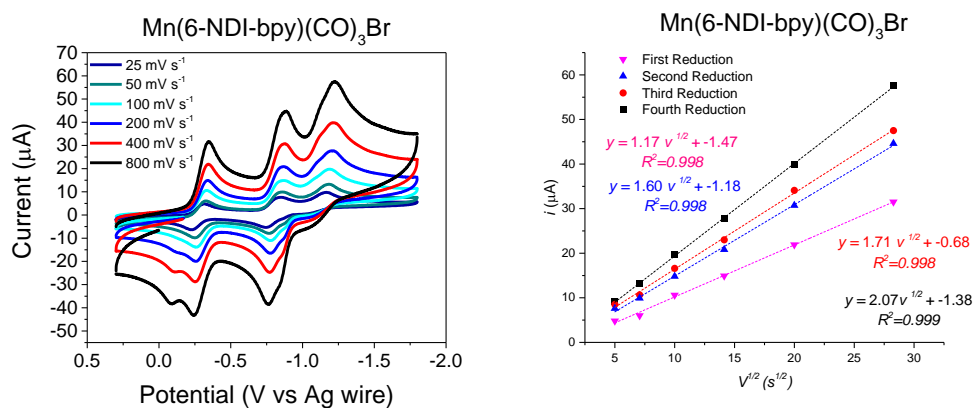


**Figure 6.18:** **A)** Cyclic voltammograms of 1.0 mM Complex **1** in N,N-DMF with 0.1 M TBAPF<sub>6</sub> solution under Argon saturation, showing response to variable scan rate. **B)** Variable scan rate plots of Complex **1**. Working electrode is glassy carbon (3 mm diameter), counter electrode is Pt, and pseudoreference is Ag wire.

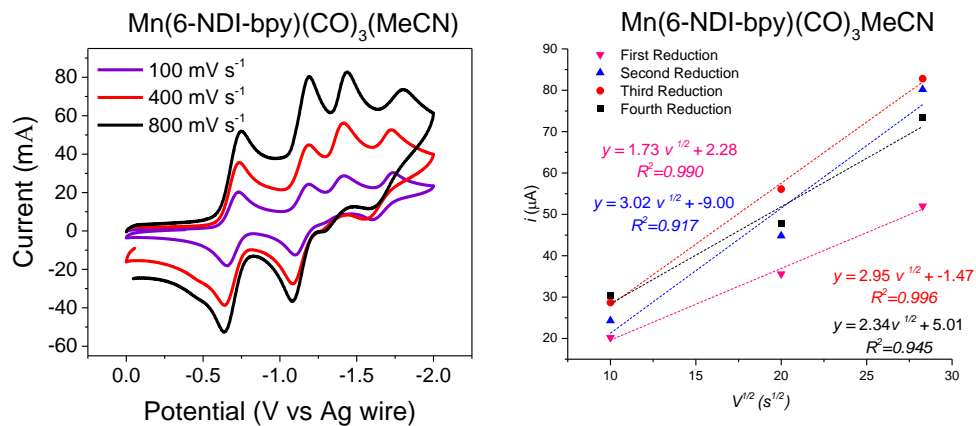


**Figure 6.19:** A) Cyclic voltammograms of 1.0 mM Complex **2** in MeCN with 0.1 M TBAPF<sub>6</sub> solution under Argon saturation, showing response to variable scan rate. B) Variable scan rate plots of Complex **2**. Working electrode is glassy carbon (3 mm diameter), counter electrode is Pt, and pseudoreference is Ag wire.

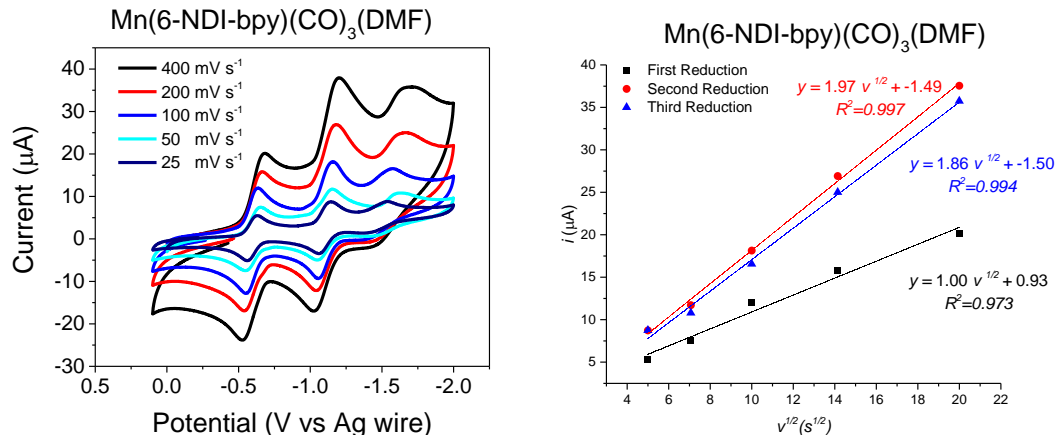


**Figure 6.20:** A) Cyclic voltammograms of 1.0 mM Complex **3** in N,N-DMF with 0.1 M TBAPF<sub>6</sub> solution under Argon saturation, showing response to variable scan rate. B) Variable scan rate plots of Complex **3**. Working electrode is glassy carbon (3 mm diameter), counter electrode is Pt, and pseudoreference is Ag wire.

## 6.9 Supplementary Details

### 6.9.1 Electronic Absorption

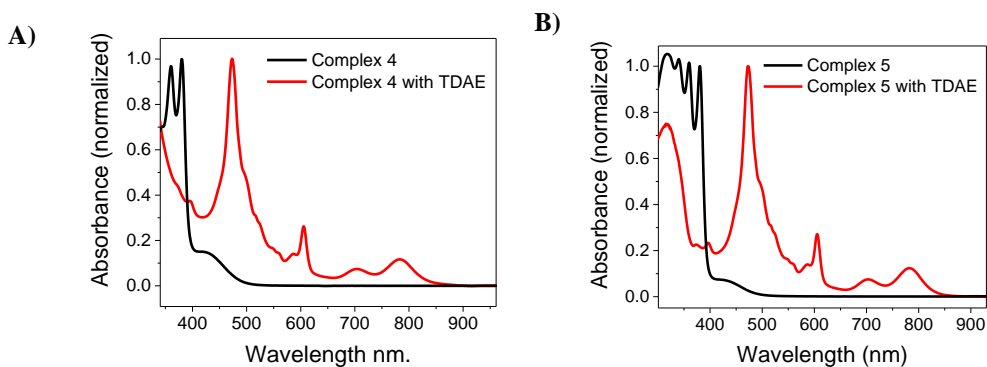


**Figure 6.21:** **A)** Electronic absorption spectra of complex **4** (DMF) with and without the TDAE reductant added. **B)** Electronic absorption spectra of complex **5** (DMF) with and without the TDAE reductant added.

### 6.9.2 Electrochemical Studies

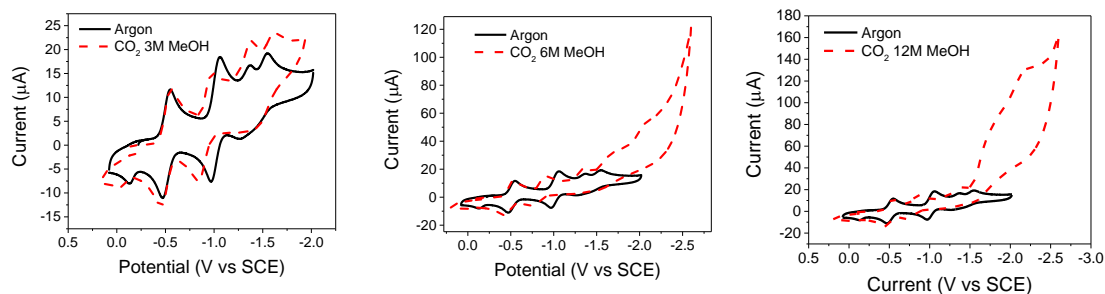


**Figure 6.22:** Cyclic voltammograms of a 1.0 mM solution of complex **4** with 0.1 M TBAPF<sub>6</sub> in DMF, under argon (black), saturated with CO<sub>2</sub> (dashed red line) with MeOH (3 M, 6 M, 12 M, respectively). Scan rate: 100 mVs<sup>-1</sup>, glassy carbon electrode, platinum counter electrode, and silver reference wire.

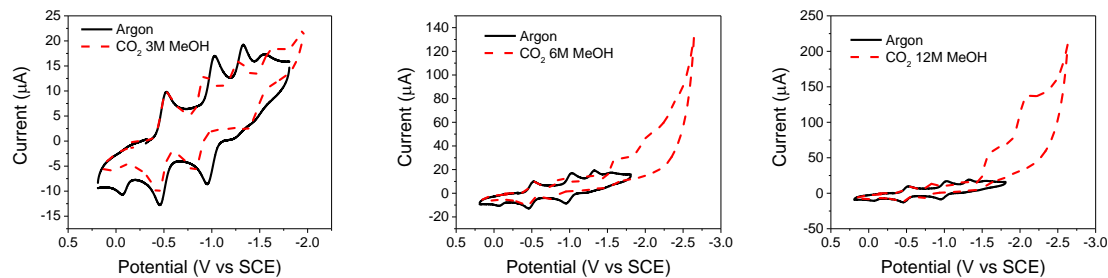


**Figure 6.23:** Cyclic voltammograms of a 1.0 mM solution of complex **5** with 0.1 M TBAPF<sub>6</sub> in DMF, under argon (black), saturated with CO<sub>2</sub> (dashed red line) with MeOH (3 M, 6 M, 12 M, respectively). Scan rate: 100 mVs<sup>-1</sup>, glassy carbon electrode, platinum counter electrode, and silver reference wire.

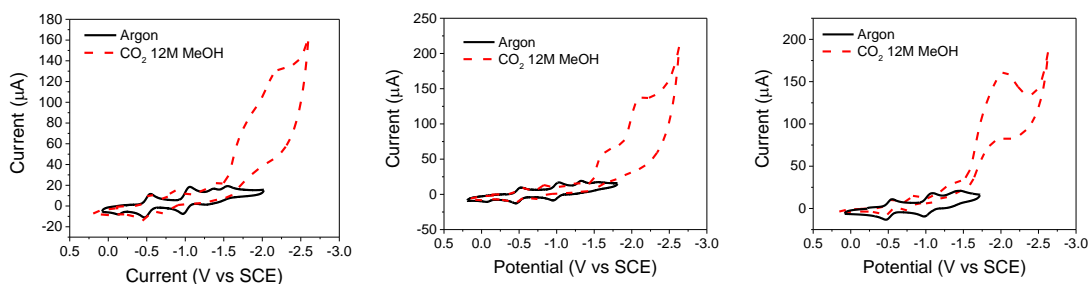


**Figure 6.24:** Cyclic voltammograms of a 1.0 mM solution of complexes **1**, **4**, and **5** with 0.1 M TBAPF<sub>6</sub> in DMF, under argon (black), saturated with CO<sub>2</sub> (dashed red line) with MeOH (12 M). Scan rate: 100 mVs<sup>-1</sup>, glassy carbon electrode, platinum counter electrode, and silver reference wire.

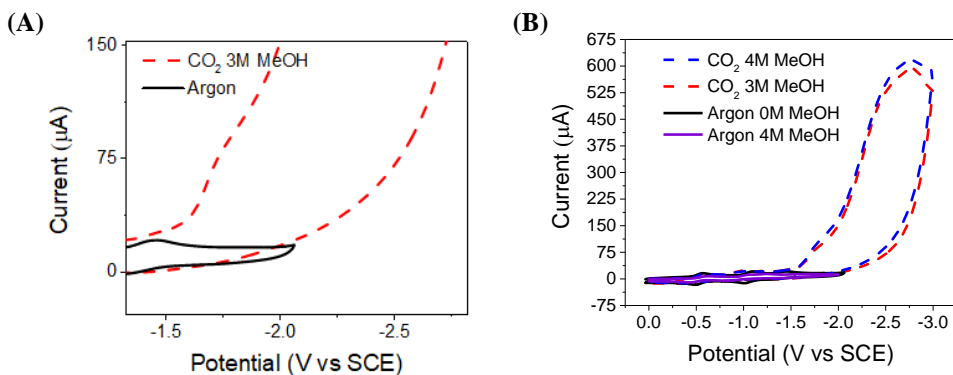


**Figure 6.25:** Cyclic voltammograms of a 1.0 mM solution of complex **3** with 0.1 M  $\text{TBAPF}_6$  in DMF, A) under argon (black), saturated with  $\text{CO}_2$  (dashed red line) with MeOH (3 M). B) under argon (black), under argon with MeOH (4M) (purple), saturated with  $\text{CO}_2$  (dashed blue line) with MeOH (4 M). Scan rate:  $100 \text{ mVs}^{-1}$ , glassy carbon electrode, platinum counter electrode, and silver reference wire.

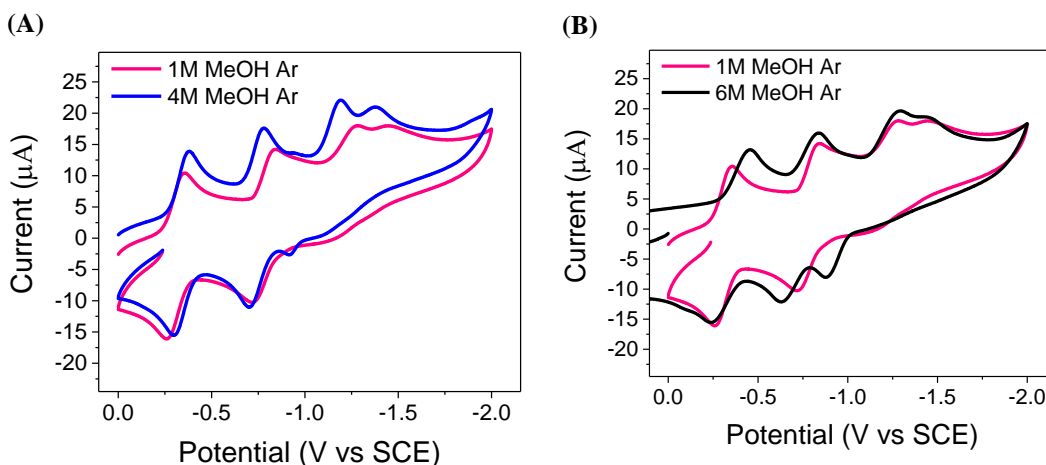


**Figure 6.26:** Cyclic voltammograms of a 1.0 mM solution of complex **1** with 0.1 M  $\text{TBAPF}_6$  in DMF, A) under argon with MeOH (1M) (pink), under argon with MeOH (4M) (blue) B) under argon with MeOH (1M) (pink), under argon with MeOH (4M) (black). Scan rate:  $100 \text{ mVs}^{-1}$ , glassy carbon electrode, platinum counter electrode, and silver reference wire.

### 6.9.3 Data Processing / Fitting for Time-Resolved Optical Spectroscopy

*Femtosecond Spectroscopy:* Prior to kinetic analysis, the fsTA & fsIR data are background/scatter-subtracted and chirp-corrected, and the visible and NIR data sets are spectrally

merged (Surface Explorer 4, Ultrafast Systems, LLC). Merging in the time-domain is accomplished in MATLAB by scaling the fsTA & nsTA dataset to the other by a wavelength-dependent factor  $f(\lambda)$ . This function is determined by the ratio of the average signal value for each data set in the 4-8 ns range, where there is sufficient temporal overlap between experiments and kinetic evolution is typically slow.<sup>123</sup> *10 Hz nsTA Data*: Kinetic data from the 10 Hz nsTA experiment are temporally smoothed with 5-point adjacent averaging prior to fitting.

#### 6.9.4 Global Analysis

The kinetic analysis was performed using home written programs in MATLAB<sup>121</sup> and was based on a global fit to (kinetic vectors following singular value decomposition). The time-resolution is given as  $w = 250$  fs (full width at half maximum, FWHM); the assumption of a uniform instrument response across the frequency domain and a fixed time-zero ( $t_0$ ) are implicit in global analysis.

*Singular Value Decomposition.* Factoring of the two-dimensional (signal vs time & frequency) data set by Singular Value Decomposition (SVD) is performed as implemented in the MATLAB software package.<sup>121</sup> This factoring produces an orthonormal set of basis spectra that describe the wavelength dependence of the species and a corresponding set of orthogonal vectors that describe the time-dependent amplitudes of the basis spectra.<sup>114</sup> These kinetic vectors are then fit using the global analysis method described below.

*Multiple-Wavelength Global Fitting.* The kinetic data from multiple different wavelength are fit using the global analysis described below. Each wavelength is given an initial amplitude that is representative of the spectral intensity at time  $t_0$ , and varied independently to fit the data.

The time/rate constants and  $t_0$  are shared between the various kinetic data and are varied globally across the kinetic data in order to fit the model(s) described below.

*Species-Associated Fitting.* We globally fit the dataset to a specified kinetic model and use the resultant populations to deconvolute the dataset and reconstruct species-associated spectra.

Kinetic model with rate matrix  $K$  for one specie:

$$K = [-k_{A \rightarrow GS}] \quad (\text{Eqn. S1})$$

Kinetic model with rate matrix  $K$  for two species:

$$K = \begin{bmatrix} -k_{A \rightarrow B} & \mathbf{0} \\ k_{A \rightarrow B} & -k_{B \rightarrow GS} \end{bmatrix} \quad (\text{Eqn. S2})$$

The MATLAB program numerically solves the differential equations through matrix methods,<sup>115</sup> then convolutes the solutions with a Gaussian instrument response function with width  $w$  (FWHM), before employing a least-squares fitting using a Levenberg-Marquardt or Simplex method to find the parameters which result in matches to the kinetic data.

*Spectral Reconstruction.* Once the fit parameters are established, they are fed directly into the differential equations, which were solved for the populations of the states in model—i.e.,  $A(t)$  and  $B(t)$ . Finally, the raw data matrix (with all the raw data) is deconvoluted with the populations as functions of time to produce the spectra associated with each species.

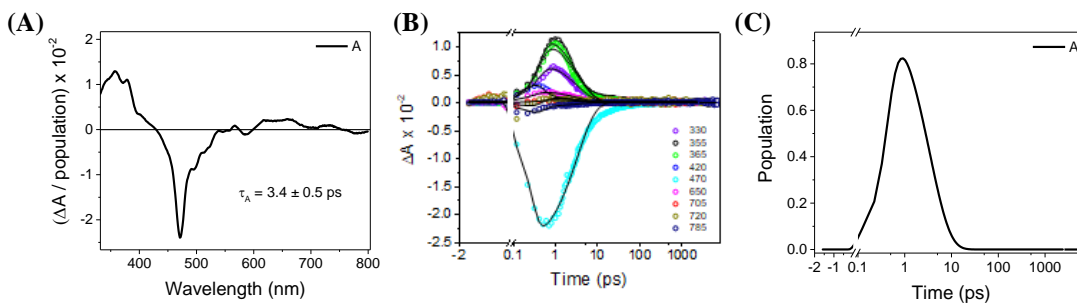


**Figure 6.27:** Complex  $4^{*-}$ .  $\lambda = 605$  nm,  $1.0 \mu\text{J/pulse}$ , DMF. (A) Species-associated spectra obtained by global fitting. (B) Transient kinetics at selected wavelengths. (C) Populations of the transient species.

$$K = [-k_{A \rightarrow GS}]$$

Initial populations:  $A_0 = 1$

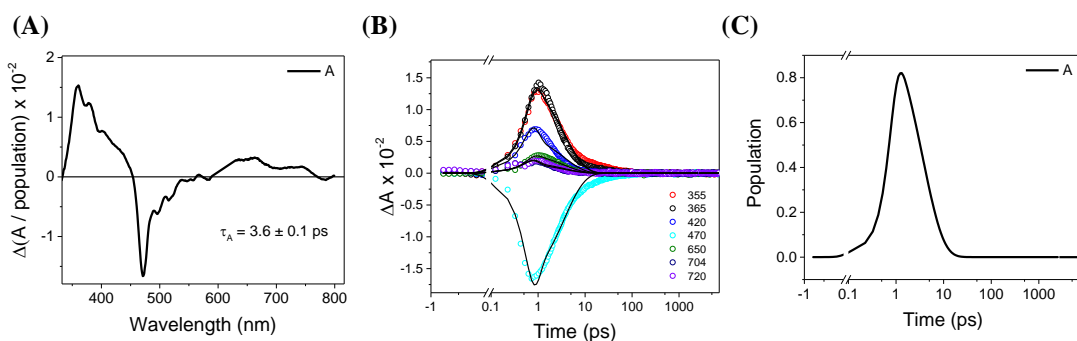


**Figure 6.28:** Complex  $5^{*-}$ .  $\lambda = 605$  nm,  $1.0 \mu\text{J/pulse}$ , DMF. (A) Species-associated spectra obtained by global fitting. (B) Transient kinetics at selected wavelengths. (C) Populations of the transient species.

$$K = [-k_{A \rightarrow GS}]$$

Initial populations:  $A_0 = 1$

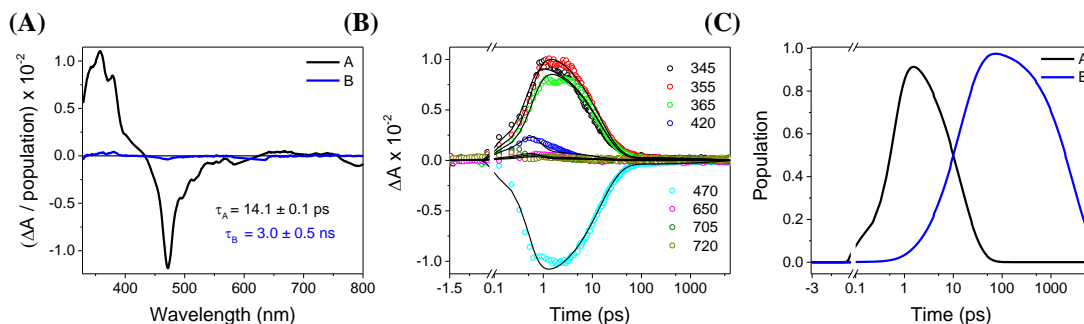


**Figure 6.29:** Complex  $1^-$ .  $\lambda = 605$  nm,  $1.0 \mu\text{J}/\text{pulse}$ , DMF. (A) Species-associated spectra obtained by global fitting. (B) Transient kinetics at selected wavelengths. (C) Populations of the transient species.

$$K = \begin{bmatrix} -k_{A \rightarrow B} & \mathbf{0} \\ k_{A \rightarrow B} & -k_{B \rightarrow GS} \end{bmatrix}$$

Initial populations:  $A_0 = 1$ ,  $B_0 = 0$

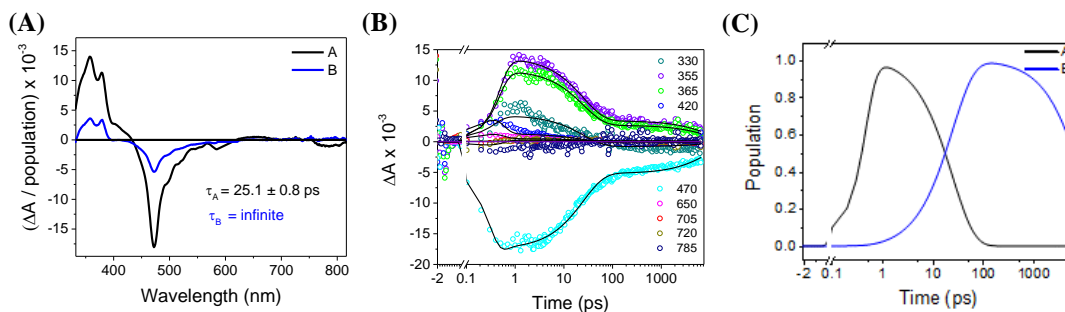


**Figure 6.30:** Complex  $2^-$ .  $\lambda = 605$  nm,  $1.0 \mu\text{J}/\text{pulse}$ , DMF. (A) Species-associated spectra obtained by global fitting. (B) Transient kinetics at selected wavelengths. (C) Populations of the transient species.

$$K = \begin{bmatrix} -k_{A \rightarrow B} & \mathbf{0} \\ k_{A \rightarrow B} & -k_{B \rightarrow GS} \end{bmatrix}$$

Initial populations:  $A_0 = 1$ ,  $B_0 = 0$

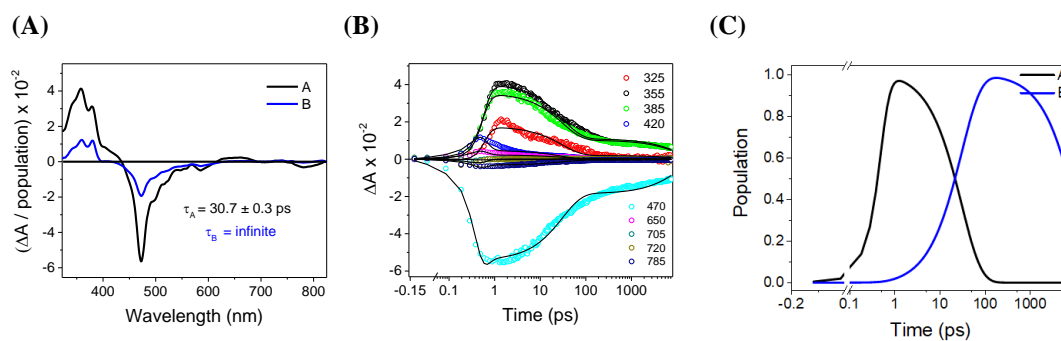


**Figure 6.31:** Complex 3<sup>-</sup>.  $\lambda = 605$  nm, 1.0  $\mu\text{J}/\text{pulse}$ , DMF. (A) Species-associated spectra obtained by global fitting. (B) Transient kinetics at selected wavelengths. (C) Populations of the transient species.

$$K = \begin{bmatrix} -k_{A \rightarrow B} & \mathbf{0} \\ k_{A \rightarrow B} & -k_{B \rightarrow GS} \end{bmatrix}$$

Initial populations:  $A_0 = 1$ ,  $B_0 = 0$

## References

1. Detz, R. J.; Reek, J. N. H.; van der Zwaan, B. C. C., The future of solar fuels: when could they become competitive? *Energy & Environmental Science* **2018**, *11* (7), 1653-1669.
2. Nicola, A.; Vincenzo, B., Solar Electricity and Solar Fuels: Status and Perspectives in the Context of the Energy Transition. *Chemistry – A European Journal* **2016**, *22* (1), 32-57.
3. Van Overstraeten, R., Crystalline silicon solar cells. *Renewable Energy* **1994**, *5* (1), 103-106.
4. Battaglia, C.; Cuevas, A.; De Wolf, S., High-efficiency crystalline silicon solar cells: status and perspectives. *Energy & Environmental Science* **2016**, *9* (5), 1552-1576.
5. Hedley, G. J.; Ruseckas, A.; Samuel, I. D. W., Light Harvesting for Organic Photovoltaics. *Chemical Reviews* **2017**, *117* (2), 796-837.
6. Kaur, N.; Singh, M.; Pathak, D.; Wagner, T.; Nunzi, J. M., Organic materials for photovoltaic applications: Review and mechanism. *Synthetic Metals* **2014**, *190*, 20-26.
7. Mazzio, K. A.; Luscombe, C. K., The future of organic photovoltaics. *Chemical Society Reviews* **2015**, *44* (1), 78-90.
8. Hagfeldt, A.; Boschloo, G.; Sun, L.; Kloo, L.; Pettersson, H., Dye-Sensitized Solar Cells. *Chemical Reviews* **2010**, *110* (11), 6595-6663.
9. Grätzel, M., Dye-sensitized solar cells. *Journal of Photochemistry and Photobiology C: Photochemistry Reviews* **2003**, *4* (2), 145-153.
10. Whittingham, M. S.; Savinell, R. F.; Zawodzinski, T., Introduction: Batteries and Fuel Cells. *Chemical Reviews* **2004**, *104* (10), 4243-4244.
11. Whittingham, M. S., Introduction: Batteries. *Chemical Reviews* **2014**, *114* (23), 11413-11413.
12. Balsara, N. P.; Newman, J., Comparing the Energy Content of Batteries, Fuels, and Materials. *Journal of Chemical Education* **2013**, *90* (4), 446-452.
13. Barber, J.; Tran, P. D., From natural to artificial photosynthesis. *Journal of The Royal Society Interface* **2013**, *10* (81).
14. McConnell, I.; Li, G.; Brudvig, G. W., Energy Conversion in Natural and Artificial Photosynthesis. *Chemistry & Biology* **2010**, *17* (5), 434-447.
15. Wasielewski, M. R., Photoinduced electron transfer in supramolecular systems for artificial photosynthesis. *Chemical Reviews* **1992**, *92* (3), 435-461.
16. Lubitz, W.; Tumas, W., Hydrogen: An Overview. *Chemical Reviews* **2007**, *107* (10), 3900-3903.
17. Rofer-DePoorter, C. K., A comprehensive mechanism for the Fischer-Tropsch synthesis. *Chemical Reviews* **1981**, *81* (5), 447-474.
18. Tran, P. D.; Wong, L. H.; Barber, J.; Loo, J. S. C., Recent advances in hybrid photocatalysts for solar fuel production. *Energy & Environmental Science* **2012**, *5* (3), 5902-5918.
19. Schneider, J.; Jia, H.; Muckerman, J. T.; Fujita, E., Thermodynamics and kinetics of CO<sub>2</sub>, CO, and H<sup>+</sup> binding to the metal centre of CO<sub>2</sub> reduction catalysts. *Chem Soc Rev* **2012**, *41* (6), 2036-51.
20. Qiao, J.; Liu, Y.; Hong, F.; Zhang, J., A review of catalysts for the electroreduction of carbon dioxide to produce low-carbon fuels. *Chemical Society Reviews* **2014**, *43* (2), 631-675.

21. Smieja, J. M.; Benson, E. E.; Kumar, B.; Grice, K. A.; Seu, C. S.; Miller, A. J. M.; Mayer, J. M.; Kubiak, C. P., Kinetic and structural studies, origins of selectivity, and interfacial charge transfer in the artificial photosynthesis of CO. *Proceedings of the National Academy of Sciences* **2012**, *109* (39), 15646-15650.
22. Smieja, J. M.; Kubiak, C. P., Re(bipy-tBu)(CO)<sub>3</sub>Cl—improved Catalytic Activity for Reduction of Carbon Dioxide: IR-Spectroelectrochemical and Mechanistic Studies. *Inorganic Chemistry* **2010**, *49* (20), 9283-9289.
23. Hawecker, J.; Lehn, J.-M.; Ziesel, R., Electrocatalytic reduction of carbon dioxide mediated by Re(bipy)(CO)<sub>3</sub>Cl (bipy = 2,2[prime or minute]-bipyridine). *Journal of the Chemical Society, Chemical Communications* **1984**, (6), 328-330.
24. Wong, K.-Y.; Chung, W.-H.; Lau, C.-P., The effect of weak Brønsted acids on the electrocatalytic reduction of carbon dioxide by a rhenium tricarbonyl bipyridyl complex. *Journal of Electroanalytical Chemistry* **1998**, *453* (1), 161-170.
25. Bourrez, M.; Molton, F.; Chardon-Noblat, S.; Deronzier, A., [Mn(bipyridyl)(CO)<sub>3</sub>Br]: an abundant metal carbonyl complex as efficient electrocatalyst for CO<sub>2</sub> reduction. *Angew Chem Int Ed Engl* **2011**, *50* (42), 9903-6.
26. Smieja, J. M.; Sampson, M. D.; Grice, K. A.; Benson, E. E.; Froehlich, J. D.; Kubiak, C. P., Manganese as a Substitute for Rhenium in CO<sub>2</sub> Reduction Catalysts: The Importance of Acids. *Inorganic Chemistry* **2013**, *52* (5), 2484-2491.
27. Hammarström, L., Accumulative Charge Separation for Solar Fuels Production: Coupling Light-Induced Single Electron Transfer to Multielectron Catalysis. *Accounts of Chemical Research* **2015**, *48* (3), 840-850.
28. Kumar, B.; Llorente, M.; Froehlich, J.; Dang, T.; Sathrum, A.; Kubiak, C. P., Photochemical and Photoelectrochemical Reduction of CO<sub>2</sub>. *Annual Review of Physical Chemistry* **2012**, *63* (1), 541-569.
29. Benson, E. E.; Kubiak, C. P.; Sathrum, A. J.; Smieja, J. M., Electrocatalytic and homogeneous approaches to conversion of CO<sub>2</sub> to liquid fuels. *Chemical Society Reviews* **2009**, *38* (1), 89-99.
30. Elgrishi, N.; Chambers, M. B.; Wang, X.; Fontecave, M., Molecular polypyridine-based metal complexes as catalysts for the reduction of CO<sub>2</sub>. *Chemical Society Reviews* **2017**, *46* (3), 761-796.
31. Tamaki, Y.; Ishitani, O., Supramolecular Photocatalysts for the Reduction of CO<sub>2</sub>. *ACS Catalysis* **2017**, *7* (5), 3394-3409.
32. Sattler, W.; Henling, L. M.; Winkler, J. R.; Gray, H. B., Bespoke Photoreductants: Tungsten Arylisocyanides. *Journal of the American Chemical Society* **2015**, *137* (3), 1198-1205.
33. Sattler, W.; Ener, M. E.; Blakemore, J. D.; Rachford, A. A.; LaBeaume, P. J.; Thackeray, J. W.; Cameron, J. F.; Winkler, J. R.; Gray, H. B., Generation of Powerful Tungsten Reductants by Visible Light Excitation. *Journal of the American Chemical Society* **2013**, *135* (29), 10614-10617.
34. Harkins, S. B.; Peters, J. C., A Highly Emissive Cu<sub>2</sub>N<sub>2</sub>Diamond Core Complex Supported by a [PNP] -Ligand. *Journal of the American Chemical Society* **2005**, *127* (7), 2030-2031.
35. Ruthkosky, M.; Castellano, F. N.; Meyer, G. J., Photodriven Electron and Energy Transfer from Copper Phenanthroline Excited States. *Inorg. Chem.* **1996**, *35* (22), 6406-6412.

36. McMillin, D. R.; Buckner, M. T.; Ahn, B. T., A light-induced redox reaction of bis(2,9-dimethyl-1,10-phenanthroline)copper(I). *Inorg. Chem.* **2002**, *16* (4), 943-945.
37. Flamigni, L.; Barbieri, A.; Sabatini, C.; Ventura, B.; Barigelletti, F., Photochemistry and Photophysics of Coordination Compounds: Iridium. In *Photochemistry and Photophysics of Coordination Compounds II*, Springer Berlin Heidelberg: Berlin, Heidelberg, 2007; Vol. 281, pp 143-203.
38. King, K. A.; Spellane, P. J.; Watts, R. J., Excited-state properties of a triply ortho-metalated iridium(III) complex. *Journal of the American Chemical Society* **1985**, *107* (5), 1431-1432.
39. Cummings, S. D.; Eisenberg, R., Tuning the excited-state properties of platinum (II) diimine dithiolate complexes. *Journal of the American Chemical Society* **1996**, *118* (8), 1949-1960.
40. Takeda, H.; Koike, K.; Morimoto, T.; Inumaru, H.; Ishitani, O., *Photochemistry and photocatalysis of rhenium(I) diimine complexes*. Elsevier Inc.: 2011; Vol. 63, p 137-186.
41. Kato, E.; Takeda, H.; Koike, K.; Ohkubo, K.; Ishitani, O., Ru(II)-Re(I) Binuclear Photocatalysts Connected by -CH<sub>2</sub>XCH<sub>2</sub>- (X = O, S, CH<sub>2</sub>) for CO<sub>2</sub> Reduction. *Chemical Science* **2015**, *6* (5), 3003-3012.
42. Kuramochi, Y.; Ishitani, O., Iridium(III) 1-Phenylisoquinoline Complexes as a Photosensitizer for Photocatalytic CO<sub>2</sub> Reduction: A Mixed System with a Re(I) Catalyst and a Supramolecular Photocatalyst. *Inorganic Chemistry* **2016**, *55* (11), 5702-5709.
43. Gabrielsson, A.; Hartl, F.; Zhang, H.; Lindsay Smith, J. R.; Towrie, M.; Vlček, A.; Perutz, R. N., Ultrafast Charge Separation in a Photoreactive Rhenium-Appended Porphyrin Assembly Monitored by Picosecond Transient Infrared Spectroscopy. *Journal of the American Chemical Society* **2006**, *128* (13), 4253-4266.
44. Tamaki, Y.; Koike, K.; Morimoto, T.; Yamazaki, Y.; Ishitani, O., Red-Light-Driven Photocatalytic Reduction of CO<sub>2</sub> using Os(II)-Re(I) Supramolecular Complexes. *Inorg. Chem.* **2013**, *52* (20), 11902-11909.
45. Gosztoła, D.; Niemczyk, M. P.; Svec, W.; Lukas, A. S.; Wasielewski, M. R., Excited Doublet States of Electrochemically Generated Aromatic Imide and Diimide Radical Anions. *The Journal of Physical Chemistry A* **2000**, *104* (28), 6545-6551.
46. Haviv, E.; Shimon, L. J. W.; Neumann, R., Photochemical Reduction of CO<sub>2</sub> with Visible Light Using a Polyoxometalate as Photoreductant. *Chemistry – A European Journal* **2017**, *23* (1), 92-95.
47. La Porte, N. T.; Martinez, J. F.; Hedstrom, S.; Rudshteyn, B.; Phelan, B. T.; Mauck, C. M.; Young, R. M.; Batista, V. S.; Wasielewski, M. R., Photoinduced electron transfer from rylenediimide radical anions and dianions to Re(bpy)(CO)<sub>3</sub> using red and near-infrared light. *Chemical Science* **2017**, *8*, 3821-3831.
48. Shirman, E.; Ustinov, A.; Ben-Shitrit, N.; Weissman, H.; Iron, M. A.; Cohen, R.; Rybtchinski, B., Stable Aromatic Dianion in Water. *The Journal of Physical Chemistry B* **2008**, *112* (30), 8855-8858.
49. Lukas, A. S.; Miller, S. E.; Wasielewski, M. R., Femtosecond Optical Switching of Electron Transport Direction in Branched Donor-Acceptor Arrays. *The Journal of Physical Chemistry B* **2000**, *104* (5), 931-940.
50. Lukas, A. S.; Bushard, P. J.; Wasielewski, M. R., Ultrafast Molecular Logic Gate Based on Optical Switching between Two Long-Lived Radical Ion Pair States. *Journal of the American Chemical Society* **2001**, *123* (10), 2440-2441.

51. Ghosh, I.; Ghosh, T.; Bardagi, J. I.; König, B., Reduction of aryl halides by consecutive visible light-induced electron transfer processes. *Science* **2014**, *346* (6210), 725-728.
52. Marchini, M.; Gualandi, A.; Mengozzi, L.; Franchi, P.; Lucarini, M.; Cozzi, P. G.; Balzani, V.; Ceroni, P., Mechanistic insights into two-photon-driven photocatalysis in organic synthesis. *Physical Chemistry Chemical Physics* **2018**, *20* (12), 8071-8076.
53. Tamaki, Y.; Watanabe, K.; Koike, K.; Inoue, H.; Morimoto, T.; Ishitani, O., Development of highly efficient supramolecular CO<sub>2</sub> reduction photocatalysts with high turnover frequency and durability. *Faraday Discussions* **2012**, *155* (0), 115-127.
54. Koike, K.; Naito, S.; Sato, S.; Tamaki, Y.; Ishitani, O., Architecture of supramolecular metal complexes for photocatalytic CO<sub>2</sub> reduction. *Journal of Photochemistry and Photobiology A: Chemistry* **2009**, *207* (1), 109-114.
55. Perutz, R.; Windle, C. D.; Câmpian, M. V., CO<sub>2</sub> photoreduction with long-wavelength light: dyads and monomers of zinc porphyrin and rhenium bipyridine. *Chemical Communications* **2012**, *48*, 8189-8191.
56. Windle, C. D.; Perutz, R. N., Advances in molecular photocatalytic and electrocatalytic CO<sub>2</sub> reduction. *Coordination Chemistry Reviews* **2012**, *256* (21-22), 2562-2570.
57. Sato, S.; Koike, K.; Inoue, H.; Ishitani, O., Highly efficient supramolecular photocatalysts for CO<sub>2</sub> reduction using visible light. *Photochemistry & Photobiological Sciences* **2007**, *6* (4), 454-461.
58. Sullivan, B. P.; Bolinger, C. M.; Conrad, D.; Vining, W. J.; Meyer, T. J., One- and two-electron pathways in the electrocatalytic reduction of CO<sub>2</sub> by fac-Re(bpy)(CO)<sub>3</sub>Cl (bpy = 2,2'-bipyridine). *J. Chem. Soc., Chem. Commun.* **1985**, (20), 1414-1416.
59. Morimoto, T.; Nakajima, T.; Sawa, S.; Nakanishi, R.; Imori, D.; Ishitani, O., CO<sub>2</sub> Capture by a Rhenium(I) Complex with the Aid of Triethanolamine. *J. Am. Chem. Soc.* **2013**, *135* (45), 16825-16828.
60. Benson, E. E.; Sampson, M. D.; Grice, K. A.; Smieja, J. M.; Froehlich, J. D.; Friebel, D.; Keith, J. A.; Carter, E. A.; Nilsson, A.; Kubiak, C. P., The Electronic States of Rhenium Bipyridyl Electrocatalysts for CO<sub>2</sub> Reduction as Revealed by X-ray Absorption Spectroscopy and Computational Quantum Chemistry. *Angewandte Chemie International Edition* **2013**, *52* (18), 4841-4844.
61. Viehbeck, A.; Goldberg, M. J.; Kovac, C. A., Electrochemical Properties of Polyimides and Related Imide Compounds. *J. Electrochem. Soc.* **1990**, *137* (5), 1460-1466.
62. Grice, K. A.; Kubiak, C. P., *Recent Studies of Rhenium and Manganese Bipyridine Carbonyl Catalysts for the Electrochemical Reduction of CO<sub>2</sub>*. Elsevier Inc.: 2014; Vol. 66, p 163-188.
63. Clark, M. L.; Cheung, P. L.; Lessio, M.; Carter, E. A.; Kubiak, C. P., Kinetic and Mechanistic Effects of Bipyridine (bpy) Substituent, Labile Ligand, and Brønsted Acid on Electrocatalytic CO<sub>2</sub> Reduction by Re(bpy) Complexes. *ACS Catalysis* **2018**, 2021-2029.
64. Johnson, F. P. A.; George, M. W.; Hartl, F.; Turner, J. J., Electrocatalytic Reduction of CO<sub>2</sub> Using the Complexes [Re(bpy)(CO)<sub>3</sub>L]<sup>n</sup> (n = +1, L = P(OEt)<sub>3</sub>, CH<sub>3</sub>CN; n = 0, L = Cl<sup>-</sup>, Otf<sup>-</sup>; bpy = 2,2'-Bipyridine; Otf<sup>-</sup> = CF<sub>3</sub>SO<sub>3</sub>) as Catalyst Precursors: Infrared Spectroelectrochemical Investigation. *Organometallics* **1996**, *15* (15), 3374-3387.
65. Stor, G. J.; Hartl, F.; van Outersterp, J. W. M.; Stufkens, D. J., Spectroelectrochemical (IR, UV/Vis) Determination of the Reduction Pathways for a Series of [Re(CO)<sub>3</sub>(αpha-

- diimine)L']<sup>0/+</sup> (L' = Halide, OTf<sup>-</sup>, THF, MeCN, n-PrCN, PPh<sub>3</sub>, P(OMe)<sub>3</sub>) Complexes. *Organometallics* **1995**, *14* (3), 1115-1131.
66. Sinopoli, A.; La Porte, N. T.; Martinez, J. F.; Wasielewski, M. R.; Sohail, M., Manganese carbonyl complexes for CO<sub>2</sub> reduction. *Coordination Chemistry Reviews* **2018**, *365*, 60-74.
67. Riplinger, C.; Carter, E. A., Influence of Weak Brønsted Acids on Electrocatalytic CO<sub>2</sub> Reduction by Manganese and Rhenium Bipyridine Catalysts. *ACS Catalysis* **2015**, *5* (2), 900-908.
68. Riplinger, C.; Sampson, M. D.; Ritzmann, A. M.; Kubiak, C. P.; Carter, E. A., Mechanistic Contrasts between Manganese and Rhenium Bipyridine Electrocatalysts for the Reduction of Carbon Dioxide. *Journal of the American Chemical Society* **2014**, *136* (46), 16285-16298.
69. Bourrez, M.; Orio, M.; Molton, F.; Vezin, H.; Duboc, C.; Deronzier, A.; Chardon-Noblat, S., Pulsed-EPR Evidence of a Manganese(II) Hydroxycarbonyl Intermediate in the Electrocatalytic Reduction of Carbon Dioxide by a Manganese Bipyridyl Derivative. *Angewandte Chemie International Edition* **2014**, *53* (1), 240-243.
70. Machan, C. W.; Sampson, M. D.; Chabolla, S. A.; Dang, T.; Kubiak, C. P., Developing a Mechanistic Understanding of Molecular Electrocatalysts for CO<sub>2</sub> Reduction using Infrared Spectroelectrochemistry. *Organometallics* **2014**, 140421073230005.
71. Mark, R.; Felix N Castellano, a.; Meyer, G. J., Photodriven Electron and Energy Transfer from Copper Phenanthroline Excited States. *Inorg. Chem.* **1996**, *35* (22), 6406-6412.
72. Tamaki, Y.; Koike, K.; Morimoto, T.; Yamazaki, Y.; Ishitani, O., Red-Light-Driven Photocatalytic Reduction of CO<sub>2</sub> using Os(II)–Re(I) Supramolecular Complexes. *Inorg. Chem.* **2013**, 131001161818006.
73. Neumann, R.; Haviv, E.; Shimon, L., Photochemical Reduction of CO<sub>2</sub> with Visible Light using a Polyoxometalate as Photoreductant. *Chemistry: A European Journal* **2016**.
74. Fujitsuka, M.; Kim, S. S.; Lu, C.; Tojo, S.; Majima, T., Intermolecular and Intramolecular Electron Transfer Processes from Excited Naphthalene Diimide Radical Anions. *The Journal of Physical Chemistry B* **2015**, *119* (24), 7275-7282.
75. Lu, C.; Fujitsuka, M.; Sugimoto, A.; Majima, T., Unprecedented Intramolecular Electron Transfer from Excited Perylenediimide Radical Anion. *J. Phys. Chem. C* **2016**, *120* (23), 12734-12741.
76. Gatti, T.; Cavigli, P.; Zangrando, E.; Iengo, E.; Chiorboli, C.; Indelli, M. T., Improving the Efficiency of the Photoinduced Charge-Separation Process in a Rhenium(I)–Zinc Porphyrin Dyad by Simple Chemical Functionalization. *Inorganic Chemistry* **2013**, *52* (6), 3190-3197.
77. Wasielewski, M. R.; Martinez, J.; La Porte, N. T.; Mauck, C. M., Photo-driven Electron Transfer from the Highly Reducing Excited State of Naphthalene Diimide Radical Anion to a CO<sub>2</sub> Reduction Catalyst within a Molecular Triad. *Faraday Discussions* **2016**.
78. Agnew, D. W.; Sampson, M. D.; Moore, C. E.; Rheingold, A. L.; Kubiak, C. P.; Figueroa, J. S., Electrochemical Properties and CO<sub>2</sub>-Reduction Ability of m-Terphenyl Isocyanide Supported Manganese Tricarbonyl Complexes. *Inorg Chem* **2016**, *55* (23), 12400-12408.
79. Connelly, N. G.; Geiger, W. E., Chemical Redox Agents for Organometallic Chemistry. *Chemical Reviews* **1996**, *96* (2), 877-910.
80. Young, R. M.; Dyar, S. M.; Barnes, J. C.; Juriček, M.; Stoddart, J. F.; Co, D. T.; Wasielewski, M. R., Ultrafast Conformational Dynamics of Electron Transfer in ExBox4+⊂Perylene. *The Journal of Physical Chemistry A* **2013**, *117* (47), 12438-12448.

81. Horwitz, N. E.; Phelan, B. T.; Nelson, J. N.; Krzyaniak, M. D.; Wasielewski, M. R., Picosecond Control of Photogenerated Radical Pair Lifetimes Using a Stable Third Radical. *The Journal of Physical Chemistry A* **2016**, *120* (18), 2841-2853.
82. Greenfield, S. R.; Wasielewski, M. R., Optical parametric amplification of femtosecond pulses tunable from the blue to the infrared with microjoule energies. *Appl. Opt.* **1995**, *34* (15), 2688-2691.
83. Shao, Y.; Gan, Z.; Epifanovsky, E.; Gilbert, A. T. B.; Wormit, M.; Kussmann, J.; Lange, A. W.; Behn, A.; Deng, J.; Feng, X.; Ghosh, D.; Goldey, M.; Horn, P. R.; Jacobson, L. D.; Kaliman, I.; Khaliullin, R. Z.; Kuś, T.; Landau, A.; Liu, J.; Proynov, E. I.; Rhee, Y. M.; Richard, R. M.; Rohrdanz, M. A.; Steele, R. P.; Sundstrom, E. J.; Woodcock, H. L.; Zimmerman, P. M.; Zuev, D.; Albrecht, B.; Alguire, E.; Austin, B.; Beran, G. J. O.; Bernard, Y. A.; Berquist, E.; Brandhorst, K.; Bravaya, K. B.; Brown, S. T.; Casanova, D.; Chang, C.-M.; Chen, Y.; Chien, S. H.; Closser, K. D.; Crittenden, D. L.; Diedenhofen, M.; DiStasio, R. A.; Do, H.; Dutoi, A. D.; Edgar, R. G.; Fatehi, S.; Fusti-Molnar, L.; Ghysels, A.; Golubeva-Zadorozhnaya, A.; Gomes, J.; Hanson-Heine, M. W. D.; Harbach, P. H. P.; Hauser, A. W.; Hohenstein, E. G.; Holden, Z. C.; Jagau, T.-C.; Ji, H.; Kaduk, B.; Khistyayev, K.; Kim, J.; Kim, J.; King, R. A.; Klunzinger, P.; Kosenkov, D.; Kowalczyk, T.; Krauter, C. M.; Lao, K. U.; Laurent, A. D.; Lawler, K. V.; Levchenko, S. V.; Lin, C. Y.; Liu, F.; Livshits, E.; Lochan, R. C.; Luenser, A.; Manohar, P.; Manzer, S. F.; Mao, S.-P.; Mardirossian, N.; Marenich, A. V.; Maurer, S. A.; Mayhall, N. J.; Neuscamman, E.; Oana, C. M.; Olivares-Amaya, R.; O'Neill, D. P.; Parkhill, J. A.; Perrine, T. M.; Peverati, R.; Prociuk, A.; Rehn, D. R.; Rosta, E.; Russ, N. J.; Sharada, S. M.; Sharma, S.; Small, D. W.; Sodt, A.; Stein, T.; Stück, D.; Su, Y.-C.; Thom, A. J. W.; Tsuchimochi, T.; Vanovschi, V.; Vogt, L.; Vydrov, O.; Wang, T.; Watson, M. A.; Wenzel, J.; White, A.; Williams, C. F.; Yang, J.; Yeganeh, S.; Yost, S. R.; You, Z.-Q.; Zhang, I. Y.; Zhang, X.; Zhao, Y.; Brooks, B. R.; Chan, G. K. L.; Chipman, D. M.; Cramer, C. J.; Goddard, W. A.; Gordon, M. S.; Hehre, W. J.; Klamt, A.; Schaefer, H. F.; Schmidt, M. W.; Sherrill, C. D.; Truhlar, D. G.; Warshel, A.; Xu, X.; Aspuru-Guzik, A.; Baer, R.; Bell, A. T.; Besley, N. A.; Chai, J.-D.; Dreuw, A.; Dunietz, B. D.; Furlani, T. R.; Gwaltney, S. R.; Hsu, C.-P.; Jung, Y.; Kong, J.; Lambrecht, D. S.; Liang, W.; Ochsenfeld, C.; Rassolov, V. A.; Slipchenko, L. V.; Subotnik, J. E.; Van Voorhis, T.; Herbert, J. M.; Krylov, A. I.; Gill, P. M. W.; Head-Gordon, M., Advances in molecular quantum chemistry contained in the Q-Chem 4 program package. *Molecular Physics* **2015**, *113* (2), 184-215.
84. Bühl, M.; Reimann, C.; Pantazis, D. A.; Bredow, T.; Neese, F., Geometries of Third-Row Transition-Metal Complexes from Density-Functional Theory. *J. Chem. Theory Comput.* **2008**, *4* (9), 1449-1459.
85. Becke, A. D., Density-Functional Thermochemistry. III. The Role of Exact Exchange. *Journal of chemical physics* **1993**, *98* (7), 5648-5652.
86. Gaussian 09 Revision D.01; Frisch, M. J. T., G. W.; Schlegel, H. B.; Scuseria, G. E.; Robb, M. A.; Cheeseman, J. R.; Scalmani, G.; Barone, V.; Mennucci, B.; Petersson, G. A.; Nakatsuji, H.; Caricato, M.; Li, X.; Hratchian, H. P.; Izmaylov, A. F.; Bloino, J.; Zheng, G.; Sonnenberg, J. L.; Hada, M.; Ehara, M.; Toyota, K.; Fukuda, R.; Hasegawa, J.; Ishida, M.; Nakajima, T.; Honda, Y.; Kitao, O.; Nakai, H.; Vreven, T.; Montgomery, J. A., Jr.; Peralta, J. E.; Ogliaro, F.; Bearpark, M.; Heyd, J. J.; Brothers, E.; Kudin, K. N.; Staroverov, V. N.; Kobayashi, R.; Normand, J.; Raghavachari, K.; Rendell, A.; Burant, J. C.; Iyengar, S. S.; Tomasi, J.; Cossi, M.; Rega, N.; Millam, N. J.; Klene, M.; Knox, J. E.; Cross, J. B.; Bakken, V.; Adamo, C.; Jaramillo, J.; Gomperts, R.; Stratmann, R. E.; Yazyev, O.; Austin, A. J.; Cammi, R.; Pomelli, C.; Ochterski, J. W.; Martin,

R. L.; Morokuma, K.; Zakrzewski, V. G.; Voth, G. A.; Salvador, P.; Dannenberg, J. J.; Dapprich, S.; Daniels, A. D.; Farkas, Ö.; Foresman, J. B.; Ortiz, J. V.; Cioslowski, J.; Fox, D. J. Gaussian, Inc., Wallingford CT, 2009.

87. Weigend, F.; Ahlrichs, R., Balanced Basis Sets of Split Valence, Triple Zeta Valence and Quadruple Zeta Valence Quality for H to Rn: Design and Assessment of Accuracy. *Physical Chemistry Chemical Physics* **2005**, *7* (18), 3297-3305.

88. Marenich, A. V.; Cramer, C. J.; Truhlar, D. G., Universal Solvation Model Based on Solute Electron Density and on a Continuum Model of the Solvent Defined by the Bulk Dielectric Constant and Atomic Surface Tensions. *Journal of Physical Chemistry B* **2009**, *113* (18), 6378-6396.

89. Improta, R.; Barone, V.; Scalmani, G.; Frisch, M. J., A State-Specific Polarizable Continuum Model Time Dependent Density Functional Theory Method for Excited State Calculations in Solution. *Journal of chemical physics* **2006**, *125* (5), 054103.

90. Improta, R.; Scalmani, G.; Frisch, M. J.; Barone, V., Toward Effective and Reliable Fluorescence Energies in Solution by a New State Specific Polarizable Continuum Model Time Dependent Density Functional Theory Approach. *Journal of chemical physics* **2007**, *127* (7), 074504.

91. Scalmani, G.; Frisch, M. J., Continuous Surface Charge Polarizable Continuum Models of Solvation. I. General Formalism. *Journal of chemical physics* **2010**, *132* (11), 114110.

92. Bauernschmitt, R.; Ahlrichs, R., Treatment of Electronic Excitations Within the Adiabatic Approximation of Time Dependent Density Functional Theory. *Chemical Physics Letters* **1996**, *256* (4), 454-464.

93. Casida, M. E.; Jamorski, C.; Casida, K. C.; Salahub, D. R., Molecular Excitation Energies to High-Lying Bound States from Time-Dependent Density-Functional Response Theory: Characterization and Correction of the Time-Dependent Local Density Approximation Ionization Threshold. *Journal of chemical physics* **1998**, *108* (11), 4439-4449.

94. Furche, F.; Ahlrichs, R., Adiabatic Time-Dependent Density Functional Methods for Excited State Properties. *Journal of chemical physics* **2002**, *117* (16), 7433-7447.

95. Scalmani, G.; Frisch, M. J.; Mennucci, B.; Tomasi, J.; Cammi, R.; Barone, V., Geometries and Properties of Excited States in the Gas Phase and in Solution: Theory and Application of a Time-Dependent Density Functional Theory Polarizable Continuum Model. *Journal of chemical physics* **2006**, *124* (9), 094107.

96. Stratmann, R. E.; Scuseria, G. E.; Frisch, M. J., An Efficient Implementation of Time-Dependent Density-Functional Theory for the Calculation of Excitation Energies of Large Molecules. *Journal of Chemical Physics* **1998**, *109* (19), 8218-8224.

97. Van Caillie, C.; Amos, R. D., Geometric Derivatives of Excitation Energies Using SCF and DFT. *Chemical physics letters* **1999**, *308* (3), 249-255.

98. Van Caillie, C.; Amos, R. D., Geometric Derivatives of Density Functional Theory Excitation Energies Using Gradient-Corrected Functionals. *Chemical Physics Letters* **2000**, *317* (1), 159-164.

99. Barone, V.; Bloino, J.; Biczysko, M., Vibrationally-Resolved Electronic Spectra in GAUSSIAN 09. *September* **2009**, *2*, 2009.

100. Burkholder, C.; Dolbier, W. R.; Medebielle, M., Reaction of the 2(bromodifluoromethyl)benzoxazole with tetrakis(dimethylamino)ethylene (TDAE) in the

presence of aldehydes. A convenient synthesis of 2-(difluoromethyl)benzoxazole alcohols. *Tetrahedron Letters* **1997**, 38 (5), 821-824.

101. Fujita, E.; Muckerman, J. T., Why Is Re–Re Bond Formation/Cleavage in [Re(bpy)(CO)<sub>3</sub>]<sub>2</sub> Different from That in [Re(CO)<sub>5</sub>]<sub>2</sub>? Experimental and Theoretical Studies on the Dimers and Fragments. *Inorganic Chemistry* **2004**, 43 (24), 7636-7647.

102. Smieja, J. M.; Kubiak, C. P., Re(bipy-tBu)(CO)<sub>3</sub>Cl–improved Catalytic Activity for Reduction of Carbon Dioxide: IR-Spectroelectrochemical and Mechanistic Studies. *Inorg. Chem.* **2010**, 49 (20), 9283-9289.

103. Johnson, F. P. A.; George, M. W.; Hartl, F.; Turner, J. J., Electrocatalytic Reduction of CO<sub>2</sub> Using the Complexes [Re(bpy)(CO)<sub>3</sub>L]<sup>n</sup> (n = +1, L = P(OEt)<sub>3</sub>, CH<sub>3</sub>CN; n = 0, L = Cl<sup>-</sup>, Otf<sup>-</sup>; bpy = 2,2'-Bipyridine; Otf<sup>-</sup> = CF<sub>3</sub>SO<sub>3</sub>) as Catalyst Precursors: Infrared Spectroelectrochemical Investigation. *Organometallics* **1996**, 15 (15), 3374-3387.

104. Hayashi, Y.; Kita, S.; Brunschwig, B. S.; Fujita, E., Involvement of a Binuclear Species with the Re–C(O)O–Re Moiety in CO<sub>2</sub> Reduction Catalyzed by Tricarbonyl Rhenium(I) Complexes with Diimine Ligands: Strikingly Slow Formation of the Re–Re and Re–C(O)O–Re Species from Re(dmb)(CO)<sub>3</sub>S (dmb = 4,4'-Dimethyl-2,2'-bipyridine, S = Solvent). *Journal of the American Chemical Society* **2003**, 125 (39), 11976-11987.

105. Schneider, J.; Vuong, K. Q.; Calladine, J. A.; Sun, X.-Z.; Whitwood, A. C.; George, M. W.; Perutz, R. N., Photochemistry and Photophysics of a Pd(II) Metalloporphyrin: Re(I) Tricarbonyl Bipyridine Molecular Dyad and its Activity Toward the Photoreduction of CO<sub>2</sub> to CO. *Inorg. Chem.* **2013**, 50 (23), 11877-11889.

106. El Nahhas, A.; Consani, C.; Blanco-Rodríguez, A. M.; Lancaster, K. M.; Braem, O.; Cannizzo, A.; Towrie, M.; Clark, I. P.; Zálíš, S.; Chergui, M.; Antonín Vlček, Jr., Ultrafast Excited-State Dynamics of Rhenium(I) Photosensitizers [Re(Cl)(CO)<sub>3</sub>(N,N)] and [Re(imidazole)(CO)<sub>3</sub>(N,N)]<sup>+</sup>: Diimine Effects. *Inorg. Chem.* **2011**, 50 (7), 2932-2943.

107. Vlček, A., Ultrafast Excited-State Processes in Re(I) Carbonyl-Diimine Complexes: From Excitation to Photochemistry. In *Photophysics of Organometallics*, Springer Berlin Heidelberg: Berlin, Heidelberg, 2009; Vol. 29, pp 115-158.

108. Blanco-Rodríguez, A. M.; Towrie, M.; Sýkora, J.; Zálíš, S.; Antonín Vlček, Jr., Photoinduced Intramolecular Tryptophan Oxidation and Excited-State Behavior of [Re(L-AA)(CO)<sub>3</sub>( $\alpha$ -diimine)]<sup>+</sup> (L = Pyridine or Imidazole, AA = Tryptophan, Tyrosine, Phenylalanine). *Inorg Chem* **2011**, 50 (13), 6122-6134.

109. Robb, M. J.; Newton, B.; Fors, B. P.; Hawker, C. J., One-Step Synthesis of Unsymmetrical N-Alkyl-N'-aryl Perylene Diimides. *The Journal of Organic Chemistry* **2014**, 79 (13), 6360-6365.

110. Ahrens, M. J.; Kelley, R. F.; Dance, Z. E. X.; Wasielewski, M. R., Photoinduced charge separation in self-assembled cofacial pentamers of zinc-5,10,15,20-tetrakis(perylene-diimide)porphyrin. *Physical Chemistry Chemical Physics* **2007**, 9 (12), 1469-1478.

111. Egbe, D. A. M.; Amer, A. M.; Klemm, E., Improved synthesis of 4-bromo-2,2'-bipyridine: a start material for low-molecular-weight model compounds. *Designed Monomers and Polymers* **2001**, 4 (2), 169-175.

112. Zalas, M.; Gierczyk, B.; Cegłowski, M.; Schroeder, G., Synthesis of new dendritic antenna-like polypyridine ligands. *Chemical Papers* **2015**, 66 (8), 733-740.

113. The Mathworks, I. *MATLAB*, Natick, Massachusetts, United States.

114. Henry, E. R.; Hofrichter, J., [8] Singular value decomposition: Application to analysis of experimental data. In *Methods in Enzymology*, Academic Press: 1992; Vol. Volume 210, pp 129-192.
115. Berberan-Santos, M. N.; Martinho, J. M. G., The integration of kinetic rate equations by matrix methods. *Journal of Chemical Education* **1990**, *67* (5), 375.
116. Kumar, B.; Llorente, M.; Froehlich, J.; Dang, T.; Sathrum, A.; Kubiak, C. P., Photochemical and Photoelectrochemical Reduction of CO<sub>2</sub>. *Annu. Rev. Phys. Chem.* **2012**, *63* (1), 541-569.
117. Appel, A. M.; Bercaw, J. E.; Bocarsly, A. B.; Dobbek, H.; Dubois, D. L.; Dupuis, M.; Ferry, J. G.; Fujita, E.; Hille, R.; Kenis, P. J. A.; Kerfeld, C. A.; Morris, R. H.; Peden, C. H. F.; Portis, A. R.; Ragsdale, S. W.; Rauchfuss, T. B.; Reek, J. N. H.; Seefeldt, L. C.; Thauer, R. K.; Waldrop, G. L., Frontiers, Opportunities, and Challenges in Biochemical and Chemical Catalysis of CO<sub>2</sub> Fixation. *Chem. Rev.* **2013**, *113* (8), 6621-6658.
118. Ghosh, I.; Ghosh, T.; Bardagi, J. I.; Koenig, B., Reduction of aryl halides by consecutive visible light-induced electron transfer processes. *Science* **2014**, *346* (6210), 725-728.
119. Ghosh, I.; Marzo, L.; Das, A.; Shaikh, R.; Koenig, B., Visible Light Mediated Photoredox Catalytic Arylation Reactions. *Acc. Chem. Res.* **2016**, *49* (8), 1566-1577.
120. La Porte, N. T.; Martinez, J.; Phelan, B. T.; Mauck, C. M.; Young, R. M.; Wasielewski, M. R., Electron-transfer sensitization of a CO<sub>2</sub> reduction catalyst with red and near-infrared light using rylene diimide radical anions and dianions. *submitted* **2016**.
121. The Mathworks, I. *MATLAB Release 2016a*, 2016a; The Mathworks, Inc.: Natick, Massachusetts, United States, 2016.
122. Zambis, T. M.; Parkhurst, L. J.; Gallup, G. A., A matrix series method for the integration of rate equations in a reaction network. An alternative to Runge-Kutta methods. *Computers & Chemistry* **1989**, *13* (3), 165-171.
123. Wu, Y.; Young, R. M.; Frascioni, M.; Schneebeli, S. T.; Spent, P.; Gardner, D. M.; Brown, K. E.; Würthner, F.; Stoddart, J. F.; Wasielewski, M. R., Ultrafast Photoinduced Symmetry-Breaking Charge Separation and Electron Sharing in Perylene diimide Molecular Triangles. *Journal of the American Chemical Society* **2015**, *137* (41), 13236-13239.
124. Vanysek, P., Reduction and Oxidation Potentials for Certain Ion Radicals. In *CRC Handbook of Chemistry and Physics*, 94 ed.; Haynes, W. M., Ed. CRC Press: Boca Raton, FL, 1999; pp 5-90.
125. Shida, T., *Electronic Absorption Spectra of Radical Ions*. Elsevier: New York, 1988.
126. Transient absorption experiments were also performed at  $\lambda_{ex} = 700$  nm and gave identical kinetic results, but with reduced signal-to-noise ratios consistent with the lower optical density of the solutions at 700 nm.
127. Fujita, E.; Muckerman, J. T., Why Is Re–Re Bond Formation/Cleavage in [Re(bpy)(CO)<sub>3</sub>] <sub>2</sub> Different from That in [Re(CO)<sub>5</sub>] <sub>2</sub>? Experimental and Theoretical Studies on the Dimers and Fragments. *Inorg. Chem.* **2004**, *43* (24), 7636-7647.
128. Machan, C. W.; Sampson, M. D.; Chabolla, S. A.; Dang, T.; Kubiak, C. P., Developing a Mechanistic Understanding of Molecular Electrocatalysts for CO<sub>2</sub> Reduction using Infrared Spectroelectrochemistry. *Organometallics* **2014**, *33* 4550–4559.
129. Carmieli, R.; Mi, Q. X.; Ricks, A. B.; Giacobbe, E. M.; Mickley, S. M.; Wasielewski, M. R., Direct Measurement of Photoinduced Charge Separation Distances in Donor-Acceptor

Systems for Artificial Photosynthesis Using OOP-ESEEM. *J. Am. Chem. Soc.* **2009**, *131* (24), 8372-8373.

130. Gust, D.; Moore, T. A.; Moore, A. L., Mimicking Photosynthetic Solar Energy Transduction. *Accounts of Chemical Research* **2001**, *34* (1), 40-48.

131. Mirkovic, T.; Ostroumov, E. E.; Anna, J. M.; van Grondelle, R.; Govindjee; Scholes, G. D., Light Absorption and Energy Transfer in the Antenna Complexes of Photosynthetic Organisms. *Chemical Reviews* **2017**, *117* (2), 249-293.

132. Su, J.; Vayssieres, L., A Place in the Sun for Artificial Photosynthesis? *ACS Energy Letters* **2016**, *1* (1), 121-135.

133. Alstrum-Acevedo, J. H.; Brenaman, M. K.; Meyer, T. J., Chemical Approaches to Artificial Photosynthesis 2. *Inorganic Chemistry* **2005**, *44*, 6802-6827.

134. Meyer, T. J., Excited-State Electron Transfer. In *Progress in Inorganic Chemistry*, John Wiley & Sons, Inc.: 2007; pp 389-440.

135. Ward, M. D., Photo-induced electron and energy transfer in non-covalently bonded supramolecular assemblies. *Chemical Society Reviews* **1997**, *26* (5), 365-375.

136. Wasielewski, M. R., Photoinduced electron transfer in supramolecular systems for artificial photosynthesis. *Chem. Rev.* **1992**, *92*, 435-461.

137. Fajer, J.; Davis, M. S.; Forman, A.; Klimov, V. V.; Dolan, E.; Ke, B., Primary electron acceptors in plant photosynthesis. *Journal of the American Chemical Society* **1980**, *102* (23), 7143-7145.

138. Hammarstrom, L.; Styring, S., Proton-coupled electron transfer of tyrosines in Photosystem II and model systems for artificial photosynthesis: the role of a redox-active link between catalyst and photosensitizer. *Energy & Environmental Science* **2011**, *4* (7), 2379-2388.

139. Liu, L.-N., Distribution and dynamics of electron transport complexes in cyanobacterial thylakoid membranes. *Biochimica et Biophysica Acta (BBA) - Bioenergetics* **2016**, *1857* (3), 256-265.

140. Arias-Rotondo, D. M.; McCusker, J. K., The photophysics of photoredox catalysis: a roadmap for catalyst design. *Chemical Society Reviews* **2016**, *45* (21), 5803-5820.

141. Pellegrin, Y.; Odobel, F., Sacrificial electron donor reagents for solar fuel production. *Comptes Rendus Chimie* **2017**, *20* (3), 283-295.

142. Kiyosawa, K.; Shiraishi, N.; Shimada, T.; Masui, D.; Tachibana, H.; Takagi, S.; Ishitani, O.; Tryk, D. A.; Inoue, H., Electron Transfer from the Porphyrin S<sub>2</sub> State in a Zinc Porphyrin-Rhenium Bipyridyl Dyad having Carbon Dioxide Reduction Activity. *The Journal of Physical Chemistry C* **2009**, *113* (27), 11667-11673.

143. Mukherjee, A.; Kokhan, O.; Huang, J.; Niklas, J.; Chen, L. X.; Tiede, D. M.; Mulfort, K. L., Detection of a charge-separated catalyst precursor state in a linked photosensitizer-catalyst assembly. *Physical Chemistry Chemical Physics* **2013**, *15* (48), 21070-21076.

144. Bartelmess, J.; Francis, A. J.; El Roz, K. A.; Castellano, F. N.; Weare, W. W.; Sommer, R. D., Light-Driven Hydrogen Evolution by BODIPY-Sensitized Cobaloxime Catalysts. *Inorg. Chem.* **2014**, *53* (9), 4527-4534.

145. Gabriellsson, A.; Lindsay Smith, J. R.; Perutz, R. N., Remote site photosubstitution in metalloporphyrin-rhenium tricarbonylbipyridine assemblies: photo-reactions of molecules with very short lived excited states. *Dalton Transactions* **2008**, (32), 4259-4269.

146. Windle, C. D.; Campian, M. V.; Duhme-Klair, A.-K.; Gibson, E. A.; Perutz, R. N.; Schneider, J., CO<sub>2</sub> photoreduction with long-wavelength light: dyads and monomers of zinc porphyrin and rhenium bipyridine. *Chemical Communications* **2012**, 48 (66), 8189-8191.
147. Windle, C. D.; George, M. W.; Perutz, R. N.; Summers, P. A.; Sun, X. Z.; Whitwood, A. C., Comparison of rhenium-porphyrin dyads for CO<sub>2</sub> photoreduction: photocatalytic studies and charge separation dynamics studied by time-resolved IR spectroscopy. *Chemical Science* **2015**, 6 (12), 6847-6864.
148. Liu, X.; Liu, J.; Pan, J.; Chen, R.; Na, Y.; Gao, W.; Sun, L., A novel ruthenium(II) tris(bipyridine)-zinc porphyrin-rhenium carbonyl triad: synthesis and optical properties. *Tetrahedron* **2006**, 62 (15), 3674-3680.
149. Gabrielsson, A.; Hartl, F.; Smith, J. R. L.; Perutz, R. N., Photo-induced ligand substitution at a remote site via electron transfer in a porphyrin-appended rhenium carbonyl supermolecule. *Chemical Communications* **2002**, (9), 950-951.
150. Morimoto, T.; Nakajima, T.; Sawa, S.; Nakanishi, R.; Imori, D.; Ishitani, O., CO<sub>2</sub> Capture by a Rhenium(I) Complex with the Aid of Triethanolamine. *Journal of the American Chemical Society* **2013**, 135 (45), 16825-16828.
151. Gholamkhash, B.; Mametsuka, H.; Koike, K.; Tanabe, T.; Furue, M.; Ishitani, O., Architecture of Supramolecular Metal Complexes for Photocatalytic CO<sub>2</sub> Reduction: Ruthenium-Rhenium Bi- and Tetranuclear Complexes. *Inorganic Chemistry* **2005**, 44 (7), 2326-2336.
152. Tamaki, Y.; Koike, K.; Morimoto, T.; Ishitani, O., Substantial improvement in the efficiency and durability of a photocatalyst for carbon dioxide reduction using a benzoimidazole derivative as an electron donor. *J. Catal.* **2013**, 304, 22-28.
153. Koike, K.; Naito, S.; Sato, S.; Tamaki, Y.; Ishitani, O., Architecture of supramolecular metal complexes for photocatalytic CO<sub>2</sub> reduction: III: Effects of length of alkyl chain connecting photosensitizer to catalyst. *Journal of Photochemistry and Photobiology, A: Chemistry* **2009**, 207 (1), 109-114.
154. Sato, S.; Koike, K.; Inoue, H.; Ishitani, O., Highly efficient supramolecular photocatalysts for CO<sub>2</sub> reduction using visible light. *Photochemical & Photobiological Sciences* **2007**, 6 (4), 454-461.
155. La Porte, N. T.; Martinez, J. F.; Hedström, S.; Rudshiteyn, B.; Phelan, B. T.; Mauck, C. M.; Young, R. M.; Batista, V. S.; Wasielewski, M. R., Photoinduced electron transfer from rylenediimide radical anions and dianions to Re(bpy)(CO)<sub>3</sub> using red and near-infrared light. *Chemical Science* **2017**, 8 (5), 3821-3831.
156. Wasielewski, M. R.; Martinez, J.; La Porte, N. T.; Mauck, C. M., Photo-driven Electron Transfer from the Highly Reducing Excited State of Naphthalene Diimide Radical Anion to a CO<sub>2</sub> Reduction Catalyst within a Molecular Triad. *Faraday Discussions* **2017**, 198, 235-249.
157. Riplinger, C.; Sampson, M. D.; Ritzmann, A. M.; Kubiak, C. P.; Carter, E. A., Mechanistic Contrasts between Manganese and Rhenium Bipyridine Electrocatalysts for the Reduction of Carbon Dioxide. *J. Am. Chem. Soc.* **2014**, 136, 16285-16298.
158. Agarwal, J.; Fujita, E.; Schaefer, H. F.; Muckerman, J. T., Mechanisms for CO Production from CO<sub>2</sub> Using Reduced Rhenium Tricarbonyl Catalysts. *Journal of the American Chemical Society* **2012**, 134 (11), 5180-5186.
159. Greenfield, S. R.; Wasielewski, M. R., Near-transform-limited visible and near-IR fs pulses from OPA using Type II B-barium borate. *Optics Letters* **1995**, 20 (12), 1394-1396.

160. Shao, Y.; Gan, Z.; Epifanovsky, E.; Gilbert, A. T.; Wormit, M.; Kussmann, J.; Lange, A. W.; Behn, A.; Deng, J.; Feng, X., Advances in Molecular Quantum Chemistry Contained in the Q-Chem 4 Program Package. *Molecular Physics* **2015**, *113* (2), 184-215.
161. Cordaro, J. G.; McCusker, J. K.; Bergman, R. G., Synthesis of mono-substituted 2,2'-bipyridines. *Chemical Communications* **2002**, (14), 1496-1497.
162. Ishiyama, T.; Murata, M.; Miyaura, N., Palladium(0)-Catalyzed Cross-Coupling Reaction of Alkoxydiboron with Haloarenes: A Direct Procedure for Arylboronic Esters. *The Journal of Organic Chemistry* **1995**, *60* (23), 7508-7510.
163. Roffia, S.; Casadei, R.; Paolucci, F.; Paradisi, C.; Bignozzi, C. A.; Scandola, F., Supramolecular electrochemistry: Redox series of cyano-bridged polynuclear bipyridine ruthenium(II) complexes. *Journal of Electroanalytical Chemistry and Interfacial Electrochemistry* **1991**, *302* (1), 157-171.
164. Keith, J. A.; Grice, K. A.; Kubiak, C. P.; Carter, E. A., Elucidation of the Selectivity of Proton-Dependent Electrocatalytic CO<sub>2</sub> Reduction by fac-Re(bpy)(CO)<sub>3</sub>Cl. *Journal of the American Chemical Society* **2013**, *135* (42), 15823-15829.
165. Gennaro, A.; Isse, A. A.; Vianello, E., Solubility and electrochemical determination of CO<sub>2</sub> in some dipolar aprotic solvents. *Journal of Electroanalytical Chemistry and Interfacial Electrochemistry* **1990**, *289* (1), 203-215.
166. Smieja, J. M.; Benson, E. E.; Kumar, B.; Grice, K. A.; Seu, C. S.; Miller, A. J. M.; Mayer, J. M.; Kubiak, C. P., Kinetic and structural studies, origins of selectivity, and interfacial charge transfer in the artificial photosynthesis of CO. *Proc. Natl. Acad. Sci. U. S. A.* **2012**, *109* (39), 15646-15650, S15646/1-S15646/9.
167. Breikss, A. I.; Abruña, H. D., Electrochemical and mechanistic studies of Re(CO)<sub>3</sub>(dmbpy)Cl and their relation to the catalytic reduction of CO<sub>2</sub>. *Journal of Electroanalytical Chemistry and Interfacial Electrochemistry* **1986**, *201* (2), 347-358.
168. Hawecker, J.; Lehn, J.-M.; Ziessel, R., Efficient photochemical reduction of CO<sub>2</sub> to CO by visible light irradiation of systems containing Re(bipy)(CO)<sub>3</sub>X or Ru(bipy)<sub>3</sub><sup>2+</sup>-Co<sup>2+</sup> combinations as homogeneous catalysts. *Journal of the Chemical Society, Chemical Communications* **1983**, (9), 536-538.
169. Sullivan, B. P.; Bolinger, C. M.; Conrad, D.; Vining, W. J.; Meyer, T. J., One- and two-electron pathways in the electrocatalytic reduction of CO<sub>2</sub> by fac-Re(bpy)(CO)<sub>3</sub>Cl (bpy = 2,2'-bipyridine). *J. Chem. Soc., Chem. Commun.* **1985**, (20), 1414-1416.
170. Schneider, T. W.; Ertem, M. Z.; Muckerman, J. T.; Angeles-Boza, A. M., Mechanism of Photocatalytic Reduction of CO<sub>2</sub> by Re(bpy)(CO)<sub>3</sub>Cl from Differences in Carbon Isotope Discrimination. *ACS Catalysis* **2016**, *6* (8), 5473-5481.
171. Sampson, M. D.; Froehlich, J. D.; Smieja, J. M.; Benson, E. E.; Sharp, I. D.; Kubiak, C. P., Direct observation of the reduction of carbon dioxide by rhenium bipyridine catalysts. *Energy Environ. Sci.* **2013**, *6* (12), 3748-3755.
172. Grice, K. A.; Gu, N. X.; Sampson, M. D.; Kubiak, C. P., Carbon monoxide release catalysed by electron transfer: electrochemical and spectroscopic investigations of [Re(bpy-R)(CO)<sub>4</sub>](OTf) complexes relevant to CO<sub>2</sub> reduction. *Dalton Trans* **2013**, *42* (23), 8498-503.
173. Benson, E. E.; Sampson, M. D.; Grice, K. A.; Smieja, J. M.; Froehlich, J. D.; Friebel, D.; Keith, J. A.; Carter, E. A.; Nilsson, A.; Kubiak, C. P., The Electronic States of Rhenium Bipyridyl

Electrocatalysts for CO<sub>2</sub> Reduction as Revealed by X-ray Absorption Spectroscopy and Computational Quantum Chemistry. *Angew. Chem. Int. Ed.* **2013**, 52 (18), 4841-4844.

174. Takeda, H.; Koike, K.; Inoue, H.; Ishitani, O., Development of an Efficient Photocatalytic System for CO<sub>2</sub> Reduction Using Rhenium(I) Complexes Based on Mechanistic Studies. *Journal of the American Chemical Society* **2008**, 130 (6), 2023-2031.

175. Kotal, C.; Weber, M. A.; Ferraudi, G.; Geiger, D., A mechanistic investigation of the photoinduced reduction of carbon dioxide mediated by tricarbonylbromo(2,2'-bipyridine)rhenium(I). *Organometallics* **1985**, 4 (12), 2161-2166.

176. Kalyanasundaram, K., Luminescence and redox reactions of the metal-to-ligand charge-transfer excited state of tricarbonylchloro-(polypyridyl)rhenium(I) complexes. *Journal of the Chemical Society, Faraday Transactions 2: Molecular and Chemical Physics* **1986**, 82 (12), 2401-2415.

177. Hori, H.; P. A. Johnson, F.; Koike, K.; Takeuchi, K.; Ibusuki, T.; Ishitani, O., Photochemistry of [Re(bipy)(CO)<sub>3</sub>(PPh<sub>3</sub>)]<sup>+</sup> (bipy = 2,2'-bipyridine) in the presence of triethanolamine associated with photoreductive fixation of carbon dioxide: participation of a chain reaction mechanism. *J. Chem. Soc., Dalton Trans.* **1997**, (6), 1019-1024.

178. Kamire, R. J.; Majewski, M. B.; Hoffeditz, W. L.; Phelan, B. T.; Farha, O. K.; Hupp, J. T.; Wasielewski, M. R., Photodriven hydrogen evolution by molecular catalysts using Al<sub>2</sub>O<sub>3</sub>-protected perylene-3,4-dicarboximide on NiO electrodes. *Chem. Sci.* **2017**, 8 (1), 541-549.

179. MATLAB *MATLAB*, The MathWorks, Inc.: Natick, MA, 2013.

180. Henry, E. R.; Hofrichter, J., Singular value decomposition: Application to analysis of experimental data. In *Methods Enzymol.*, Ludwig Brand, M. L. J., Ed. Academic Press: 1992; Vol. Volume 210, pp 129-192.

181. Berberan-Santos, M. N.; Martinho, J. M. G., The integration of kinetic rate equations by matrix methods. *J. Chem. Educ.* **1990**, 67 (5), 375-9.

182. Wasielewski, M. R., Energy, Charge, and Spin Transport in Molecules and Self-Assembled Nanostructures Inspired by Photosynthesis. *The Journal of Organic Chemistry* **2006**, 71 (14), 5051-5066.

183. Wasielewski, M. R., Self-Assembly Strategies for Integrating Light Harvesting and Charge Separation in Artificial Photosynthetic Systems. *Accounts of Chemical Research* **2009**, 42 (12), 1910-1921.

184. Hawecker, J.; Lehn, J.-M.; Ziessel, R., Efficient photochemical reduction of CO<sub>2</sub> to CO by visible light irradiation of systems containing Re(bipy)(CO)<sub>3</sub>X or Ru(bipy)<sub>2</sub><sup>2+</sup>-Co<sup>2+</sup> combinations as homogeneous catalysts. *Journal of the Chemical Society, Chemical Communications* **1983**, (9), 536-538.

185. Chabolla, S. A.; Dellamary, E. A.; Machan, C. W.; Tezcan, F. A.; Kubiak, C. P., Combined steric and electronic effects of positional substitution on dimethyl-bipyridine rhenium(I)tricarbonyl electrocatalysts for the reduction of CO<sub>2</sub>. *Inorganica Chimica Acta* **2014**, 422, 109-113.

186. Frayne, L.; Das, N.; Paul, A.; Amirjalayer, S.; Buma, W. J.; Woutersen, S.; Long, C.; Vos, J. G.; Pryce, M. T., Photo- and Electrochemical Properties of a CO<sub>2</sub> Reducing Ruthenium–Rhenium Quaterpyridine-Based Catalyst. *ChemPhotoChem* **2018**.

187. Kuramochi, Y.; Ishitani, O.; Ishida, H., Reaction mechanisms of catalytic photochemical CO<sub>2</sub> reduction using Re(I) and Ru(II) complexes. *Coordination Chemistry Reviews* **2017**.

188. Koike, K.; Grills, D. C.; Tamaki, Y.; Fujita, E.; Okubo, K.; Yamazaki, Y.; Saigo, M.; Mukuta, T.; Onda, K.; Ishitani, O., Investigation of excited state, reductive quenching, and intramolecular electron transfer of Ru(ii)-Re(i) supramolecular photocatalysts for CO<sub>2</sub> reduction using time-resolved IR measurements. *Chemical Science* **2018**, *9* (11), 2961-2974.
189. Bingöl, B.; Durrell, A. C.; Keller, G. E.; Palmer, J. H.; Grubbs, R. H.; Gray, H. B., Electron Transfer Triggered by Optical Excitation of Phenothiazine-tris(meta-phenylene-ethynylene)-(tricarbonyl)(bpy)(py)rhenium(I). *The Journal of Physical Chemistry B* **2013**, *117* (16), 4177-4182.
190. La Porte, N. T.; Martinez, J. F.; Chaudhuri, S.; Hedström, S.; Batista, V. S.; Wasielewski, M. R., Photoexcited radical anion super-reductants for solar fuels catalysis. *Coordination Chemistry Reviews* **2018**, *361*, 98-119.
191. La Porte, N. T.; Martinez, J.; Hedstrom, S.; Rudshiteyn, B.; Phelan, B. T.; Mauck, C. M.; Young, R. M.; Batista, V. S.; Wasielewski, M. R., Photoinduced Electron Transfer from Rylenediimide Radical Anions and Dianions to Re(bpy)(CO)<sub>3</sub> using Red and Near-infrared Light. *Chemical Science* **2017**.
192. Miyaura, N.; Suzuki, A., Palladium-Catalyzed Cross-Coupling Reactions of Organoboron Compounds. *Chemical Reviews* **1995**, *95* (7), 2457-2483.
193. Takeda, H.; Koike, K.; Morimoto, T.; Inumaru, H.; Ishitani, O., Photochemistry and photocatalysis of rhenium(I) diimine complexes. In *Advances in Inorganic Chemistry*, Eldik, R. v.; Stochel, G., Eds. Academic Press: 2011; Vol. 63, pp 137-186.
194. Vlček, A., Ultrafast Excited-State Processes in Re(I) Carbonyl-Diimine Complexes: From Excitation to Photochemistry. In *Photophysics of Organometallics*, Lees, A. J., Ed. Springer Berlin Heidelberg: Berlin, Heidelberg, 2010; pp 115-158.
195. Koike, K.; Naito, S.; Sato, S.; Tamaki, Y.; Ishitani, O., Architecture of supramolecular metal complexes for photocatalytic CO<sub>2</sub> reduction: III: Effects of length of alkyl chain connecting photosensitizer to catalyst. *Journal of Photochemistry and Photobiology A: Chemistry* **2009**, *207* (1), 109-114.
196. Martinez, J. F.; La Porte, N. T.; Mauck, C. M.; Wasielewski, M. R., Photo-driven electron transfer from the highly reducing excited state of naphthalene diimide radical anion to a CO<sub>2</sub> reduction catalyst within a molecular triad. *Faraday Discuss.* **2017**, *198*, 235-249.
197. Martinez, J. F.; La Porte, N. T.; Wasielewski, M. R., Electron Transfer from Photoexcited Naphthalene Diimide Radical Anion to Electrocatalytically Active Re(bpy)(CO)<sub>3</sub>Cl in a Molecular Triad. *The Journal of Physical Chemistry C* **2018**, *122* (5), 2608-2617.
198. Hoffmann, R., Interaction of orbitals through space and through bonds. *Accounts of Chemical Research* **1971**, *4* (1), 1-9.
199. Constable, E. C.; Henney, R. P. G.; Leese, T. A.; Tocher, D. A., Cyclometallation reactions of 6-phenyl-2,2[prime or minute]-bipyridine; a potential C,N,N-donor analogue of 2,2[prime or minute]: 6[prime or minute],2[double prime]-terpyridine. Crystal and molecular structure of dichlorobis(6-phenyl-2,2[prime or minute]-bipyridine)ruthenium(II). *Journal of the Chemical Society, Dalton Transactions* **1990**, (2), 443-449.
200. Sampson, M. D.; Froehlich, J. D.; Smieja, J. M.; Benson, E. E.; Sharp, I. D.; Kubiak, C. P., Direct observation of the reduction of carbon dioxide by rhenium bipyridine catalysts. *Energy & Environmental Science* **2013**, *6* (12), 3748-3755.
201. Johnson, F. P. A.; George, M. W.; Hartl, F.; Turner, J. J., Electrocatalytic Reduction of CO<sub>2</sub> Using the Complexes [Re(bpy)(CO)<sub>3</sub>L]<sub>n</sub> (n = +1, L = P(OEt)<sub>3</sub>, CH<sub>3</sub>CN; n = 0, L = Cl<sup>-</sup>, Otf-

- ; bpy = 2,2'-Bipyridine; Otf- = CF<sub>3</sub>SO<sub>3</sub>) as Catalyst Precursors: Infrared Spectroelectrochemical Investigation. *Organometallics* **1996**, *15* (15), 3374-3387.
202. Grills, D. C.; Farrington, J. A.; Layne, B. H.; Lyman, S. V.; Mello, B. A.; Preses, J. M.; Wishart, J. F., Mechanism of the Formation of a Mn-Based CO<sub>2</sub> Reduction Catalyst Revealed by Pulse Radiolysis with Time-Resolved Infrared Detection. *Journal of the American Chemical Society* **2014**, *136* (15), 5563-5566.
203. Takeda, H.; Koizumi, H.; Okamoto, K.; Ishitani, O., Photocatalytic CO<sub>2</sub> reduction using a Mn complex as a catalyst. *Chemical Communications* **2014**, *50* (12), 1491-1493.
204. Machan, C. W.; Stanton, C. J.; Vandezande, J. E.; Majetich, G. F.; Schaefer, H. F.; Kubiak, C. P.; Agarwal, J., Electrocatalytic Reduction of Carbon Dioxide by Mn(CN)(2,2'-bipyridine)(CO)<sub>3</sub>: CN Coordination Alters Mechanism. *Inorganic Chemistry* **2015**, *54* (17), 8849-8856.
205. Sampson, M. D.; Nguyen, A. D.; Grice, K. A.; Moore, C. E.; Rheingold, A. L.; Kubiak, C. P., Manganese catalysts with bulky bipyridine ligands for the electrocatalytic reduction of carbon dioxide: eliminating dimerization and altering catalysis. *J Am Chem Soc* **2014**, *136* (14), 5460-71.
206. Stanbury, M.; Compain, J.-D.; Chardon-Noblat, S., Electro and photoreduction of CO<sub>2</sub> driven by manganese-carbonyl molecular catalysts. *Coordination Chemistry Reviews* **2018**, *361*, 120-137.
207. Sampson, M. D.; Kubiak, C. P., Manganese Electrocatalysts with Bulky Bipyridine Ligands: Utilizing Lewis Acids To Promote Carbon Dioxide Reduction at Low Overpotentials. *Journal of the American Chemical Society* **2016**, *138* (4), 1386-1393.
208. Cheung, P. L.; Machan, C. W.; Malkhasian, A. Y. S.; Agarwal, J.; Kubiak, C. P., Photocatalytic Reduction of Carbon Dioxide to CO and HCO<sub>2</sub>H Using fac-Mn(CN)(bpy)(CO)<sub>3</sub>. *Inorganic Chemistry* **2016**, *55* (6), 3192-3198.
209. Zhang, J.-X.; Hu, C.-Y.; Wang, W.; Wang, H.; Bian, Z.-Y., Visible light driven reduction of CO<sub>2</sub> catalyzed by an abundant manganese catalyst with zinc porphyrin photosensitizer. *Applied Catalysis A: General* **2016**, *522*, 145-151.
210. Wang, X.; Thiel, I.; Fedorov, A.; Coperet, C.; Mougél, V.; Fontecave, M., Site-isolated manganese carbonyl on bipyridine-functionalities of periodic mesoporous organosilicas: efficient CO<sub>2</sub> photoreduction and detection of key reaction intermediates. *Chemical Science* **2017**, *8* (12), 8204-8213.
211. Fei, H.; Sampson, M. D.; Lee, Y.; Kubiak, C. P.; Cohen, S. M., Photocatalytic CO<sub>2</sub> Reduction to Formate Using a Mn(I) Molecular Catalyst in a Robust Metal–Organic Framework. *Inorganic Chemistry* **2015**, *54* (14), 6821-6828.
212. Morimoto, T.; Tanabe, J.; Sakamoto, K.; Koike, K.; Ishitani, O., Selective H<sub>2</sub> and CO production with rhenium(I) biscarbonyl complexes as photocatalyst. *Res Chem Intermed* **2013**, *39* (1), 437-447.
213. Benson, E. E.; Sampson, M. D.; Grice, K. A.; Smieja, J. M.; Froehlich, J. D.; Friebel, D.; Keith, J. A.; Carter, E. A.; Nilsson, A.; Kubiak, C. P., The Electronic States of Rhenium Bipyridyl Electrocatalysts for CO<sub>2</sub> Reduction as Revealed by X-ray Absorption Spectroscopy and Computational Quantum Chemistry. *Angewandte Chemie International Edition* **2013**, *52* (18), 4841-4844.
214. Abdellah, M.; El-Zohry, A. M.; Antila, L. J.; Windle, C. D.; Reisner, E.; Hammarström, L., Time-Resolved IR Spectroscopy Reveals a Mechanism with TiO<sub>2</sub> as a Reversible Electron

- Acceptor in a TiO<sub>2</sub>–Re Catalyst System for CO<sub>2</sub> Photoreduction. *Journal of the American Chemical Society* **2017**, *139* (3), 1226-1232.
215. Ngo, K. T.; McKinnon, M.; Mahanti, B.; Narayanan, R.; Grills, D. C.; Ertem, M. Z.; Rochford, J., Turning on the Protonation-First Pathway for Electrocatalytic CO<sub>2</sub> Reduction by Manganese Bipyridyl Tricarbonyl Complexes. *Journal of the American Chemical Society* **2017**, *139* (7), 2604-2618.
216. Hedström, S.; Chaudhuri, S.; La Porte, N. T.; Rudshiteyn, B.; Martinez, J. F.; Wasielewski, M. R.; Batista, V. S., Thousandfold Enhancement of Photoreduction Lifetime in Re(bpy)(CO)<sub>3</sub> via Spin-Dependent Electron Transfer from a Perylenediimide Radical Anion Donor. *Journal of the American Chemical Society* **2017**, *139* (46), 16466-16469.
217. Bard, A. J.; Faulkner, L. R., *Electrochemical Methods*. Wiley: New York, 1980.
218. Savéant, J. M.; Vianello, E., Potential-sweep chronoamperometry theory of kinetic currents in the case of a first order chemical reaction preceding the electron-transfer process. *Electrochimica Acta* **1963**, *8* (12), 905-923.
219. Gabrielsson, A.; Hartl, F.; Zhang, H.; Smith, J. R. L.; Towrie, M.; Antonin Vlcek, J.; Perutz, R. N., Ultrafast Charge Separation in a Photoactive Rhenium-Appended Porphyrin Assembly Monitored by Picosecond Transient Infrared Spectroscopy. *Journal of the American Chemical Society* **2006**, *128*, 4253-4266.
220. Kamire, R. J.; Majewski, M. B.; Hoffeditz, W. L.; Phelan, B. T.; Farha, O. K.; Hupp, J. T.; Wasielewski, M. R., Photodriven hydrogen evolution by molecular catalysts using Al(2)O(3)-protected perylene-3,4-dicarboximide on NiO electrodes †Electronic supplementary information (ESI) available: Experimental details; additional electrochemical and photoelectrochemical characterization, UV-Vis spectra, and fsTA results; quantification of evolved hydrogen; and DFT-computed ground state structure of PMI diester. See DOI: 10.1039/c6sc02477g. *Chemical Science* **2017**, *8* (1), 541-549.

## Jose Fabian Martinez

1427 West Lunt Ave #2, Chicago, IL 60626  
541-400-0071 | josemartinez2018@u.northwestern.edu

### EDUCATION

---

- 2013-2018    **NORTHWESTERN UNIVERSITY**    Evanston, IL  
*Doctor of Philosophy in Organic Chemistry*
- Thesis Advisor – Michael R. Wasielewski
  - Thesis – Radical Anions for Artificial Photosynthesis
- 2009-2013    **CORNELL COLLEGE**    Mount Vernon, IA  
*Bachelor of Arts in Computer Science & Chemistry*
- Honors: American Chemical Society Scholarship, Federation of American Societies Biology Grant, Cum Laude
  - President Cornell College ACS Chemistry Club Chapter

### EXPERIENCE

---

- 2018-20XX    **Wilson Sonsini Goodrich & Rosati Professional Corporation**    Palo Alto, CA  
*Scientific Advisor, 2018*
- Patents and innovation team
- 2013-2018    **Northwestern University**    Evanston, IL  
*Graduate Student, Prof Michael R. Wasielewski, 2013-2018*
- Synthesis and catalyst design for electron transfer to CO<sub>2</sub> reduction catalysts
  - Present monthly research updates to ANSER Center
  - Scholarly publications in multiple journals
- Chemistry Skills: Organic Synthesis, Retrosynthesis & Molecular Design, GC-MS, LC-MS, <sup>1</sup>H <sup>13</sup>C <sup>19</sup>F <sup>31</sup>P NMR, FTIR & Raman Spectroscopy, UV-Visible Spectroscopy, HPLC, Optics, TLC, Flash Chromatography, CV Voltammetry, MalDI-TOF-MS, Schlenk Line Techniques, Wet Bench Chemistry, Ultrafast Spectroscopy, Chemical Titration, X-Ray Crystallography
- 2016-2018    **Innovation and New Ventures Office – Northwestern University**    Evanston, IL  
*Patentability and Marketing Analyst Intern, June 2016 – June 2018*
- Conduct searches on prior art/intellectual property landscape/technical publications to advise on disclosures
  - Engaging with patent lawyers, inventors, and invention managers to collect additional data and discuss IP
  - Integrating market data to assess the addressable market while developing market disclosures for clients
  - Technologies: Chemistry – Computer Software/Apps/Hardware – Medical Devices – Life Sciences – Batteries
- 2013    **Northwestern University**    Evanston, IL  
*Visiting Scientist, Dave Harris, May – Sept 2013*
- Developed and synthesized class of bridging ligands (2,5-diarylamine-3,6-dihalogen-benzoquinone) with respect to single chain magnets.
  - Characterized and analyzed products with LC-MS and <sup>1</sup>H <sup>13</sup>C NMR

- 2013-2014 **Northwestern University** Evanston, IL  
*Organic Chemistry TA, Sept 2013 – Aug 2014*
- Directed and supervised weekly Organic Chemistry lab for a group of 15 students
  - Graded lab reports, exams, and held weekly tutoring hours for NU's entire organic undergraduate division
- 2010-2013 **Cornell College** Mount Vernon, IA  
*Office Manager, Aug 2010 – May 2013*
- Reviewed and edited 500+ resumes and cover letters for Cornell College's student body
  - Provide Cornell College's student body with information on careers, internships, and graduate school.
  - Proctor practice MCAT and DAT exams.
- 2011-2013 **Cornell College** Mount Vernon, IA  
*Resident Assistant, Aug 2010 – May 2013*
- Serve as a mentor and advisor for 22 first year students in a Living and Learning community
  - Create, plan, and implement educational, social, and recreational floor programs.
- 2011-2013 **Cornell College** Mount Vernon, IA  
*Chemistry Department Assistant, Aug 2011 – May 2013*
- Train students in the Analytical Chemistry course to use lab instruments.
  - Class tutor for Organic Chemistry 2, Organic Chemistry 1, and General Chemistry.
- 2012 **Rutgers, the State University of New Jersey** New Brunswick, NJ  
*Research Assistant, Prof Alan Goldman, May – Aug 2012*
- Developed first synthesis route to Iridium NH<sub>2</sub>-Pincer Catalyst for alkane dehydrogenation with respect to Jet-Fuel production under Michael Haibach
  - Characterized and analyzed products with <sup>1</sup>H <sup>13</sup>C <sup>31</sup>P NMR
  - Oral and poster presentation of research before faculty and graduate students at Rutgers Summer Symposium
- 2011 **University of Illinois Urbana-Champaign (UIUC)** Urbana, IL  
*Research Fellow, Prof Andrzej Wieckowski, May – Aug 2011*
- Prepared and analyzed samples of porphyrins with various transition metals adsorbed on Au with Raman Spectroscopy
  - Presented research before faculty, post doctorates, and graduate students at UIUC's Summer Symposium
  - Research accepted to be presented at ACS National Meeting San Diego March 2012
- 2006-2011 **Columbia Gorge Hotel** Hood River, OR  
*Assistant Banquet Captain, June – Aug 2011*
- Assisted in directing team of banquet servers to accomplish tasks to fulfill a bride and groom's dream wedding.

**PUBLICATIONS**

---

13. **Martínez, J. F.**; La Porte, N. T.; Sinopoli, A.; Sohail, M.; Wasielewski, M. R., Ten-thousand-fold Enhancement of Photoreduction Lifetime in Mn(bpy)(CO)<sub>3</sub>X Leading to Key Transient Intermediates via Substituent Location Dependence of a Naphthalene Diimide Radical Anion Chromophore. *In preparation* **2018**.
12. **Martínez, J. F.**; La Porte, N. T.; Chaudhuri, S.; Sinopoli, A.; Bae, Y. J.; Sohail, M.; Batista, V. S.; Wasielewski, M. R., Substituent Location Dependence of Photoinduced Electron Transfer Lifetimes to Re(bpy)(CO)<sub>3</sub>X from a Naphthalene Diimide Radical Anion Donor: Effects of Electronic Coupling and Gibbs Free Energy. *In preparation* **2018**.
11. **Martínez, J. F.**; La Porte, N. T.; Wasielewski, M. R., Photoinduced Electron Transfer to Mn(bpy)(CO)<sub>3</sub>X and Re(bpy)(CO)<sub>3</sub>X from Naphthalene Diimide Radical Anion Donors via a Saturated CH<sub>2</sub> Bridge. *In preparation* **2018**.
10. Sinopoli, A.; La Porte, N. T.; **Martínez, J. F.**; Wasielewski, M. R.; Sohail, M., Manganese carbonyl complexes for CO<sub>2</sub> reduction. *Coordination Chemistry Reviews* **2018**, *365*, 60-74.
9. La Porte, N. T.; **Martínez, J. F.**; Chaudhuri, S.; Hedström, S.; Batista, V. S.; Wasielewski, M. R., Photoexcited radical anion super-reductants for solar fuels catalysis. *Coordination Chemistry Reviews* **2018**, *361*, 98-119.
8. **Martínez, J. F.**; La Porte, N. T.; Wasielewski, M. R., Electron Transfer from Photoexcited Naphthalene Diimide Radical Anion to Electrocatalytically Active Re(bpy)(CO)<sub>3</sub>Cl in a Molecular Triad. *The Journal of Physical Chemistry C* **2018**, *122* (5), 2608-2617.
7. Hedström, S.; Chaudhuri, S.; La Porte, N. T.; Rudshteyn, B.; **Martínez, J. F.**; Wasielewski, M. R.; Batista, V. S., Thousandfold Enhancement of Photoreduction Lifetime in Re(bpy)(CO)<sub>3</sub> via Spin-Dependent Electron Transfer from a Perylenediimide Radical Anion Donor. *Journal of the American Chemical Society* **2017**, *139* (46), 16466-16469.
6. Hammarström, L.; **Martínez, J.**; Cogdell, R.; Tolod, K. R.; Kibler, A.; Inoue, H.; Gust, D.; Cassiola, F.; Nocera, D.; Ishitani, O.; Di Fonzo, F.; Domen, K.; Setoyama, T.; Kudo, A., Integration of systems for demonstrating realistic devices: general discussion. *Faraday Discussions* **2017**, *198* (0), 539-547.
5. Artero, V.; Hammarström, L.; Fan, F.; Whang, D. R.; **Martínez, J.**; Harriman, A.; Noguchi, T.; Karlsson, J.; Summers, P.; Itoh, S.; Cogdell, R.; Kibler, A.; Ehrmaier, J.; Tamiaki, H.; Fujita, E.; Shima, S.; Yoshino, S.; Inoue, H.; Wasielewski, M.; Corry, T.; Gust, D.; Cassiola, F.; Ishida, H.; Takagi, K.; Kang, S. O.; Li, C.; Sun, L.; Park, H.; Hashimoto, H.; Amao, Y.; Son, E. J.; Kamiya, N.; Shen, J.-R.; Yamaguchi, K., Biological approaches to artificial photosynthesis, fundamental processes and theoretical approaches: general discussion. *Faraday Discussions* **2017**, *198* (0), 147-168.
4. Wang, M.; Artero, V.; Hammarström, L.; **Martínez, J.**; Karlsson, J.; Gust, D.; Summers, P.; Machan, C.; Brueggeller, P.; Windle, C. D.; Kageshima, Y.; Cogdell, R.; Tolod, K. R.; Kibler, A.; Apaydin, D. H.; Fujita, E.; Ehrmaier, J.; Shima, S.; Gibson, E.; Karadas, F.; Harriman, A.; Inoue, H.; Kudo, A.; Takayama, T.; Wasielewski, M.; Cassiola, F.; Yagi, M.; Ishida, H.; Franco, F.; Kang, S. O.; Nocera, D.; Li, C.; Di Fonzo, F.; Park, H.; Sun, L.; Setoyama, T.; Kang, Y. S.; Ishitani, O.; Shen, J.-R.; Son, H.-J.; Masaoka, S., Molecular catalysts for artificial photosynthesis: general discussion. *Faraday Discussions* **2017**, *198* (0), 353-395.
3. Kumagai, H.; Hammarström, L.; Whang, D. R.; Shinohara, Y.; **Martínez, J.**; Karlsson, J.; Summers, P.; Windle, C. D.; Kodera, M.; Cogdell, R.; Tolod, K. R.; Apaydin, D. H.; Fujita, E.; Kibler, A.; Fan, F.; Gibson, E. A.; Usami, H.; Iwase, A.; Inoue, H.; Kudo, A.; Gust, D.; Domen,

K.; Cassiola, F.; Takagi, K.; Kang, S. O.; Yamakata, A.; Li, C.; Sun, L.; Park, H.; Kang, Y. S.; Li, R.; Di Fonzo, F.; Setoyama, T.; Ishitani, O., Inorganic assembly catalysts for artificial photosynthesis: general discussion. *Faraday Discussions* **2017**, *198* (0), 481-507.

2. La Porte, N. T.; **Martinez, J.**; Hedstrom, S.; Rudshetyn, B.; Phelan, B. T.; Mauck, C. M.; Young, R. M.; Batista, V. S.; Wasielewski, M. R., Photoinduced Electron Transfer from Rylenediimide Radical Anions and Dianions to Re(bpy)(CO)<sub>3</sub> using Red and Near-infrared Light. *Chemical Science* **2017**.

1. **Martinez, J.**; La Porte, N. T.; Mauck, C. M., Wasielewski, M. R.; Photo-driven Electron Transfer from the Highly Reducing Excited State of Naphthalene Diimide Radical Anion to a CO<sub>2</sub> Reduction Catalyst within a Molecular Triad. *Faraday Discussions* **2016**.

## **PRESENTATIONS**

---

Artificial Photosynthesis: Faraday Discussion. Ritsumeikan University, Kyoto, Japan 2017  
Northwestern Black Graduate Student Association: 20th Annual Research Conference and Symposium. Chicago, IL 2017

Cornell College Symposium. Mount Vernon, IA 2012-2103

Rutgers, the State University of New Jersey Summer Symposium. New Brunswick, NJ 2011

University of Illinois Urbana-Champaign. Urbana, IL 2010

## **ADDITIONAL SKILLSETS & EXPERIENCES**

---

2014-2016	Niles West High School Mentorship Program	Evanston, IL
2016-2018	Hayt Elementary School – Chemistry demonstrations in Spanish for underrepresented minorities	Chicago, IL
2013-2017	Northwestern Triathlon competed ITU 2015 World Championship	Evanston, IL

**Writing Skills:** Completed Medill School of Journalism course on best practices for science writing/communication for the masses

**Computer Skills:** JAVA programmer | Certified LabView Associate Developer | MATLAB | Microsoft Office | SQL | SciFinder | Patsnap

- Algorithms and Data Structures, Computer Networks, Data Management Systems (MySQL), Computer Organization, Software Engineering, Mashups, Linear Algebra, Differential Equations, Discrete Mathematics

Thesis title: Photoexcited Rylenediimide Radical Anions and Dianions for the Photoreduction of Carbon Dioxide Reduction Catalysts

Title of thesis may also be: Super Reductants for Artificial Photosynthesis: Synthesis and Mechanistic Understandings for the Photoreduction of Rhenium(I)/Manganese(I) Tris Carbonyl Diimine Catalysts by Naphthalene & Perylene Diimide Radical Anions and Dianions